uOttawa

L'Université canadienne
Canada's university

FACULTÉ DES ÉTUDES SUPÉRIEURES ET POSTOCTORALES

uOttawa

L'Université canadienne
Canada's university

FACULTY OF GRADUATE AND POSDOCTORAL STUDIES

Michael Paciocco
AUTEUR DE LA THÈSE / AUTHOR OF THESIS

M.A.Sc. (Mechanical Engineering)
GRADE / DEGREE

School of Information Technology and Engineering
FACULTÉ, ÉCOLE, DÉPARTEMENT / FACULTY, SCHOOL, DEPARTMENT

Measurements of Pulsatile Flow in an Idealized Ventricular Assist Device

TITRE DE LA THÈSE / TITLE OF THESIS

Stavros Tavoularis
DIRECTEUR (DIRECTRICE) DE LA THÈSE / THESIS SUPERVISOR

CO-DIRECTEUR (CO-DIRECTRICE) DE LA THÈSE / THESIS CO-SUPERVISOR

Edgar Matida

Catherine Mavriplis

Gary W. Slater
Le Doyen de la Faculté des études supérieures et postdoctorales / Dean of the Faculty of Graduate and Postdoctoral Studies

Measurements of Pulsatile Flow in an Idealized Ventricular Assist Device

Michael C. Paciocco

Thesis submitted to the Faculty of Graduate and Postdoctoral Studies
in partial fulfillment of the requirements for the degree of

MASTER OF APPLIED SCIENCE

in Mechanical Engineering

Ottawa-Carleton Institute for Mechanical and Aerospace Engineering
University of Ottawa
Ottawa, Ontario, Canada

December 1, 2009

Your file Votre référence
ISBN: 978-0-494-61182-1
Our file Notre référence
ISBN: 978-0-494-61182-1

Abstract

Ventricular Assist Devices (VAD) are mechanical pumps connected to the human circulatory system in order to assist the left ventricle of diseased hearts in pumping blood to the body. Currently, both pulsatile and non-pulsatile VAD are used, primarily as a bridge to heart transplantation, with new generation devices under development to become alternatives to transplantation. Negative interactions between the biological components of the flow and the mechanical system, such as poor washout, recirculation, thrombosis and hemolysis need to be minimized in order to improve performance and longevity of both the device and the patient.

The present research is an experimental study of flow in a highly idealized, diaphragm-type, pulsatile-flow VAD. Its objective is to document in detail the motions of the fluid and the diaphragm so that they can be used for the validation of ongoing numerical simulations of flows in such devices, and more generally to assist in the validation of computational methods involving fluid-structure interaction. Measurements of the flow field were collected using both Laser Doppler Velocimetry (LDV) and Particle Image Velocimetry (PIV). The PIV system was used to measure the instantaneous velocity variation along each of six different planes at several different times during the cycle, whereas the two-component LDV system was used to measure the time-dependent velocity at several points of interest over the entire cycle. The images recorded by the PIV system camera have also been used to determine the instantaneous shape and position of the diaphragm at different times during the cycle.

Representative and averaged PIV images showed that the inlet jet created a core

vortex in the VAD that is the primary means of mixing. The development and motion of this vortex over the VAD operational cycle was documented for use in future modelling. A previously unobserved vortex was also documented. This vortex appeared in the vertical plane, beneath the inlet jet at peak injection, and moved along the path of the jet during the injection phase. It is believed that this vortex is created by the interaction of the inlet jet and the diaphragm in motion during injection and represents a region of recirculation in the flow, as well as possible flow separation. Other regions of recirculation were identified in the area directly adjacent to the outlet jet during ejection of the flow, and along the surface of the VAD directly opposite of the outlet tube just prior to the beginning of the ejection cycle. Areas of stagnant flow were also observed, particularly in the inlet and outlet tubes in periods of inactivity. The flow during ejection was localized in the region of the VAD directly adjacent to the outlet tube. The ejection has a longer period and a lower peak velocity than the injection.

The motion of the VAD diaphragm was also studied and it was found that the diaphragm deformation was influenced by the inlet jet. The diaphragm shape was nearly axisymmetric during some parts of the cycle, but highly skewed during other parts. Small-scale motions were also present in the diaphragm, and fluctuated from one cycle to another, adding to irregularities in the flow. Dimensional analysis of the flow strongly suggested that the unsteady nature of the flow was the dominant feature of the flowfield.

Recommendations for future experimental work include the addition of valves and a mock circulatory loop, as well as the use of different settings for the LDV and PIV systems for different parts of the VAD and different parts of the cycle.

To Antonio, Maria, and Pasquale Turco and Angela Paciocco - Good role models are hard to come by.

Acknowledgments

Inestimable thanks to my parents Domenico and Rosanna Paciocco, my siblings David and Cristina, and my uncle Sergio for their unflagging support during this trial. None of this would have been possible without your encouragement, patience, and grace.

Gratitude goes out to my supervisor, Dr. Stavros Tavoularis, for providing me with this opportunity, and his insight and guidance throughout this project. Recognition goes out to the efforts of the University of Ottawa, as well as John Perrins, Leo Denner, James MacDermid, Mike Burns and Stan Weedmark of the Mechanical Engineering Department's machine shop for their time, advice and assistance in bringing this project to fruition.

Acknowledgement and thanks to the friends I made at the University of Ottawa; Andrew Cameron, Dr. Dongil Chang, George Choueiri, Matthew Doyle, Derek Lastiwka, Julia Turriff and Christina Vanderwel for their assistance and camaraderie over the years.

Contents

Nomenclature

A	area
C_1	arbitrary constant
C_1	material constant
d	diameter
d_p	average seeding particle diameter
E	uncertainty
f	frequency
H	Material Thickness
P	static pressure
p	order of convergence
Q	flow rate
r	radius
Re	Reynolds number
r	vector magnitude or distance
St	Strouhal number
SV	Stroke Volume

T	period
t	time
U	velocity magnitude
u, v, w	streamwise, crossflow/secondary flow, and spanwise velocity components
V	volume
Wm	Womersley number
x, y,z	cartesian coordinates

Greek symbols

α	flowrate coefficient
Δ	difference in property
δ	relative change in a flow parameter
Λ	wavelength
μ	dynamic viscosity
ρ	density
ϕ	phase angle
Ω	angular frequency

Subscripts

B	bulk property
D_h	hydraulic diameter
in	conditions or property at inlet boundary
max	maximum value
out	conditions or property at outlet boundary

Other notation

$\vec{g}$	vector
$\overline{\overline{g}}$	space-time area weighted average
$\overline{\widetilde{g}}$	space-time mass weighted average
$\bar{g}$	time average
$\widetilde{g}$	density weighted average
$\langle g \rangle$	ensemble of realizations
g'	fluctuating component

Acronyms

CFD	computational fluid dynamics
FSI	fluid structure interaction
LDV	laser Doppler velocimetry
PIV	particle image velocimetry
RBC	red blood cell
VAD	ventricular assist device

List of Figures

List of Tables

Main Part

Chapter 1

Introduction

Ventricular Assist Devices (VAD) are mechanical pumps connected to the human circulatory system in order to assist the left ventricle of diseased hearts in pumping blood to the body. There are two main types of available VAD: pulsatile pumps, which produce a periodically varying flow mimicking the biological operation of the ventricle, and non-pulsatile, centrifugal or axial pumps, producing continuous flow. Both types are effective, which demonstrates that the pulsatility of natural hearts is not necessary to sustain life (Doyle (2004)). Improvements in numerical modelling of flow features, with special consideration given to the impact of the design on possible adverse effects, such as hemolysis and thrombosis, will yield designs that are safer and more practical for wider use.

1.1 Motivation

For thousands of people in advanced stages of heart disease, especially those facing potentially fatal conditions such as congestive heart failure, a heart transplant remains the treatment option with the highest chance of long-term survival. Unfortunately, donor supplies are dramatically outpaced by ever-increasing demand, and this trend is expected to continue well into the future. This demand makes necessary the development and continual improvement of alternative methods of supporting the cardiovascular system in critical times, until a more permanent solution becomes available Depending on the circumstances of the specific individual, mechanical means of supporting cardiovascular function, such as the use of a VAD, can be considered for three types of treatment (Gray and Selzman (2006)).

- Bridge to recovery: when damage to the left ventricle is expected to heal through other means of treatment, a VAD can be implanted on a temporary basis to compensate for the loss of cardiovascular capacity, while this treatment is administered.
- Bridge to transplant: when a delay is expected before a donor heart for transplant is available, a VAD can be implanted to compensate for the loss of cardiovascular capacity until the donor heart becomes available for the transplant operation.
- Destination therapy: an increasing trend is to permanently implant a VAD into a patient to compensate for the loss of cardiovascular capacity and provide quality of life on an outpatient basis.

Recent studies have also determined that, while VAD implantation has increased overall survival rates, difficulties arising from features of the VAD design may also contribute to serious patient complications, requiring aggressive treatments that pose significant risk to the health of the patient (Haddad et al. (2004)). The growing trend in VAD use as a bridge to transplant and as a final destination therapy requires a comprehensive understanding of the interactions between the blood and the mechanical system. Negative interactions between the biological components of the flow and the mechanical system such as poor washout, recirculation, thrombosis and hemolysis should be minimized in order to improve performance and longevity of both the device and the patient.

1.2 Objective and Scope

The present research is an experimental study of flow in a highly idealized diaphragm-type, pulsatile-flow VAD. The objective is to document in detail the velocity field variation throughout the cycle so that it can be used for the validation of ongoing numerical simulations of VAD operation (Doyle et al. (2008)) and to serve as a benchmark for validating future analyses involving fluid structure interaction. In particular, this study will focus on the measurement of the following properties:

- Variation of the shape and position of a flexible circular diaphragm that is clamped around its perimeter
- Temporal and spatial variation of flow velocity throughout the cycle
- Vortex formation and evolution throughout the cycle
- Other distinguishable flow patterns

The study will be carried out using an experimental apparatus which simulates an idealized pulsatile-flow VAD. Measurements of the flow field will be collected using both Laser Doppler Velocimetry (LDV) and Particle Image Velocimetry (PIV) measurement systems. The PIV system will measure the instantaneous velocity variation along each of six different planes at several different time steps, while the LDV system will take time-dependent two-component velocity measurements at several points of interest over the entire cycle. Both measurement systems will operate over several cycles and the results will be phase-averaged to remove the effects of cycle-to-cycle variations. The images recorded by the PIV system camera will be also used to determine the shape and position of the diaphragm at different times during the cycle. The PIV results will be analyzed to identify characteristic flow patterns, particularly vortices, recirculation regions and stagnation regions. The study will include a systematic documentation of the variations of the flow velocity, vorticity and strain rate inside the VAD over the operational cycle, and comparison to results of other related studies.

1.3 Outline

The following Chapter provides a literature review of previous and ongoing studies of VAD, as well as summarizing the major challenges that are present in the design, numerical modelling, and experimental measurement of these systems. Chapter 3 describes the experimental apparatus and measurement procedure. Measurements of the flowrate and the motion of the diaphragm are described in Chapter 4, whereas Chapter 5 provides the LDV measurement results and Chapter 6 provides the PIV results. Chapter 7 provides additional discussion of these results including comparison to previous experimental and numerical results. Conclusions and recommendations for future experimental studies and numerical simulations are contained in Chapter 8.

Chapter 2

Literature Review

2.1 *In Vivo* Studies of VAD

The University of Ottawa Heart Institute recently completed a comparative study of several patients using the Novacor VAD (WorldHeart Inc. Oakland, CA, USA) and the Thoratec VAD (Thoratec Laboratories Corporation Inc., Pleasanton, CA, USA). It was observed that, although VAD implantation increased survival rates overall, many patients suffered serious complications arising from thrombus formation, requiring aggressive anti-coagulation therapy (Haddad et al. (2004)). A separate *in vivo* study using the Novacor VAD was conducted in bovines to test the validity of lumped parameter numerical modelling. The interaction between the living ventricle and the VAD was studied closely, and it was observed that the existing numerical models adequately captured this interaction (Vandenberghe et al. (2006)).

The two main adverse effects common to Ventricular Assist Devices (VAD) are hemolysis and thrombosis. Hemolysis is the damaging or destruction of red blood cells

(RBC) in the flow field. Thrombosis is the end result of a complex series of biochemical and biomechanical processes that activate the platelets, which subsequently combine to form a thrombus. Thrombosis results in the creation of clots in the blood and is potentially fatal to a patient (Day and McDaniel (2005a)).

2.2 Numerical Simulations of VAD

The elementary equations and underlying assumptions for the modelling of blood flow have been studied for some time and are well understood. Blood is considered to be a quasi-homogeneous non-Newtonian suspension. Nevertheless, by applying certain simplifications and assumptions which are valid under certain conditions, one may model blood as a Newtonian fluid. This model is only valid for relatively small time intervals, under conditions for which the lumped parameter "well mixed solution" assumption applies, and for shear rates greater than 200 s^{-1} (Kleinstreuer (2006)). Early numerical models assumed a steady flow, which is valid for non-pulsatile VAD pumps, such as centrifugal or axial pumps. The purpose of these simulations was to model the contribution of bulk turbulent stress and compare it to wall shear stresses and other factors in the flow field. These early two-dimensional models used a steady flow state with known inflow and outflow conditions and the k-ϵ turbulence model and compared with existing experimental results (Kim et al. (1992)).

Computational Fluid Dynamics (CFD) is widely used to model VAD designs and suggest modifications to existing designs. One of the benefits of CFD as a design tool is its ability to detect adverse effects early in the design cycle of a given VAD, provided of course that the numerical models and applied conditions are valid. In particular, modelling the interactions between the device surfaces and blood under physiological conditions can be used to predict regions where hemolysis and thrombosis may occur (Verdonck (2002)). For example, the k-ϵ turbulence model was used to model the flow in a microaxial VAD in order to estimate the wall effects. The simulations were useful in predicting regions where flow-induced hemolysis might occur when compared to experimental results. Another result of this study was to determine the probability of inducing hemolysis based on shear stress and exposure using both the k-ϵ and k-ω turbulence models (Apel et al. (2001)).

CFD has been used in previous studies of pulsatile-type VAD pumps. The Novacor VAD is a sac-type pulsatile VAD that is compressed by two plates, and has been studied using lumped parameter circulation models to evaluate its performance. These models have helped in identifying the sensitivity of the VAD to a range of parameters, such as the volumetric flow rates at the inlet and pressure in the inlet and outlet, but provided very little information on the motion of the fluid in the flow field (Yu et al. (2001)). CFD studies may also account for the differences in flow characteristics when using Newtonian and non-Newtonian models as well as predict hemolysis in VAD operation (Burgreen et al. (2001)).

Developing a valid model for Fluid Structure Interactions (FSI) in VAD studies presents a significant challenge. A successful FSI model for VAD systems must fully couple the motion of a flexible structure, such as a collapsing sac wall or a free flexible diaphragm, and the flow of blood. At the same time, a successful FSI model for the VAD is required to isolate the instantaneous local flow characteristics from cyclical variations. Recent

FSI models tested for a sac-type VAD implementation show generally good agreement with experimental results (Avrahami et al. (2006), Doyle et al. (2008)). FSI simulations by Doyle *et al.* (Doyle et al. (2008)) have described the general characteristics of the flow in an idealized diaphragm-type pulsatile VAD. These numerical simulations also included models for determining the possible occurrence of thrombosis during a given cycle, and suggested that thrombosis would occur in areas of stagnation, recirculation, and low shear stress, including, for example, regions adjacent to the inlet and outlet tubes. In contrast, hemolysis is generally considered to occur in areas of high shear stresses (Avrahami et al. (2006)). A recent numerical simulation was carried out that coupled FSI with known flow conditions in a pulsatile VAD model (Moosavi et al. (2008)); its results showed that the maximum values of the velocity, the velocity gradient, and the shear occur near the inlet and outlet valves.

2.3 Experimental Studies of VAD

Early experimental investigations of VAD models focussed on the identification of common flow features, such as areas of stagnation, recirculation and high shear (Mann et al. (1987)). These early experiments applied flow visualization which demonstrated that higher stroke volumes in pulsatile VAD pumps decreased recirculation and stagnation in the blood chamber (Mussivand et al. (1988)). Hot film probes were used in a study to measure wall shear in a VAD pump under normal operating conditions (Baldwin et al. (1988)); this study also concluded that whereas thrombosis is the product of low shear, hemolysis would occur in regions of high shear . The Heartsaver VAD (WorldHeart Inc.

Oakland, CA, USA) was the subject of a parametric study in which pressure measurements and flow visualization and image analysis were combined. This study observed that the wall shear stresses were not linearly related to the pulsation rate or the pressure conditions at the inlet and outlet tubes, and that increasing the diameter of the inlet or outlet tubes lowered velocity and turbulence, but also increased stagnation in the flow field (Mussivand et al. (1999)). Parametric studies have also been conducted on the sensitivity of the VAD flow to the orientation of mechanical heart valves (MHV), which have suggested an optimum orientation of 45 degrees for mixing and washout of the VAD. These conditions and orientations of MHV fall outside the scope of this study, but are important considerations for future experiments and implementations (Kreider et al. (2006)). This study was followed by a comparative analysis between CFD modelling and PIV measurements of the velocity profile and scalar strain in normal VAD operation (Medvitz et al. (2007)), which recommended increased focus on the understanding of the dynamics of the diaphragm and the fluid mixing in the VAD.

Many experimental models for the behavior of the human circulatory system have been developed and evaluated for their ability to model the non-linearities present in human circulation. A valid model of the circulatory system under physiological conditions is required to properly evaluate the performance of VAD design (Conlon (2006)). Studies of unsteady flows in sac-type VAD models using a simplified mock circulation loop and Laser Doppler Velocimetry (LDV) measurements have been conducted to generate ensemble averages of the velocity distribution in the flow field. Flow visualization techniques were also used to qualitatively describe the characteristics of the flow. Bulk measurements of residence times were taken, and the effects of altering stroke volume and heart rate were examined. The results of these experiments determined that the VAD had a higher sensitivity to changes in the stroke volume than in the pulsation frequency (Jin and Clark (1993)).

An experimental study with an idealized operation of a pulsatile VAD model was conducted. The objective of this study was to model the dynamics of normal VAD operation in order to develop models for fluid-structure interaction (FSI) and moving boundary conditions. The flow was assumed to be laminar, unsteady, Newtonian, incompressible and isothermal for the purposes of developing a numerical model. A hydraulic piston with a hemispherical head was used to simulate the idealized motion of a diaphragm under normal operation (Konig and Clark (2001)). The results suggested that transition to turbulence was a function of both the Reynolds number (Re) and the Womersley number (Wm) and that the critical Reynolds number Re_c was given by the formula

$$\mathrm{Re}_c = c\mathrm{Wm} \tag{2.1}$$

where c is a constant in the range from 250 to 1000. The Wormersley number is a dimensionless measure of the importance of unsteadiness on the characteristics of periodic viscous flows, and is defined as

$$\mathrm{Wm} = R\left(\frac{\Omega\rho}{\mu}\right)^{\frac{1}{2}} \tag{2.2}$$

where, for VAD, R can be taken to be the radius of the inlet or outlet tube, Ω is the angular frequency of pulsation, ρ is the density of the working fluid, and μ is the dynamic viscosity. A low value of the Womersley number would suggest that viscous effects would dominate the flow, such that the pressure and velocity profiles would be fully developed in the inlet and outlet tubes (Konig et al. (1999)).

2.4 PIV Studies

A feature common to flow in VAD that is difficult to model numerically is the rapid change in direction over the operating cycle. This also presents a challenge in the selection of methods and measuring systems for experiments: either a measurement system with a high sampling rate such as Laser Doppler Velocimetry (LDV) can be used to capture the temporal variation of the local velocity, or a Particle Image Velocimetry system can be used to map the velocity variation over a planar section of the flow field at specific points in time. Successful PIV measurements in a periodic flow such as a VAD require a careful selection of the measurement times and the time discretization scheme (Konstantinidis et al. (2004)). PIV was proved to be a powerful measurement tool for studying fluid flow in VAD systems, but useful information can only be obtained with practical models for predicting hemolysis and thrombosis (Qian et al. (2007)). A comparative study on a centrifugal VAD was carried out comparing CFD results to PIV measurements (Day et al. (2002)). The differences in these results highlight the requirements for better turbulence models and boundary conditions.

Studies have also been conducted to determine the effect of heart rate and the duration of a given pump cycle in causing flow-induced hemolysis in a pulsatile VAD pump. The results showed that while increased heart rates prevented stagnation of the flow, they also increased shear, which would increase flow-induced hemolysis, while not producing a noticeable effect on mixing in the blood chamber (Oley et al. (2005)). Recent PIV studies have been performed on a centrifugal VAD pump using both steady and unsteady flow conditions. In the steady flow study, the heart rate was altered outside the specified design rate, but still within the range of possible physiological values. PIV was used to identify and study regions of high and low shear, as well as stagnation. This study determined that lower heart rates produced stagnation and recirculation, thus increasing the probability of thrombosis, while higher heart rates yielded increased levels of hemolysis (Day and McDaniel (2005a)). The unsteady case determined that the inlet and outlet velocity and pressure profiles differed due to acceleration and pulsatility of the flow field. It was also noted that a pulsatile or quasi-pulsatile flow will result in better washout and mixing in the pump, thus reducing the stationary recirculation regions that would be present in a steady flow case (Day and McDaniel (2005b)).

The effects of a flexible diaphragm on the flow in a pulsatile VAD must be understood for any FSI model to yield an accurate result. This is especially important when determining the flow field when the fluid is entering and ejecting from the VAD. An experimental study was conducted on the 70 cc Penn State VAD (Arrow International, Reading, PA, USA) using a mock circulatory loop to simulate the physiological compliances for inlet and outlet conditions. The characteristics of the flow were observed in two cases: one for which the flexible diaphragm was glued to a hydraulic piston, and one for which the diaphragm was free to deform. In the glued case, a single large vortex was observed during VAD filling and is considered to be the primary mechanism of VAD washout. In the free diaphragm case the inflow waveform was different from that in the glued case. Furthermore, while the inlet and outlet waveforms were similar in the glued case, the free diaphragm case displayed no such similarity. The peak in the outlet velocity was significantly lower than the peak inlet velocity in the glued diaphragm case, but the fluid ejection took place over a longer period of time, so that the overall mass of fluid in the VAD pump remained consistent over time. It was suggested that material effects such as buckling at the edge of the diaphragm may be a contributing factor to the non-linearities in the free diaphragm motion. This study suggested that the small scale motions observed in the free diaphragm case were characteristics of efficiency loss, and that the overall pump performance was not significantly sensitive to the thickness of the diaphragm within a given range (Hochareon et al. (2003)).

Further investigation was conducted using PIV to measure shear rates at the walls of the VAD as well as velocity. While many possible factors contribute to the uncertainty of such a study, recent developments in PIV image analysis significantly reduced the potential for error. Current PIV methods thus provided for accurate wall shear estimation for use in evaluating the performance of pulsatile VAD (Hochareon et al. (2004c)). PIV measurements were taken at times of peak velocities and vortex activity in the VAD operational cycle. There were several instances of a change of sign in the wall shear at the inlet during peak injection into the VAD pump, suggesting local flow separation. High shear was observed near the valves and the inlet, suggesting that these regions will likely induce hemolysis during periods of peak flow. There were also signs of low shear along the surface of the VAD in the regions adjacent to the inlet and outlet tubes as well as the surface located directly opposite to these tubes, making them likely candidates as regions where thrombosis would occur (Hochareon et al. (2004b)). Further study focused specifically on the region of the VAD surface opposing the inlet and outlet tubes in order to confirm the existence of flow conditions that would induce thrombosis. These results were then correlated with earlier *in vivo* studies of VAD in bovines (Hochareon et al. (2004a)). A recent review of pulsatile VAD research focusing on the Penn State 50 cc pulsatile model focused on the effects of turbulence. This review noted that many measurements of some regions were incomplete due to interference from the diaphragm, as well as demonstrating the importance of the Strouhal number St as a means of comparing the performances of different pulsatile pumps (Deutsch et al. (2006)). In order to properly define the values for VAD operation, a dimensional analysis was conducted to find the correct time, length and velocity scales (Bachmann et al. (2000)) In the most general case, the Reynolds and Strouhal numbers are defined as follows

$$\mathrm{Re} = \frac{UL\rho}{\mu} \tag{2.3}$$

$$\mathrm{St} = \frac{UT}{L} \tag{2.4}$$

where U is the velocity scale, T is the timescale, and L is the length scale For pulsatile VAD geometry, the scales were chosen as follows (Bachmann et al. (2000))

$$T = \frac{1}{f} \tag{2.5}$$

$$L = d \tag{2.6}$$

$$U = \frac{8Q}{\pi d^2} = \frac{8\ f\ SV}{\pi d^2} \tag{2.7}$$

where Q is the flowrate, d is the inlet tube diameter, f is the frequency, and SV is the stroke volume. These relationships lead to the following equation for the Reynolds number in periodic VAD flow (Bachmann et al. (2000))

$$\mathrm{Re} = \frac{8\rho}{\pi\mu}\frac{f\,SV}{d} \tag{2.8}$$

The Strouhal number is a dimensionless parameter that measures the ratio between the local acceleration of a pulsatile flow and the differences in velocity at a point in a given flow. For VAD, the Strouhal number can be defined by the equation (Bachmann et al. (2000))

$$\mathrm{St} = \frac{4}{\pi}\frac{SV}{d^3} \tag{2.9}$$

Chapter 3

Experimental Facilities and Procedures

3.1 Experimental Apparatus

The design of the VAD model for this experiment was based on an earlier model used at Brunel University (Konig et al. (1999)). The experimental setup included the VAD model, two reservoirs for the working and driving fluids, respectively, the solenoid-valve assembly, and the motor-piston assembly that set the driving fluid in motion. The VAD model was constructed from two acrylic blocks; each block was machined into a hemi-spherical chamber with a diameter of 70 mm and was fine-polished to a smooth and clean surface. The lower chamber containsed a single tube with a diameter of 19 mm connecting it to the driving fluid reservoir, as shown in Figures 3.4, 3.5 and 3.6 (Vergniaud (2001)). The driving fluid reservoir, displayed in Figure 3.7, had walls made of acrylic material (plexiglass) with a thickness of 9.5 mm and inner dimensions measuring 133.4 mm × 141.3 mm × 136.6 mm. Its far wall had a circular opening with a diameter of 114.3 mm machined to accommodate a circular plate with a diameter of 88.9 mm, on which a latex diaphragm was attached and which served as a piston being connected to the motor-piston assembly. The opposing wall had a circular opening that was aligned with the tube in the lower VAD chamber, as displayed in Figure 3.7 (Vergniaud (2001)). The upper chamber contained the working fluid and two tubes, each having a diameter of 19 mm, with centres 30 mm apart, whose ends are at a distance of 78.5 mm from the centre of the hemisphere and which lead to the valves and the working fluid tank, as shown in Figures 3.1, 3.2 and 3.3 (Vergniaud (2001)). The ends of these two tubes were alternately blocked by a 19 mm thick sliding plate, displayed in Figure 3.9, made of teflon and machined with openings with centers 25.4 mm apart to simulate, the opening and closing of the valves in the left ventricle.

The opening and closing of the valves are accomplished by the motion of this plate, which is enforced by the activation of a dual-action solenoid (Murphy RP2307B, FW Murphy, Tulsa, Oklahoma, USA) as displayed in Figure 3.12 (Vergniaud (2001)). The solenoid is mounted on a steel frame, which is bolted on the laboratory floor and is not in contact with the main assembly to minimize vibrations of the VAD due to the solenoid motion. The working fluid tank, displayed in Figure 3.8 is constructed of plexiglass 9.5 mm thick; with inner sides measuring 305 mm x 305 mm x 298 mm and operates with its free surface open to the atmosphere and was usually filled to a depth of 265 mm, as shown in Figure 3.11 (Vergniaud (2001)). The lower chamber has a single tube extending 55 mm from the centre of the hemisphere and leading to the driving fluid reservoir, which is sealed on one side by a diaphragm consisting of six layers of natural rubber latex (A.R. Medicom, Lachine, Québec, Canada), each with a thickness of 0.18 mm and stacked together without any adhesive for a total thickness of 1.08 mm. This diaphragm is driven by a piston on its side attached to the circular plate of the driving fluid tank. All three tubes in the VAD have a diameter of 19 mm and are also fine polished. The upper and lower chambers are separated by a diaphragm of natural rubber latex (A.R. Medicom, Lachine, Québec, Canada) with a thickness of 0.18 mm. The natural rubber latex diaphragm used in this set up differs from that used in a previous experiment, which used a neoprene material; the natural rubber latex diaphragm was also not prestretched (Vergniaud (2001)). The natural rubber latex used in all diaphragms is assumed to deform as a neo-Hookean material, according to the equation (Verron et al. (2001))

$$\Delta P = 32\frac{C_1 H \Delta^3}{R^4} \tag{3.1}$$

where ΔP is the applied pressure, H is the material thickness, C_1 is a material constant, R is the radius of the disk, and Δ is the maximum displacement (Christensen and Feng (1986)). For the current set-up, the material is natural latex rubber with $C_1 \simeq 141.5$ kPa (Verron et al. (2001)), $R = 35$ mm, $H = 0.18$ mm, and $-13 < \Delta < 14$ mm, from which the pressure field along the surface of the diaphragm can be estimated. The driving fluid used in this study is distilled water, which fills the bottom half of the VAD assembly and the driving fluid reservoir. Flow of the driving fluid into and out of the lower VAD chamber is generated by the motion of the diaphragm described in the previous paragraph, attached to a reciprocating piston with a 20.2 mm stroke, which is driven by a mechanism including a connecting rod, a cam and an electric motor. This system is illustrated in Figure 3.13.

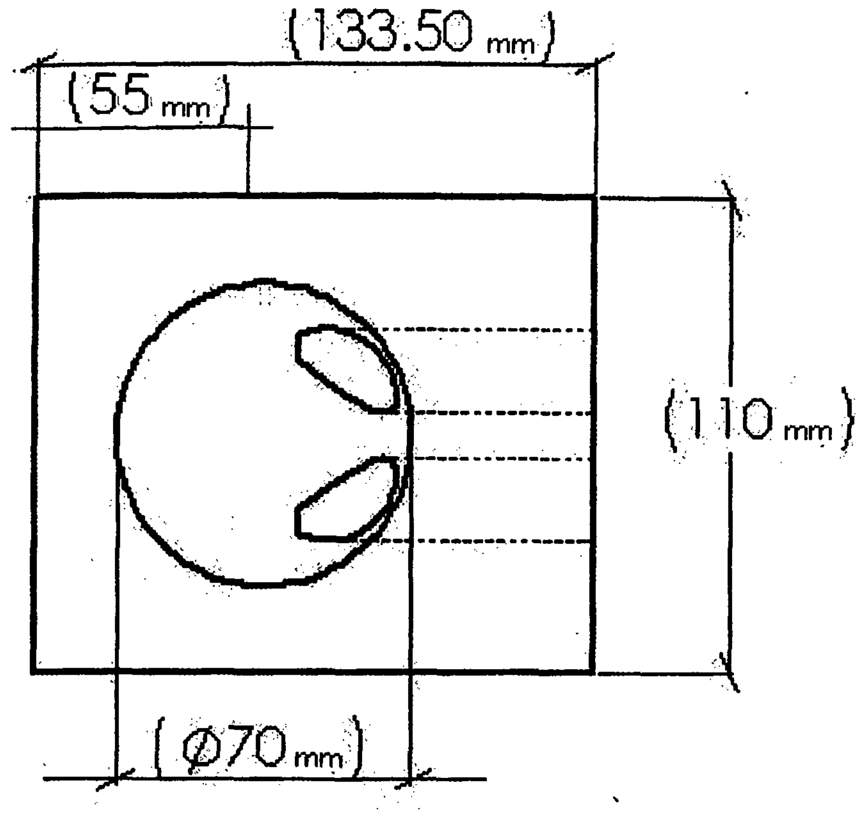

Figure 3.1: VAD upper chamber (top view)

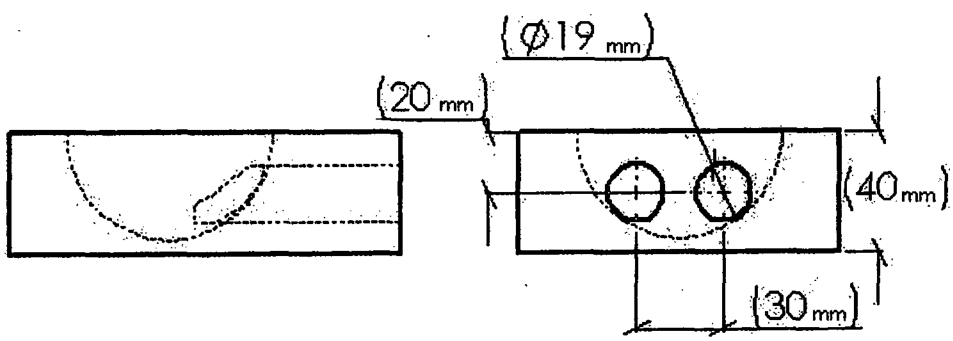

Figure 3.2: VAD upper chamber (side views)

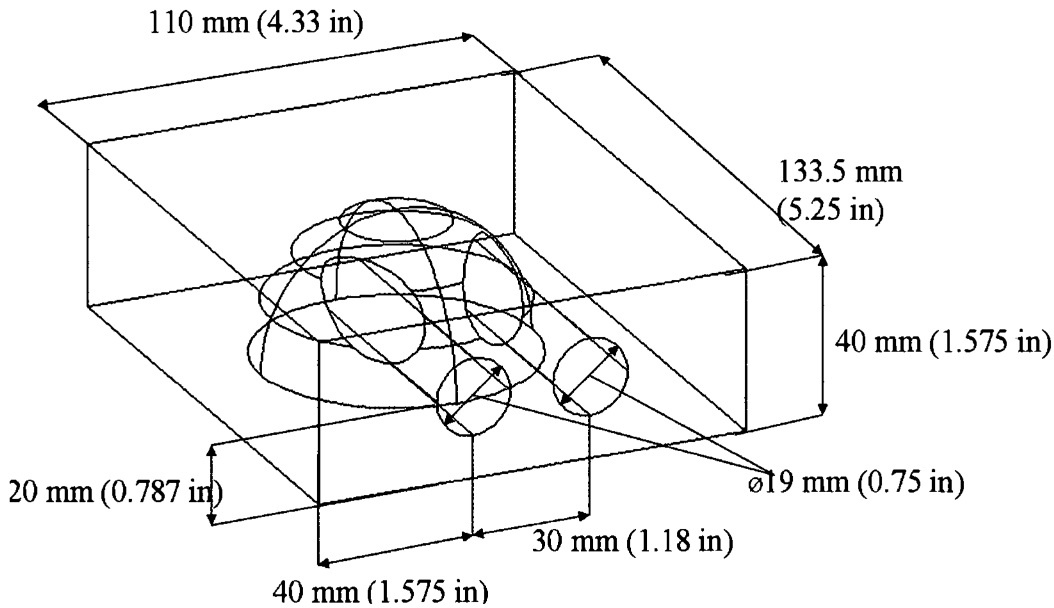

Figure 3.3: VAD top schematic view

The displacement of driving fluid from its tank into and out of the lower chamber of the VAD model causes corresponding deformation of the VAD diaphragm, which in turn displaces the working fluid. The working fluid is a mixture of 60% (by volume) saturated aqueous solution of ammonium thiocyanate and 40% glycerol. Its viscosity approximates that of whole blood and its refractive index matches the refractive index of the acrylic walls, as shown in Table 3.1; it also contains naturally buoyant crystals which circumvent the need for seeding the flow with foreign particles. During normal operation of the apparatus, the VAD pulsation period was $T_{av} = 1.32$ s. The operation of the valves is synchronized with the movement of the driving fluid piston such that the plate moves to block the opening of the outlet tube and free the opening of the inlet tube to allow the VAD to fill as the driving fluid is drawn out of the lower VAD chamber by the motion of the motor-piston assembly.

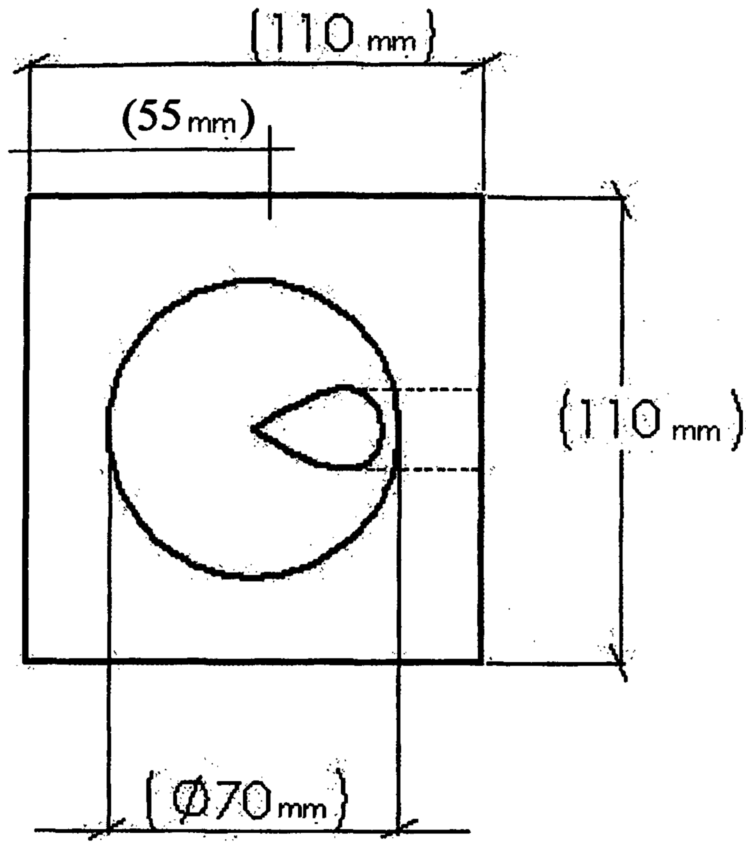

Figure 3.4: VAD lower chamber (top view)

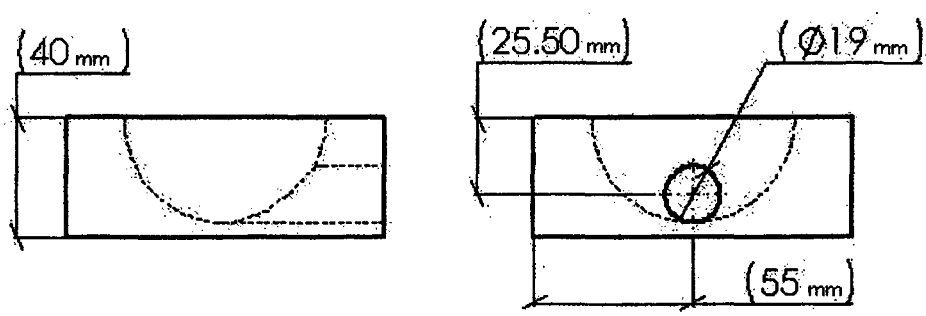

Figure 3.5: VAD lower chamber (side view)

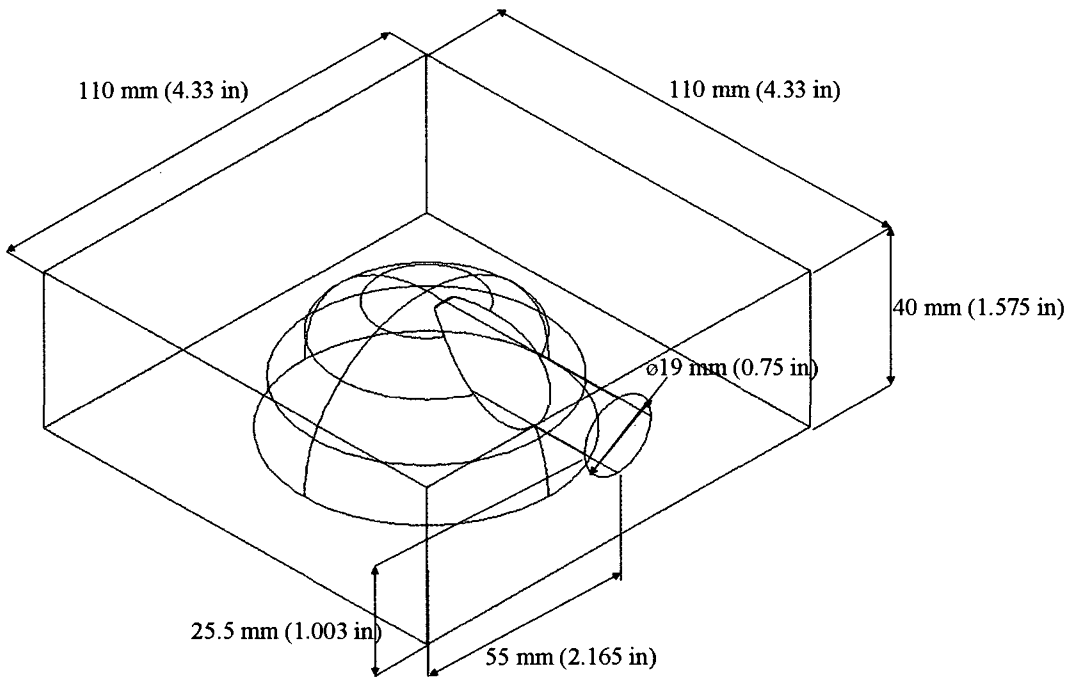

Figure 3.6: VAD bottom schematic view

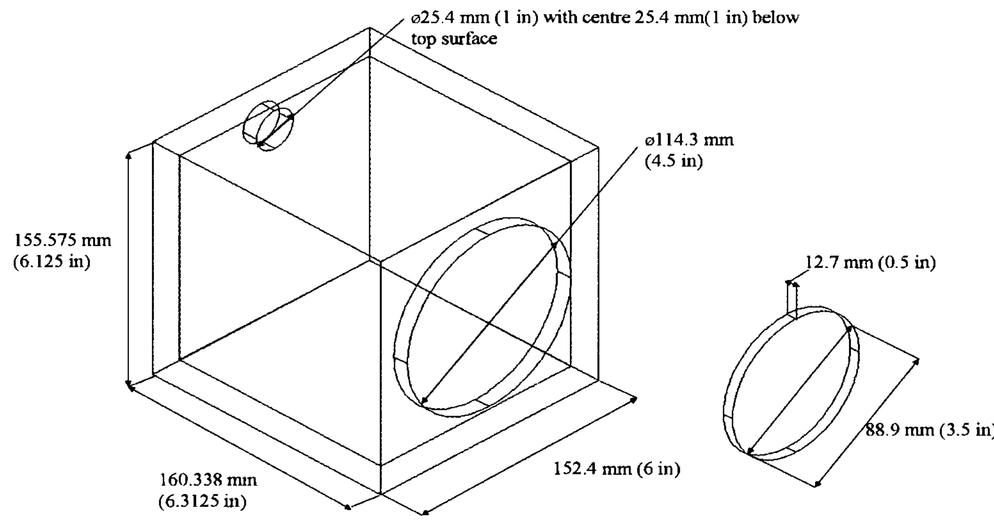

Figure 3.7: Driving fluid reservoir schematic view

Table 3.1: Working Fluid Properties

Material	ρ (kg/m^3)	μ (Pa s)	Refractive Index
Blood	1060	4.66×10^{-3}	–
Working Fluid	1155	3.8×10^{-3}	1.488

Similarly, when the filling cycle peaks, the plate moves to free the opening of the outlet tube and to block the opening of the inlet tube. The solenoid is synchronized with the motion of the motor-piston assembly with the use of two impulse triggers connected to a relay circuit mounted on the arc of the camshaft. This relay is also connected to a circuit which outputs a square wave as the solenoid is activated; this serves as a trigger input into the measurement systems, permitting the monitoring of the starting time and the duration of each cycle.

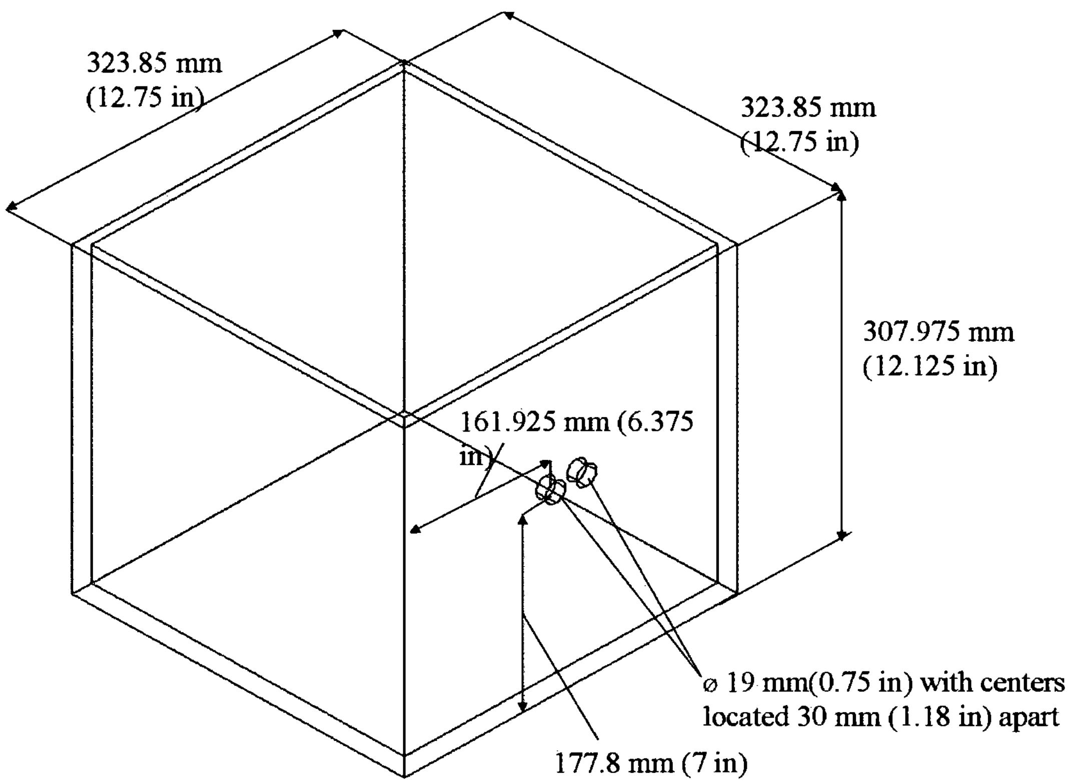

Figure 3.8: Working fluid reservoir schematic view

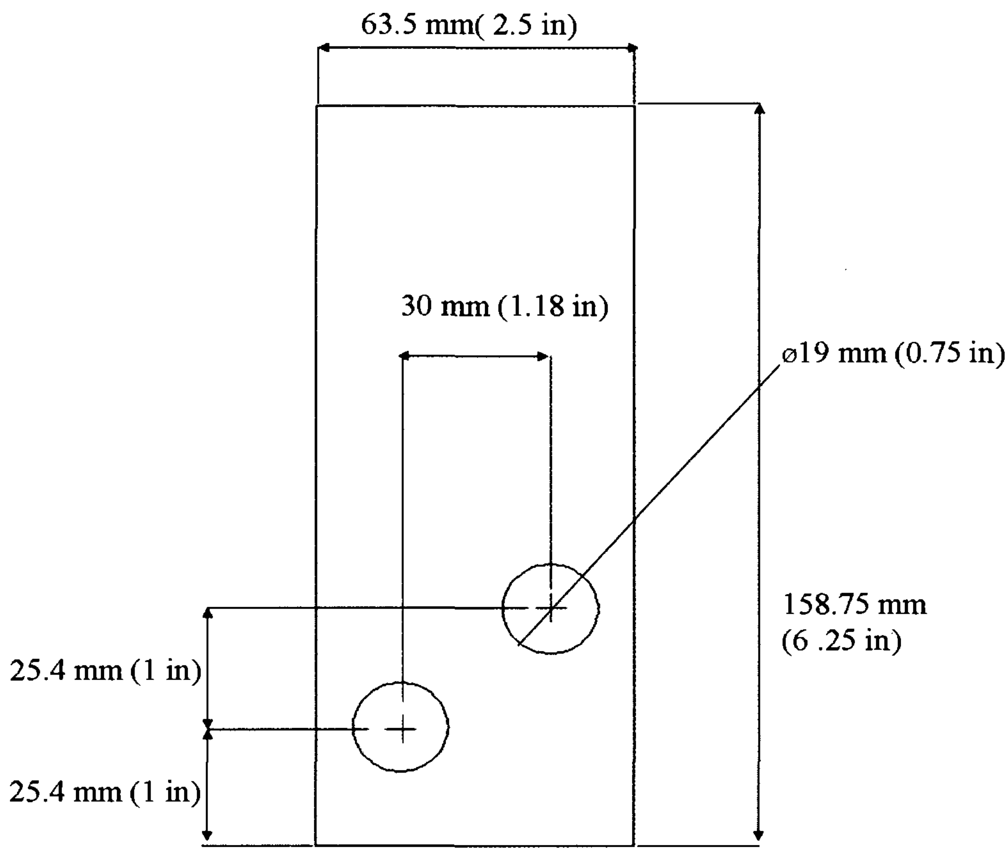

Figure 3.9: Sliding plate schematic view

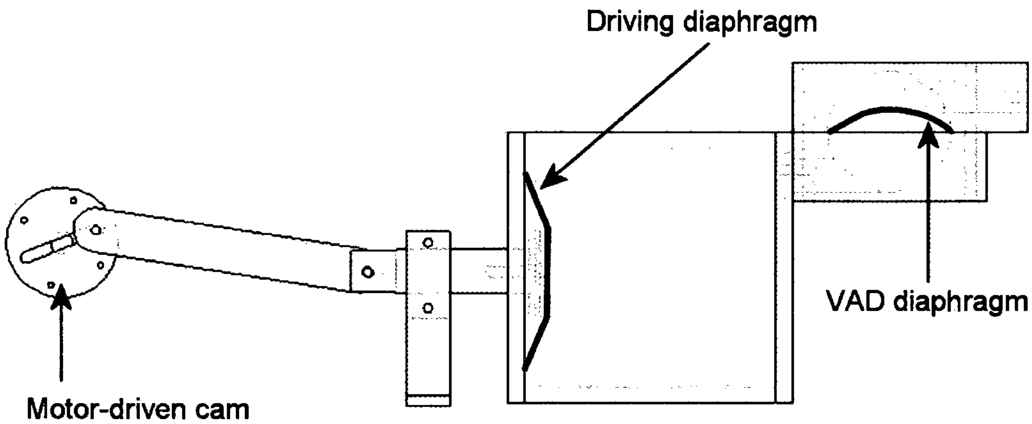

Figure 3.10: Experimental set up driving fluid section diagram (reprinted with permission from Vergniaud (2001))

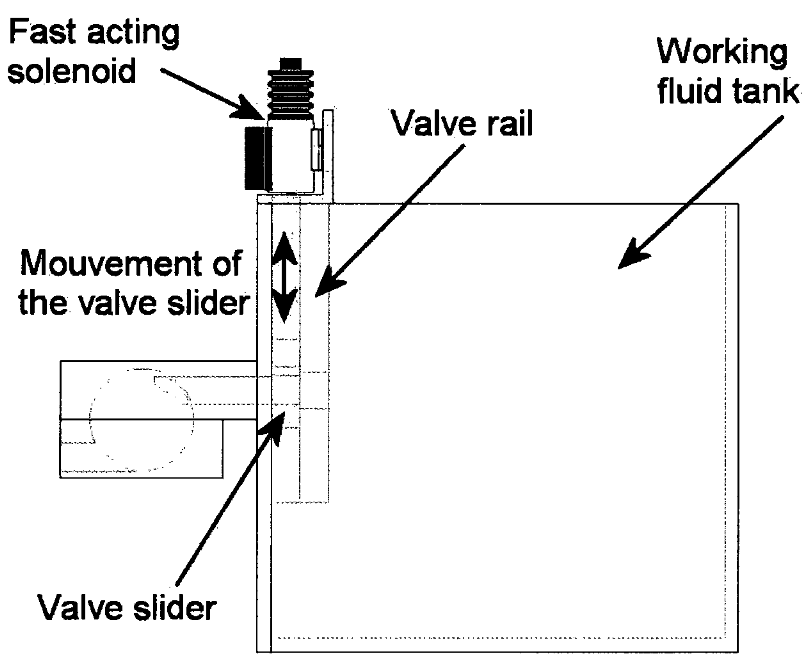

Figure 3.11: Experimental set up working fluid section diagram (reprinted with permission from Vergniaud (2001))

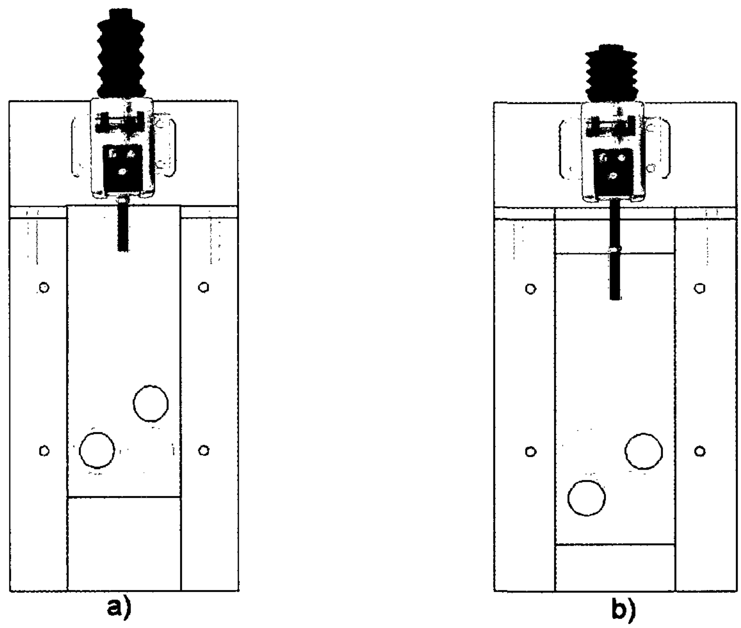

Figure 3.12: Experimental set up solenoid operation diagram (reprinted with permission from Vergniaud (2001))

3.2 LDV Measurement Method

Laser Doppler Velocimetry (LDV) measures the instantaneous velocity of particles transported by a fluid within a measuring volume that is sufficiently small for the velocity to be considered as a point measurement. In the dual beam configuration, which is the one used in the present work, the coherent, monochromatic, linearly polarized beam of a continuous wave laser passes through a beam splitter and is split into two parallel beams. One of these beams is then directed into a Bragg cell which shifts its frequency. The two beams then exit the laser emitter though a convergent lens, and create a measuring volume at their intersection. This measuring volume, due to the frequency shifting of the Bragg cell, is composed of a series of moving light and dark fringes along the axis of interest.

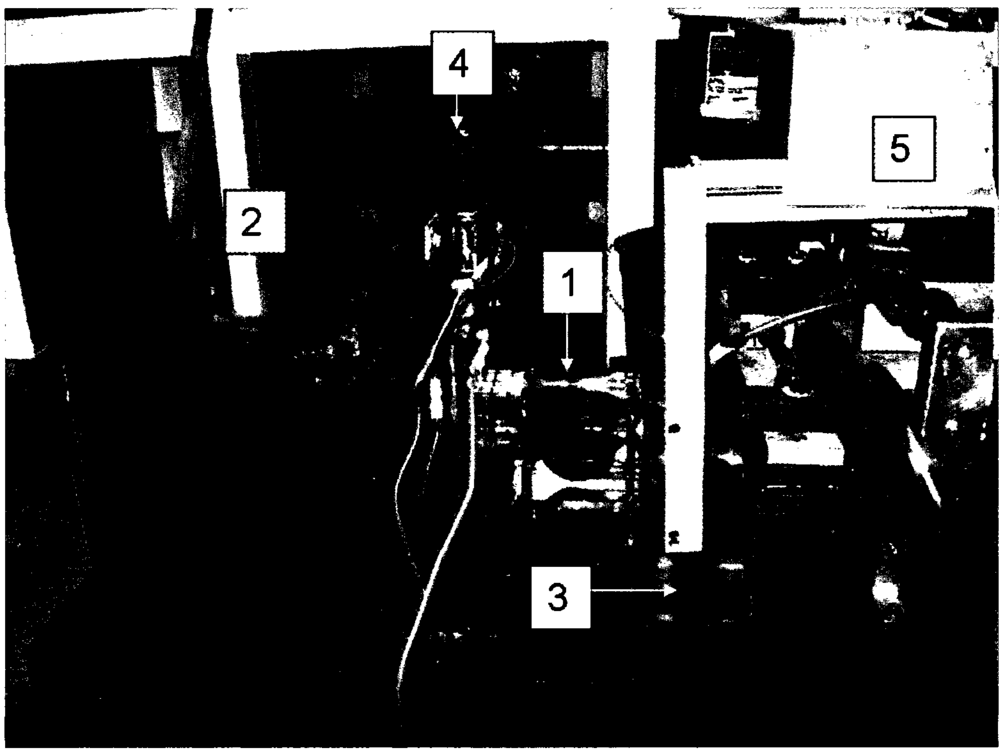

Figure 3.13: Photograph of the experimental set-up; 1 VAD; 2 working fluid reservoir; 3 driving fluid reservoir; 4 solenoid; 5 LDV traversing system

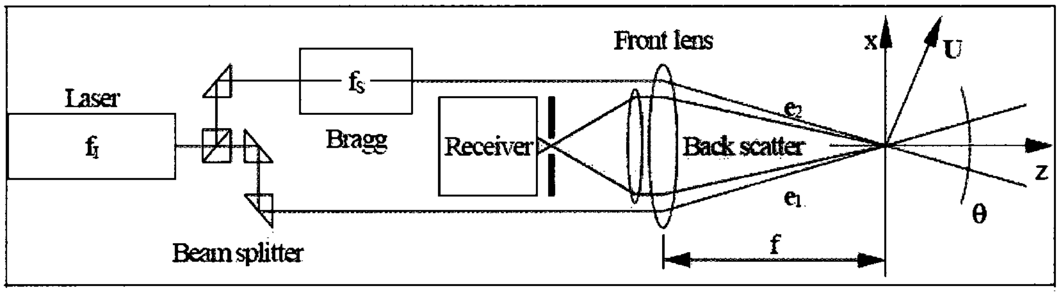

Figure 3.14: typical dual-beam LDV setup (reprinted with permission from Dantec Dynamics)

When a particle travels through the measurement volume, it emits light which is modulated by the Doppler frequency, which is detected by a receiver (Tavoularis (2005)). A typical set up for a dual beam LDV operating in backscatter mode is illustrated in Figure 3.14 (Dynamics (2008)).

Two-component LDV measurements were taken using an LDV system (Dantec Dynamics, Skovlunde, Denmark), which uses an Argon-ion laser (Lexel Laser 95L-5, Fremont, California, USA) set at a power output of 1W, and emitting light beams with main spectral energy peaks at the wavelengths 514.5 nm and 488 nm. The beams are split into two pairs of beams and enter the Bragg cell which shifts the frequency of one of the beams in each pair by 40 MHz. These beams are then routed through a transmitter (Dantec 60X41) and fiber-optic cable into a LDV head, which was fixed with a lens with a focal length of 160 mm mounted on a traversing system. The beams, when in proper alignment, created an ellipsoidal measuring volume with dimensions approximately 658 μm $\times$78 μm $\times$78 μm for the 514.5 nm wavelength beams and 624 μm $\times$74 μm $\times$74 μm for the 488 nm wavelength beams. The LDV system is used in a backscatter data collection mode using a BSA F50 60N20 Flow Processor and the data are collected and analyzed using BSA Flow

Software, version 4.50.

For the purposes of clarity and consistency with previous numerical and experimental VAD work, a coordinate system was defined with its origin at the centre of the upper VAD chamber on the same plane as the VAD diaphragm at rest, as shown in Figure 3.15. The z-axis is aligned with the vertical direction, whereas the x-axis is taken to be parallel to the inlet and outlet tube axes, and the y-axis is referred to as the spanwise direction of the VAD.

Measurements were collected at various points in the upper chamber of the VAD, as shown in Figure 3.15, with the locations also listed in Table 3.2. In order to collect data on all the components of the velocity, measurements at each location were taken using two orientations of the LDV optics: one to capture the u and v components of the velocity, and another to capture the u and w components. This was not possible at locations at which the view was interrupted by the motion of the diaphragm. In both cases, the u component was measured using the 514.5 nm beams. The measurement system was set to accept an input signal from the VAD system to mark the beginning of a given cycle, and indicating that the LDV processor would use a burst analysis method for data analysis. Flow measurement data were set to be fully coincident, so that the two velocity components would be collected at the same time. Although this lowered the overall data collection rate, it provided the most consistent information for the flowfield. The LDV system was set to sample using frequency shifting, with a maxium sensitivity of 1600 V and ranges of values for the velocity set for ± 1.2 ms^{-1} in the x-axis, and ± 1 ms^{-1} in the y-axis and in the z-axis. Finally, the data for each point were collected for 100 cycles and then exported into MATLAB for

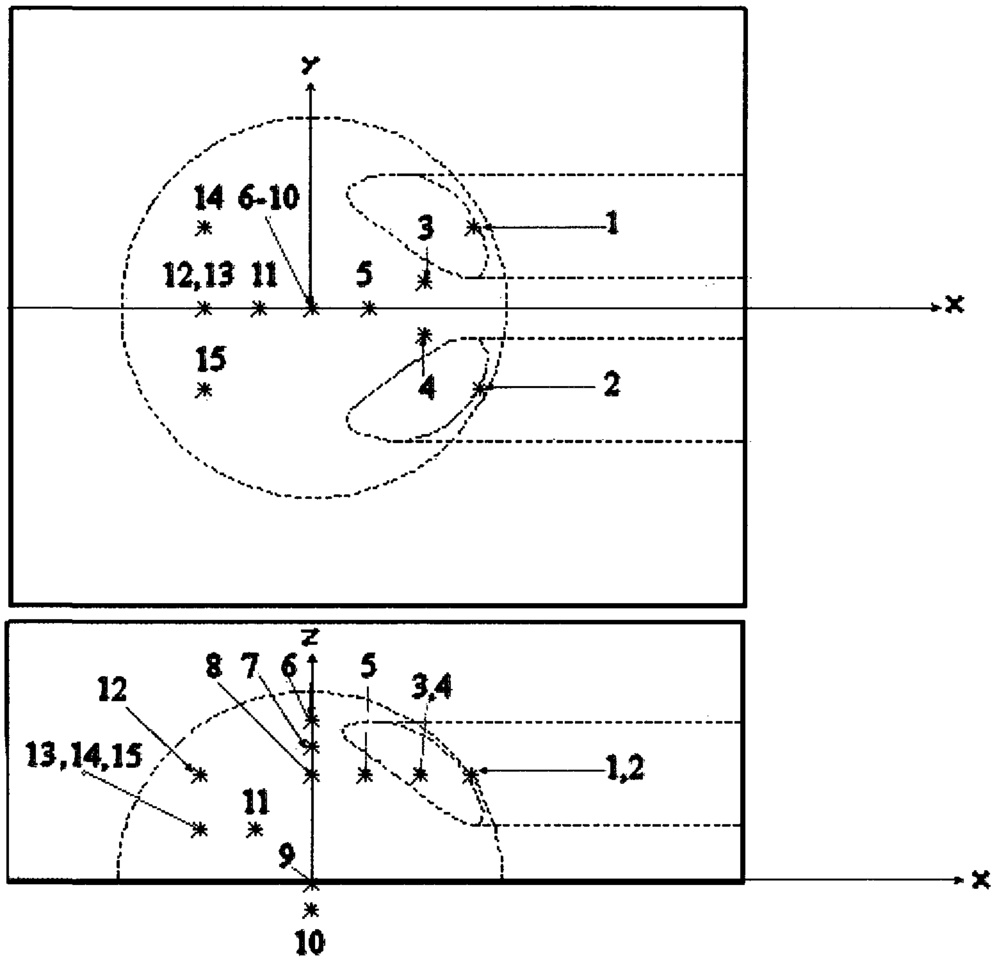

Figure 3.15: coordinate system and selected locations for LDV measurement

Table 3.2: LDV Measurements Points (mm)

Point	x	y	z
1	29	15	20
2	29	-15	20
3	20	5	20
4	20	-5	20
5	10	0	20
6	0	0	30
7	0	0	25
8	0	0	20
9	0	0	0
10	0	0	-5
11	-10	0	10
12	-20	0	20
13	-20	0	10
14	-20	15	10
15	-20	-15	10

ensemble averaging.

3.3 PIV Measurement Method

Particle Image Velocimetry (PIV) measures the variation of the instantaneous flow velocity projection on a planar cross-section of the flow. In the typical PIV setup, laser beams are emitted through a cylindrical prism to create a planar sheet of light with a non-uniform intensity, but as the PIV system does not measure variations in light intensity, this is not a concern in these experiments. This light sheet illuminates a plane section of flowfield that has been properly seeded; a digital camera is positioned so that its field of view is parallel to the light sheet. Two light pulses are generated by two twin lasers separated by a short time increment Δt, with the digital camera recording both images on separate frames. These images are then processed using a cross-correlation algorithm to

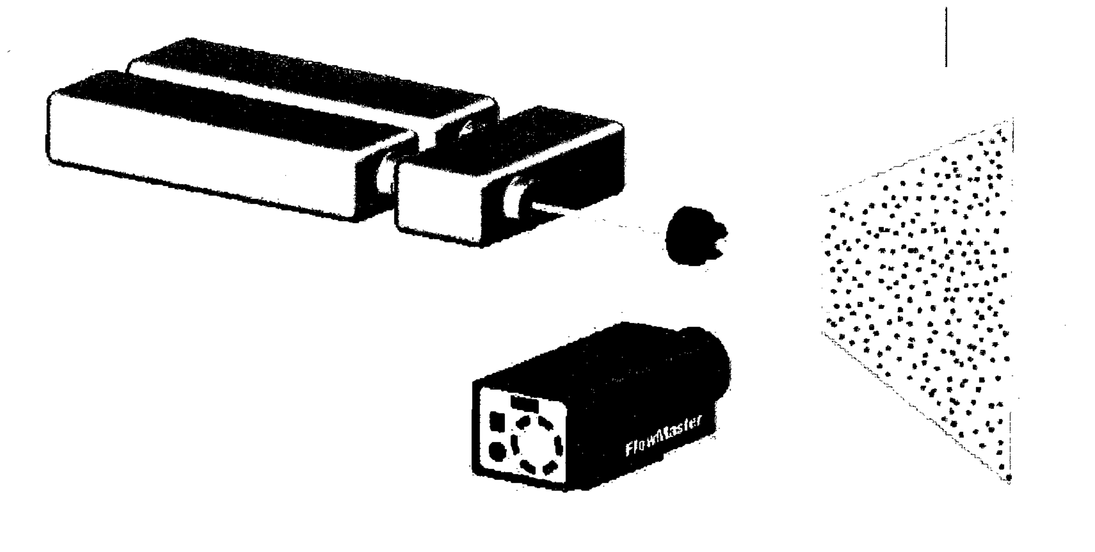

Figure 3.16: Typical PIV set up (reprinted with permission from LaVision)

determine the two-dimensional velocity field (Tavoularis (2005)). A typical PIV system is illustrated in Figure 3.16 (GmbH (2007)).

The LaVision PIV System (LaVision GmbH, Goettingen, Germany) uses a Neodymium:YAG dual cavity pulsed laser (New Wave Research Solo PIV 120XT, Fremont, California, USA), capable of producing pulses with an energy of up to 120 mJ per pulse at a wavelength of 532 nm. A cylindrical lens with a focal length of -10 mm was used to create a laser sheet (LaVision 1108405) across a chosen plane of the VAD, which clearly illuminated the crystals in the flow. To capture the images, the LaVision Imager Pro X4M CCD camera was used; in normal PIV operation, it can record two successive images of 2048 $\times$ 2048 pixels each. The camera used a Nikon lens with a focal length of 50 mm and an f-stop of 1.8, augmented by a Vivitar macro focusing lens (Vivitar, Oxnard, California, USA) in order to obtain the best possible resolution of the VAD field. The camera axis was set perpendicular to the laser sheet; in cases for which a vertical laser sheet was required, a highly reflective right-angle laser prism was mounted onto the traversing system in order to deflect the laser sheet. The camera is controlled by a camera controller, which in turn is synchronized with both the laser and the computer by a programmable timing unit (LaVision 1108058) into which the trigger input from the experimental apparatus could be connected. The effects of ambient light sources were minimized by using a dark shroud over the experimental apparatus and adding an interference filter to the lens that only allowed for light from the 532 nm wavelength to pass (LaVision 1108501). The images were then processed in a personal computer using DaVis 7.2 PIV analysis software.

PIV measurements were taken on three vertical planes that were parallel to the y-axis and on three horizontal planes, as displayed in Figures 3.17 and 3.18, respectively. The $z = 20$ mm plane contains the axes of the inlet and outlet tubes, whereas the $z = 11$ and 29 mm planes are nearly tangent to the inlet and outlet tubes. The $y = 0$ vertical plane is the plane of symmetry of the VAD and the $y = -15$ and 15 mm planes contain the axes of the inlet and outlet tubes (Figure 3.2 shows that the axes of these tubes are 30 mm apart). Using a calibration sheet to set up the PIV equipment, a resolution of 20 pixels/mm was obtained, and the time increment between successive frames for PIV was set at $\Delta t = 1$ ms. In order to get flowfield information for a few representative cycles, the PIV used the camera's onboard memory (512 MB) to obtain a maximum of 35 pairs of images at the relatively high acquisition rate of 6.84 Hz, which gives an average of approximately

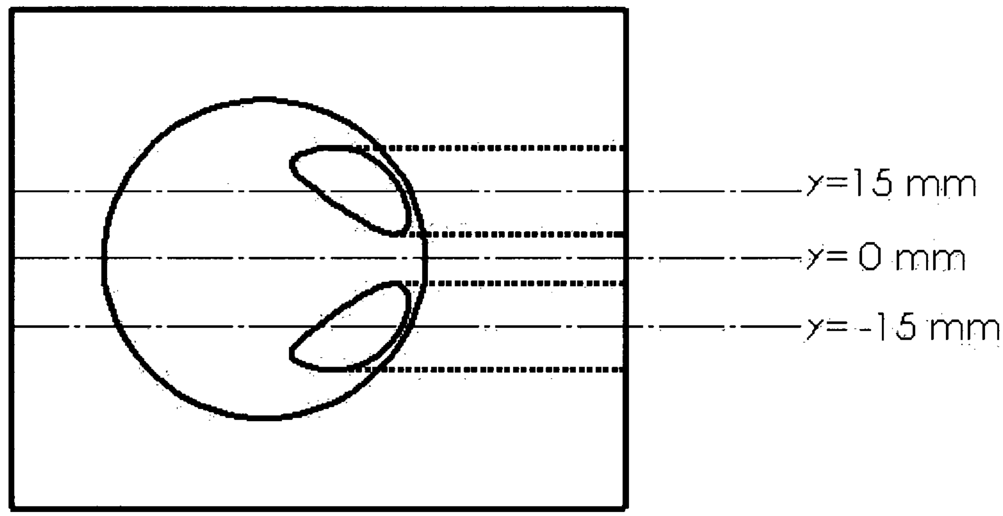

Figure 3.17: Selected vertical planes for PIV measurement

9 pairs of images per cycle. In a second method, the sampling was triggered externally at the instant at which the solenoid extended, opening the inlet valve and closing the outlet valve, and pairs of images were taken at a fixed phase during 50 consecutive cycles, so that phase (ensemble) averaging could be applied. Phase data were collected at intervals of 100 ms, with $t = 0$ representing the opening of the inlet valve and the closing of the outlet valve by the solenoid. These measurements are taken for every 100 ms in the cycle, for 50 cycles for each time point. All of these images were then processed by the software, using a multipass interrogation window size starting at 128×128 pixels and resolving to 16×16 pixels. Figure 3.19 illustrates schematically the PIV setup for a typical horizontal plane.

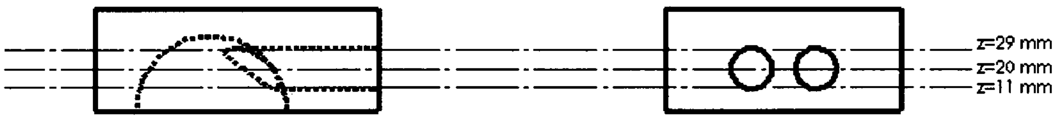

Figure 3.18: Selected horizontal planes for PIV measurement

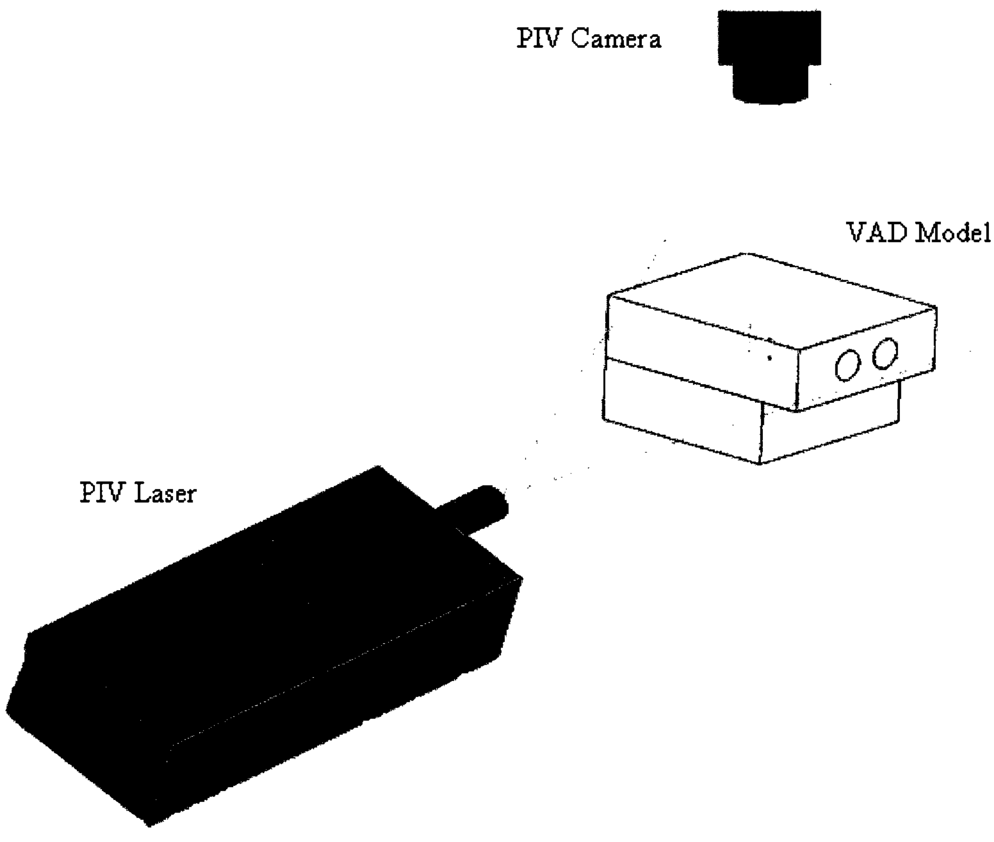

Figure 3.19: PIV set-up for horizontal plane measurement

3.4 Diaphragm Position Measurement Method

The PIV images from the vertical planes were sorted by inspection and a representative image for each time step was selected. The position of the diaphragm along the z-axis at that time step was measured at 15 points along the centerline x-axis. Uncertainty in these measurements was introduced, among other things, by reflections of the laser sheet on the diaphragm surface, as well as image distortions by small-scale motions of the diaphragm; the total uncertainty was estimated to be no more than 0.5 mm, which is acceptable for the present purposes. Cycle-to-cycle variations were more significant. For this reason, representative images at each time step were selected rather than phase averages.

Chapter 4

Flowrate and Diaphragm Motion

4.1 VAD Period and Ideal Flowrate

The average period of the VAD operation was measured to be $T = 1306 \pm 19$ ms, which corresponds to a rate of approximately 46.0 ± 0.7 bpm (beats per minute). This rate was the highest achievable by the apparatus and, although measurably lower than the standard heart rate of 70 bpm for adult male humans, it was considered to be sufficiently close to it for the purposes of these experiments. The time origin of each cycle was selected such that diastole began at $\frac{t}{T} = 0$ and systole began at $\frac{t}{T} = 0.5$. A simplified model of the driving fluid piston kinematics, described in Appendix C, was used to estimate the volume of working fluid displaced by the diaphragm during VAD operation. The idealized results were then used to determine the stroke volume as

$$SV = \Delta V_{\mathrm{max}} = 6.25 \times 10^{-5}\ \mathrm{m}^3 = 62.5\ \mathrm{cc} \tag{4.1}$$

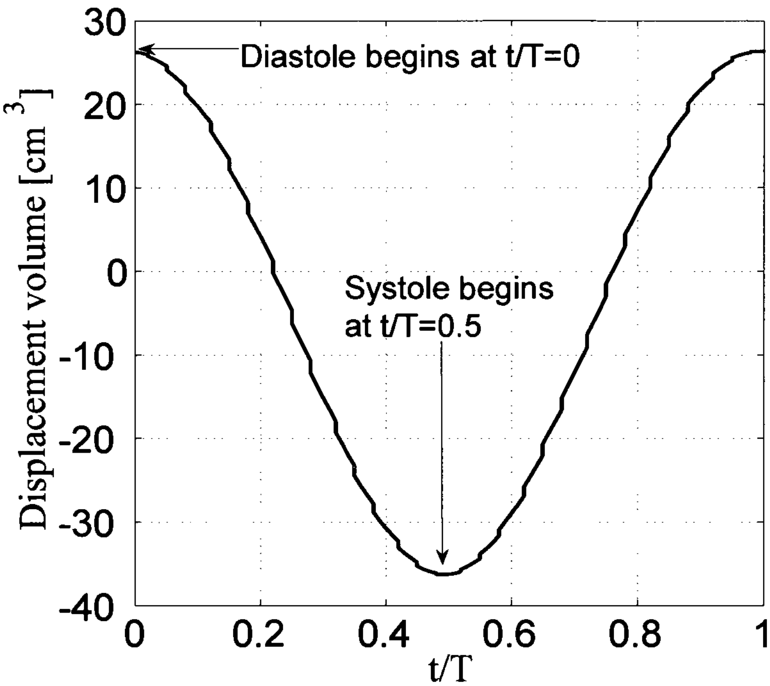

Figure 4.1: Idealized working fluid volume displacement

where ΔV_{max} is the difference between the maximum and minimum displaced volumes during the VAD operational cycle. Then, the time-averaged flowrate was calculated as

$$\overline{Q} = \frac{\Delta V_{\mathrm{max}}}{T} = 4.79 \times 10^{-5}\ \mathrm{m^3 s^{-1}} = 2.87\ \mathrm{L\ min^{-1}} \tag{4.2}$$

Figure 4.1 shows the ideal fluid volume displacement variation and Figure 4.2 shows the corresponding ideal flowrate variation during the VAD cycle. Unfortunately, it turned out that the driving fluid diaphragm did not deform ideally and so the flowrate variation was more complex than the ideal one; this issue will be discussed in detail in Chapter 7.

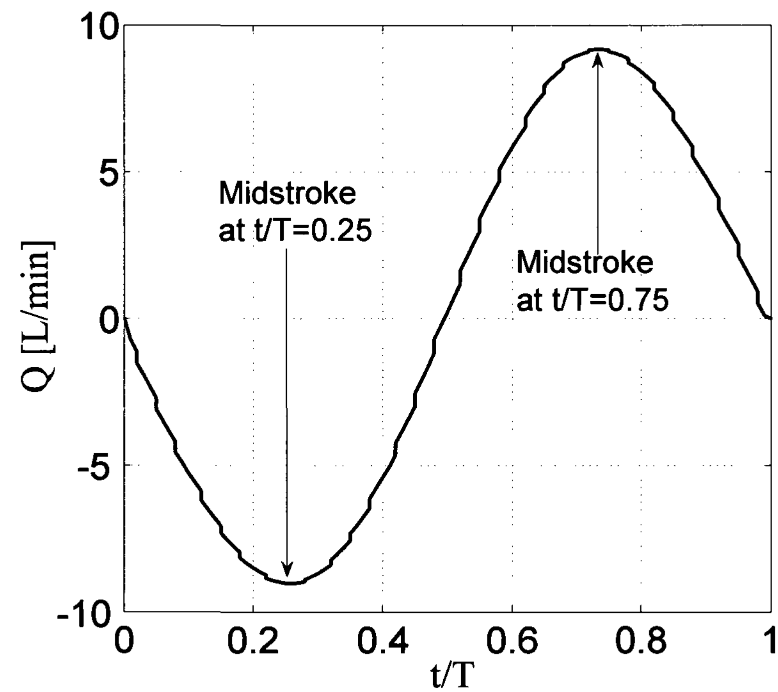

Figure 4.2: Ideal flowrate

4.2 Diaphragm Motion

The shapes and positions of diaphragm contours on vertical VAD cross-sectional planes were determined from images recorded by the PIV camera during PIV measurements. Figures 4.3-4.5 present images taken with the laser light sheet illuminating the centreplane of the VAD at three representative instants during the operational cycle. At the beginning of the ejection phase ("systole"), at $\frac{t}{T} = \frac{7}{13}$, the VAD diaphragm was nearly ellipsoidal and it was entirely in the lower hemisphere of the VAD, as shown in Figure 4.3. As the piston advanced, it displaced water from the working fluid tank into the lower hemisphere of the VAD, and the VAD diaphragm responded by deforming towards the $z = 0$ plane, although it did not preserve an axis-symmetric shape, but was skewed, with the highest point on the positive x-axis, as can be seen at $\frac{t}{T} = \frac{10}{13}$ in Figure 4.4. At the beginning of diastole, the diaphragm became again nearly ellipsoidal, and was entirely in the upper hemisphere of the VAD at $\frac{t}{T} = \frac{0}{13}$. At this instant, the diaphragm was also completely asymmetric, with its apex in the positive domain of the x-axis, as can be seen in Figure 4.5.

Similar images were taken at 13 time instants during each cycle over 50 cycles with the light sheet at one of three planes having $y = -15, 0$ and 15 mm. From each image, the position of the diaphragm along the z-axis was measured at 15 points along the x-axis. Considering that there was some cycle-to-cycle variation, a representative image among the 50 that were recorded at each instant was chosen by inspection and used to represent the diaphragm location. These measurements were then entered into a MATLAB program (see Appendix A) to generate typical time histories of the contour defined as the intersection of the diaphragm and the corresponding illuminated vertical plane. Figures 4.6-4.8 show

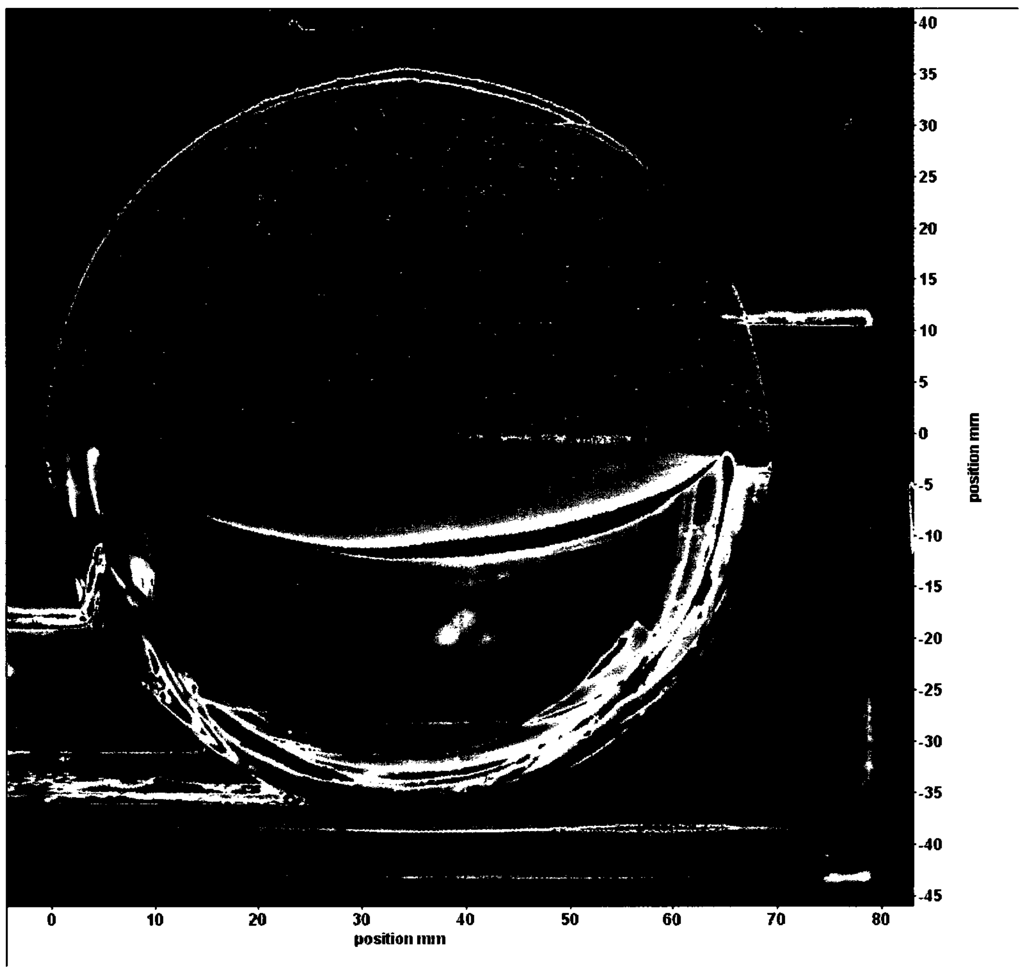

Figure 4.3: Side view of the VAD showing a representative diaphragm appearance at $\frac{t}{T} = \frac{7}{13}$

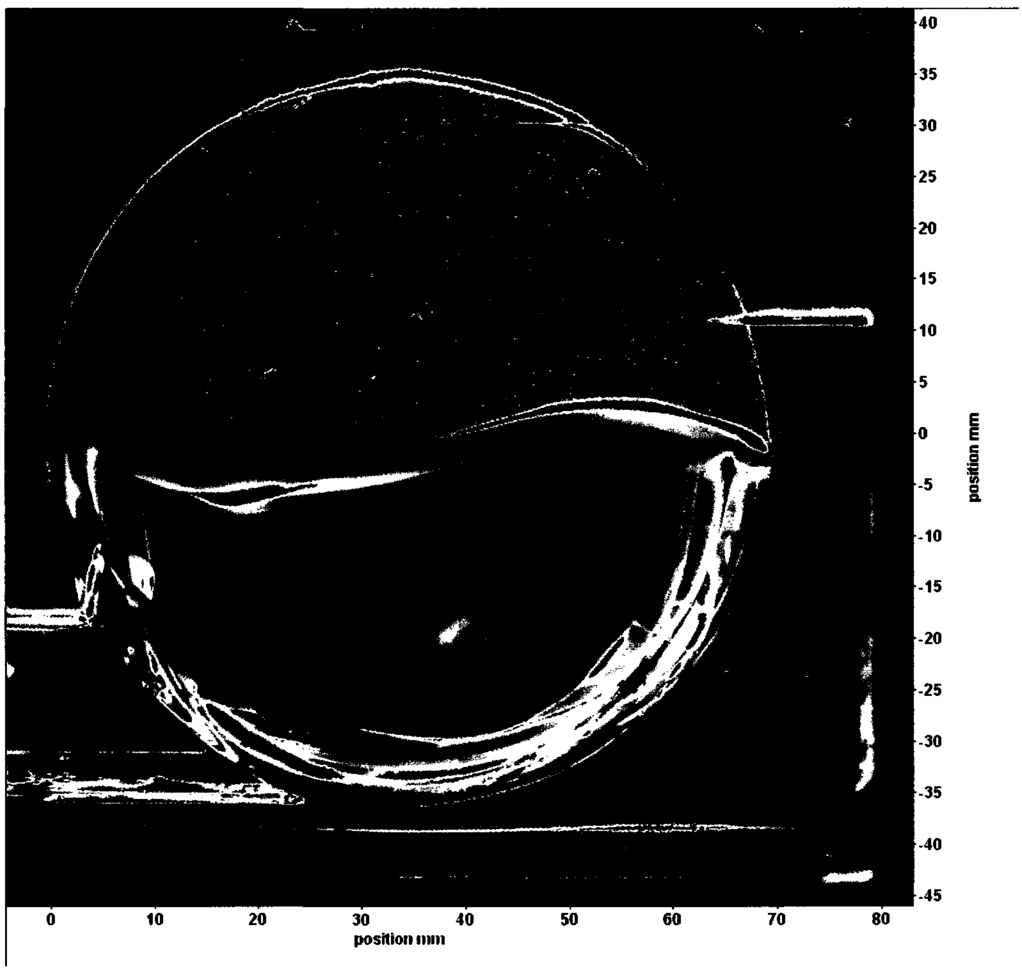

Figure 4.4: Side view of the VAD showing a representative diaphragm appearance at $\frac{t}{T} = \frac{10}{13}$

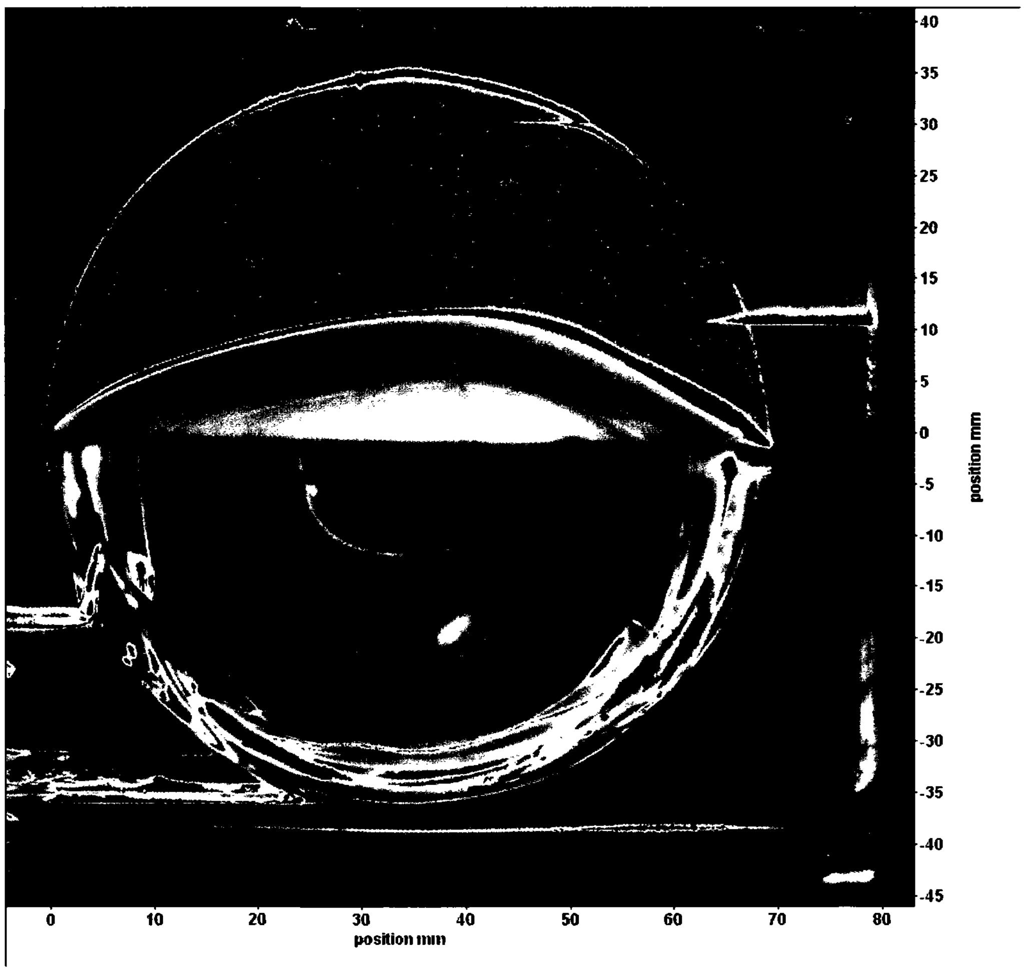

Figure 4.5: Side view of the VAD showing a representative diaphragm appearance at $\frac{t}{T} = \frac{0}{13}$

the results at the 13 selected times during the VAD period T. The contour plots show that, from the systolic phase at $\frac{t}{T} = \frac{12}{13}$ until early diastole at $\frac{t}{T} = \frac{4}{13}$, the diaphragm shape is approximately planar-symmetric. However, from $\frac{t}{T} = \frac{5}{13}$ until $\frac{t}{T} = \frac{11}{13}$, the $y = 15$ mm plane, which corresponds to the region of the diaphragm closest to the inlet tube, experiences a stronger expansion in the negative z-direction. This clearly shows that the diaphragm motion was asymmetric. The cause of this particular motion, as well as the likely effects on the overall performance of the system, will be discussed in Chapter 7.

.

.

.

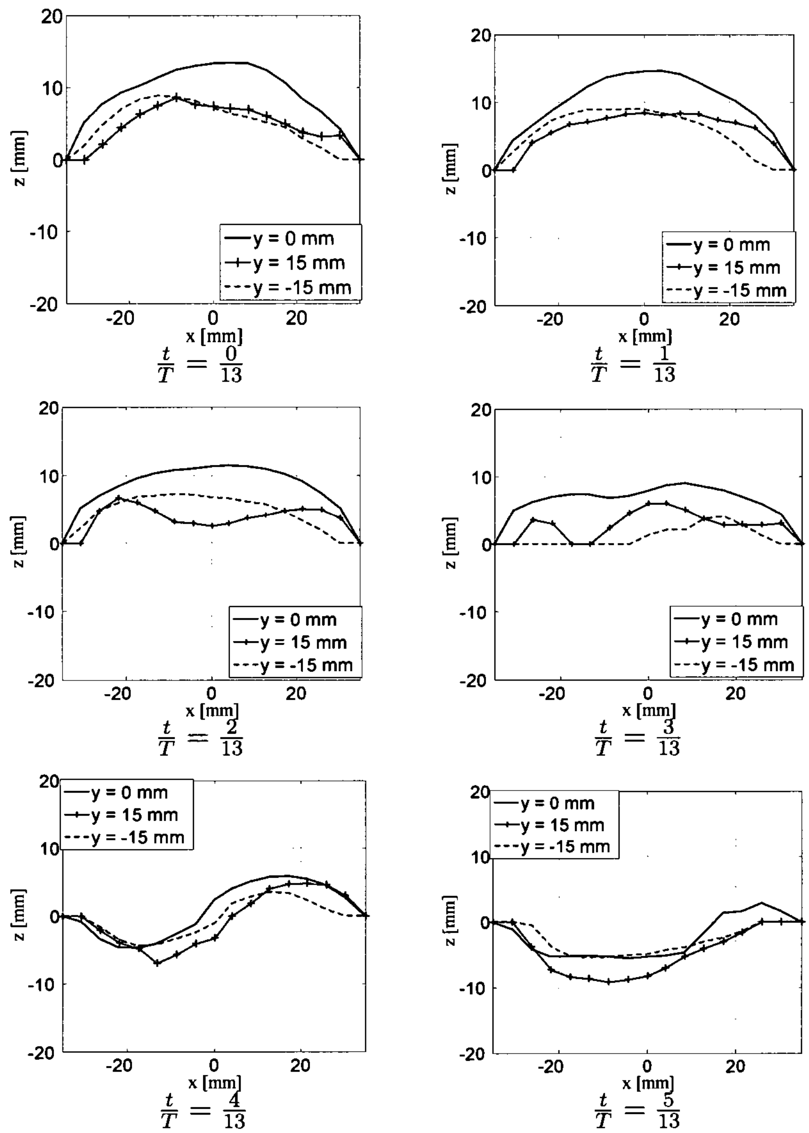

Figure 4.6: Representative diaphragm contours on three vertical planes

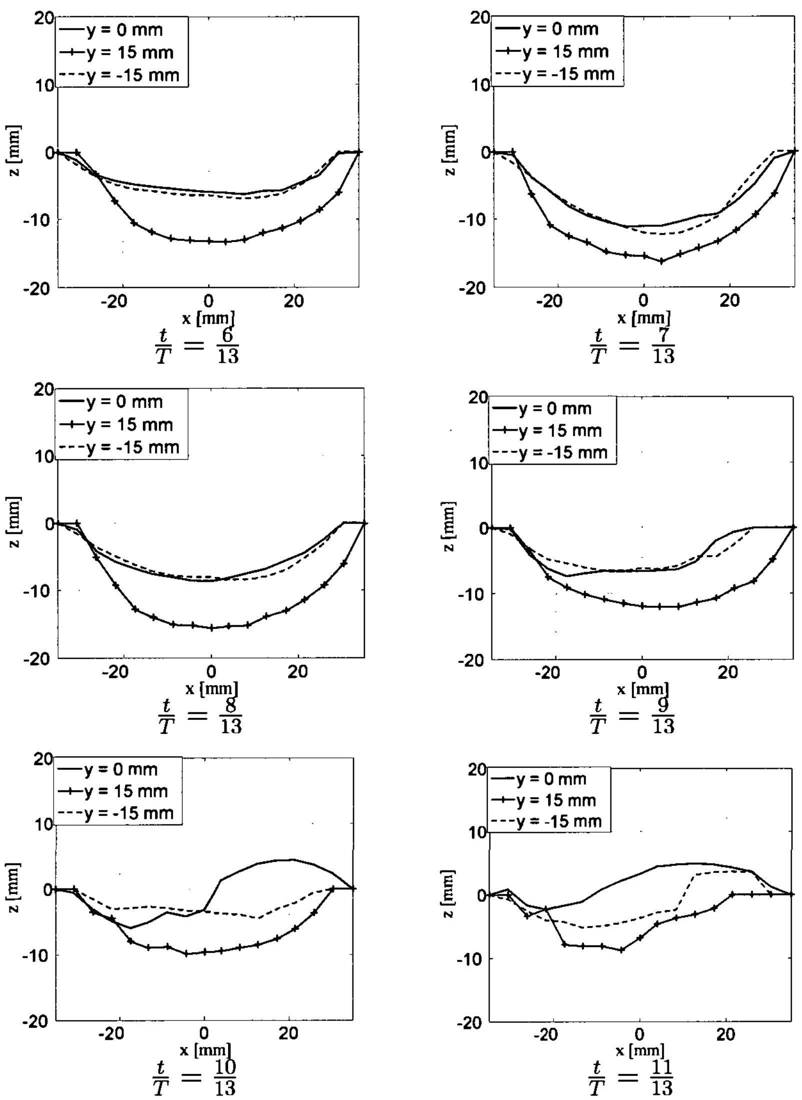

Figure 4.7: Representative diaphragm contours on three vertical planes (continued)

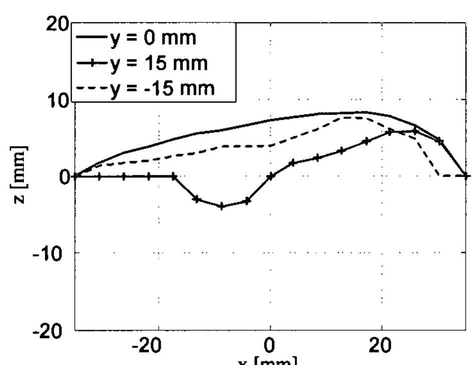

$\frac{t}{T} = \frac{12}{13}$

Figure 4.8: Representative diaphragm motion plots (continued)

Chapter 5

Local Flow Velocity Variation During the Cycle

Figures 5.1-5.9 show the temporal variations of phase-averaged velocity components (denoted by angle brackets, for example, $< u >$), the corresponding standard deviations with respect to the phase averages (denoted by primes, for example, u') and representative cycles, all measured using the LDV measurement system described in Chapter 3. Results for each of the u, v, and w components for the 15 selected points that were identified in Chapter 3 are plotted separately, in Figures 5.1-5.3 for u, in Figures 5.4-5.6 for v, and in Figures 5.7-5.9 for w. Because the diaphragm blocked the path of the LDV beams when taking measurements for the w velocity component at Points 9 and 10, no corresponding measurements could be obtained. A prominent feature of the velocity variation is the presence of a "valley" between two strong peaks during diastole (VAD filling) at Point 1 on the axis of the inlet tube and of a similar valley during systole (VAD emptying) at Point

2 on the axis of the outlet tube. These measurements are consistent with previous measurements using this same apparatus and motor by Vergniaud (2001), who observed similar valleys in the velocities in the inlet and outlet tubes, although less pronounced than in this study. The differences between the present results and those of Vergniaud can be attributed to the differences in locations of measurement volumes, as well as slight modifications to the apparatus. LDV measurements collected from other regions of the VAD show general agreement with measurements from the same regions measured by Vergniaud (Vergniaud (2001)). Physical reasons for the complicated velocity variation and a method for obtaining corrected estimates of the flowrate variation through the VAD will be discussed in the following chapter.

The peak velocity magnitudes measured by the LDV occurred during peak diastole at Point 1 and peak systole at Point 2; in both cases, the u component was dominant and the magnitudes of the v and w components were much smaller. The peak velocity magnitude during diastole was 1.22 m/s at $\frac{t}{T} = 0.4$ and the peak systolic velocity magnitude was 1.08 m/s at $\frac{t}{T} = 0.85$. When comparing the u velocity variations at Points 3 and 4, which have equal distances from the inlet and outlet tubes, respectively, one may observe that the peak velocity at Point 3 is much higher in magnitude than that at Point 4. Points 5-8, located along the x-axis, experience oscillations in velocity during the cycle, with most of the oscillations occurring during diastole in the $x - y$ plane, as displayed in Figure 5.2 as well as Figure 5.5 and Figure 5.8. The flow velocities at Point 9, located at the center of the VAD, and Point 10, which is covered by the diaphragm during part of the cycle, are very small during the entire cycle. The velocity components at Points $11 - 15$ are oscillatory, with the highest magnitude measured for the w component, as shown in Figures 5.8 and 5.9. This indicates that the flow on average was moving in the negative z-direction, which was consistent with the fact that the flow in this region was influenced by the motion of the diaphragm.

The high level of velocity variations in the geometry suggests a high level of washout. The flow in the negative x-domain (Points $11 - 15$) was fully three-dimensional, with significant contributions from all velocity components, which suggests the presence of fully three-dimensional flow structures, such as the vortex core observed in the PIV measurements.

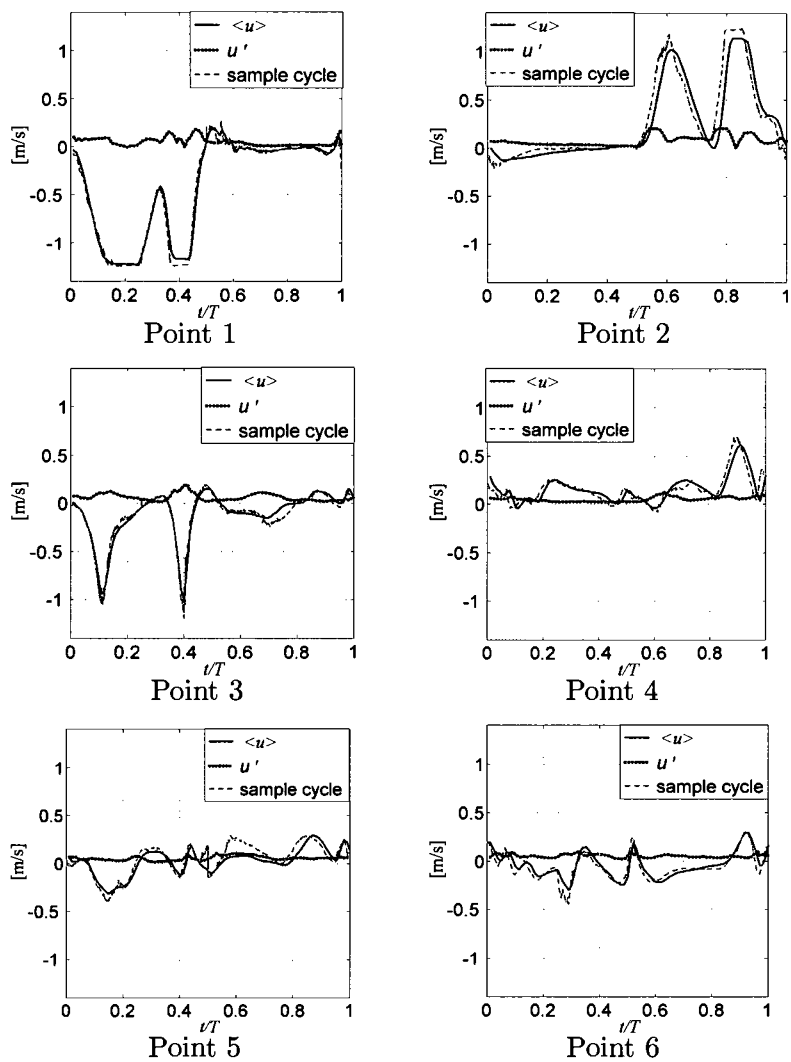

Figure 5.1: Phase Averaged LDV x-velocity graphs

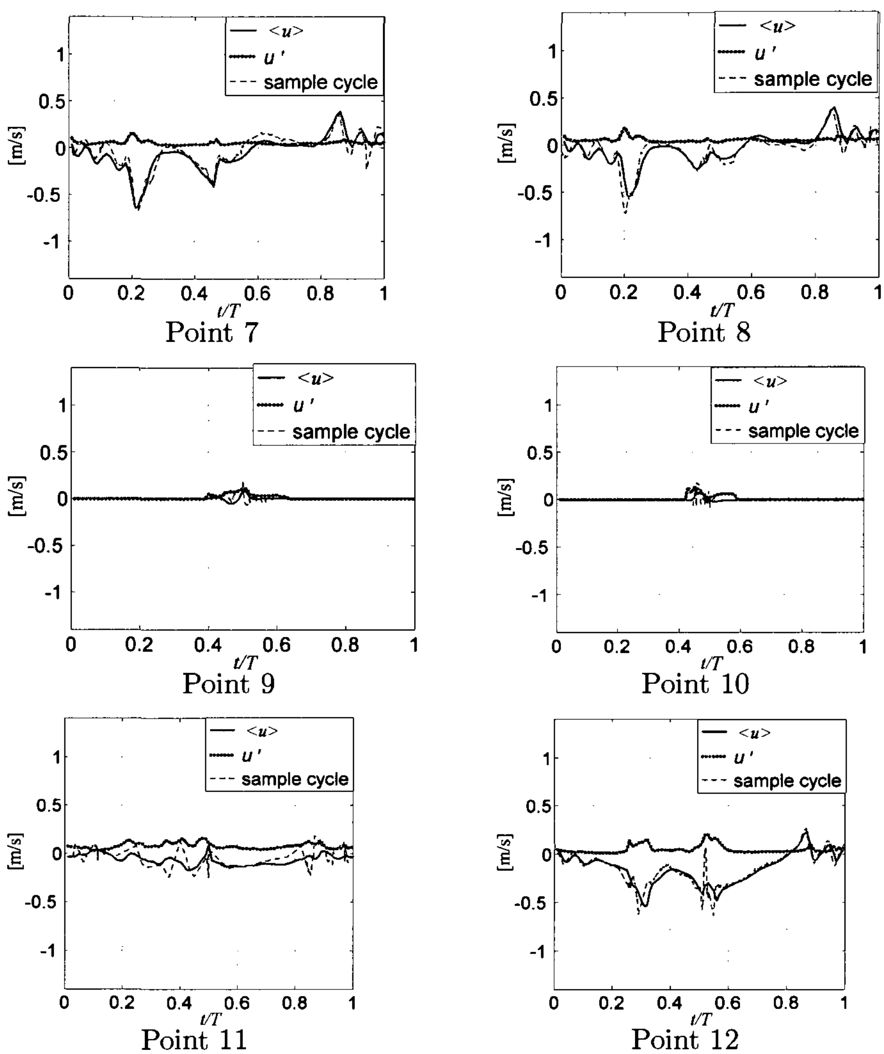

Figure 5.2: Phase Averaged LDV x-velocity graphs (continued)

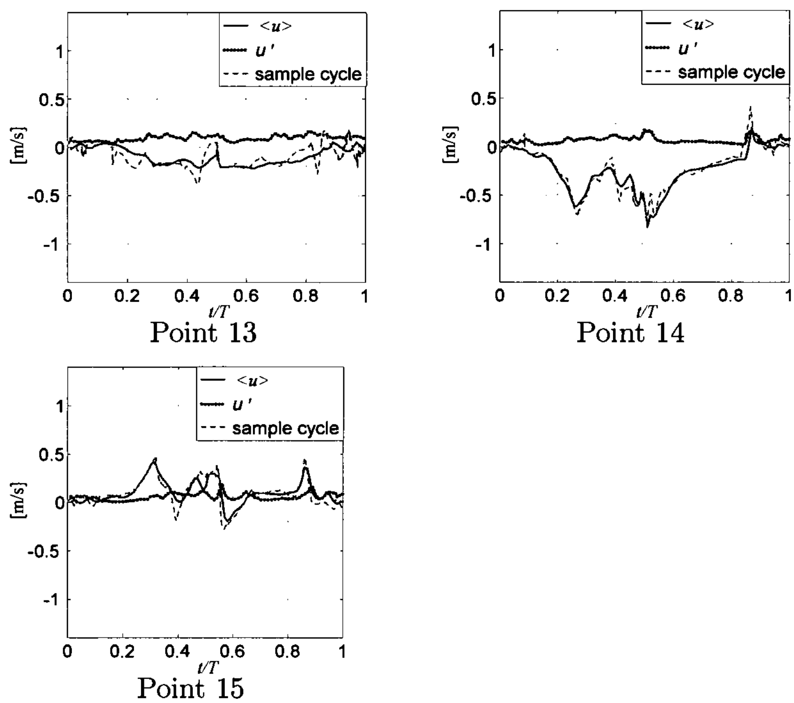

Figure 5.3: Phase Averaged LDV x-velocity graphs (continued)

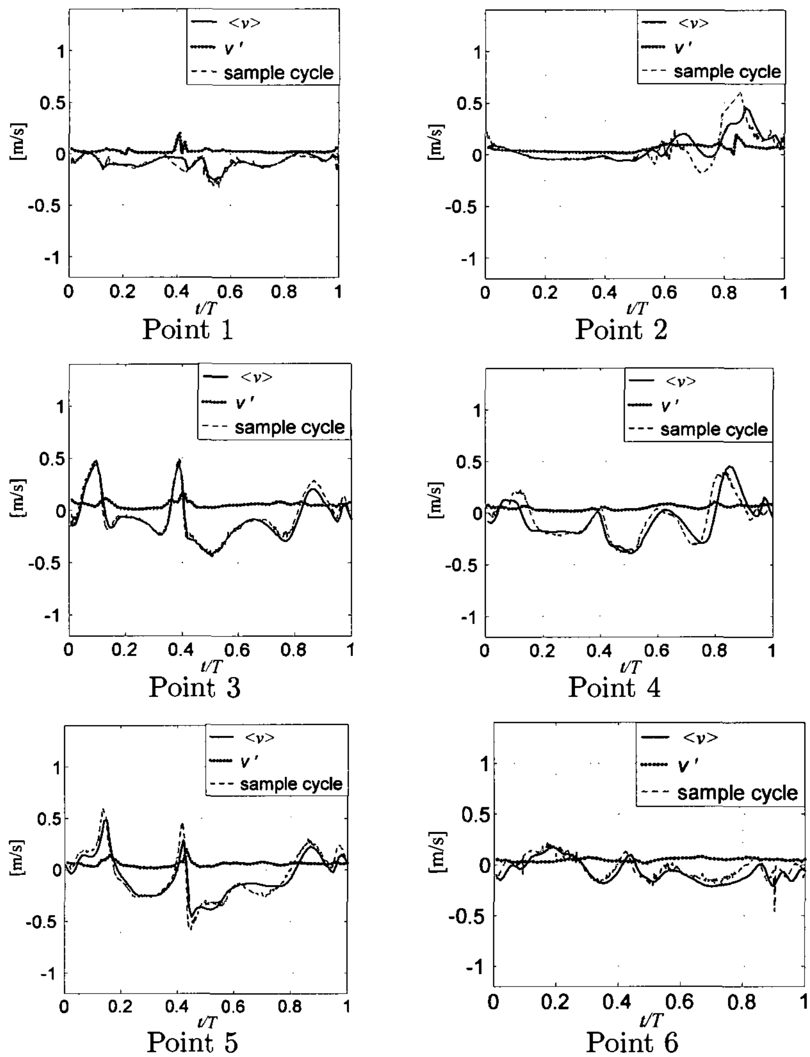

Figure 5.4: Phase Averaged LDV y-velocity graphs

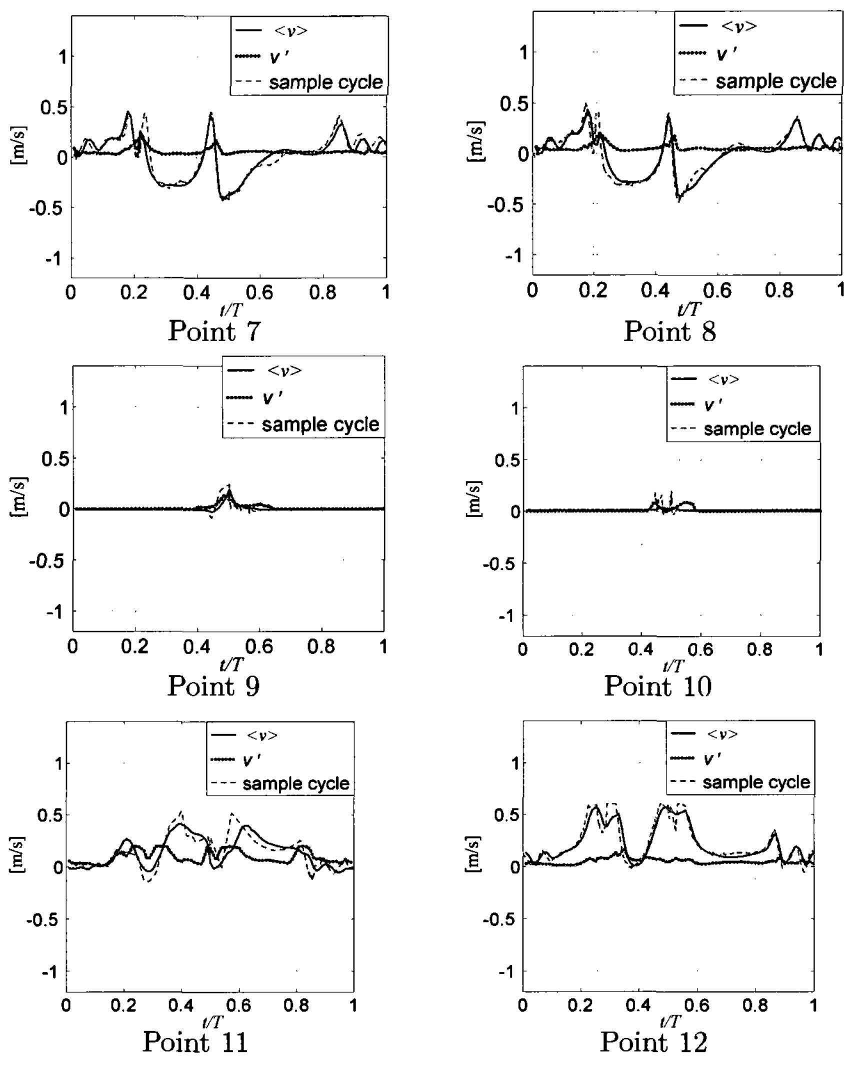

Figure 5.5: Phase Averaged LDV y-velocity graphs (continued)

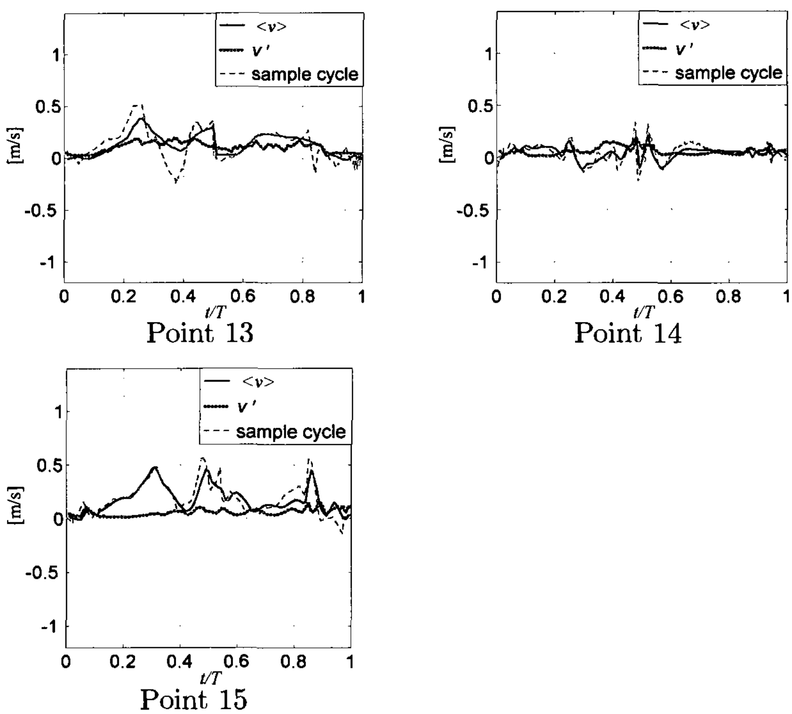

Figure 5.6: Phase Averaged LDV y-velocity graphs (continued)

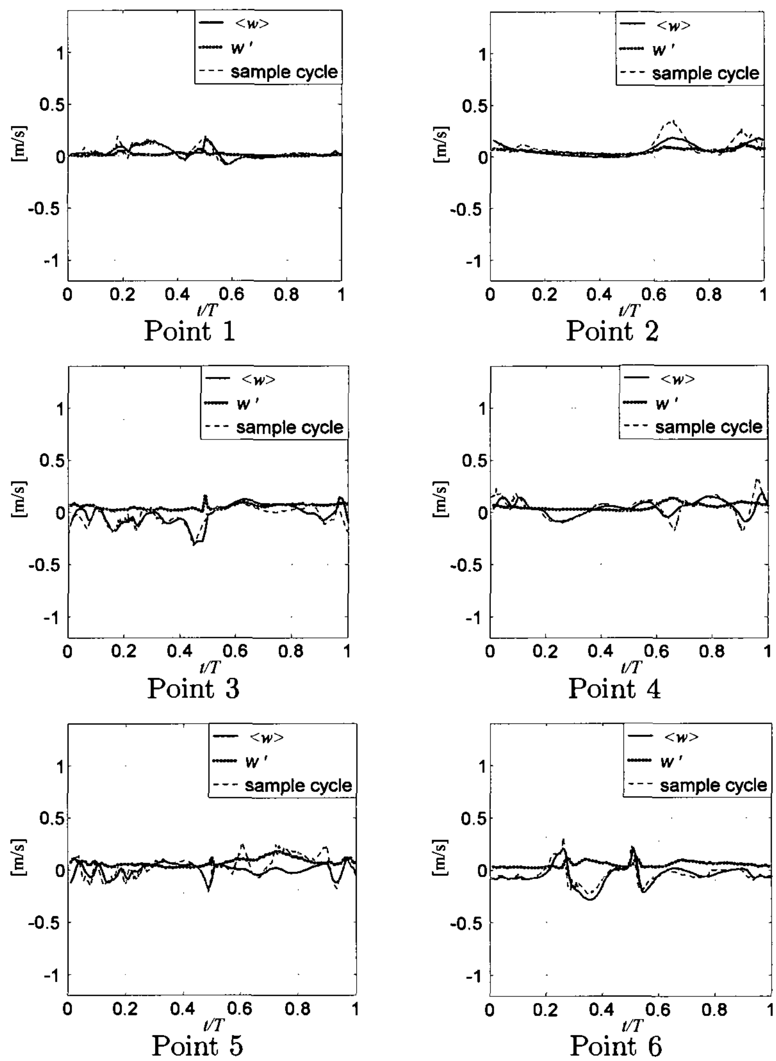

Figure 5.7: Phase Averaged LDV z-velocity graphs

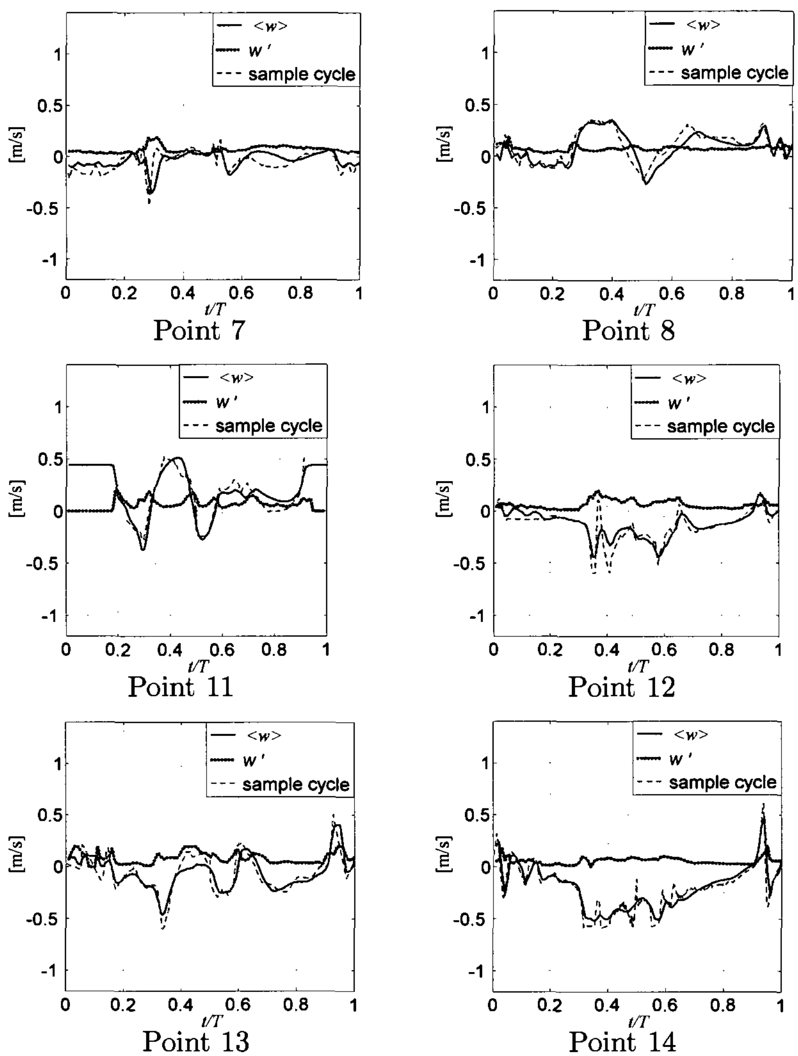

Figure 5.8: Phase Averaged LDV z-velocity graphs (continued)

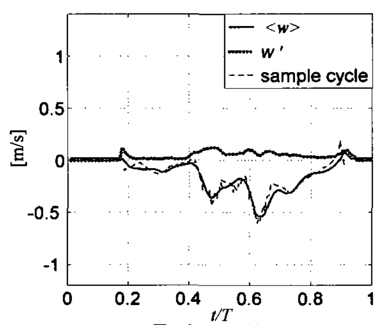

Point 15

Figure 5.9: Phase Averaged LDV z-velocity graphs (continued)

Chapter 6

PIV Results

6.1 Selection of PIV Interframe Time Interval

The velocity in the present apparatus varied rapidly in both time and space. This creatds particular difficulties when trying to optimize the settings of the PIV measuring system, particularly when selecting an interframe time interval Δt (i.e., the time interval between the two pulses of the laser sheet that are used to measure particle displacement). If Δt is too large, the method would be unable to record the motion of fast particles and to capture rapid changes in velocity; if it is too small, the measured velocity map would become too noisy. Any choice of Δt would be a compromise and cannot be optimal for the entire flow field and the entire cycle. In order to choose the most effective Δt early in the experimental procedure, it was decided to take representative PIV images of a cycle using different Δt values. This was accomplished using the PIV camera's onboard memory to obtain a maximum of 35 pairs of images at the relatively high acquisition rate of 6.84 Hz, which gives an average of approximately 9 pairs of images per cycle, in order to observe several successive cycles to compare with time-averaged results that were obtained later in the study. The representative method allowed for rapid comparison of mulitple tests in order to determine the optimal Δt value.

The results are illustrated in Figure 6.1, which shows the velocity field on the $z = 20$ mm plane at approximately the same time in the VAD operation cycle $\left(\frac{t}{T} \simeq \frac{4}{9}\right)$, but with different Δt between successive frames. For $\Delta t = 2$ ms the average flow velocity is much lower than that for $\Delta t = 1$ ms, and for $\Delta t = 5$ ms the inlet flow appears to be almost entirely stagnant. For shorter time intervals, the uncertainty increases, creating noisy signals in low velocity regions, particularly in areas of low velocity, as displayed by the high velocity regions displayed along the VAD boundary and the outlet tube for $\Delta t = 0.5$ and $\Delta t = 0.25$ in Figure 6.1. This is the result of the high levels of uncertainty when using such a short time interval. These differences are more clearly displayed in an overview of representative cycles in the following section.

The interframe interval of $\Delta t = 1$ ms was thus determined to be an optimal compromise, capable of capturing the low-velocity, small scale flow features with relatively small uncertainty, as well as transient and high velocity flow features.

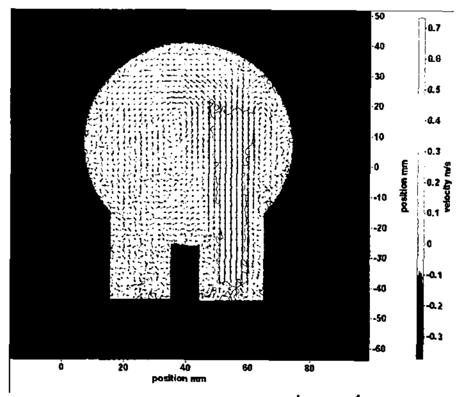

$\Delta t = 0.25$ ms, $\frac{t}{T} \simeq \frac{4}{9}$

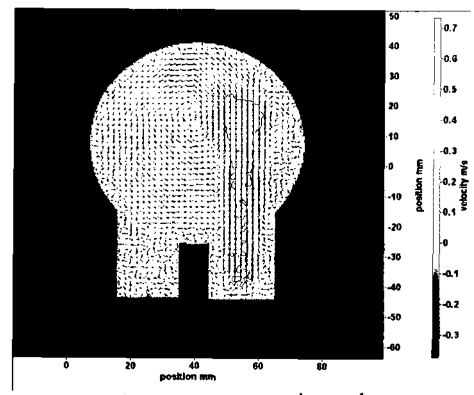

$\Delta t = 0.5$ ms, $\frac{t}{T} \simeq \frac{4}{9}$

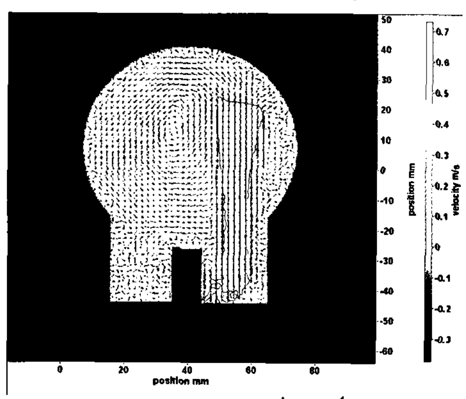

$\Delta t = 1$ ms, $\frac{t}{T} \simeq \frac{4}{9}$

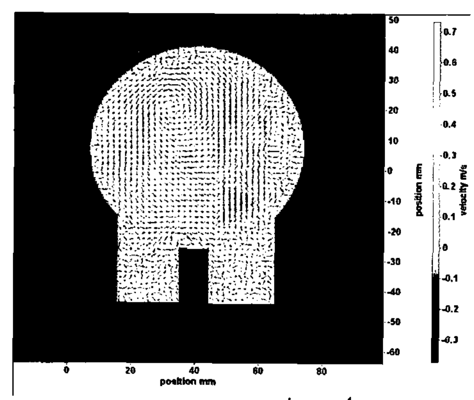

$\Delta t = 2$ ms, $\frac{t}{T} \simeq \frac{4}{9}$

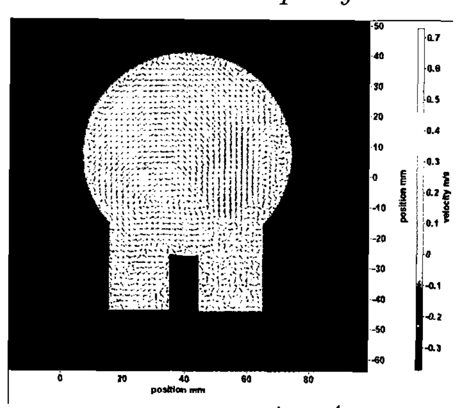

$\Delta t = 5$ ms, $\frac{t}{T} \simeq \frac{4}{9}$

Figure 6.1: Velocity maps measured with PIV for different interframe time intervals

6.2 Representative Cycle Flow Overview

Figures 6.2-6.28 display representative cycles of VAD operation for three PIV interframe times, Δt = 1, 0.5 and 0.25 ms. Figures 6.2-6.10 display the z = 20 mm $x - y$ plane, Figures 6.11-6.19 display an $x - z$ plane containing the axis of the inlet tube (y = 15 mm), and Figures 6.20-6.28 display an $x - z$ plane containing the axis of the outlet tube ($y = -15$ mm). Note that, although there are some cycle-to-cycle variations, these can be ignored for the purpose of comparisons of results obtained with different Δt.

After the outlet valve has closed and the inlet valve has opened, the residual flow through the outlet tube was clearly visible at $\frac{t}{T} \simeq \frac{1}{9}$ in Figure 6.2. Note however the regions of moderate velocity flow for the $\Delta t = 0.25$ ms case in Figure 6.2. The flow in the outlet tube was highly disorganized and the flow velocity in the VAD was very low at $\frac{t}{T} \simeq \frac{2}{9}$ in Figure 6.3, while there are some indications of the beginning of diastole with inlet jets forming in Figure 6.3 and Figure 6.12. The diastolic phase continues until it peaks at $\frac{t}{T} \simeq \frac{4}{9}$ in Figure 6.5 and Figure 6.14. The measured peak velocities were $U = 0.80$ ms^{-1} for $\Delta t = 1$ ms, $U = 0.74$ ms^{-1} for $\Delta t = 0.5$ ms, and $U = 0.84$ ms^{-1} for $\Delta t = 0.25$ ms. Such differences are probably representing cycle-to-cycle variations and measurement uncertainty, as they are not very significant and also they do not show a monotonic dependence of peak velocity on Δt. At $\frac{t}{T} \simeq \frac{5}{9}$ in Figure 6.15, it can be observed that the maximum velocity observed in the inlet jet increases with decreasing Δt values.

Systole begins at $\frac{t}{T} \simeq \frac{6}{9}$ and continues until $\frac{t}{T} \simeq \frac{9}{9}$, with two separate systolic peaks occuring, the first at $\frac{t}{T} \simeq \frac{7}{9}$, and a higher peak at $\frac{t}{T} \simeq \frac{9}{9}$, as displayed in Figures 6.25-6.28. A general trend in Figures 6.7-6.10 as well as Figures 6.25-6.28 is that the maximum velocity

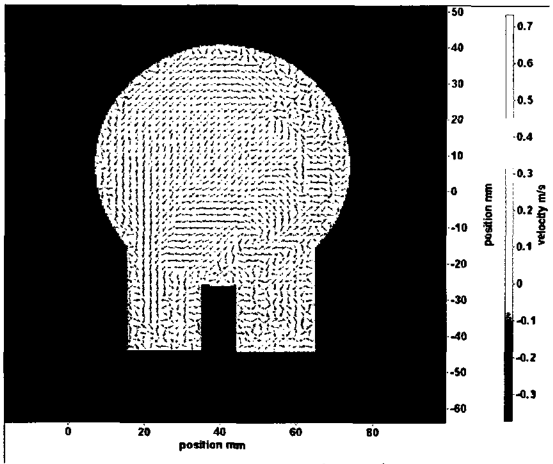

$\Delta t = 1$ ms, $\frac{t}{T} \simeq \frac{1}{9}$

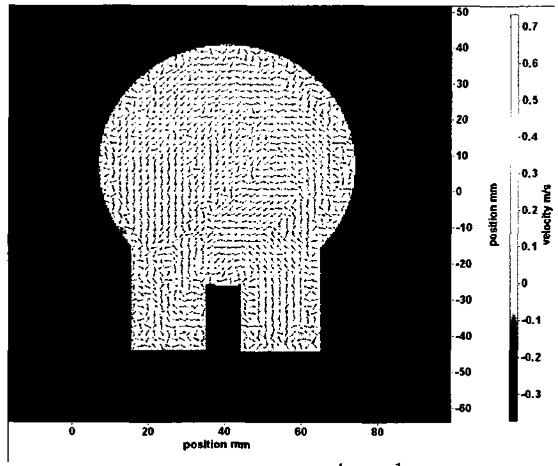

$\Delta t = 0.5$ ms, $\frac{t}{T} \simeq \frac{1}{9}$

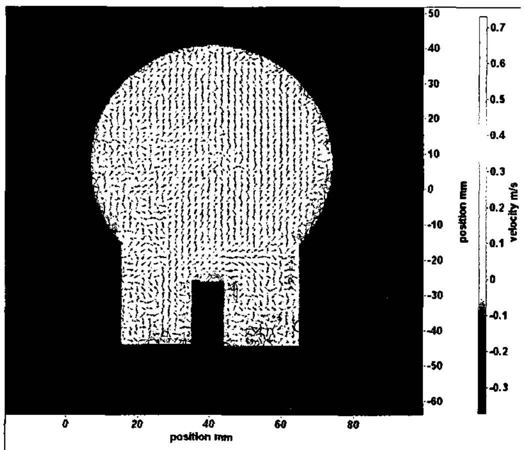

$\Delta t = 0.25$ ms, $\frac{t}{T} \simeq \frac{1}{9}$

Figure 6.2: XY representative PIV maps (z= 20 mm)

measured increased with decreasing Δt values. However, with decreasing Δt values, more false high velocity values were also measured, such as velocities of $U > 0.75$ ms^{-1} in the inlet tube during systole. These patterns are explained in detail in the following chapter.

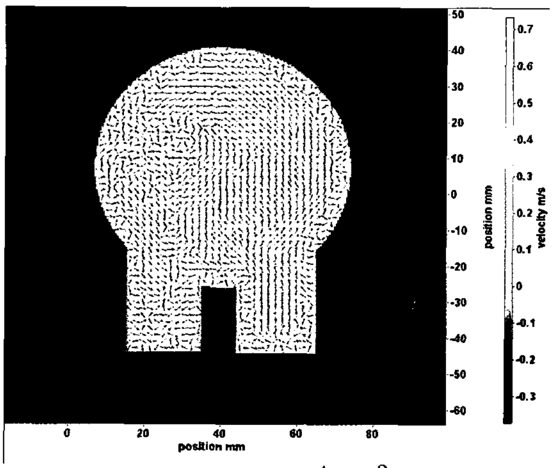

$\Delta t = 1$ ms, $\frac{t}{T} \simeq \frac{2}{9}$

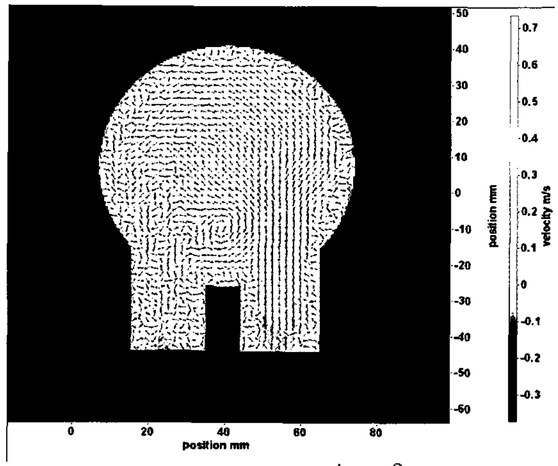

$\Delta t = 0.5$ ms, $\frac{t}{T} \simeq \frac{2}{9}$

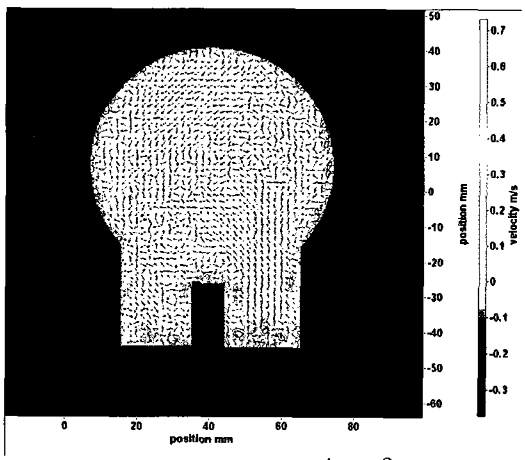

$\Delta t = 0.25$ ms, $\frac{t}{T} \simeq \frac{2}{9}$

Figure 6.3: XY representative PIV maps (z= 20 mm) (continued)

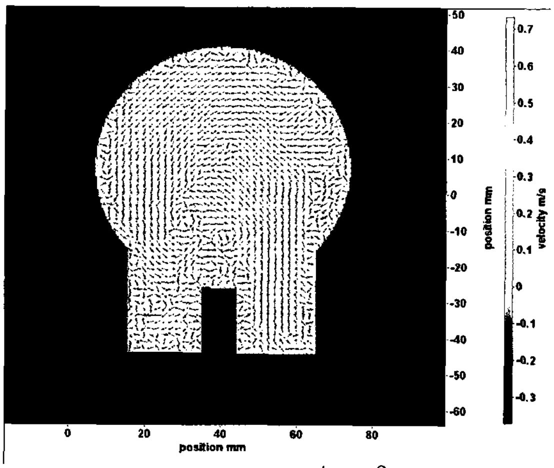

$\Delta t = 1$ ms, $\frac{t}{T} \simeq \frac{3}{9}$

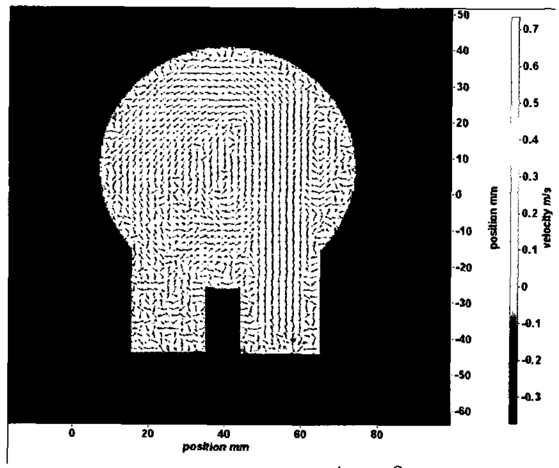

$\Delta t = 0.5$ ms, $\frac{t}{T} \simeq \frac{3}{9}$

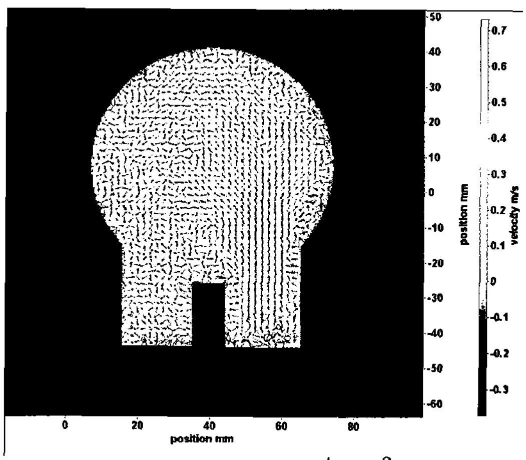

$\Delta t = 0.25$ ms, $\frac{t}{T} \simeq \frac{3}{9}$

Figure 6.4: XY representative PIV maps (z= 20 mm) (continued)

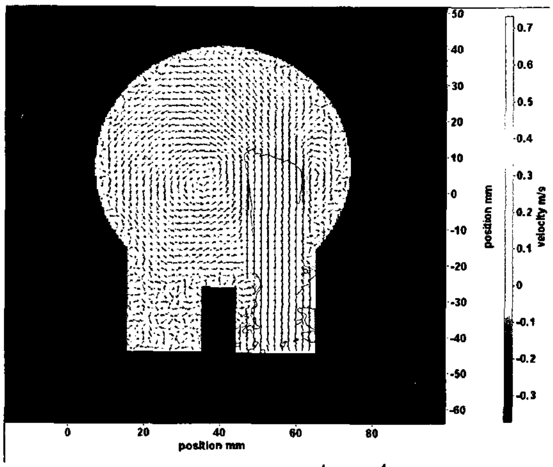

$\Delta t = 1$ ms, $\frac{t}{T} \simeq \frac{4}{9}$

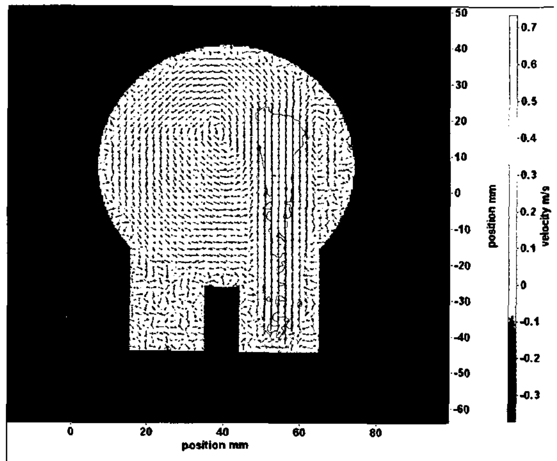

$\Delta t = 0.5$ ms, $\frac{t}{T} \simeq \frac{4}{9}$

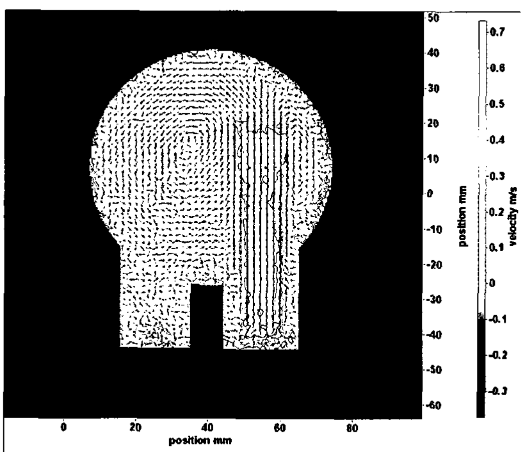

$\Delta t = 0.25$ ms, $\frac{t}{T} \simeq \frac{4}{9}$

Figure 6.5: XY representative PIV maps (z= 20 mm) (continued)

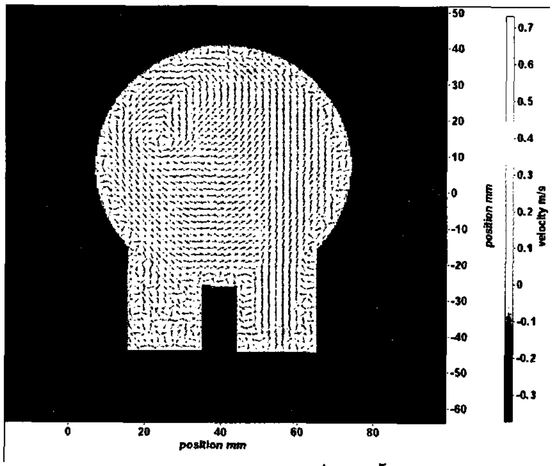

$\Delta t = 1$ ms, $\frac{t}{T} \simeq \frac{5}{9}$

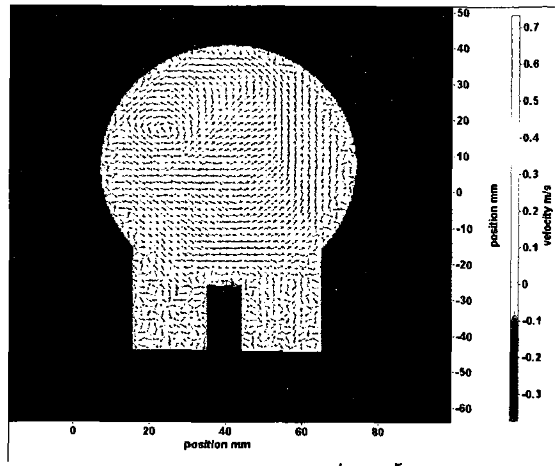

$\Delta t = 0.5$ ms, $\frac{t}{T} \simeq \frac{5}{9}$

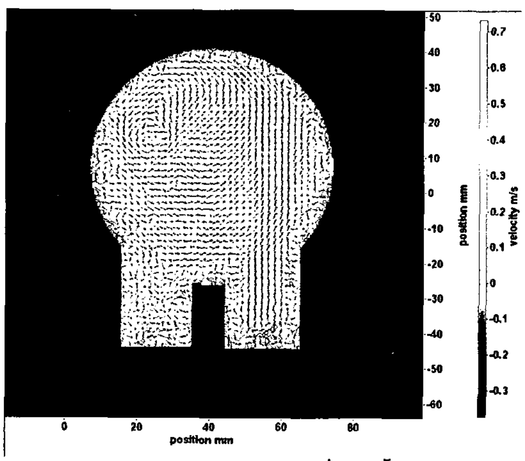

$\Delta t = 0.25$ ms, $\frac{t}{T} \simeq \frac{5}{9}$

Figure 6.6: XY representative PIV maps (z= 20 mm) (continued)

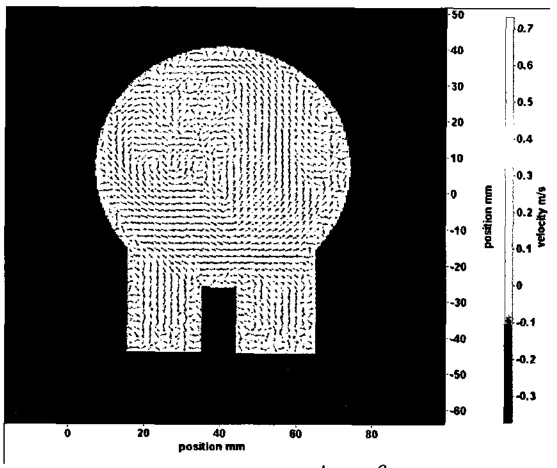

$\Delta t = 1$ ms, $\frac{t}{T} \simeq \frac{6}{9}$

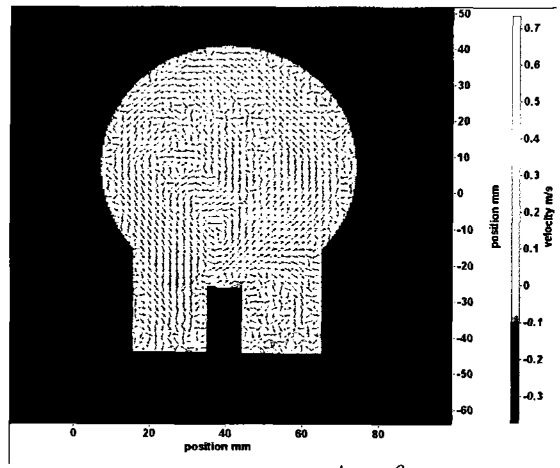

$\Delta t = 0.5$ ms, $\frac{t}{T} \simeq \frac{6}{9}$

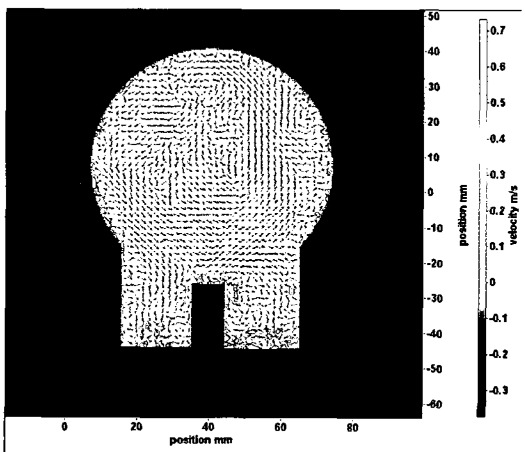

$\Delta t = 0.25$ ms, $\frac{t}{T} \simeq \frac{6}{9}$

Figure 6.7: XY representative PIV maps (z= 20 mm) (continued)

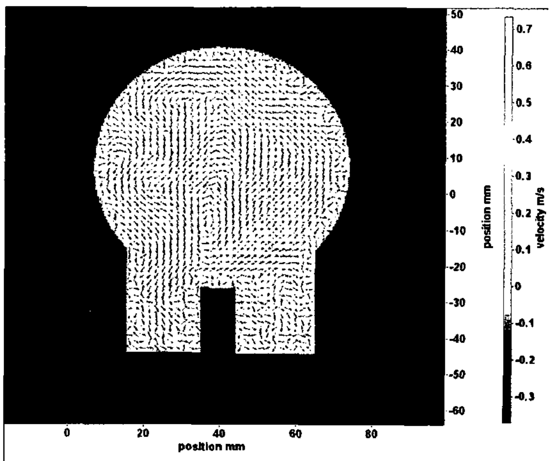

$\Delta t = 1$ ms, $\frac{t}{T} \simeq \frac{7}{9}$

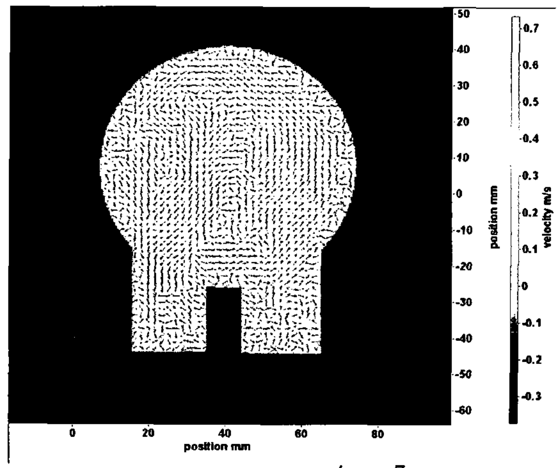

$\Delta t = 0.5$ ms, $\frac{t}{T} \simeq \frac{7}{9}$

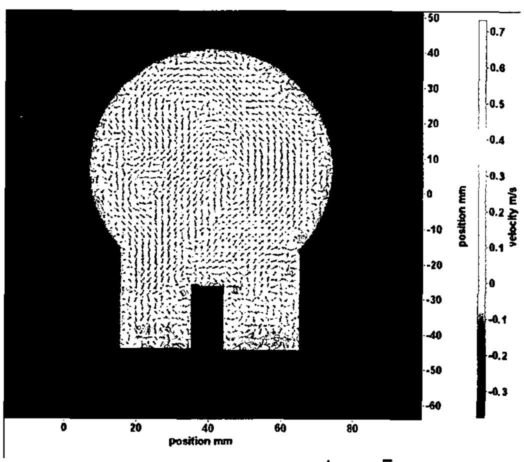

$\Delta t = 0.25$ ms, $\frac{t}{T} \simeq \frac{7}{9}$

Figure 6.8: XY representative PIV maps (z= 20 mm) (continued)

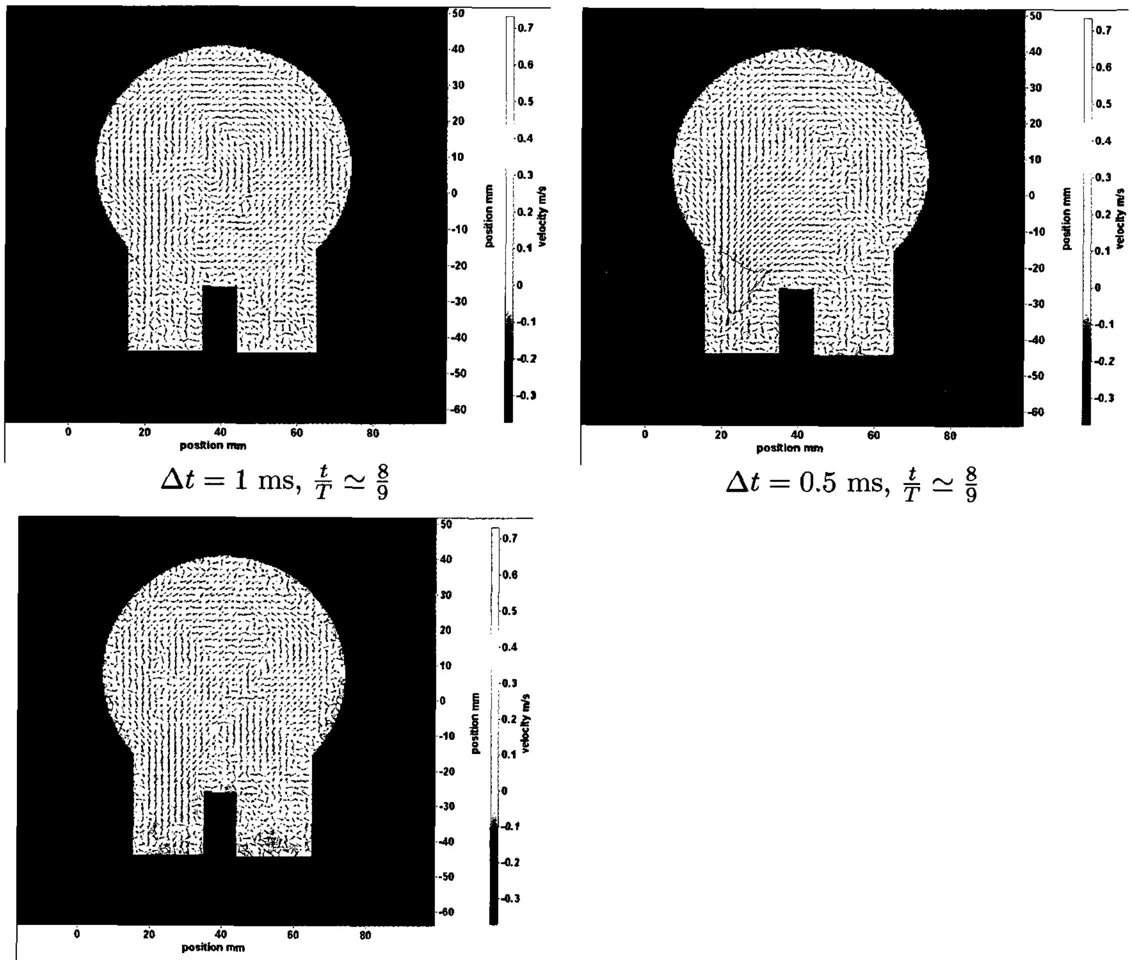

$\Delta t = 1$ ms, $\frac{t}{T} \simeq \frac{8}{9}$

$\Delta t = 0.5$ ms, $\frac{t}{T} \simeq \frac{8}{9}$

$\Delta t = 0.25$ ms, $\frac{t}{T} \simeq \frac{8}{9}$

Figure 6.9: XY representative PIV maps (z= 20 mm) (continued)

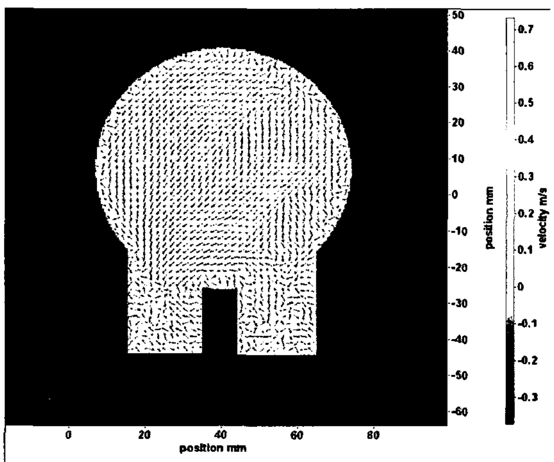

$\Delta t = 1$ ms, $\frac{t}{T} \simeq \frac{9}{9}$

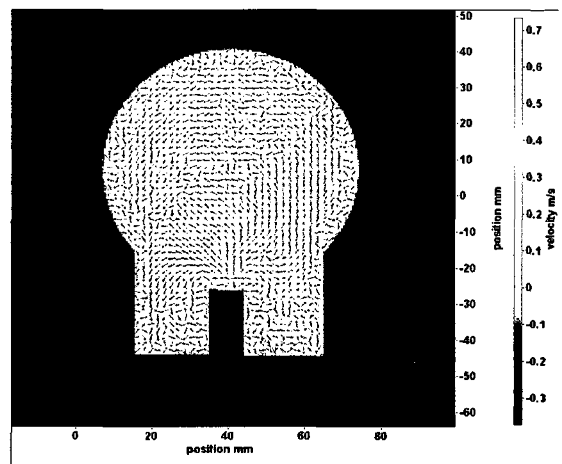

$\Delta t = 0.5$ ms, $\frac{t}{T} \simeq \frac{9}{9}$

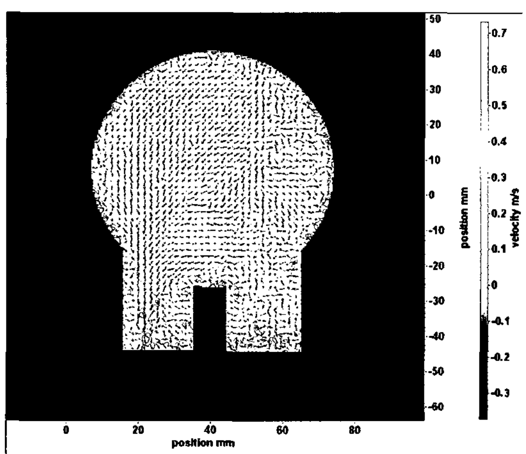

$\Delta t = 0.25$ ms, $\frac{t}{T} \simeq \frac{9}{9}$

Figure 6.10: XY representative PIV maps (z= 20 mm) (continued)

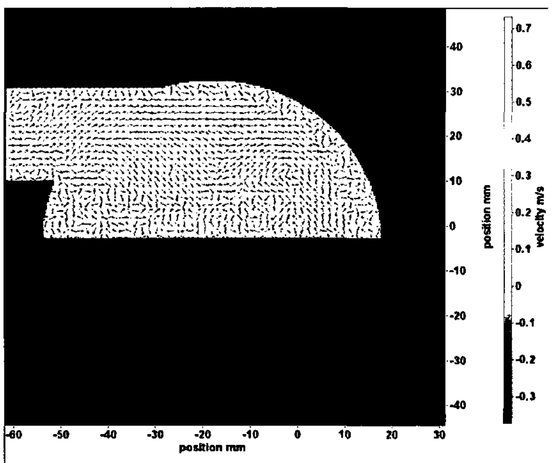

$\Delta t = 1$ ms, $\frac{t}{T} \simeq \frac{1}{9}$

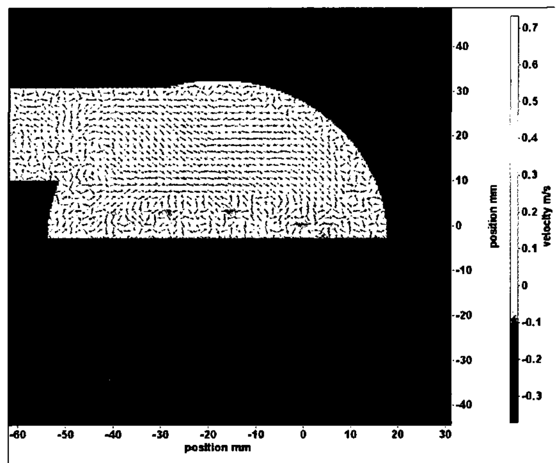

$\Delta t = 0.5$ ms, $\frac{t}{T} \simeq \frac{1}{9}$

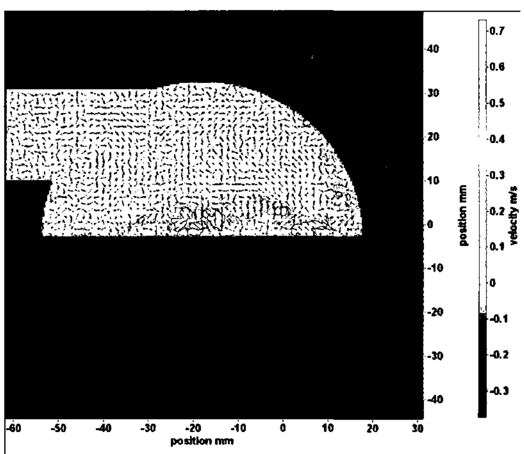

$\Delta t = 0.25$ ms, $\frac{t}{T} \simeq \frac{1}{9}$

Figure 6.11: XZ representative PIV maps (y= 15 mm)

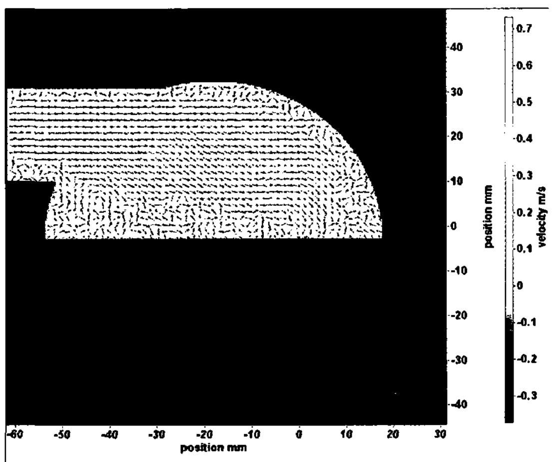

$\Delta t = 1$ ms, $\frac{t}{T} \simeq \frac{2}{9}$

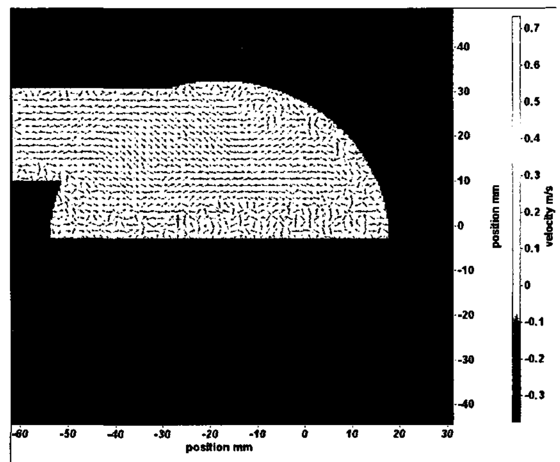

$\Delta t = 0.5$ ms, $\frac{t}{T} \simeq \frac{2}{9}$

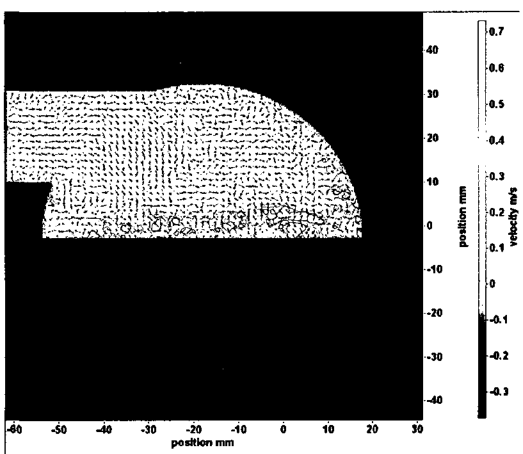

$\Delta t = 0.25$ ms, $\frac{t}{T} \simeq \frac{2}{9}$

Figure 6.12: XZ representative PIV maps (y= 15 mm) (continued)

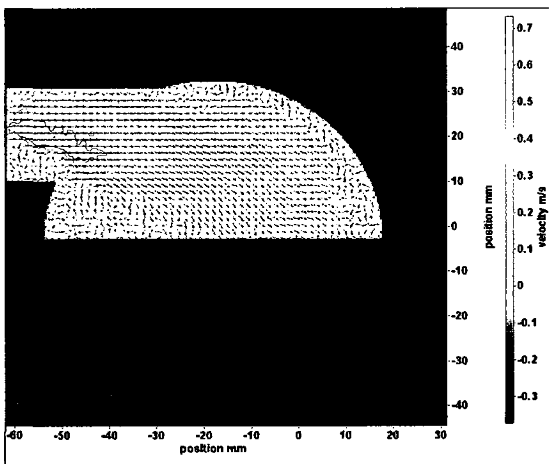

$\Delta t = 1$ ms, $\frac{t}{T} \simeq \frac{3}{9}$

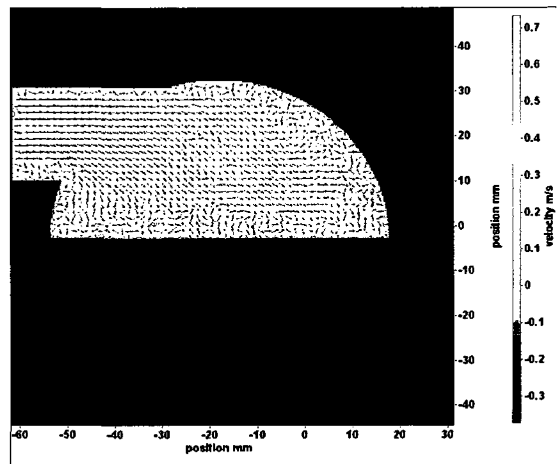

$\Delta t = 0.5$ ms, $\frac{t}{T} \simeq \frac{3}{9}$

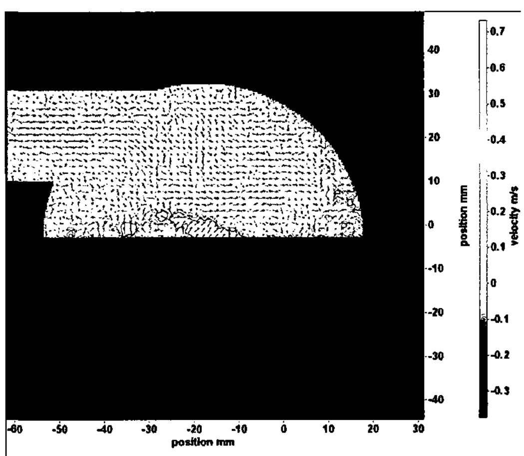

$\Delta t = 0.25$ ms, $\frac{t}{T} \simeq \frac{3}{9}$

Figure 6.13: XZ representative PIV maps (y= 15 mm) (continued)

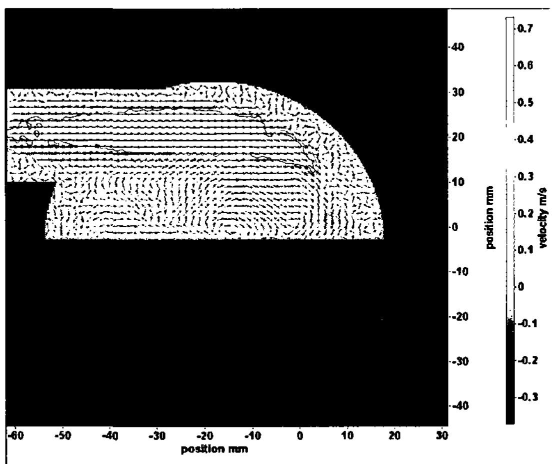

$\Delta t = 1$ ms, $\frac{t}{T} \simeq \frac{4}{9}$

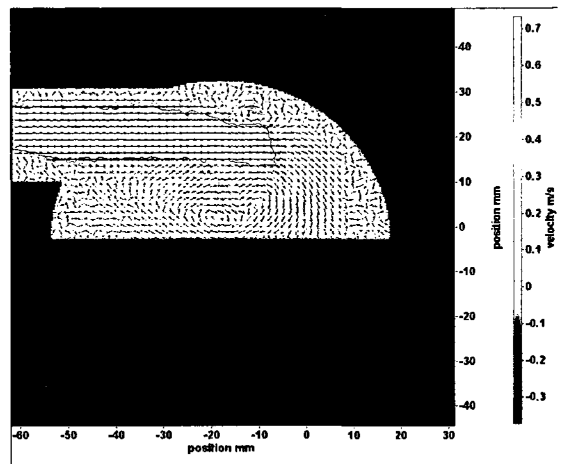

$\Delta t = 0.5$ ms, $\frac{t}{T} \simeq \frac{4}{9}$

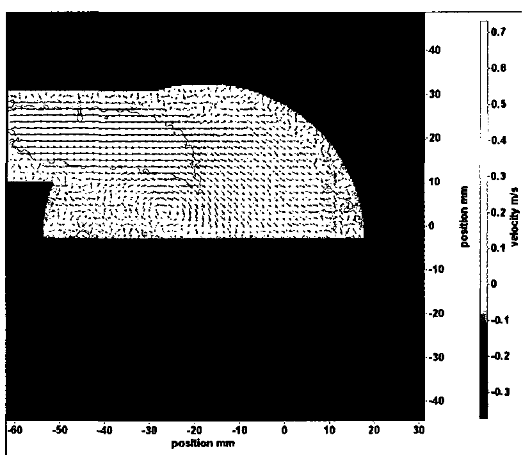

$\Delta t = 0.25$ ms, $\frac{t}{T} \simeq \frac{4}{9}$

Figure 6.14: XZ representative PIV maps (y= 15 mm) (continued)

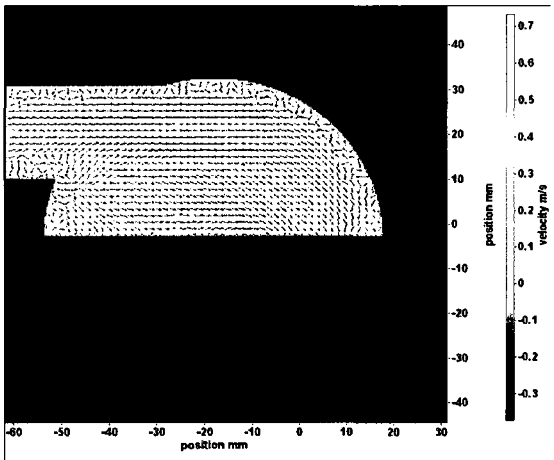

$\Delta t = 1$ ms, $\frac{t}{T} \simeq \frac{5}{9}$

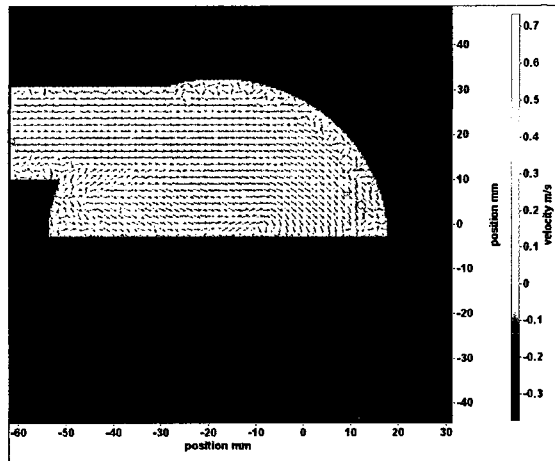

$\Delta t = 0.5$ ms, $\frac{t}{T} \simeq \frac{5}{9}$

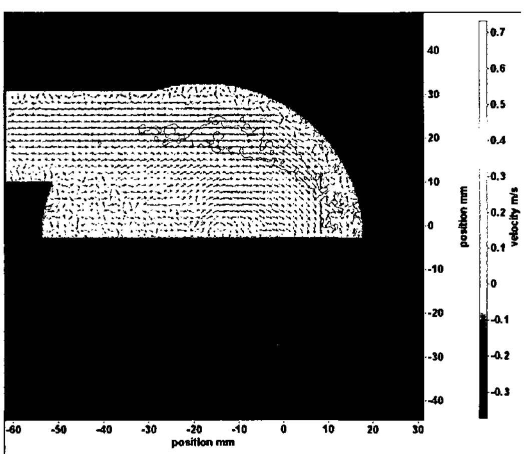

$\Delta t = 0.25$ ms, $\frac{t}{T} \simeq \frac{5}{9}$

Figure 6.15: XZ representative PIV maps (y= 15 mm) (continued)

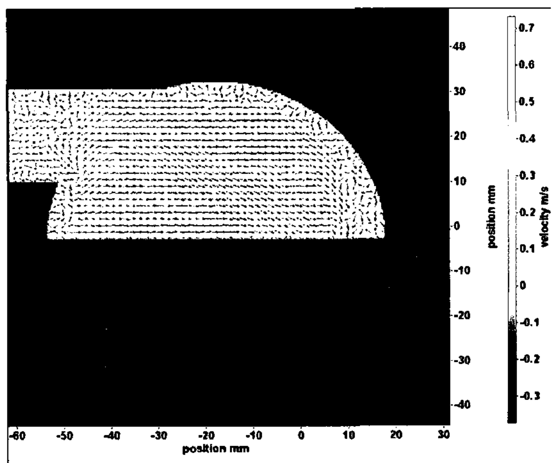

$\Delta t = 1$ ms, $\frac{t}{T} \simeq \frac{6}{9}$

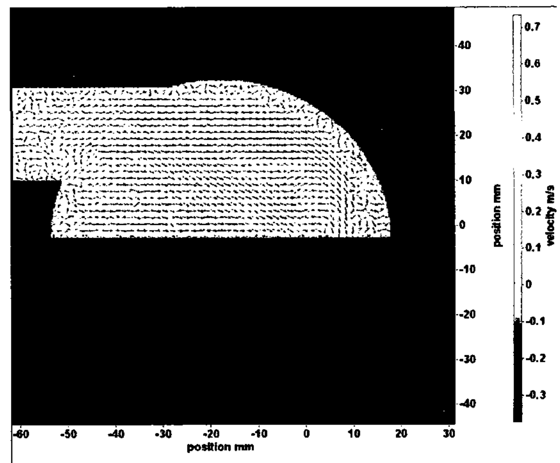

$\Delta t = 0.5$ ms, $\frac{t}{T} \simeq \frac{6}{9}$

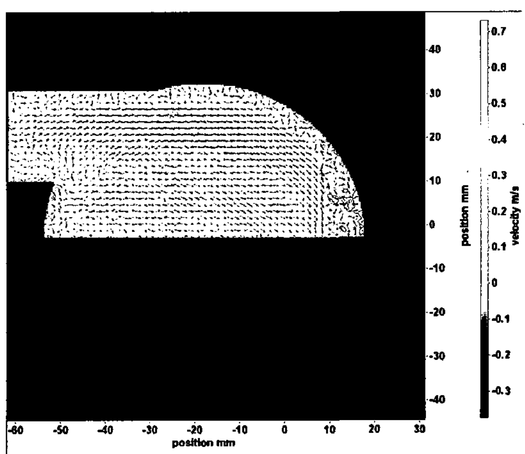

$\Delta t = 0.25$ ms, $\frac{t}{T} \simeq \frac{6}{9}$

Figure 6.16: XZ representative PIV maps (y= 15 mm) (continued)

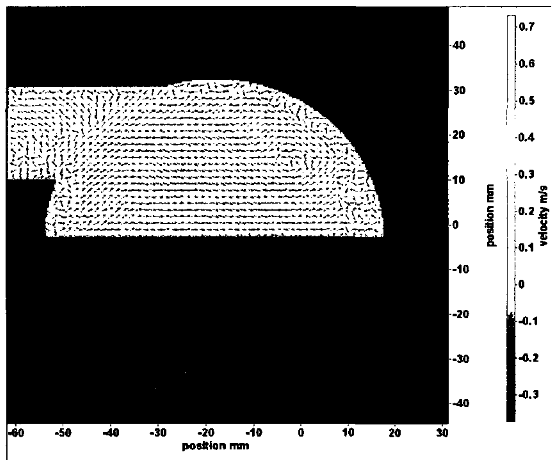

$\Delta t = 1$ ms, $\frac{t}{T} \simeq \frac{7}{9}$

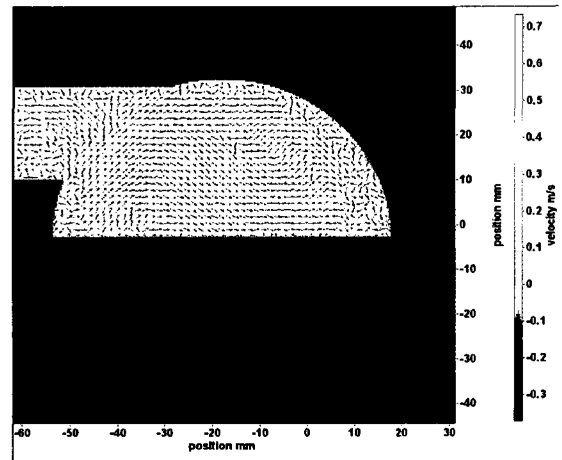

$\Delta t = 0.5$ ms, $\frac{t}{T} \simeq \frac{7}{9}$

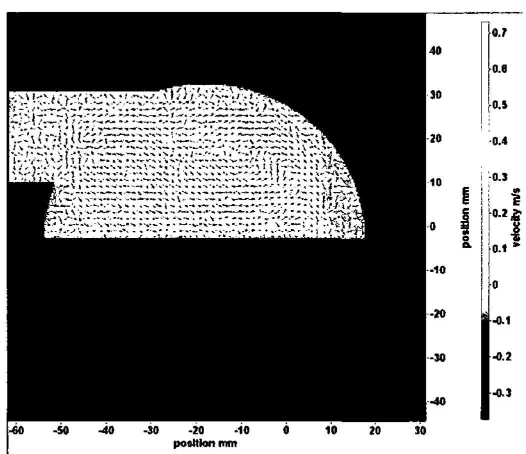

$\Delta t = 0.25$ ms, $\frac{t}{T} \simeq \frac{7}{9}$

Figure 6.17: XZ representative PIV maps (y= 15 mm) (continued)

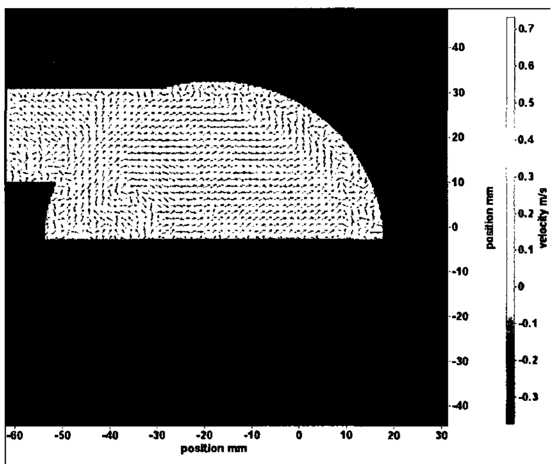

$\Delta t = 1$ ms, $\frac{t}{T} \simeq \frac{8}{9}$

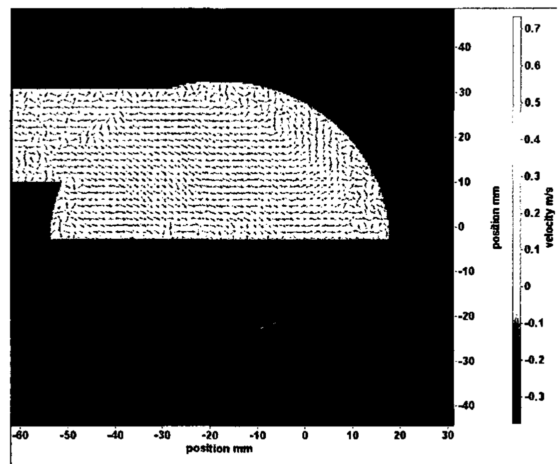

$\Delta t = 0.5$ ms, $\frac{t}{T} \simeq \frac{8}{9}$

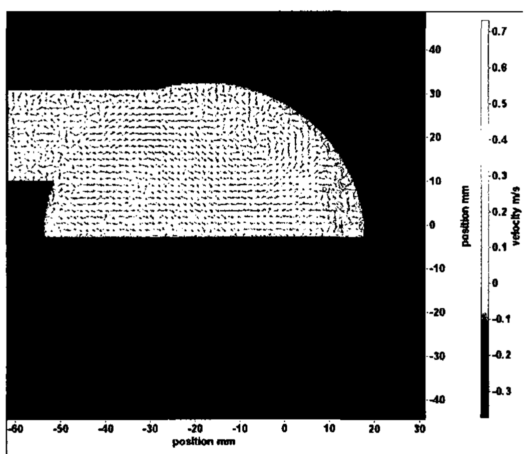

$\Delta t = 0.25$ ms, $\frac{t}{T} \simeq \frac{8}{9}$

Figure 6.18: XZ representative PIV maps (y= 15 mm) (continued)

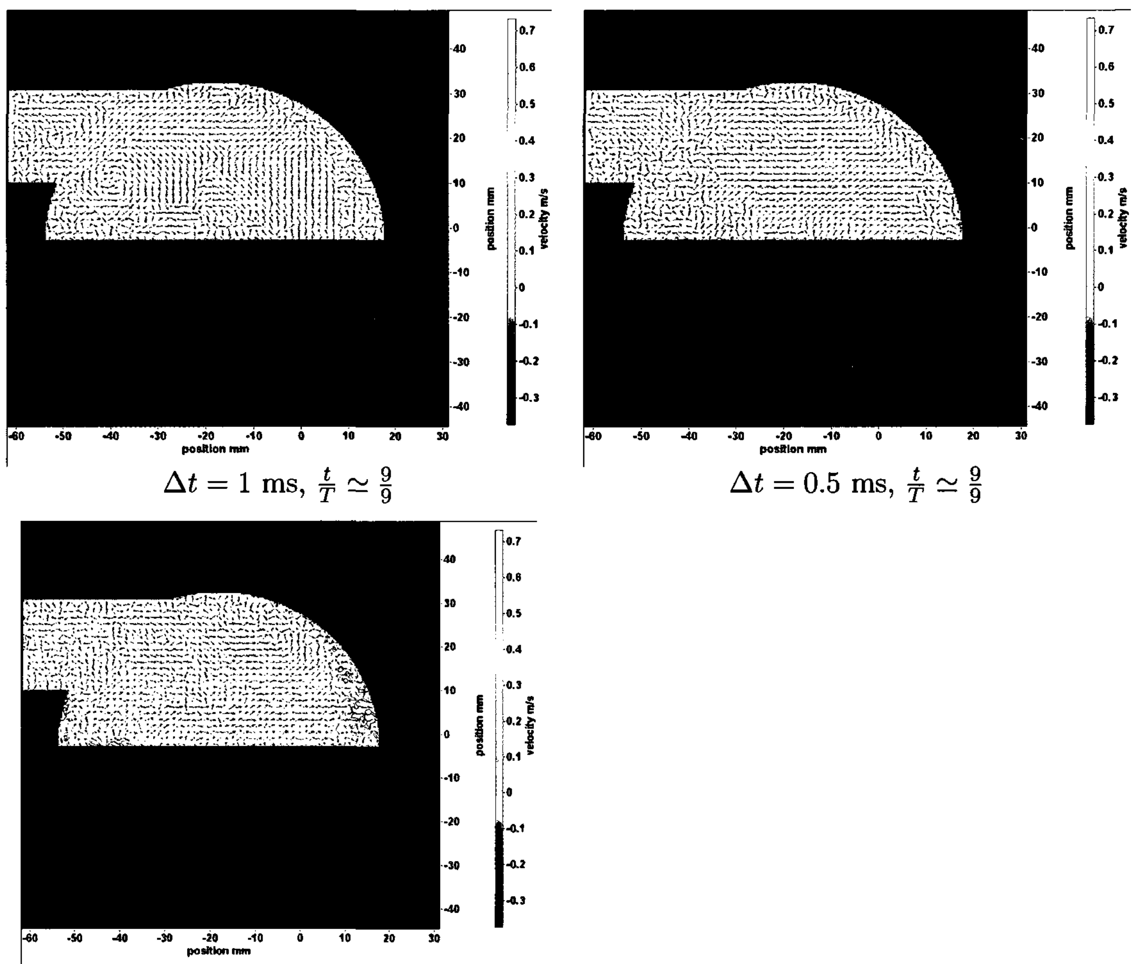

$\Delta t = 1$ ms, $\frac{t}{T} \simeq \frac{9}{9}$

$\Delta t = 0.5$ ms, $\frac{t}{T} \simeq \frac{9}{9}$

$\Delta t = 0.25$ ms, $\frac{t}{T} \simeq \frac{9}{9}$

Figure 6.19: XZ representative PIV maps (y= 15 mm) (continued)

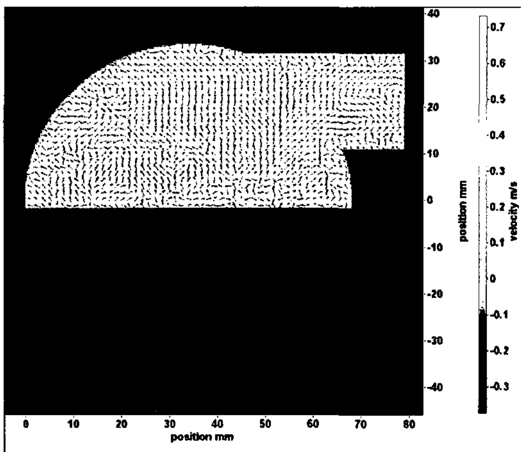

$\Delta t = 1$ ms, $\frac{t}{T} \simeq \frac{1}{9}$

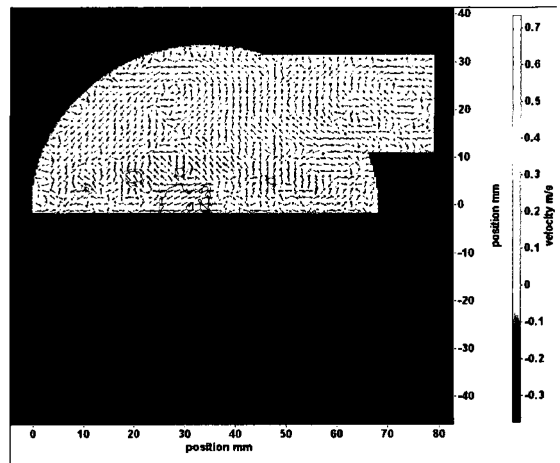

$\Delta t = 0.5$ ms, $\frac{t}{T} \simeq \frac{1}{9}$

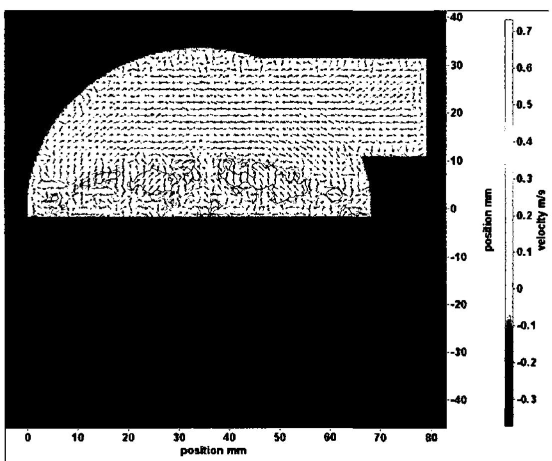

$\Delta t = 0.25$ ms, $\frac{t}{T} \simeq \frac{1}{9}$

Figure 6.20: XZ representative PIV maps (y= -15 mm)

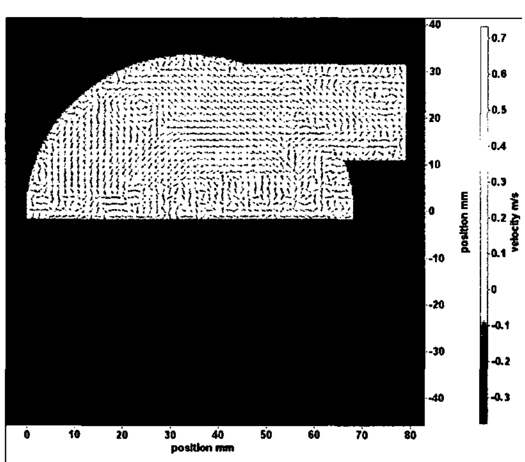

$\Delta t = 1$ ms, $\frac{t}{T} \simeq \frac{2}{9}$

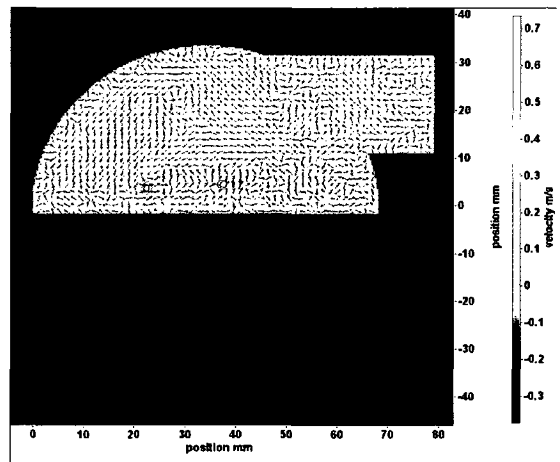

$\Delta t = 0.5$ ms, $\frac{t}{T} \simeq \frac{2}{9}$

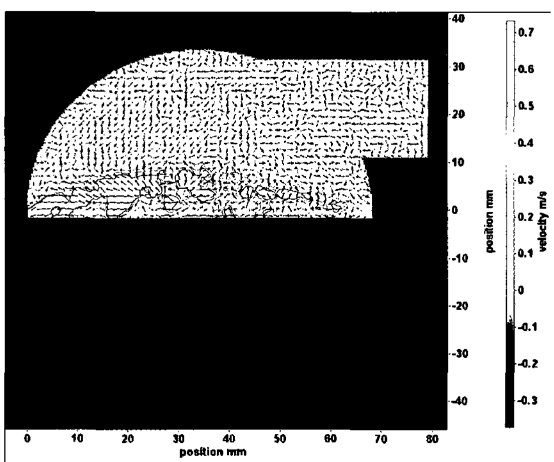

$\Delta t = 0.25$ ms, $\frac{t}{T} \simeq \frac{2}{9}$

Figure 6.21: XZ representative PIV maps (y= -15 mm) (continued)

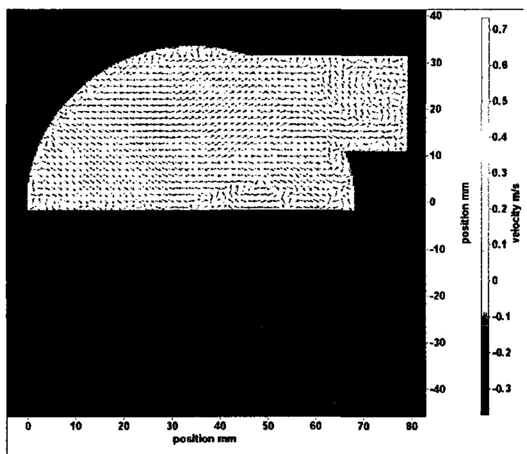

$\Delta t = 1$ ms, $\frac{t}{T} \simeq \frac{3}{9}$

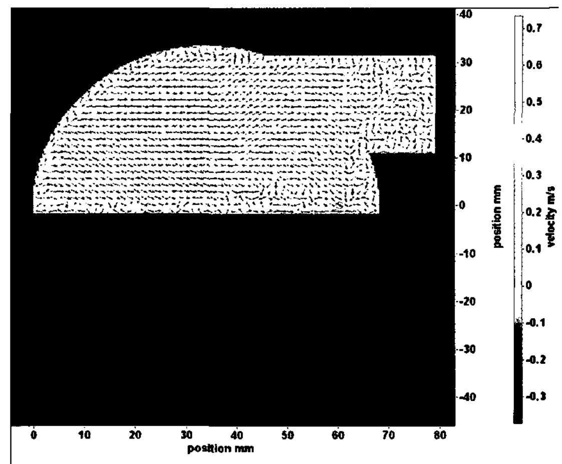

$\Delta t = 0.5$ ms, $\frac{t}{T} \simeq \frac{3}{9}$

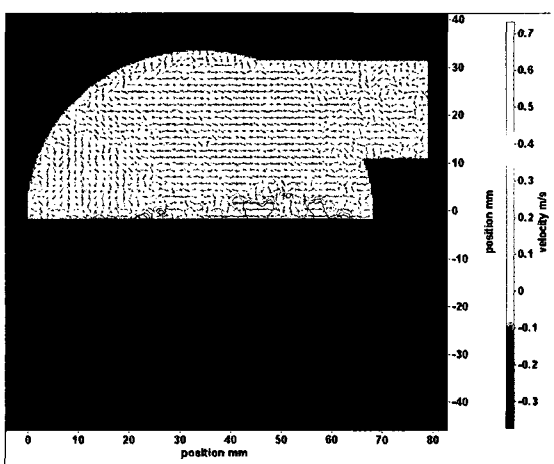

$\Delta t = 0.25$ ms, $\frac{t}{T} \simeq \frac{3}{9}$

Figure 6.22: XZ representative PIV maps (y= -15 mm) (continued)

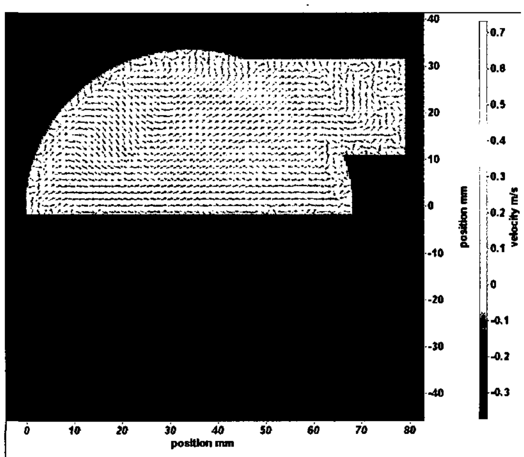

$\Delta t = 1$ ms, $\frac{t}{T} \simeq \frac{4}{9}$

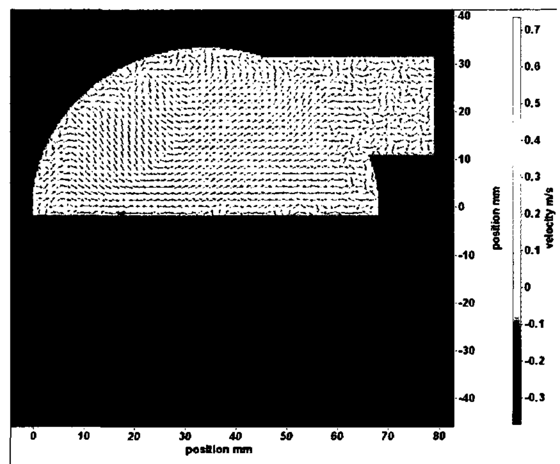

$\Delta t = 0.5$ ms, $\frac{t}{T} \simeq \frac{4}{9}$

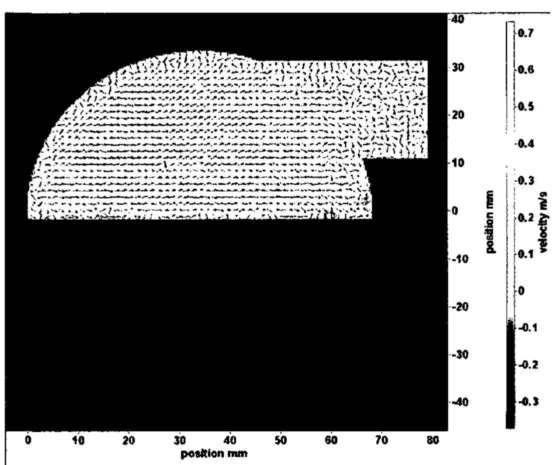

$\Delta t = 0.25$ ms, $\frac{t}{T} \simeq \frac{4}{9}$

Figure 6.23: XZ representative PIV maps (y= -15 mm) (continued)

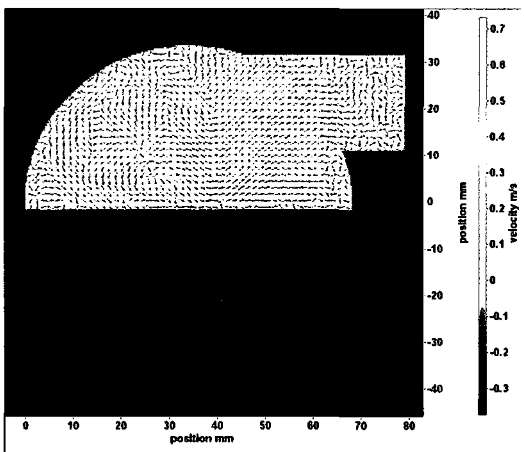

$\Delta t = 1$ ms, $\frac{t}{T} \simeq \frac{5}{9}$

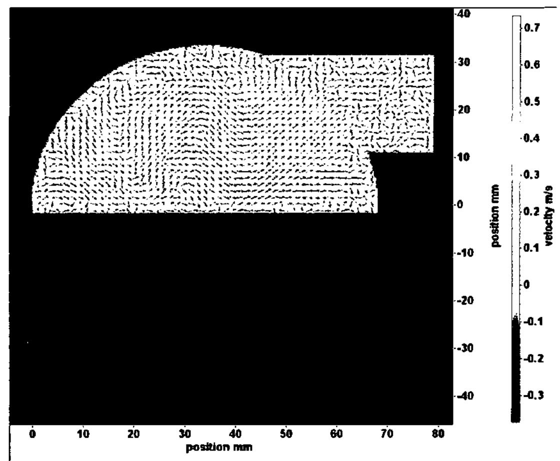

$\Delta t = 0.5$ ms, $\frac{t}{T} \simeq \frac{5}{9}$

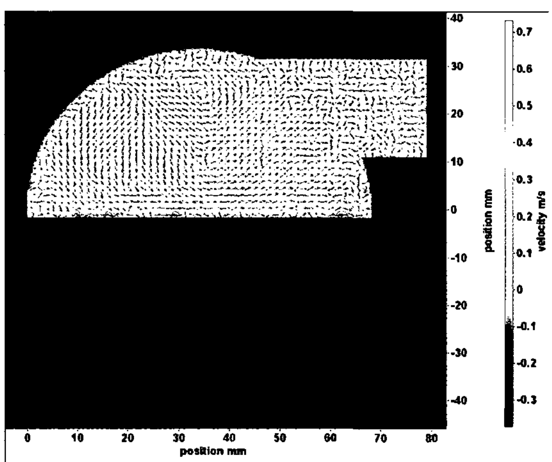

$\Delta t = 0.25$ ms, $\frac{t}{T} \simeq \frac{5}{9}$

Figure 6.24: XZ representative PIV maps (y= -15 mm) (continued)

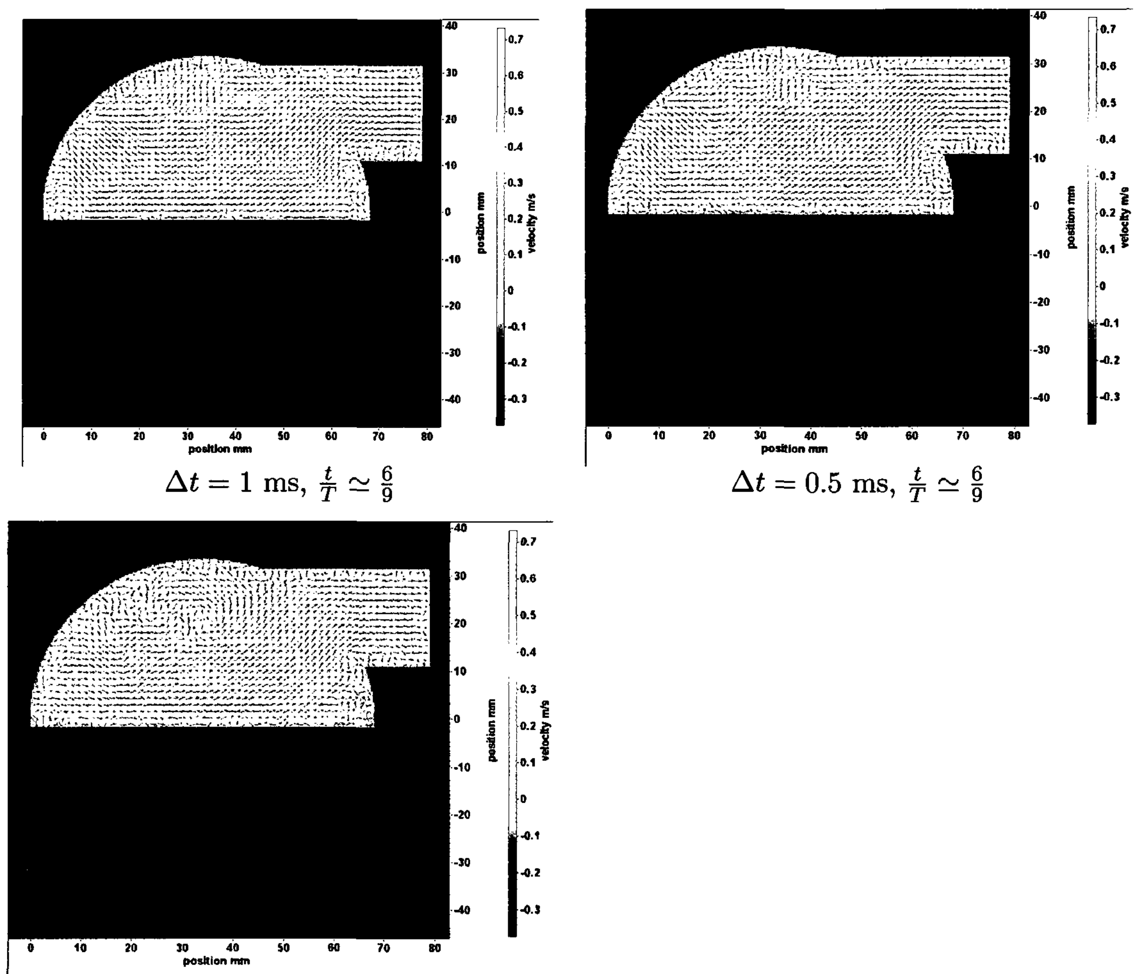

$\Delta t = 1$ ms, $\frac{t}{T} \simeq \frac{6}{9}$

$\Delta t = 0.5$ ms, $\frac{t}{T} \simeq \frac{6}{9}$

$\Delta t = 0.25$ ms, $\frac{t}{T} \simeq \frac{6}{9}$

Figure 6.25: XZ representative PIV maps (y= -15 mm) (continued)

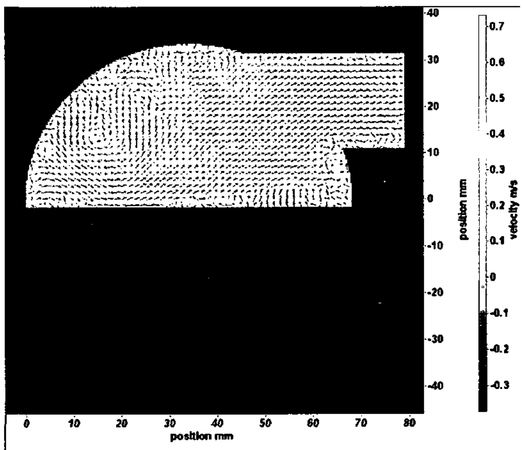

$\Delta t = 1$ ms, $\frac{t}{T} \simeq \frac{7}{9}$

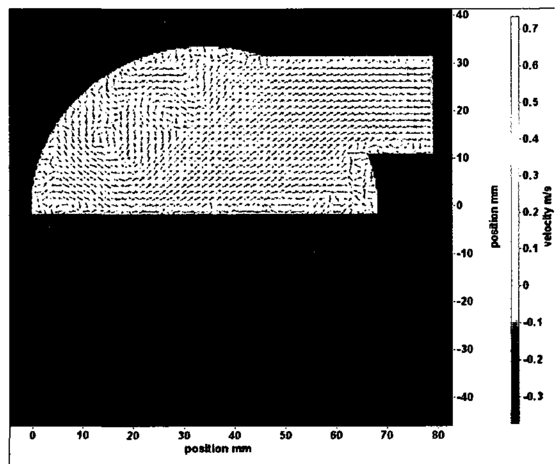

$\Delta t = 0.5$ ms, $\frac{t}{T} \simeq \frac{7}{9}$

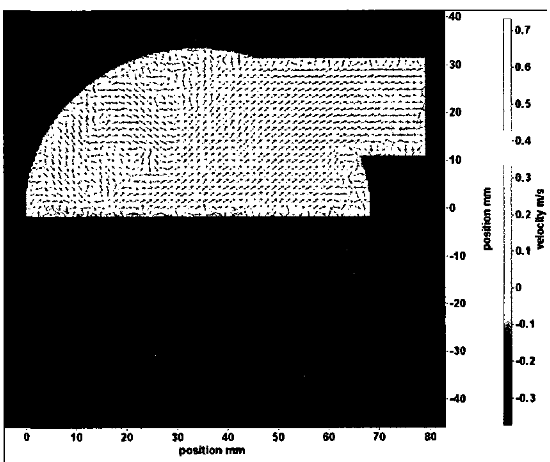

$\Delta t = 0.25$ ms, $\frac{t}{T} \simeq \frac{7}{9}$

Figure 6.26: XZ representative PIV maps (y= -15 mm) (continued)

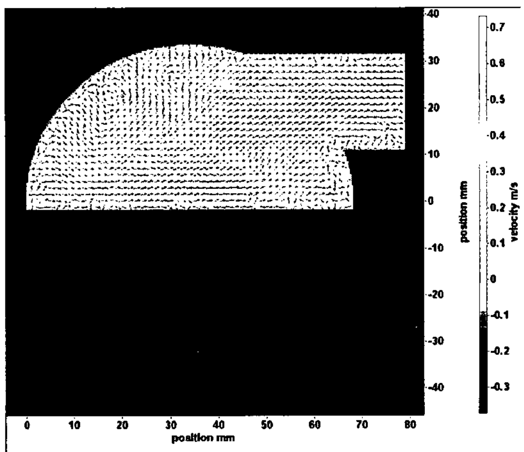

$\Delta t = 1$ ms, $\frac{t}{T} \simeq \frac{8}{9}$

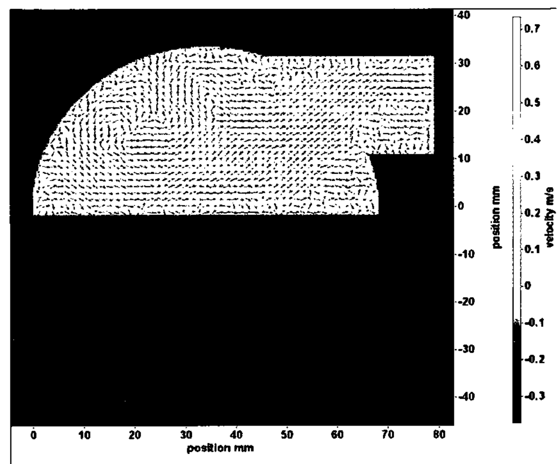

$\Delta t = 0.5$ ms, $\frac{t}{T} \simeq \frac{8}{9}$

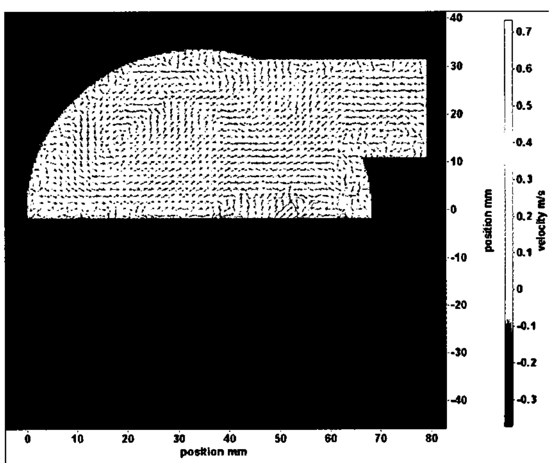

$\Delta t = 0.25$ ms, $\frac{t}{T} \simeq \frac{8}{9}$

Figure 6.27: XZ representative PIV maps (y= -15 mm) (continued)

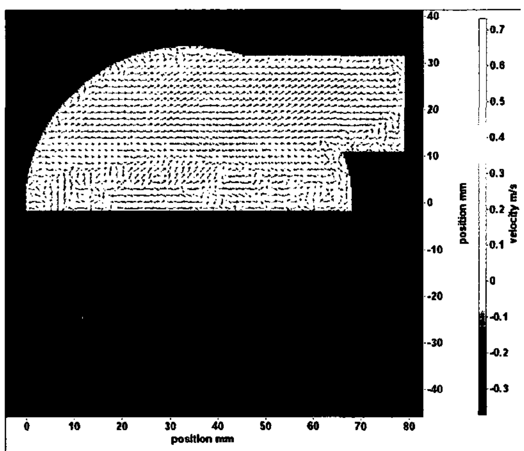

$\Delta t = 1$ ms, $\frac{t}{T} \simeq \frac{9}{9}$

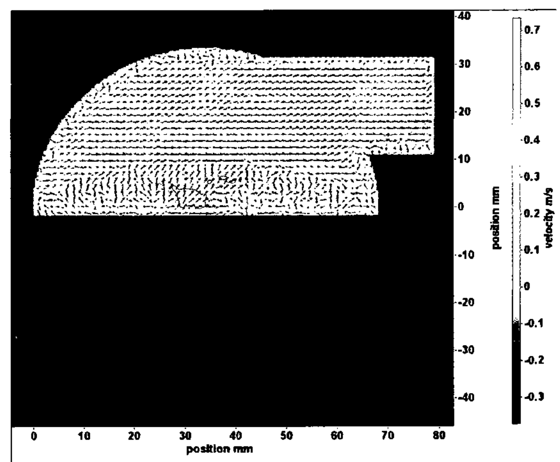

$\Delta t = 0.5$ ms, $\frac{t}{T} \simeq \frac{9}{9}$

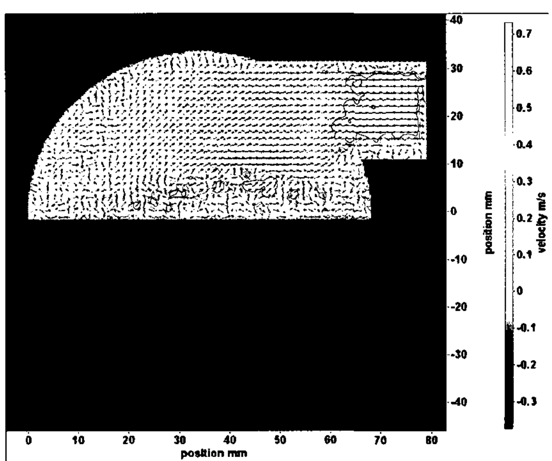

$\Delta t = 0.25$ ms, $\frac{t}{T} \simeq \frac{9}{9}$

Figure 6.28: XZ representative PIV maps (y= -15 mm) (continued)

6.3 Velocity Maps

The results of the PIV measurements are presented in the following sections. The scales for these figures were selected for best visual contrast, and do not represent the full velocity range encountered in operation. Interference from the diaphragm in the $z = 11$ mm plane caused reflections that prevented reliable measurements from being taken. Included in this chapter are the averaged results on the three planes with $z = 20$ mm and $y = 15, 0$ and -15 mm. The results for the $z = 29$ mm plane have been included in Appendix C.

At $\frac{t}{T} = \frac{0}{13}$, there was still flow present in the outlet tube as the outlet valve closes and the inlet valve opens (Figure 6.29), and no inlet flow was yet present (Figure 6.33). The velocity throughout the VAD began to decrease as the diaphragm began to expand in the negative z-direction at $\frac{t}{T} = \frac{1}{13}$ (Figure 6.29). There were no visible flow structures or vortices during this time and the flow was nearly stagnant. Figure 6.33 illustrates the formation of the inlet jet as fluid was drawn in from the reservoir at $\frac{t}{T} = \frac{2}{13}$, and this continued until the diastolic peak at $\frac{t}{T} = \frac{5}{13}$, as shown in Figure 6.30, where a maximum value of $U = 0.9$ m/s was recorded. During the injection, the formation and development of a vortex in the $x - y$ plane as it washes out of the VAD was observed in Figure 6.30, as well as a vortex in the $x - z$ plane in Figure 6.34. The $x - y$ and $x - z$ vortices mix the injected fluid with the fluid already present in the VAD, and provide washout of the VAD, as the centres of vortices could be seen moving in position from the area adjacent to the inlet opening along the x-axis from $\frac{t}{T} = \frac{4}{13}$ until the end of diastole at $\frac{t}{T} = \frac{7}{13}$ (Figures 6.30, and 6.34). Although much of the VAD volume was affected by the diastolic washout, regions of low velocity were present in the region directly adjacent to both the inlet and outlet tubes, as well as within the outlet tube during this period (Figure 6.29). Note that the path of the inlet jet during diastole was fairly straight and only changed when the jet approached the opposite wall.

The mixing phase continued until the beginning of systole at $\frac{t}{T} = \frac{8}{13}$, as the diaphragm reached its maximum deflection in the negative z-domain and the inlet valve closed and the outlet valve opened. The flow velocity in the inlet region decreased while the velocity in the outlet increased, as displayed in Figures 6.31 and 6.39. There were two noticeable peaks in the ejection cycle, the first at $\frac{t}{T} = \frac{9}{13}$, displayed in Figures 6.31 and 6.39, and the second at $\frac{t}{T} = \frac{12}{13}$, which was observed in Figures 6.56 and 6.40. The maximum velocity observed during ejection was $U = 1.02$ m/s at $\frac{t}{T} = \frac{12}{13}$. During the ejection of the fluid into the reservoir, a region of stagnant flow was present in the inlet tube, as can be seen in Figures 6.32 and 6.36. Additional regions of low velocity could be observed in the region opposite the outlet tube in Figures 6.39 and 6.40, and in the central region of the VAD in Figure 6.44.

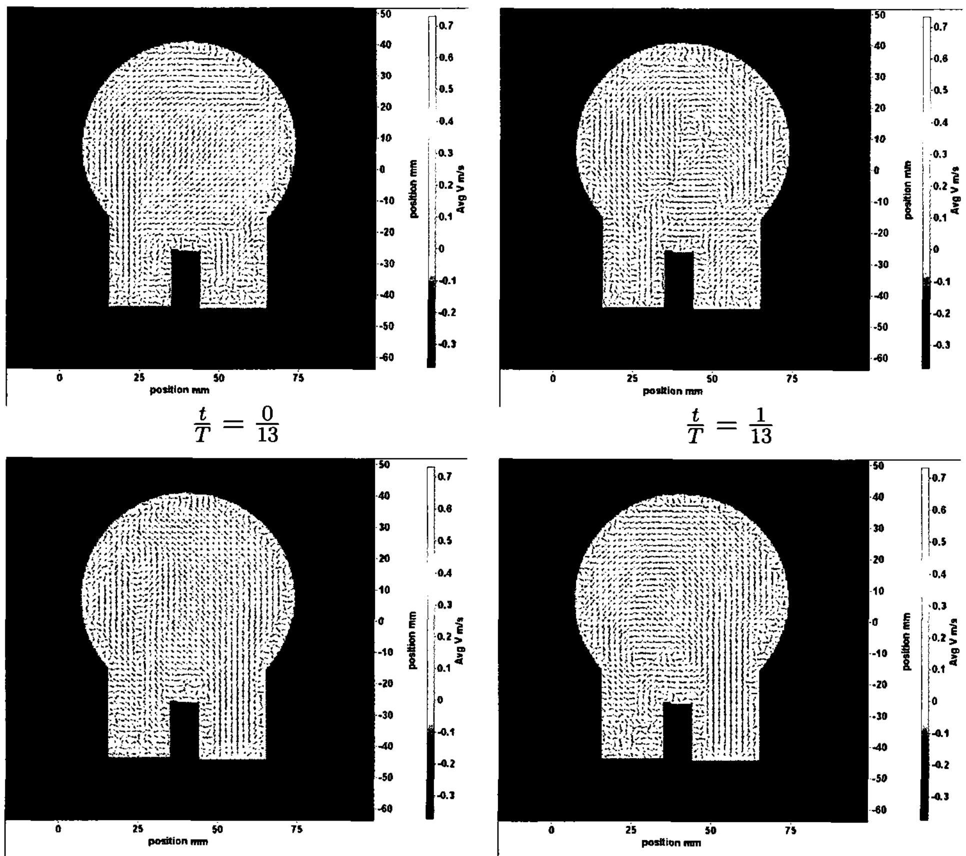

$\frac{t}{T} = \frac{0}{13}$ $\frac{t}{T} = \frac{1}{13}$

$\frac{t}{T} = \frac{2}{13}$ $\frac{t}{T} = \frac{3}{13}$

Figure 6.29: Average PIV XY velocity maps (z=20 mm)

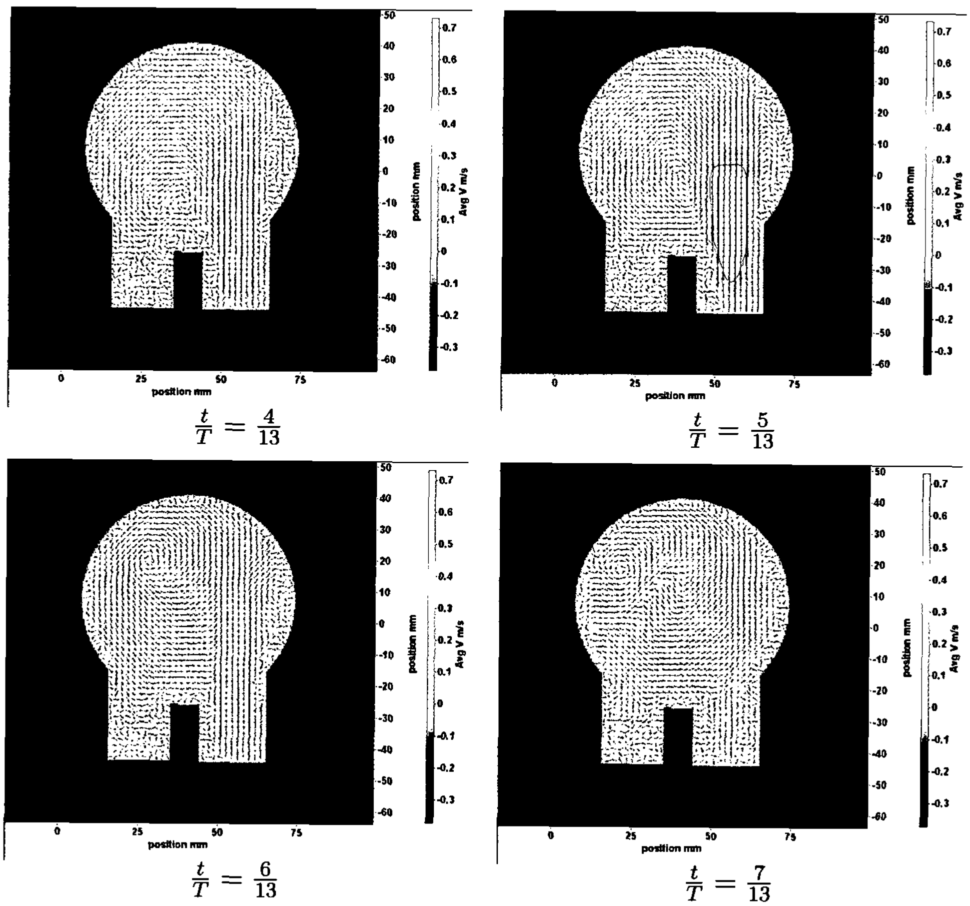

Figure 6.30: Average PIV XY velocity maps (z=20 mm) (continued)

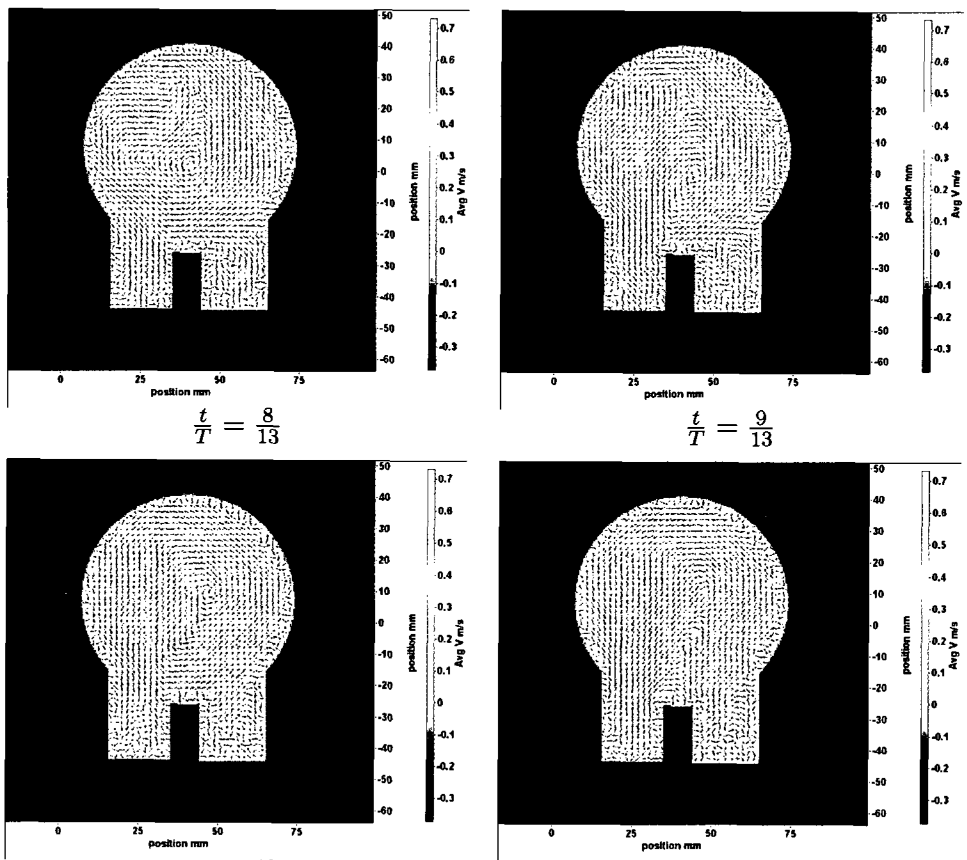

$\frac{t}{T} = \frac{8}{13}$ $\frac{t}{T} = \frac{9}{13}$

$\frac{t}{T} = \frac{10}{13}$ $\frac{t}{T} = \frac{11}{13}$

Figure 6.31: Average PIV XY velocity maps (z=20 mm) (continued)

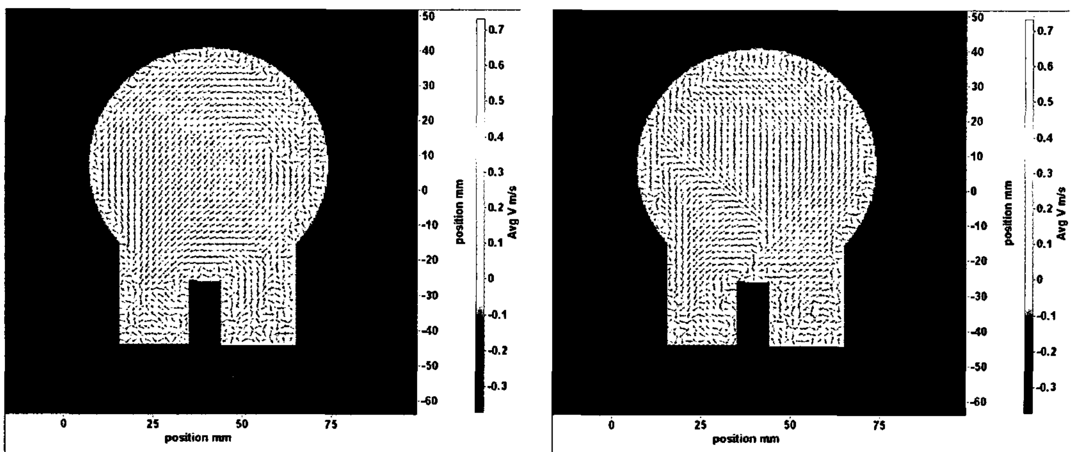

$\frac{t}{T} = \frac{12}{13}$ $\qquad$ $\frac{t}{T} \simeq \frac{13}{13}$

Figure 6.32: Average PIV XY velocity maps (z=20 mm) (continued)

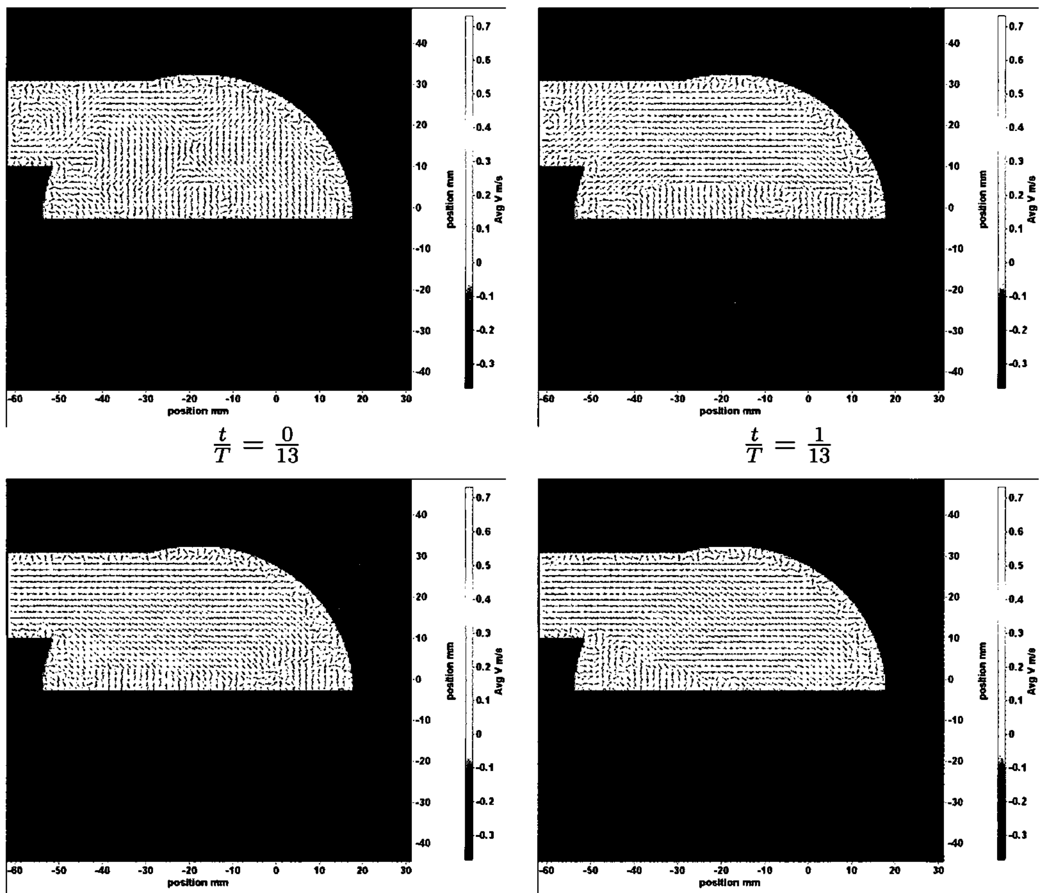

$\frac{t}{T} = \frac{0}{13}$ $\frac{t}{T} = \frac{1}{13}$

$\frac{t}{T} = \frac{2}{13}$ $\frac{t}{T} = \frac{3}{13}$

Figure 6.33: Average PIV XZ velocity maps (y=15 mm)

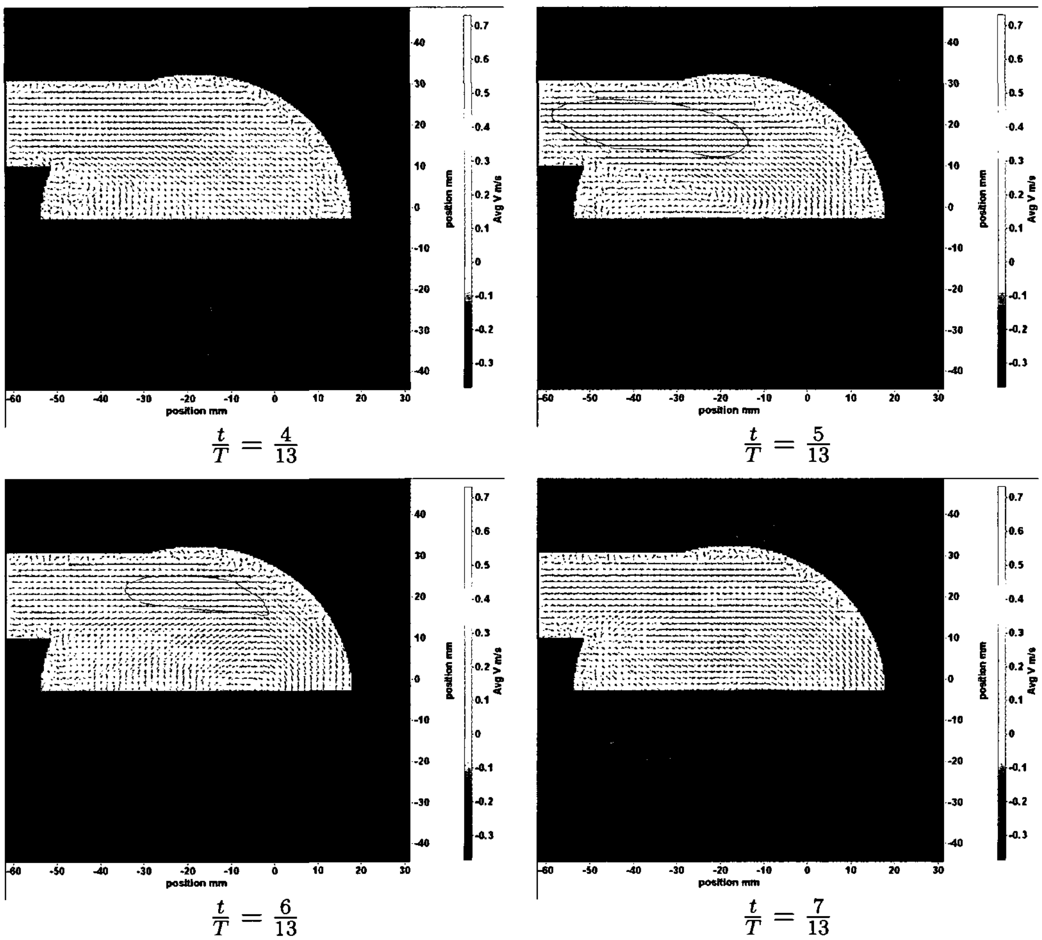

Figure 6.34: Average PIV XZ velocity maps (y=15 mm) (continued)

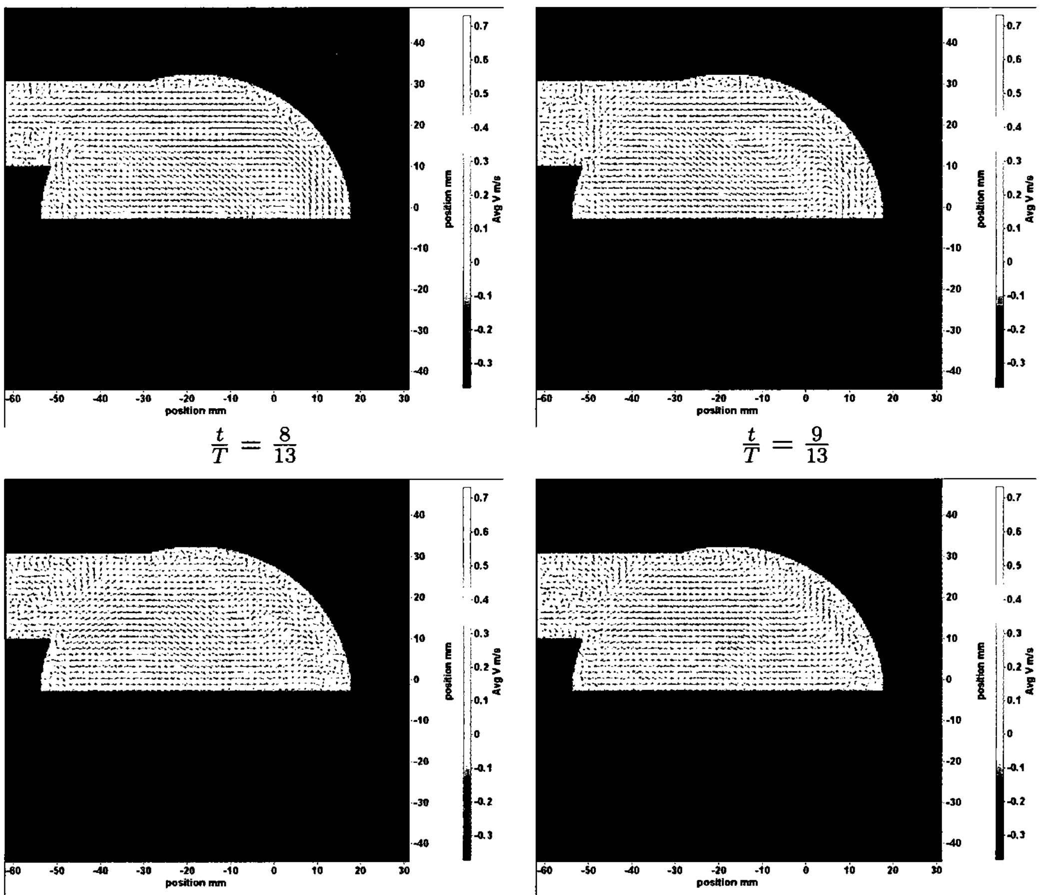

$\frac{t}{T} = \frac{8}{13}$ $\frac{t}{T} = \frac{9}{13}$

$\frac{t}{T} = \frac{10}{13}$ $\frac{t}{T} = \frac{11}{13}$

Figure 6.35: Average PIV XZ velocity maps (y=15 mm) (continued)

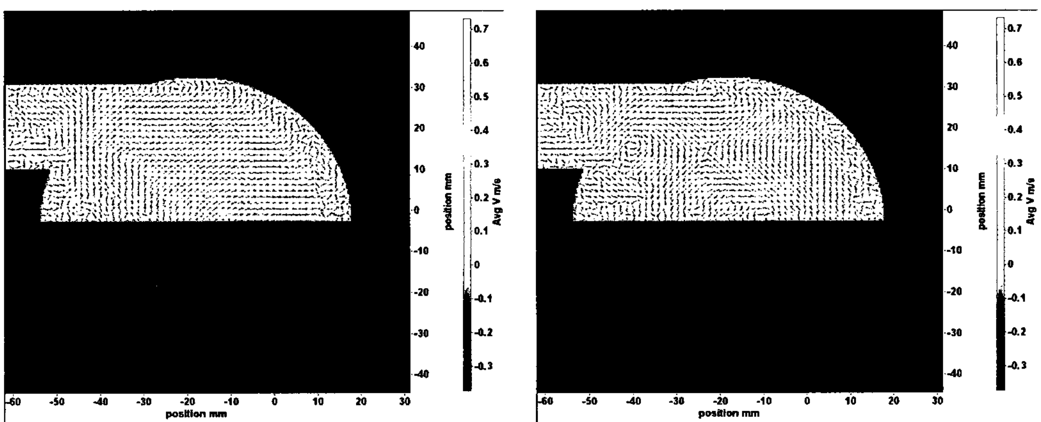

$\frac{t}{T} = \frac{12}{13}$ $\frac{t}{T} \simeq \frac{13}{13}$

Figure 6.36: Average PIV XZ velocity maps (y=15 mm) (continued)

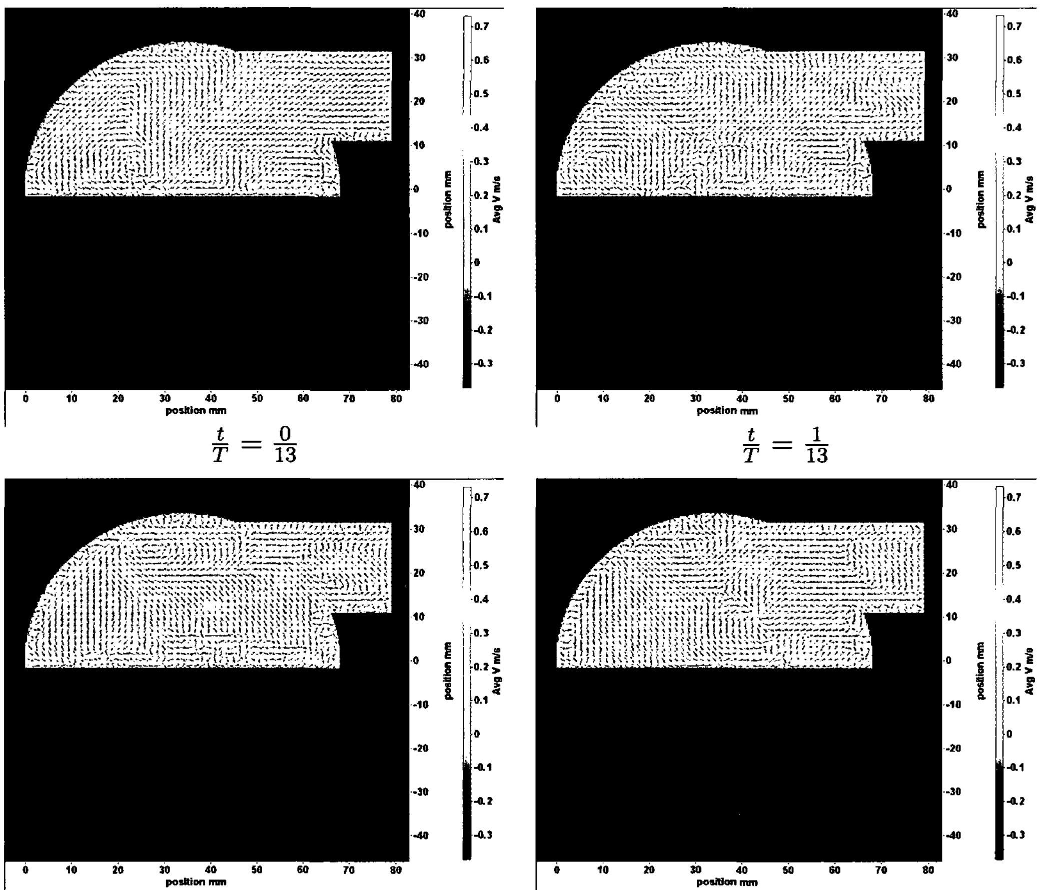

$\frac{t}{T} = \frac{0}{13}$ $\frac{t}{T} = \frac{1}{13}$

$\frac{t}{T} = \frac{2}{13}$ $\frac{t}{T} = \frac{3}{13}$

Figure 6.37: Average PIV XZ velocity maps (y= -15 mm)

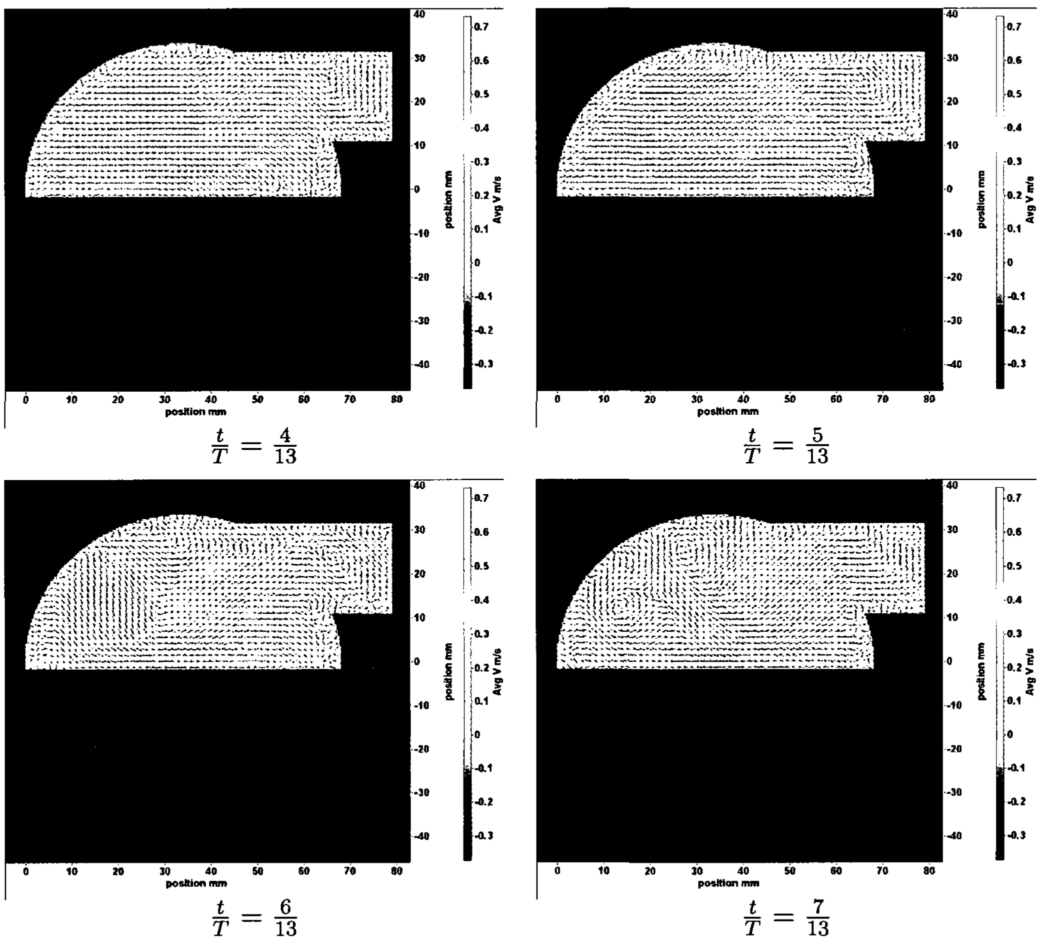

Figure 6.38: Average PIV XZ velocity maps (y= -15 mm) (continued)

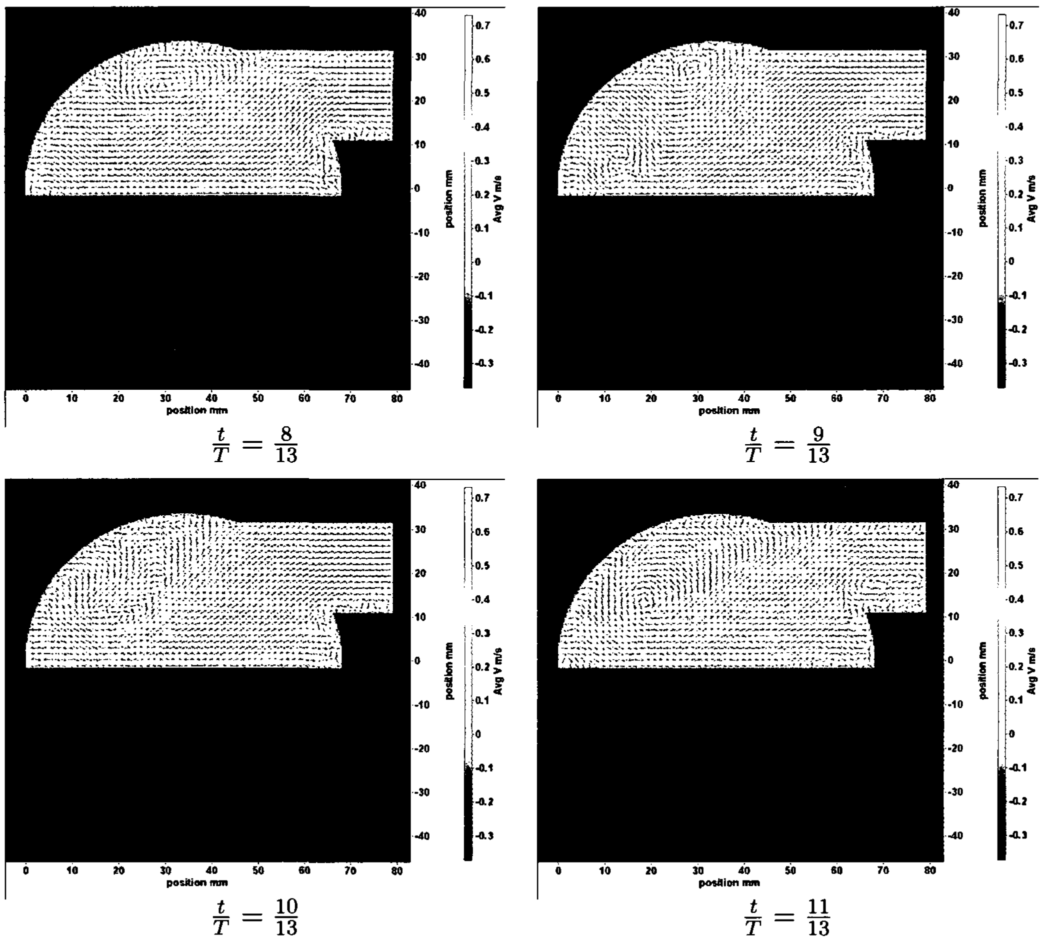

Figure 6.39: Average PIV XZ velocity maps (y= -15 mm) (continued)

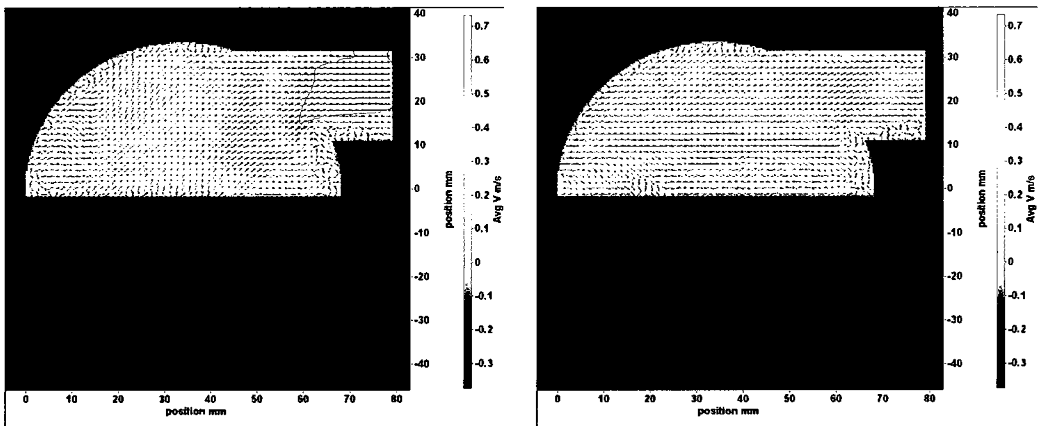

$\frac{t}{T} = \frac{12}{13}$ $\frac{t}{T} \simeq \frac{13}{13}$

Figure 6.40: Average PIV XZ velocity maps (y= -15 mm) (continued)

6.4 Vorticity

At $\frac{t}{T} = \frac{0}{13}$, while the inlet valve was opened and the outlet valve was closed, the vorticity throughout the VAD was low, with some remnants present along the boundaries of the outlet tube visible in Figures 6.49 and 6.53. This vorticity was dissipated by $\frac{t}{T} = \frac{1}{13}$ as displayed in Figure 6.53 and regions of vorticity were observed forming as early as $\frac{t}{T} = \frac{2}{13}$ along the surface of the inlet tube in Figures 6.45 and 6.53, with maximum magnitudes of approximately ± 200 s^{-1}. A pair of counter rotating vortices could be observed beginning at $\frac{t}{T} = \frac{3}{13}$ in Figures 6.45 and 6.53, indicating that the vortices form along the outer surface of the VAD inlet and outlet tubes and travel into the VAD where they mix the injected fluid with the fluid already present in the VAD. At $\frac{t}{T} = \frac{5}{13}$, peak vorticity values of ± 325 s^{-1} were measured in Figure 6.54. The vortical fluid was then dispersed throughout the VAD as shown in Figure 6.54. The high vorticity region into the centre of the VAD can be observed as the positive vorticity region that was stretched and dispersed, while the strong negative

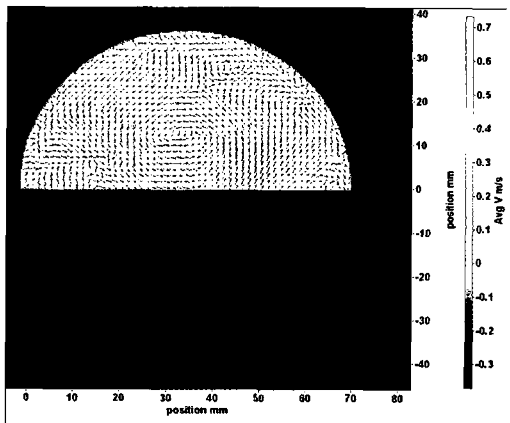

$\frac{t}{T} = \frac{0}{13}$

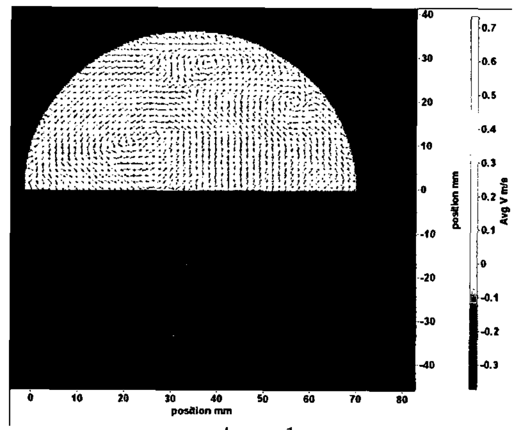

$\frac{t}{T} = \frac{1}{13}$

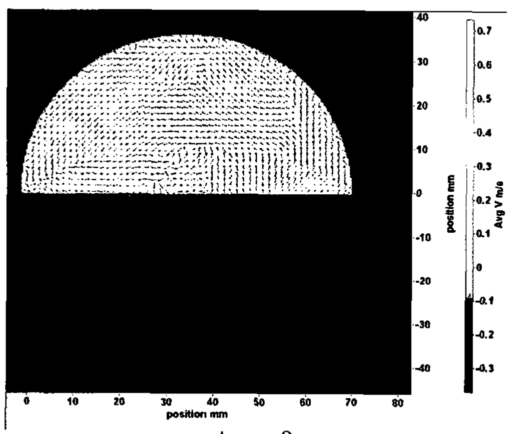

$\frac{t}{T} = \frac{2}{13}$

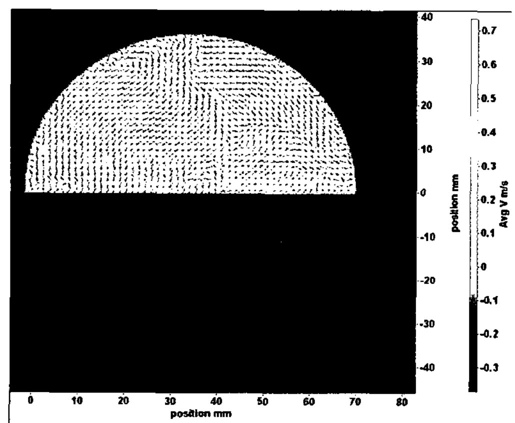

$\frac{t}{T} = \frac{3}{13}$

Figure 6.41: Average PIV XZ velocity maps (y= 0 mm)

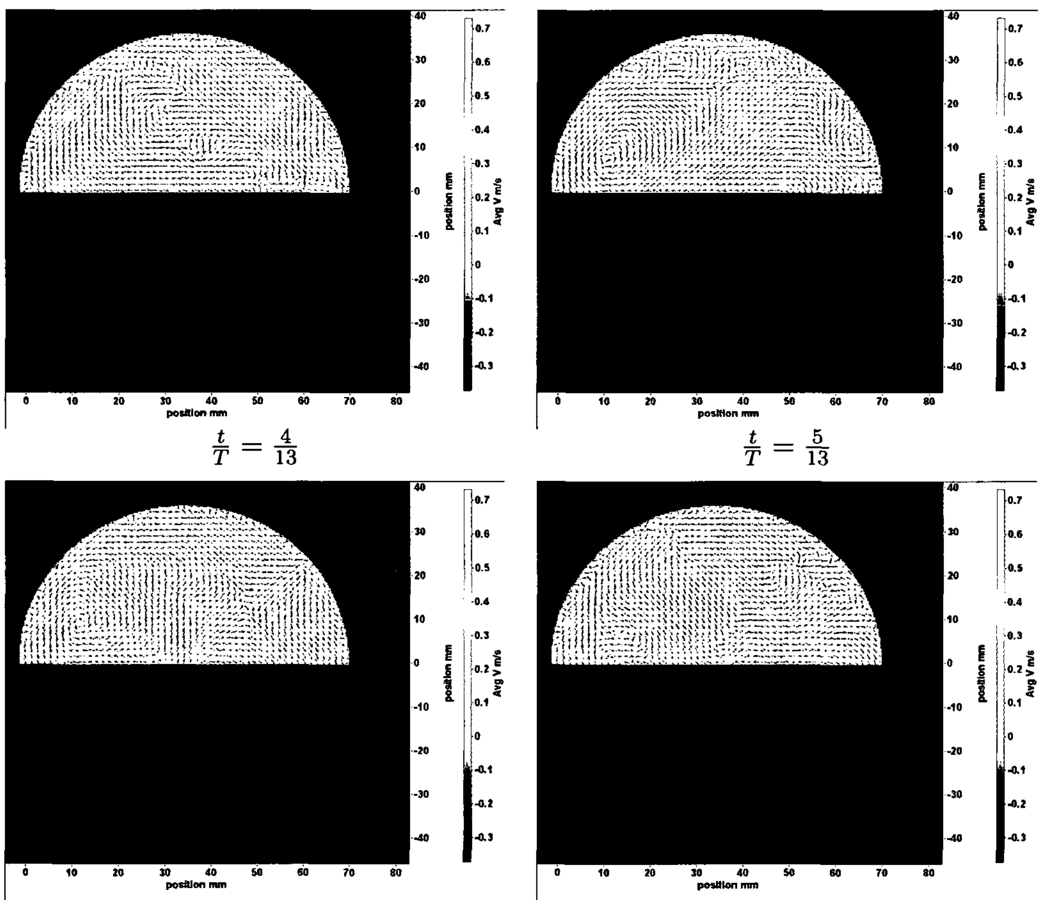

$\frac{t}{T} = \frac{4}{13}$ $\frac{t}{T} = \frac{5}{13}$

$\frac{t}{T} = \frac{6}{13}$ $\frac{t}{T} = \frac{7}{13}$

Figure 6.42: Average PIV XZ velocity maps (y= 0 mm) (continued)

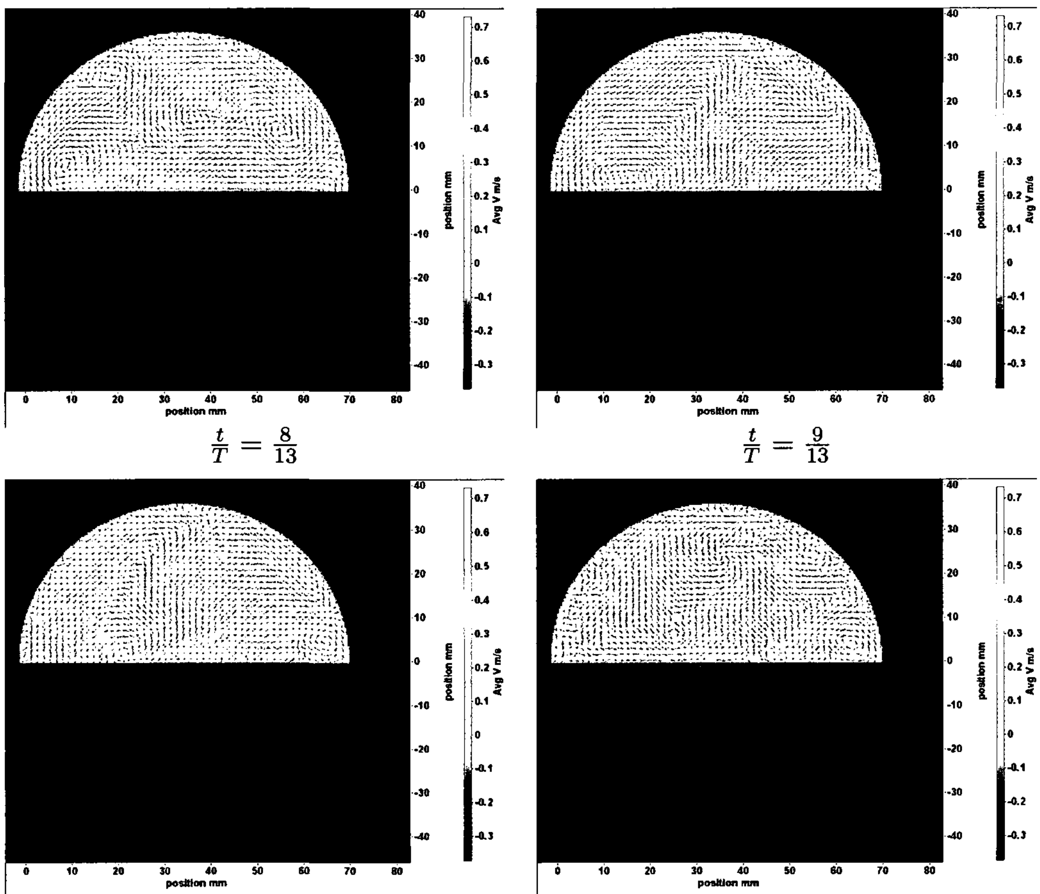

$\frac{t}{T} = \frac{8}{13}$ $\frac{t}{T} = \frac{9}{13}$

$\frac{t}{T} = \frac{10}{13}$ $\frac{t}{T} = \frac{11}{13}$

Figure 6.43: Average PIV XZ velocity maps (y= 0 mm) (continued)

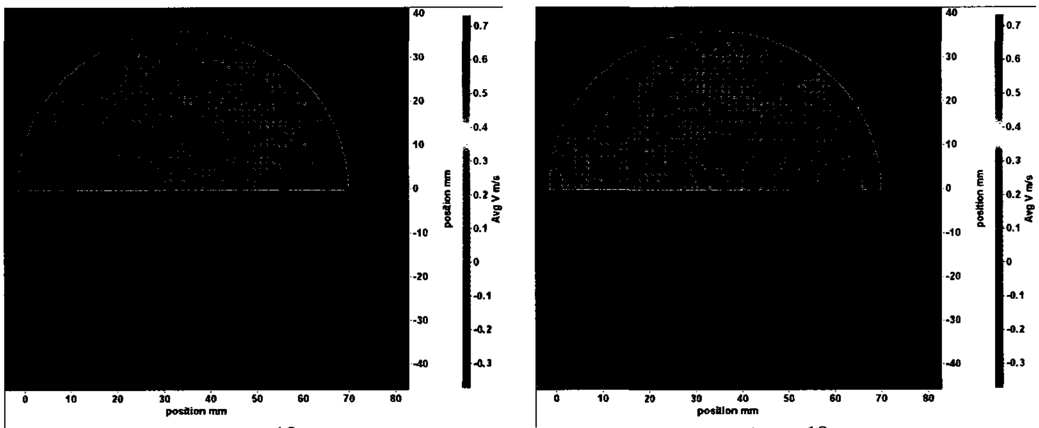

$\frac{t}{T} = \frac{12}{13}$ $\qquad$ $\frac{t}{T} \simeq \frac{13}{13}$

Figure 6.44: Average PIV XZ velocity maps (y= 0 mm) (continued)

region of vorticity moved along the outer circumference, creating a "washing" effect. The peak vorticity during this phase of the VAD cycle did not exceed ± 250 s^{-1}. Note that the vorticity dispersion in Figure 6.54 seems to follow the path of the inlet jet, suggesting that the region of the VAD directly adjacent to the inlet tube does not experience the same washout as other regions, and thus was a point of flow recirculation. At the beginning of systole at $\frac{t}{T} = \frac{8}{13}$, the inlet valve has closed and the outlet valve has opened. A region of high vorticity can be observed in the region directly adjacent to the outlet tube in Figure 6.51 along the lower surface. The ejection cycle was displayed in Figures 6.55 and 6.51 as well as in Figures 6.52 and 6.56. Vorticity was concentrated in the regions near the outlet tube, as well as along the surface of the outlet tube. In these regions the peak vorticity values increased back again towards ± 300 s^{-1}, with particularly strong regions of negative vorticity present along the lower surface of the outlet tube. This suggests that whereas the regions of positive vorticity contribute to mixing during the injection of the fluid into the VAD, the strong negative regions of vorticity contribute to mixing during ejection of

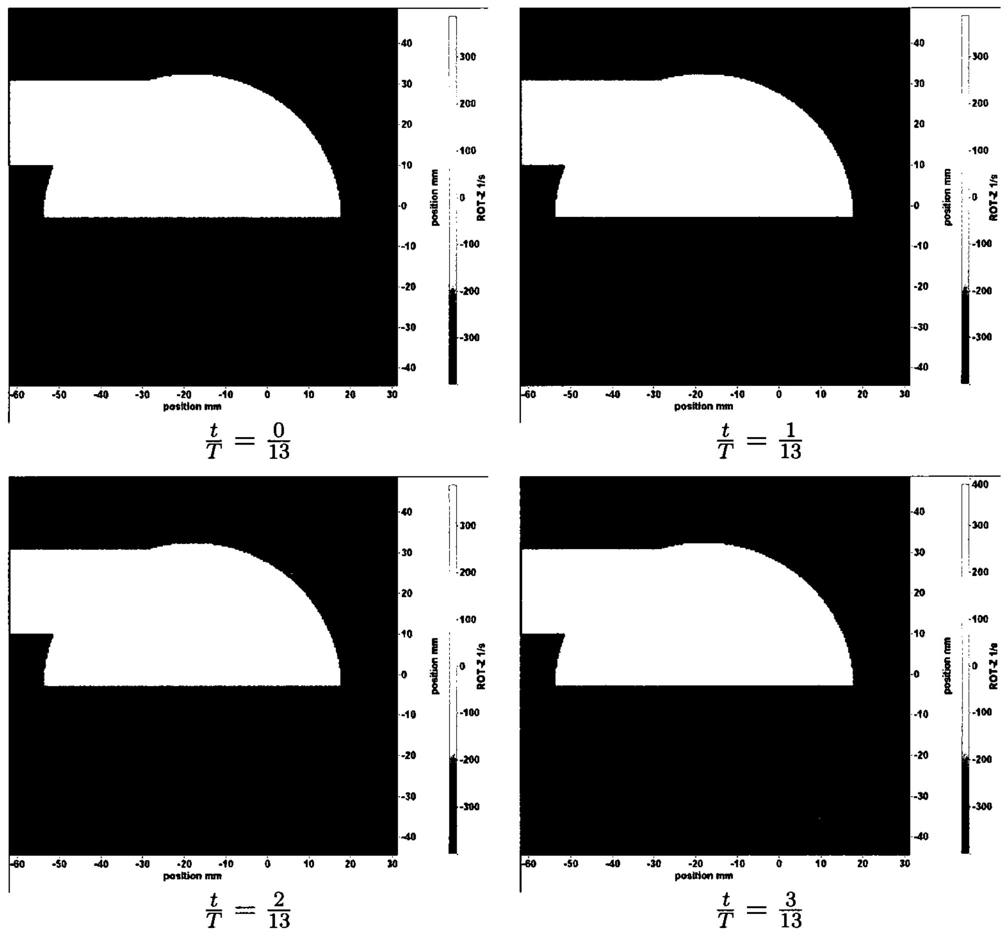

Figure 6.45: Average PIV XZ vorticity maps (y= 15 mm)

the fluid. This will be further discussed in the next chapter.

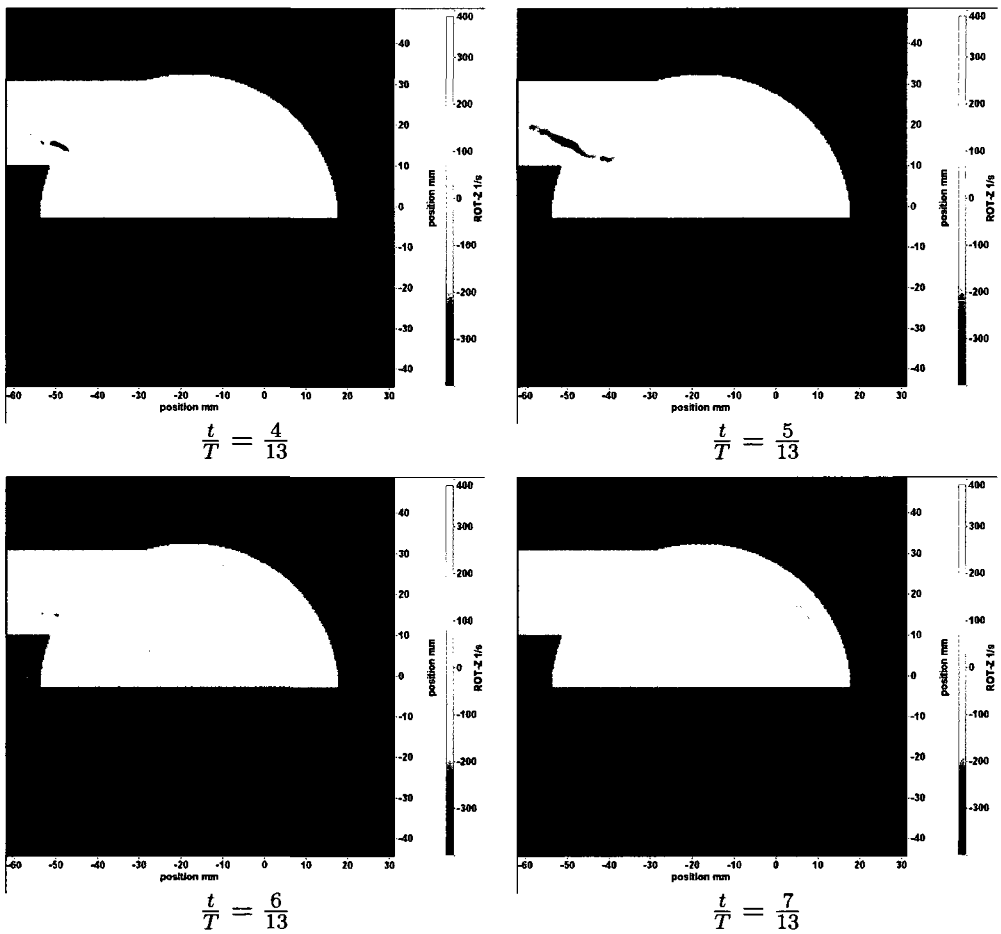

Figure 6.46: Average PIV XZ vorticity maps (y= 15 mm) (continued)

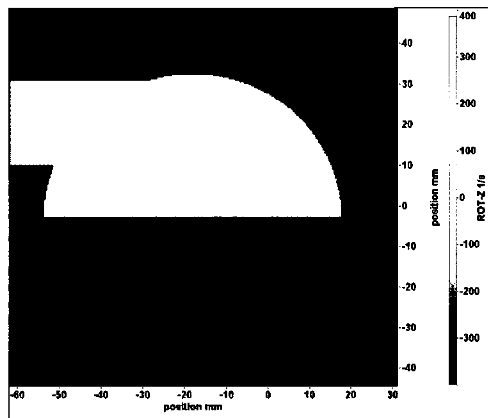

$\frac{t}{T} = \frac{8}{13}$

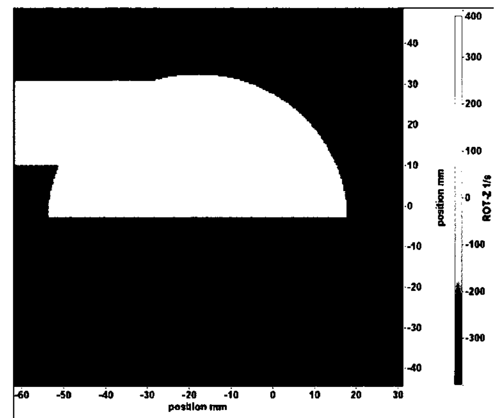

$\frac{t}{T} = \frac{9}{13}$

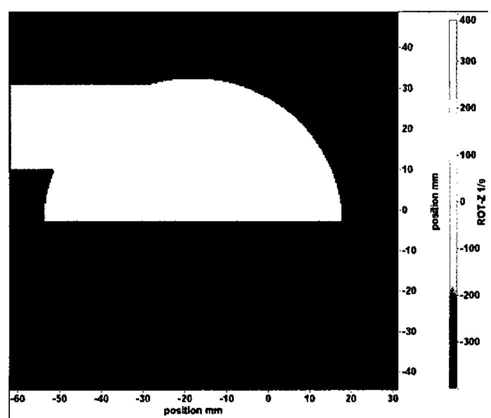

$\frac{t}{T} = \frac{10}{13}$

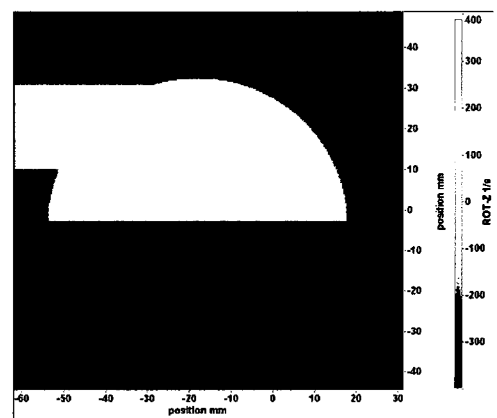

$\frac{t}{T} = \frac{11}{13}$

Figure 6.47: Average PIV XZ vorticity maps (y= 15 mm) (continued)

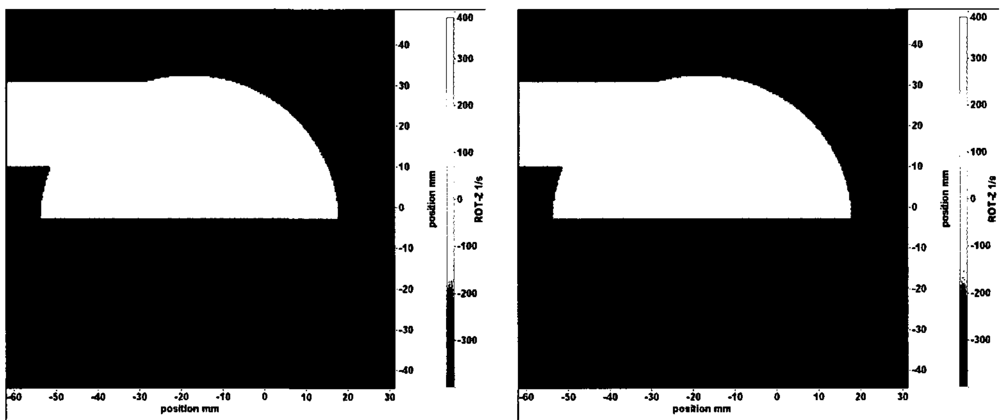

$\frac{t}{T} = \frac{12}{13}$ $\qquad$ $\frac{t}{T} \simeq \frac{13}{13}$

Figure 6.48: Average PIV XZ vorticity maps (y= 15 mm) (continued)

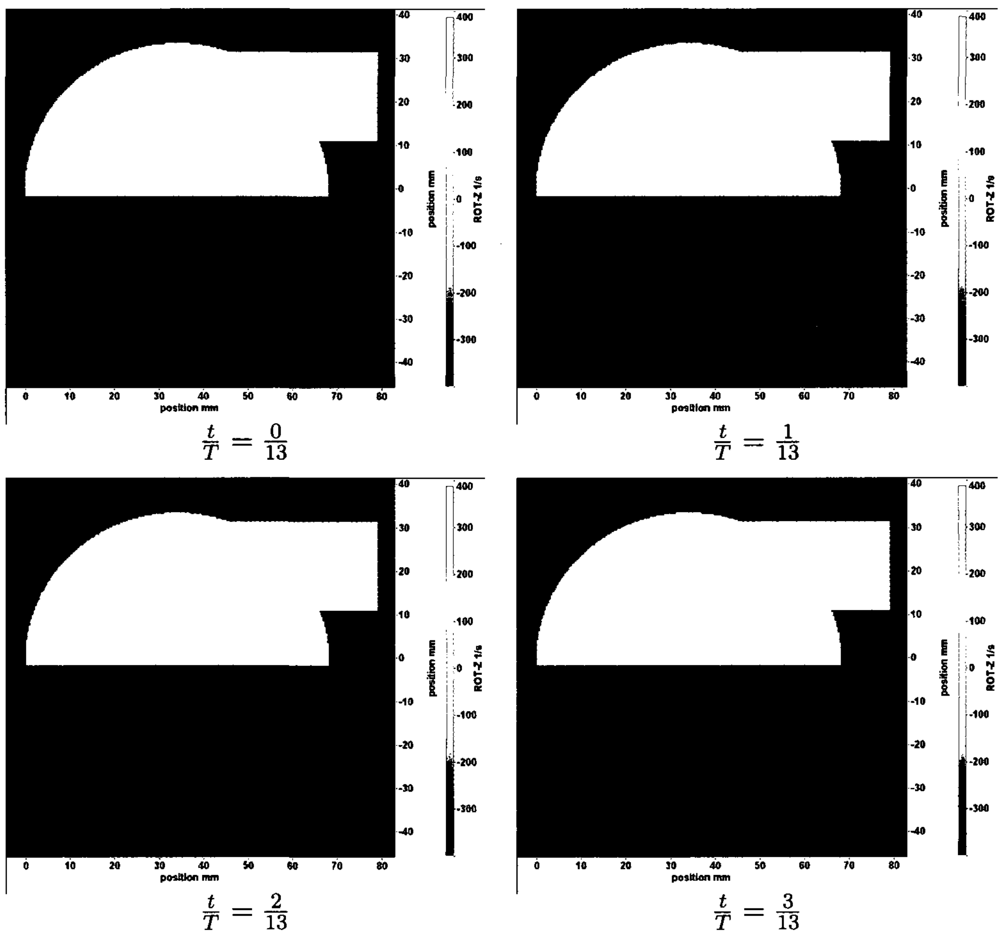

Figure 6.49: Average PIV XZ vorticity maps (y= -15 mm)

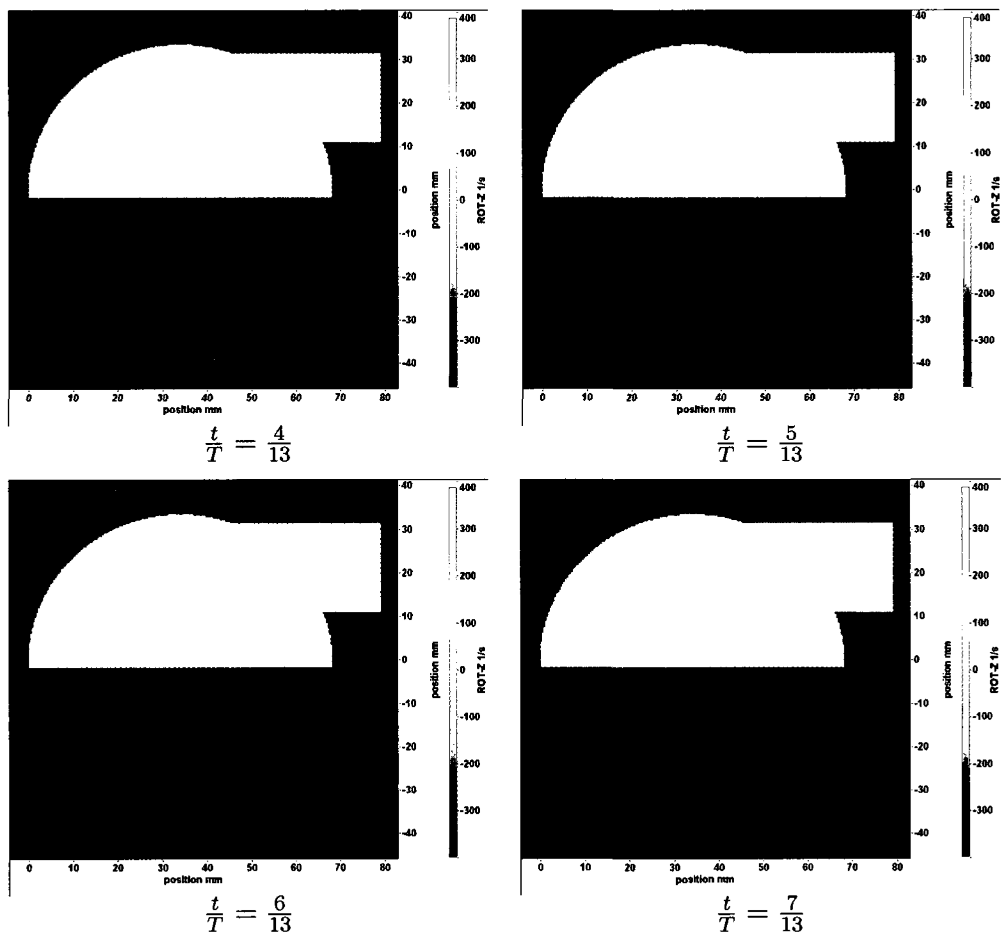

Figure 6.50: Average PIV XZ vorticity maps (y= -15 mm) (continued)

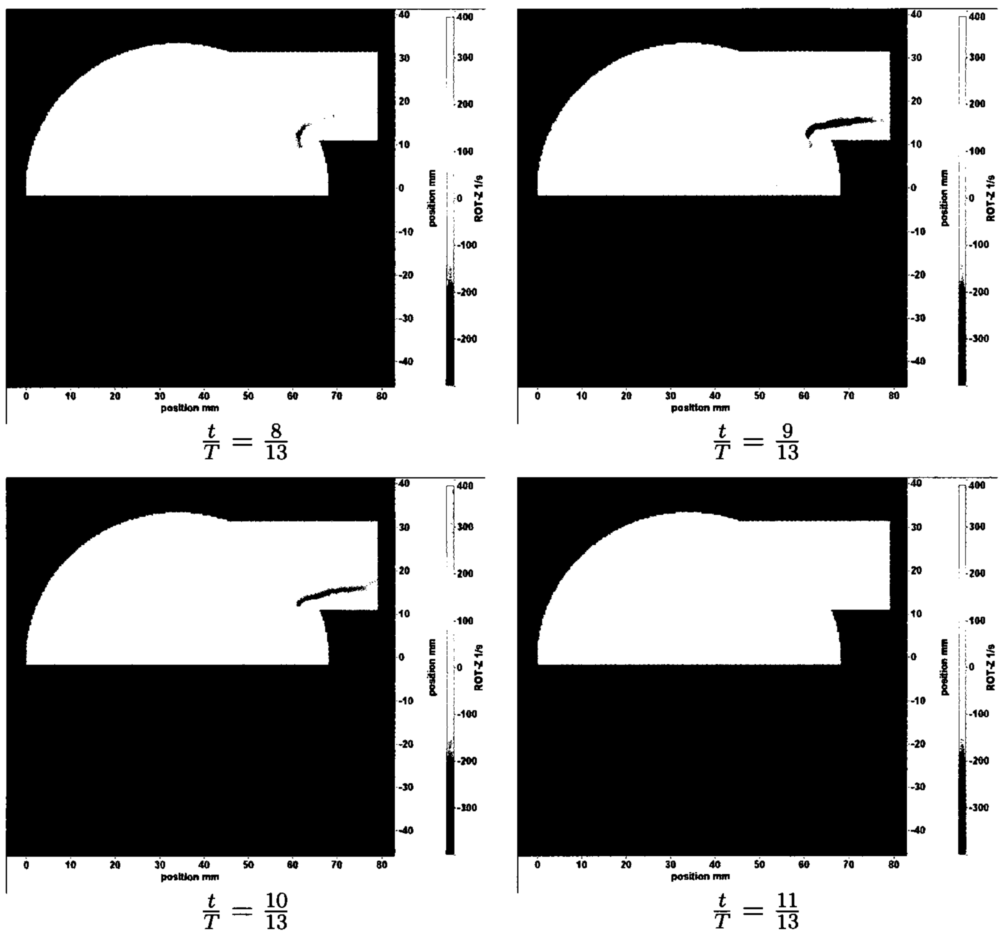

Figure 6.51: Average PIV XZ vorticity maps (y= -15 mm) (continued)

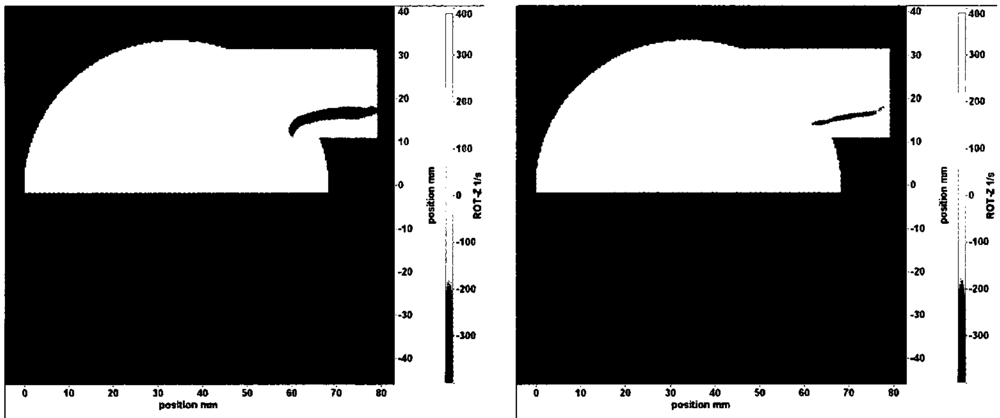

$\frac{t}{T} = \frac{12}{13}$ $\frac{t}{T} \simeq \frac{13}{13}$

Figure 6.52: Average PIV XZ vorticity maps (y= -15 mm) (continued)

6.5 Swirling Strength

The measurements taken by the PIV system allow for the determination of the imaginary portion of the eigenvalue of the local velocity gradient tensor, which was expressed as

$$-\left(\frac{\delta u}{\delta y}\frac{\delta v}{\delta x} - \frac{1}{2}\frac{\delta u}{\delta x}\frac{\delta v}{\delta y} + \frac{1}{4}\left(\frac{\delta u}{\delta x}\right)^2\left(\frac{\delta v}{\delta y}\right)^2\right) \tag{6.1}$$

The positive values of equation 6.1 are referred to as the swirling strength. Figures 6.57-6.72 display the phase-averaged swirling strength contours during the VAD operational cycle. No significant regions of high swirling strength were present until diastole began at $\frac{t}{T} = \frac{3}{13}$, when regions of high swirling strength form along the edges of the inlet tube (Figure 6.69). These regions grew throughout the VAD during diastole (Figures 6.58 and 6.62). In the outlet region, no regions of high swirling strength were formed until late diastole (Figure 6.66).

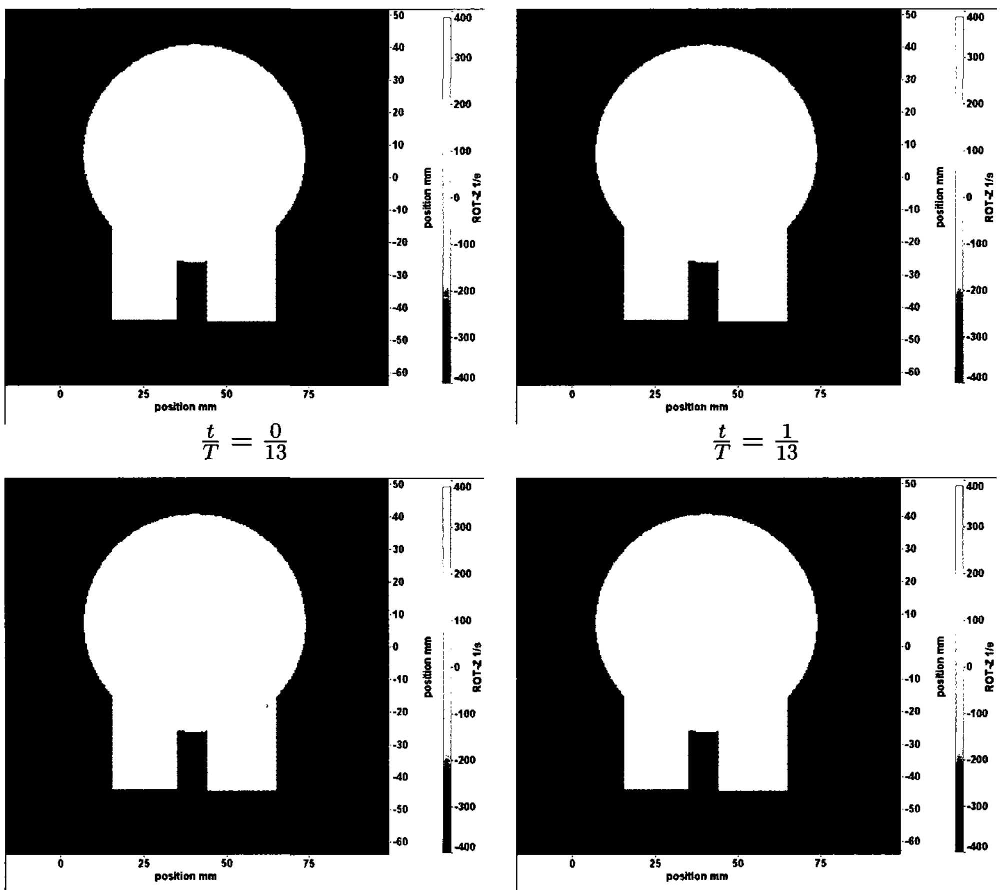

$\frac{t}{T} = \frac{0}{13}$ $\frac{t}{T} = \frac{1}{13}$

$\frac{t}{T} = \frac{2}{13}$ $\frac{t}{T} = \frac{3}{13}$

Figure 6.53: Average PIV XY vorticity maps (z= 20 mm)

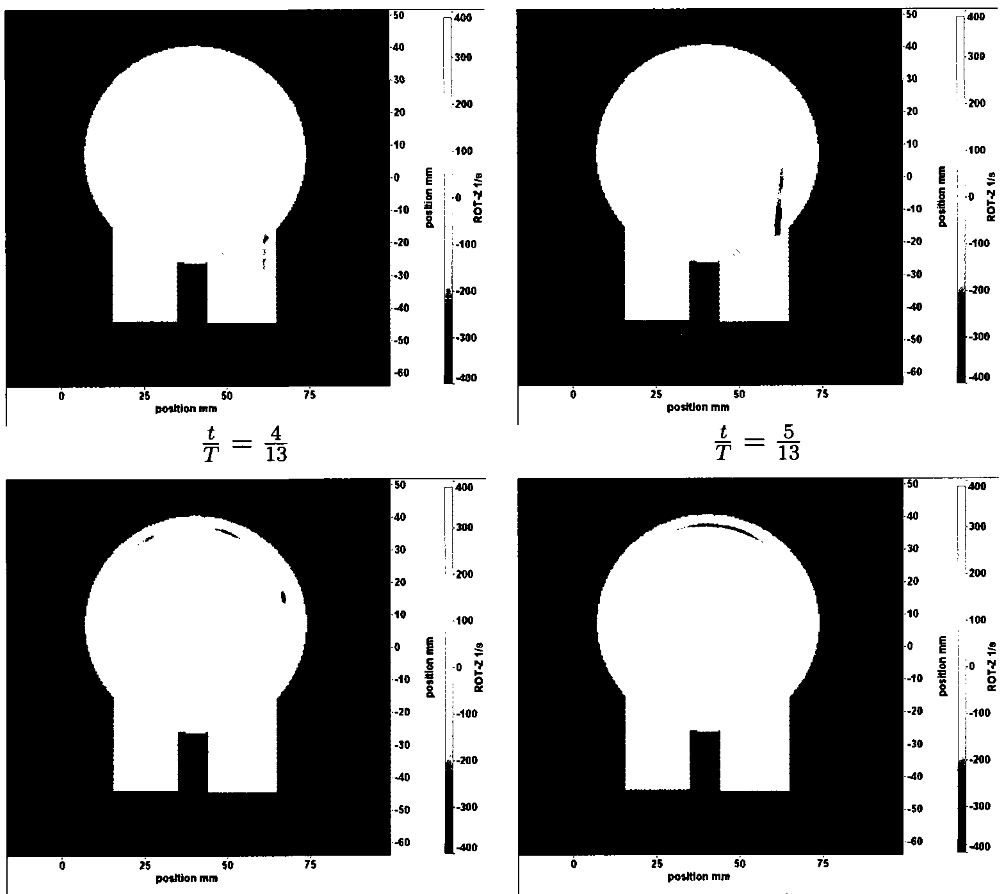

$\frac{t}{T} = \frac{4}{13}$ $\frac{t}{T} = \frac{5}{13}$

$\frac{t}{T} = \frac{6}{13}$ $\frac{t}{T} = \frac{7}{13}$

Figure 6.54: Average PIV XY vorticity maps (z= 20 mm) (continued)

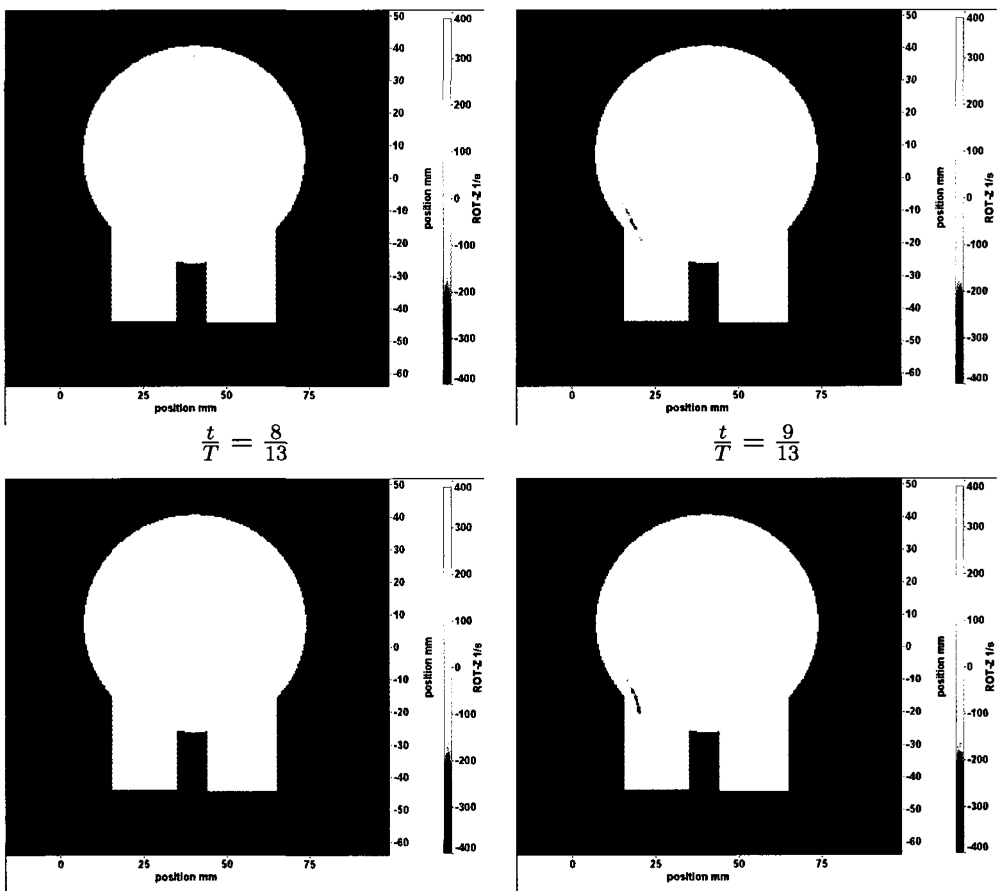

$\frac{t}{T} = \frac{8}{13}$ $\frac{t}{T} = \frac{9}{13}$

$\frac{t}{T} = \frac{10}{13}$ $\frac{t}{T} = \frac{11}{13}$

Figure 6.55: Average PIV XY vorticity maps (z= 20 mm) (continued)

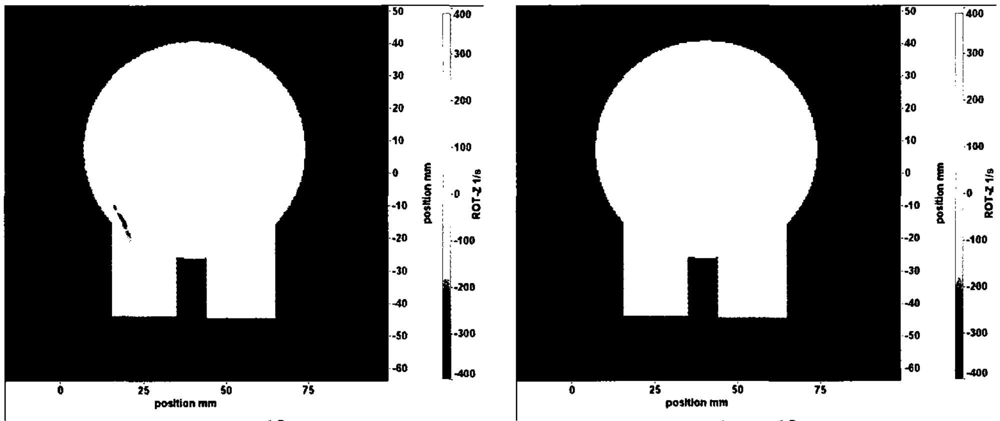

$\frac{t}{T} = \frac{12}{13}$ $\frac{t}{T} \simeq \frac{13}{13}$

Figure 6.56: Average PIV XY vorticity maps (z= 20 mm) (continued)

During late diastole (Figures 6.59 and 6.72), regions of high swirling strength were seen to move from the inlet tube towards the wall opposite the inlet and outlet tubes, in a motion similar to that of the core vortex from $\frac{t}{T} = \frac{5}{13}$ to $\frac{t}{T} = \frac{7}{13}$. Regions of high swirling strength of the order of 400 s^{-2} were also observed to grow during late diastole and early systole (Figures 6.63 and 6.67). This pattern was similar to the growth and dispersion of vorticity in the VAD during diastole and mixing. Regions of swirling strength in excess of 500 s^{-2} were also visible in areas of potential recirculation.

During systole, the regions of high swirl decrease in the inlet and central regions from $\frac{t}{T} = \frac{9}{13}$ until $\frac{t}{T} = \frac{11}{13}$ (Figures 6.59 and 6.63). Regions of strong swirl during this time were observed to appear and grow as shown in Figures 6.71 and 6.67. At the systolic peak at $\frac{t}{T} = \frac{12}{13}$, the regions of strongest swirl were observed on the wall of the VAD outlet tube, where the swirling strength was as high as 600 s^{-2} (Figure 6.68). Figure 6.68 also shows a region of high swirling strength near the VAD wall and the diaphragm, suggesting that this may be a region of recirculation. Figures 6.72 and 6.68 also show a region of swirling

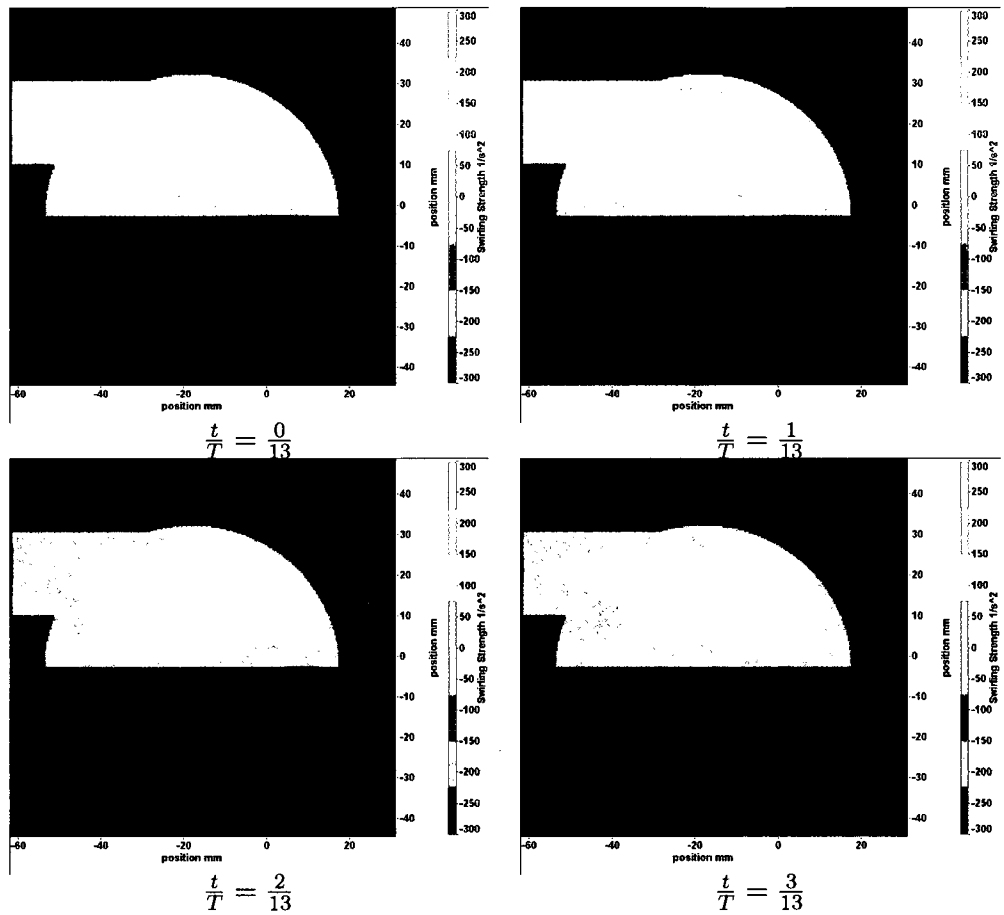

Figure 6.57: Average PIV XZ Swirl strength maps (y= 15 mm)

strength with an average value of 60 s^{-2} along the VAD wall opposite to the outlet tube where a vortex was identified by the PIV velocity maps.

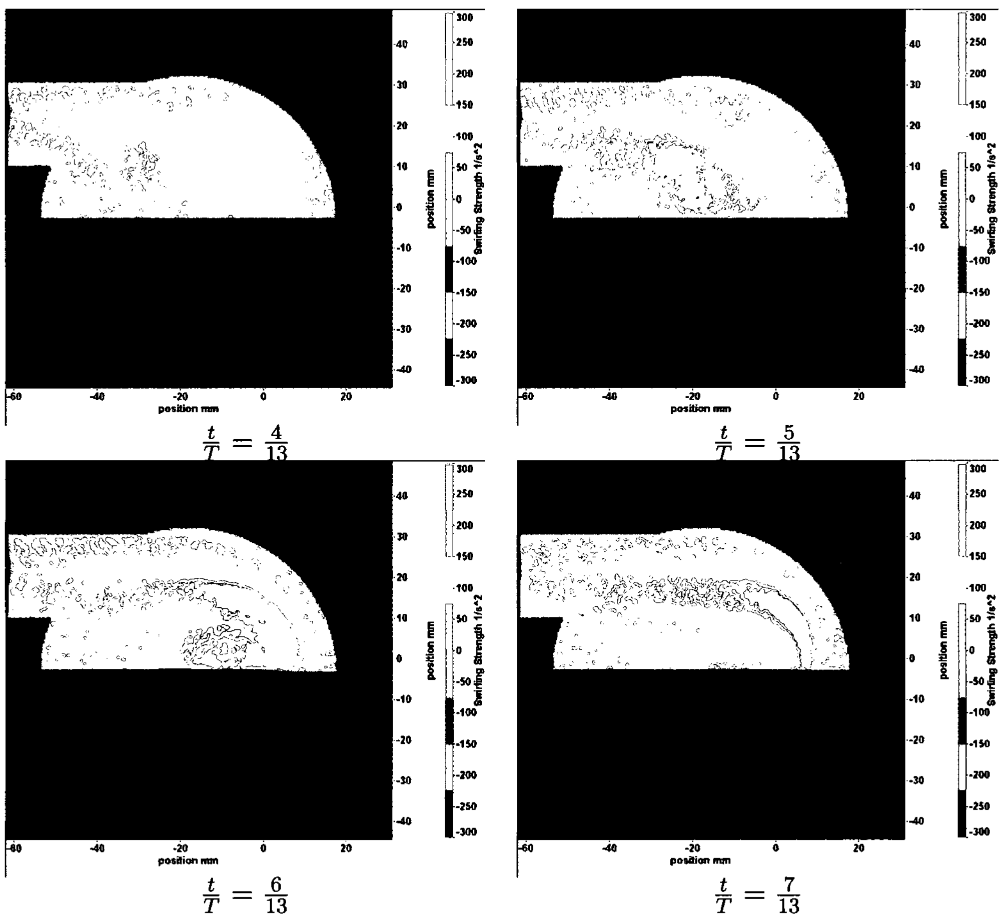

Figure 6.58: Average PIV XZ Swirl strength maps (y= 15 mm) (continued)

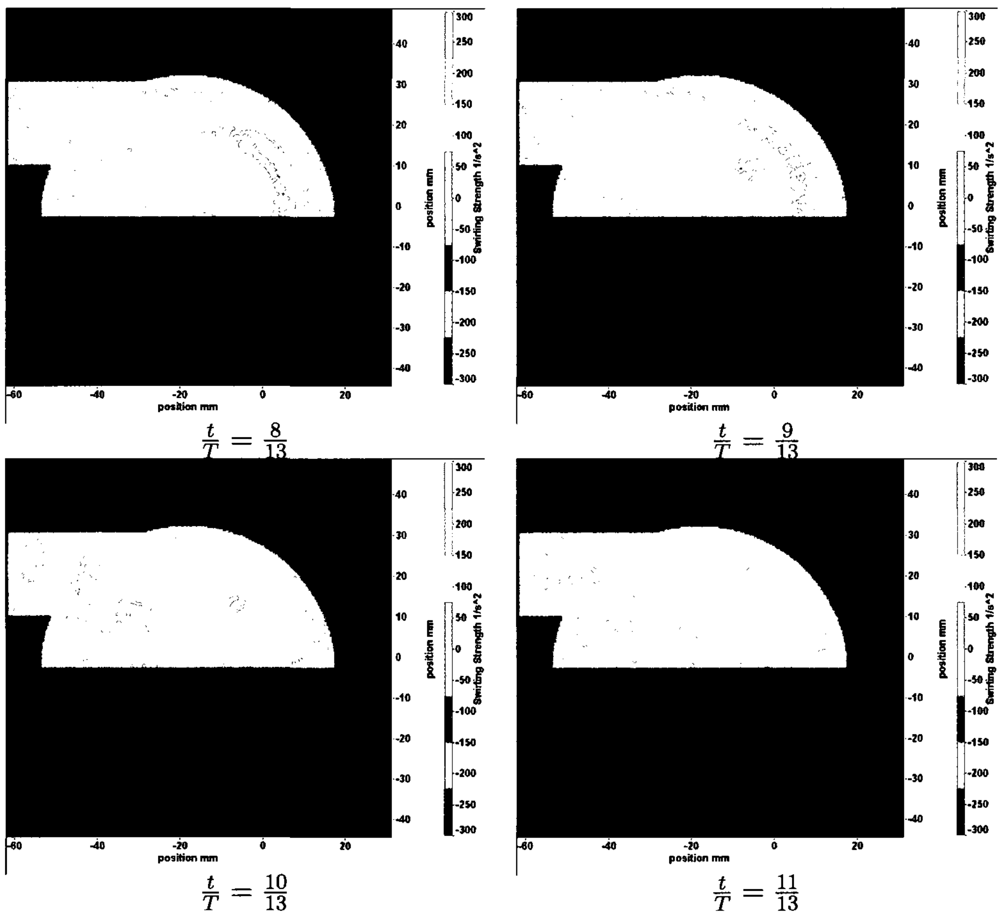

Figure 6.59: Average PIV XZ Swirl strength maps (y= 15 mm) (continued)

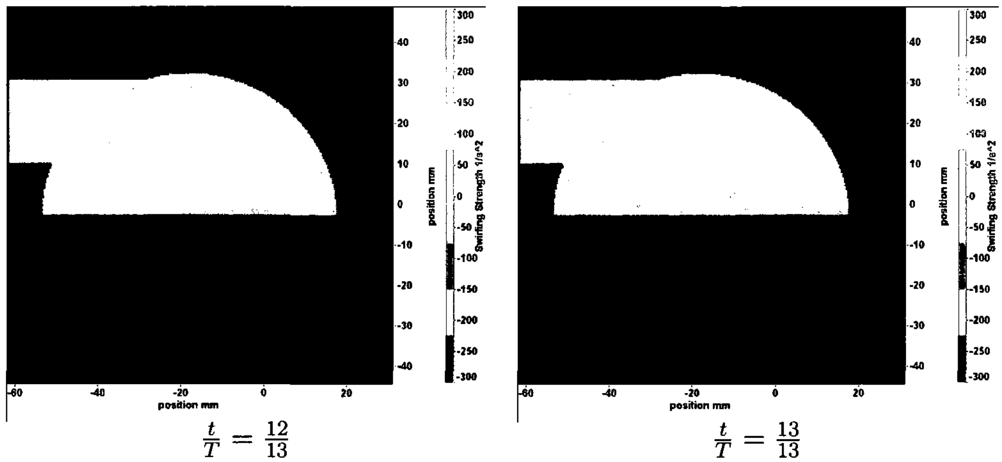

Figure 6.60: Average PIV XZ Swirl strength maps (y= 15 mm) (continued)

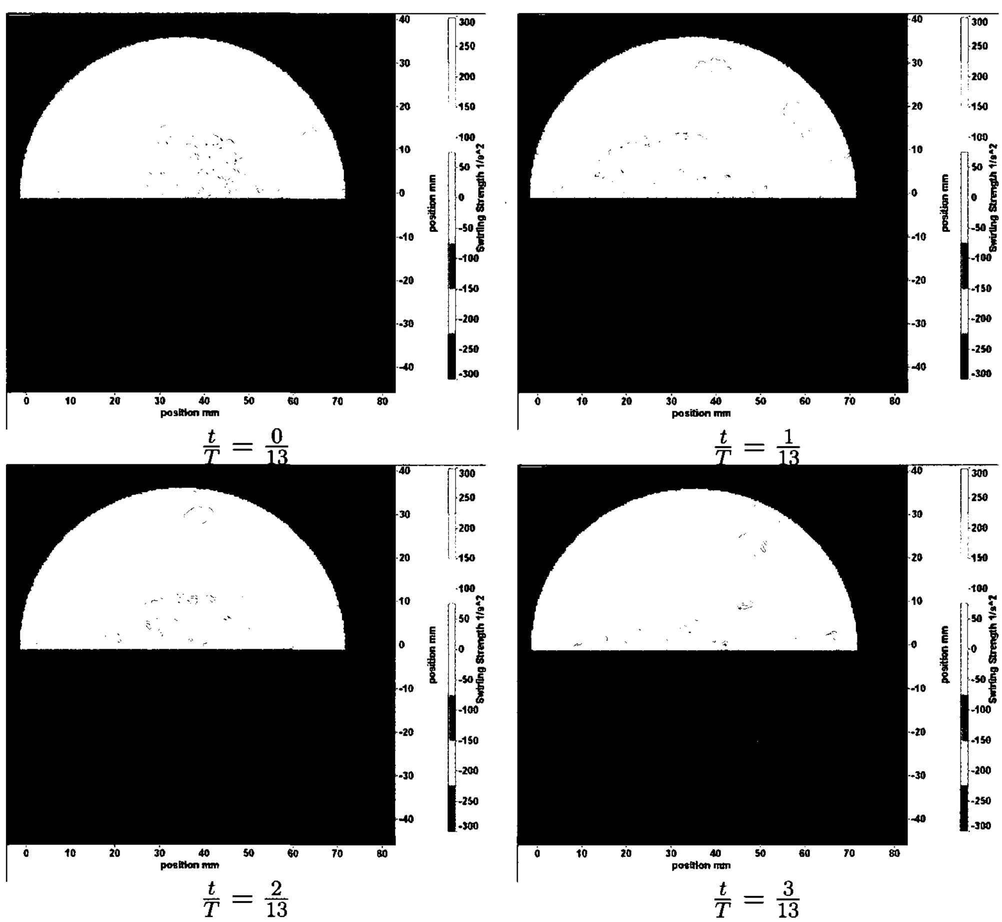

Figure 6.61: Average PIV XZ Swirl strength maps (y= 0 mm)

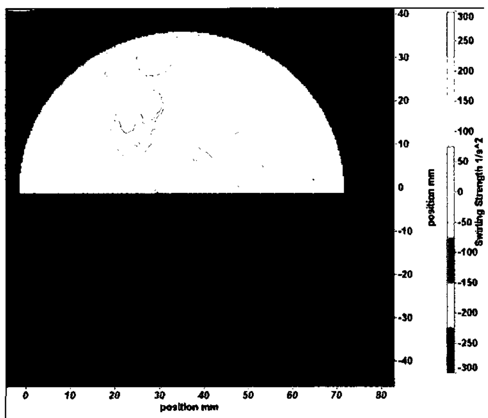

$\frac{t}{T} = \frac{4}{13}$

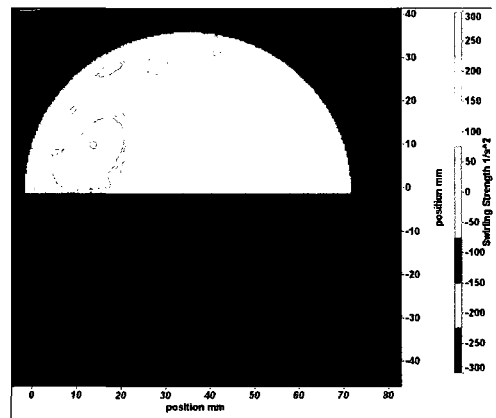

$\frac{t}{T} = \frac{5}{13}$

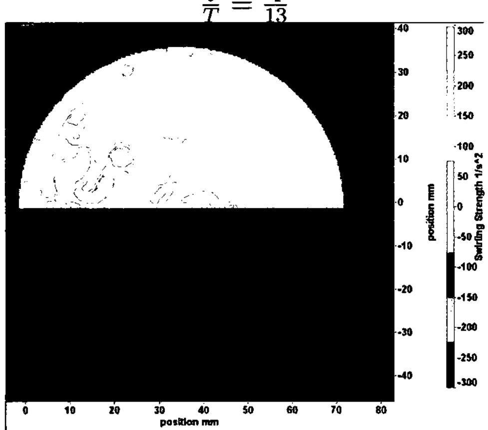

$\frac{t}{T} = \frac{6}{13}$

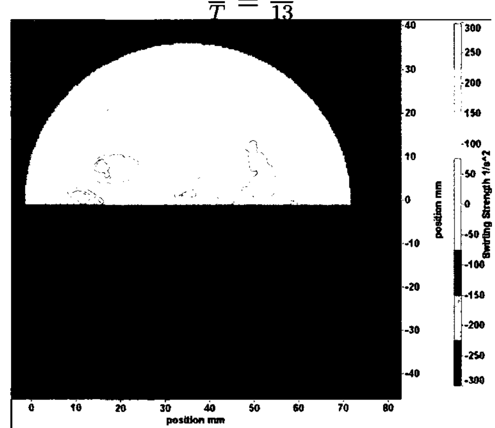

$\frac{t}{T} = \frac{7}{13}$

Figure 6.62: Average PIV XZ Swirl strength maps (y= 0 mm) (continued)

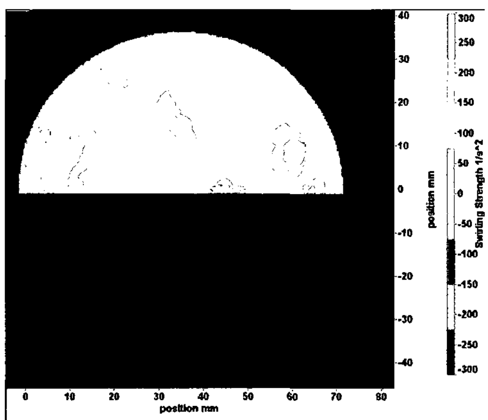

$\frac{t}{T} = \frac{8}{13}$

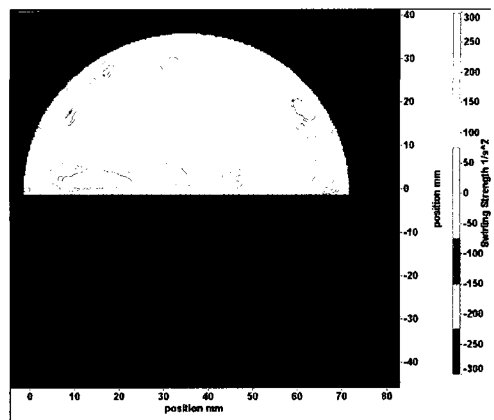

$\frac{t}{T} = \frac{9}{13}$

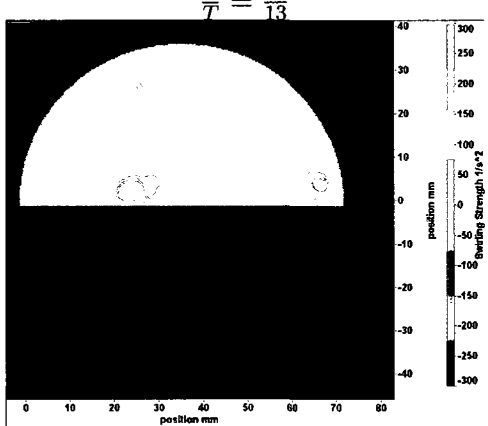

$\frac{t}{T} = \frac{10}{13}$

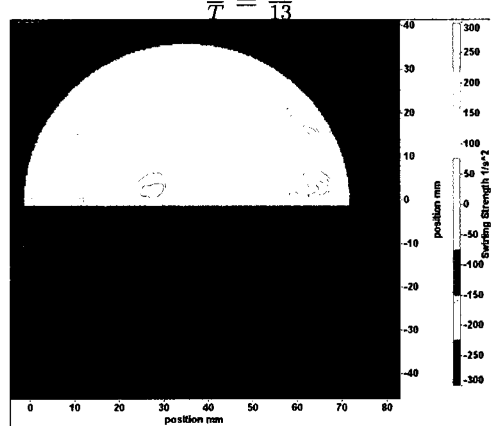

$\frac{t}{T} = \frac{11}{13}$

Figure 6.63: Average PIV XZ Swirl strength maps (y= 0 mm) (continued)

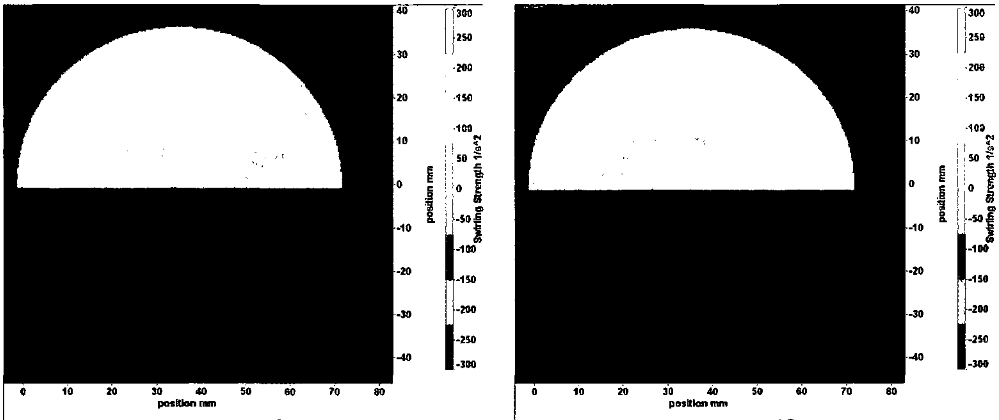

$\frac{t}{T} = \frac{12}{13}$ $\frac{t}{T} = \frac{13}{13}$

Figure 6.64: Average PIV XZ Swirl strength maps (y= 0 mm) (continued)

6.6 Strain Rate

The shearing component of the strain rate tensor on the $x - y$ plane is defined as

$$\varepsilon = \frac{1}{2}\left(\frac{\delta u}{\delta x} + \frac{\delta v}{\delta y}\right) \tag{6.2}$$

For Newtonian fluids, the corresponding shear stress is proportional to this strain rate component, as

$$\sigma = \mu\varepsilon \tag{6.3}$$

where the viscosity of the fluid in this experiment was $\mu = 3.8 \times 10^{-3}$ Pa s. If ε is measured in units of s^{-1}, it would produce a value for shear in units of Pa. Because shear in biological flows is commonly expressed in units of dynes/cm^2 the conversion

$$1 \text{ Pa} = 10 \text{ dynes/cm}^2 \tag{6.4}$$

was applied to the results for the sake of comparison with similar studies, which corresponds to a viscosity value of $\mu = 3.8 \times 10^{-2}$ dynes s/cm^2. Figures 6.73-6.88 show the strain rate

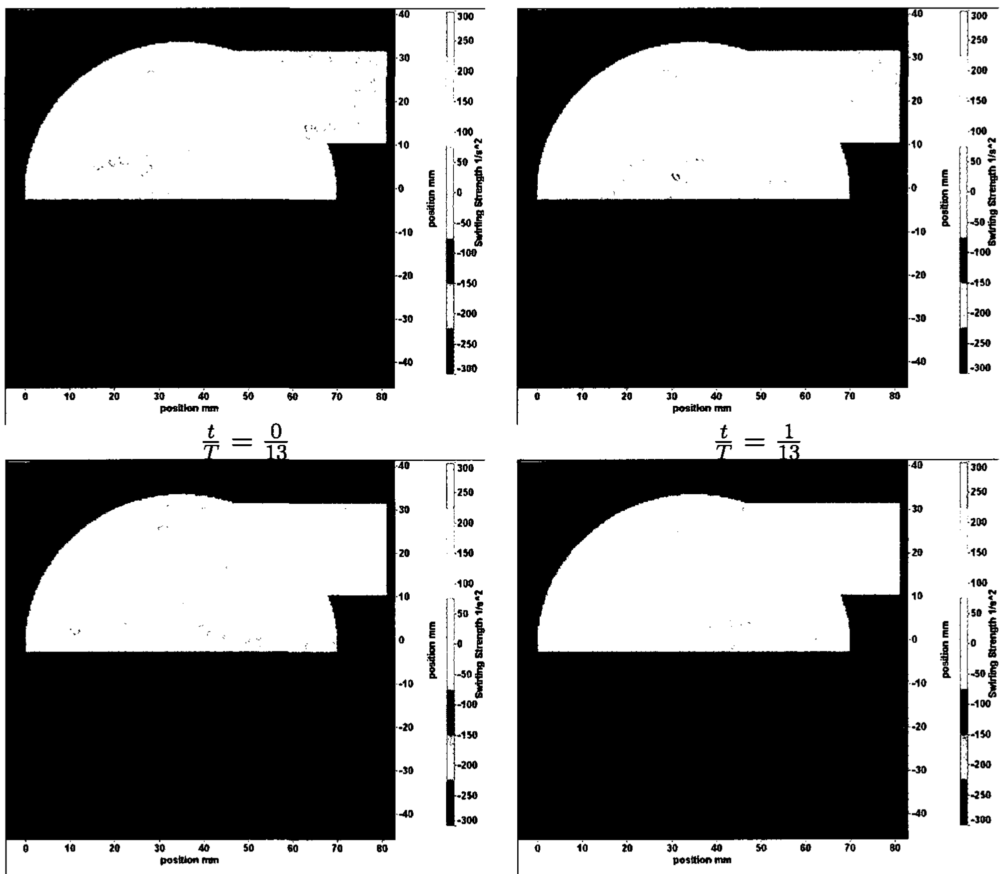

$\frac{t}{T} = \frac{0}{13}$ $\frac{t}{T} = \frac{1}{13}$

$\frac{t}{T} = \frac{2}{13}$ $\frac{t}{T} = \frac{3}{13}$

Figure 6.65: Average PIV XZ Swirl strength maps (y= -15 mm)

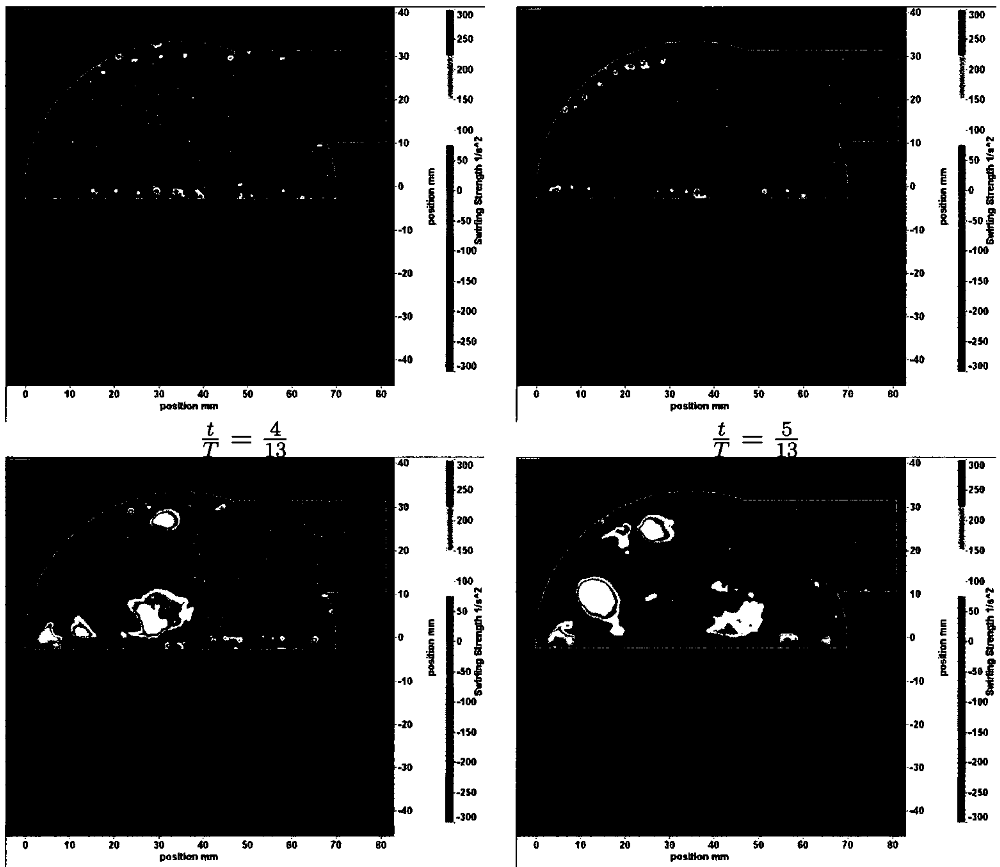

$\frac{t}{T} = \frac{4}{13}$ $\frac{t}{T} = \frac{5}{13}$

$\frac{t}{T} = \frac{6}{13}$ $\frac{t}{T} = \frac{7}{13}$

Figure 6.66: Average PIV XZ Swirl strength maps (y= -15 mm) (continued)

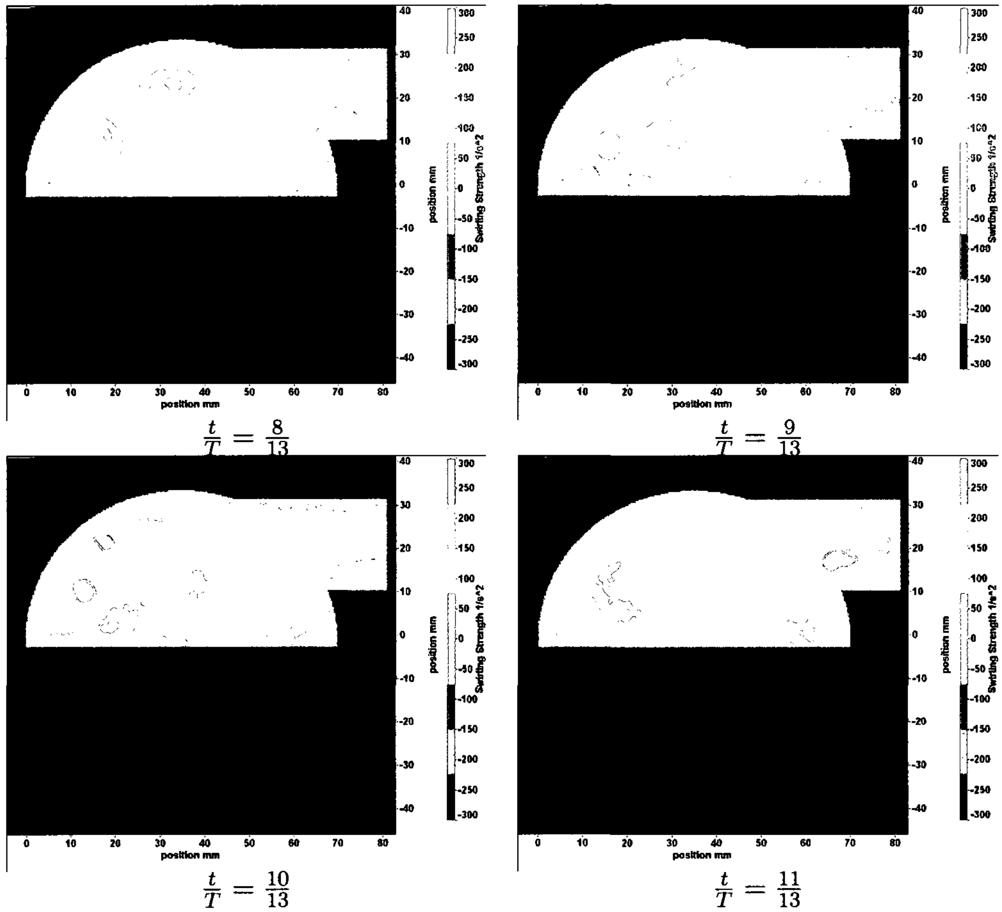

$\frac{t}{T} = \frac{8}{13}$ $\frac{t}{T} = \frac{9}{13}$

$\frac{t}{T} = \frac{10}{13}$ $\frac{t}{T} = \frac{11}{13}$

Figure 6.67: Average PIV XZ Swirl strength maps (y= -15 mm) (continued)

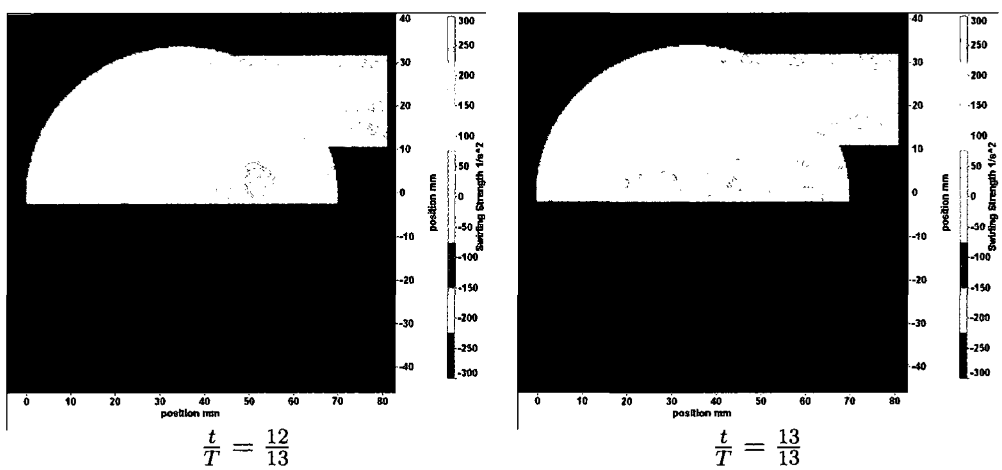

$\frac{t}{T} = \frac{12}{13}$ $\frac{t}{T} = \frac{13}{13}$

Figure 6.68: Average PIV XZ Swirl strength maps (y= -15 mm) (continued)

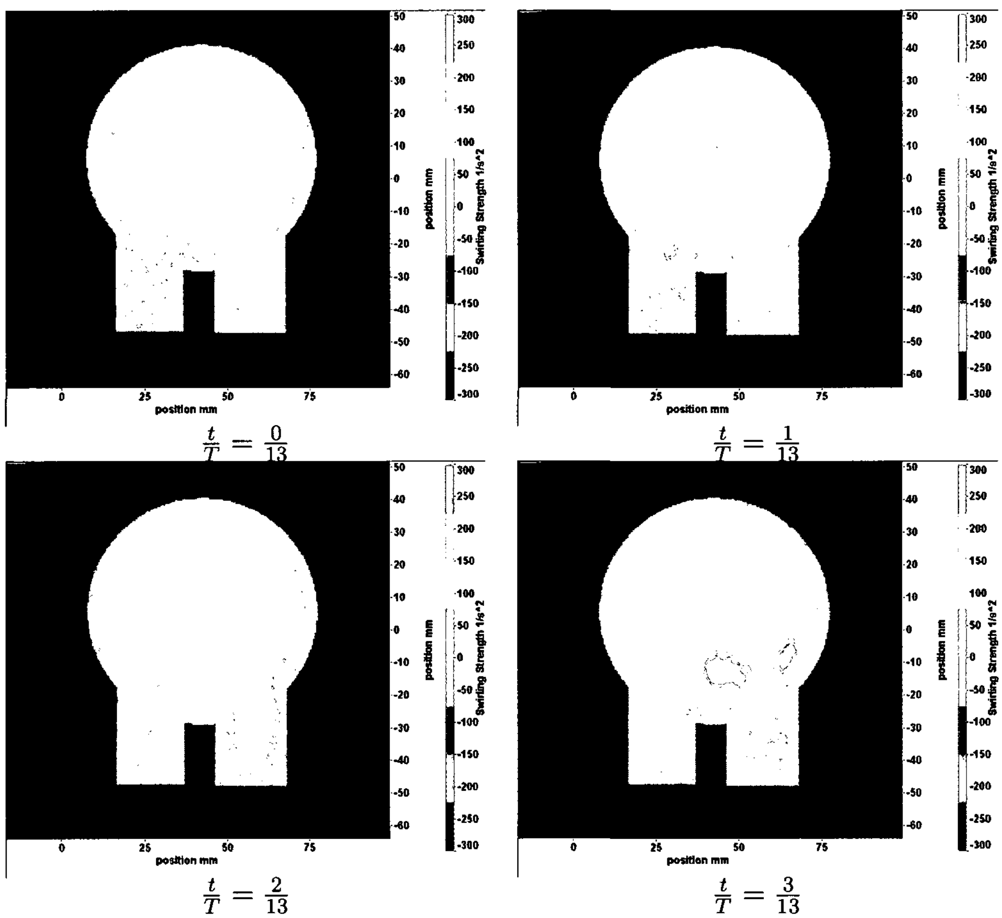

Figure 6.69: Average PIV XY Swirl strength maps (z= 20 mm)

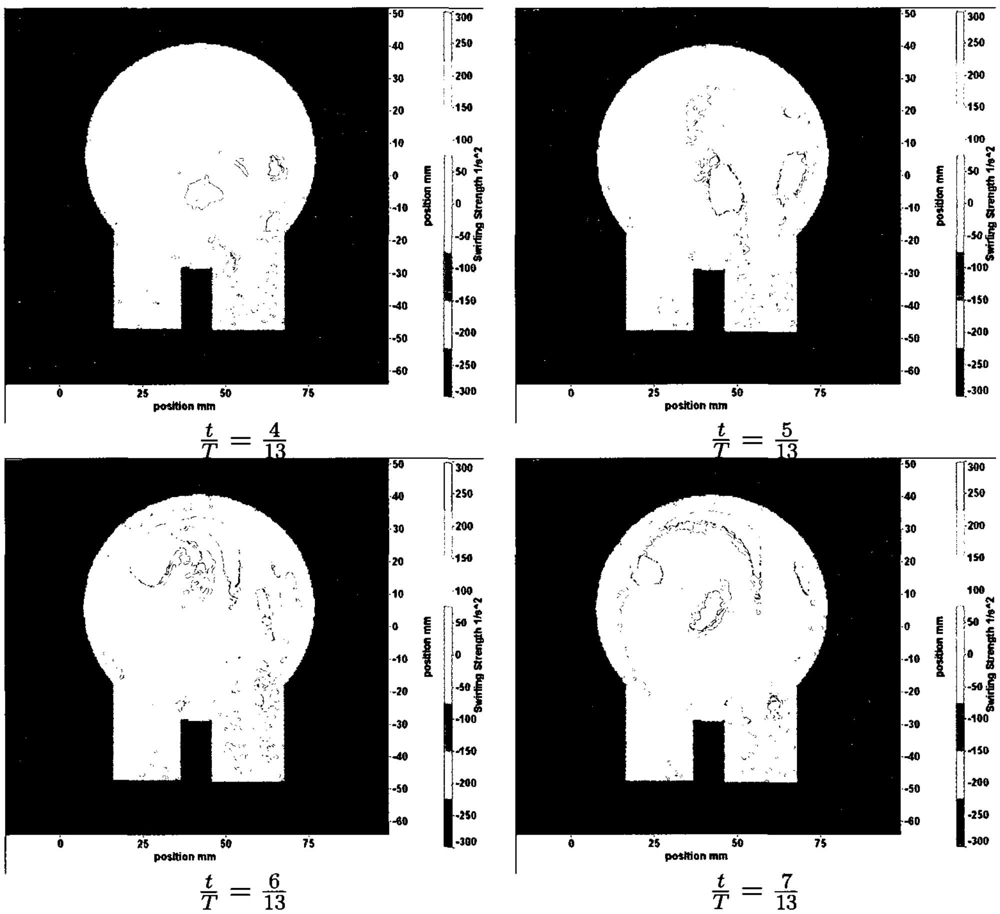

Figure 6.70: Average PIV XY Swirl strength maps (z= 20 mm) (continued)

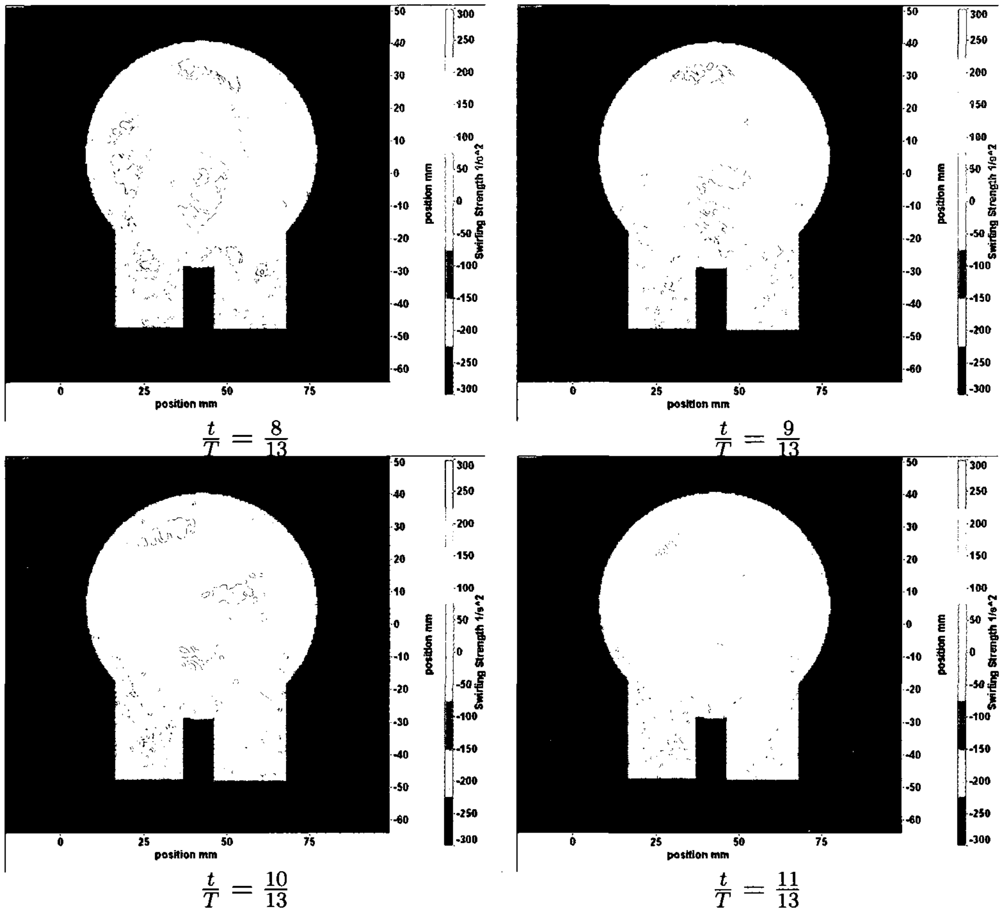

Figure 6.71: Average PIV XY Swirl strength maps (z= 20 mm) (continued)

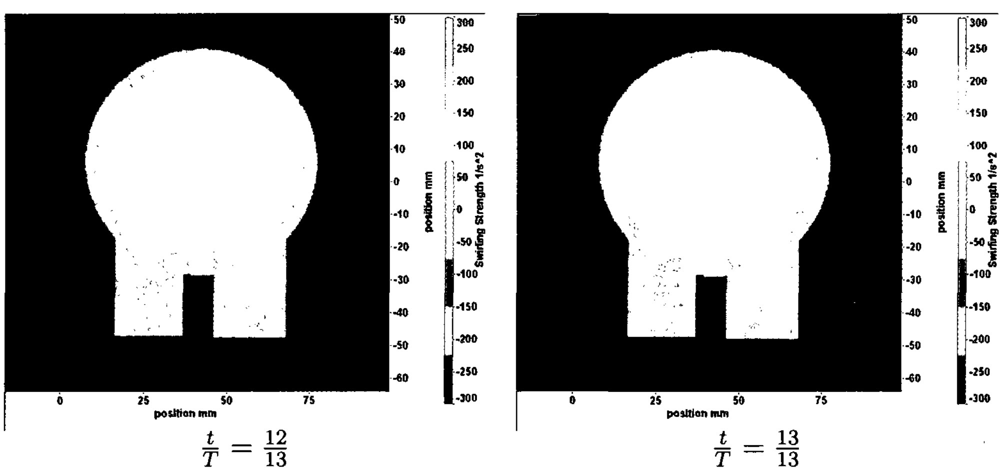

Figure 6.72: Average PIV XY Swirl strength maps (z= 20 mm) (continued)

contours for the VAD geometry. The inlet plane contours are presented in Figures 6.73-6.76; Figures 6.77-6.80 display the contours for the centreplane of the VAD, and Figures 6.81-6.84 display the contours for the outlet plane; Figures 6.85-6.88 display the contours in the $x - y$ plane along the centreplane of the inlet and outlet tubes.

During early diastole (Figures 6.73 and 6.85), the highest strain was observed along the wall of the VAD, where the maximum strain rate value of $\varepsilon = 80$ s^{-1} was observed at $\frac{t}{T} = \frac{0}{13}$. The region of high strain rate was noticeably larger at $\frac{t}{T} = \frac{1}{13}$ (Figures 6.73 and 6.85) along the VAD wall as the injection volume increases. This general pattern continues until the inlet jet forms at $\frac{t}{T} = \frac{3}{13}$, when two streams of high strain were present during the injection, one which had an average strain rate value of 80 s^{-1} and a second one with a lower value 60 s^{-1}. However, it is important to note that each stream had a core of rapidly changing strain rate as it traveled into the VAD during diastole, and this core region expands and stretches, as displayed at peak diastole at $\frac{t}{T} = \frac{6}{13}$ (Figures 6.74 and 6.86). A region near the wall of the inlet was shown undergoing a rapid decrease in strain rate value from $\frac{t}{T} = \frac{4}{13}$ to $\frac{t}{T} = \frac{5}{13}$ (Figures 6.74 and 6.86), which may indicate a detachment of the shear layer during injection. Note that during diastole, there was little change in the strain rate maps along the centreplane of the VAD (Figure 6.77) and the outlet region was observed to be undergoing a net decrease in strain rate (Figure 6.81).

As diastole ended and systole began, shortly after peak injection at $\frac{t}{T} = \frac{6}{13}$, the high-strain regions dissipated into other areas of the VAD, as shown in Figure 6.74. During this same period, the contour maps in Figure 6.78 show several regions with changing strain rate along the VAD walls but the pattern in the interior remained relatively fixed. Figure

6.86 displays a change in the strain rate along the VAD wall adjacent to the inlet tube from $\frac{t}{T} = \frac{6}{13}$ to $\frac{t}{T} = \frac{7}{13}$ as a region of low strain rate was eliminated after peak injection; this suggests the elimination of a vortex after peak injection as the injected fluid was mixed with the existing volume. Regions of changing strain rate are also visible on the VAD wall adjacent to both the inlet and the outlet tubes as well as the surface directly opposite to the inlet and outlet tubes.

At the systolic peak at $\frac{t}{T} = \frac{12}{13}$ (Figures 6.84 and 6.88) the peak strain rate measured in the outlet tube has a value of $\varepsilon = 200\ \mathrm{s}^{-1}$. Figure 6.84 displays many regions of rapidly changing strain rate near the surfaces of the outlet tube as two streams of high strain rate were generated and expanded and stretched into the outlet tube. The strongest region of rapidly changing strain rate was along the lower surface of the VAD, suggesting that this may be an area of shear layer detachment from the bulk flow. Figure 6.88 shows a region of high strain rate along the VAD surface adjacent to the outlet tube at $\frac{t}{T} = \frac{12}{13}$. The effects of these regions of strain and their changes over the VAD operational cycle are discussed in the following chapter.

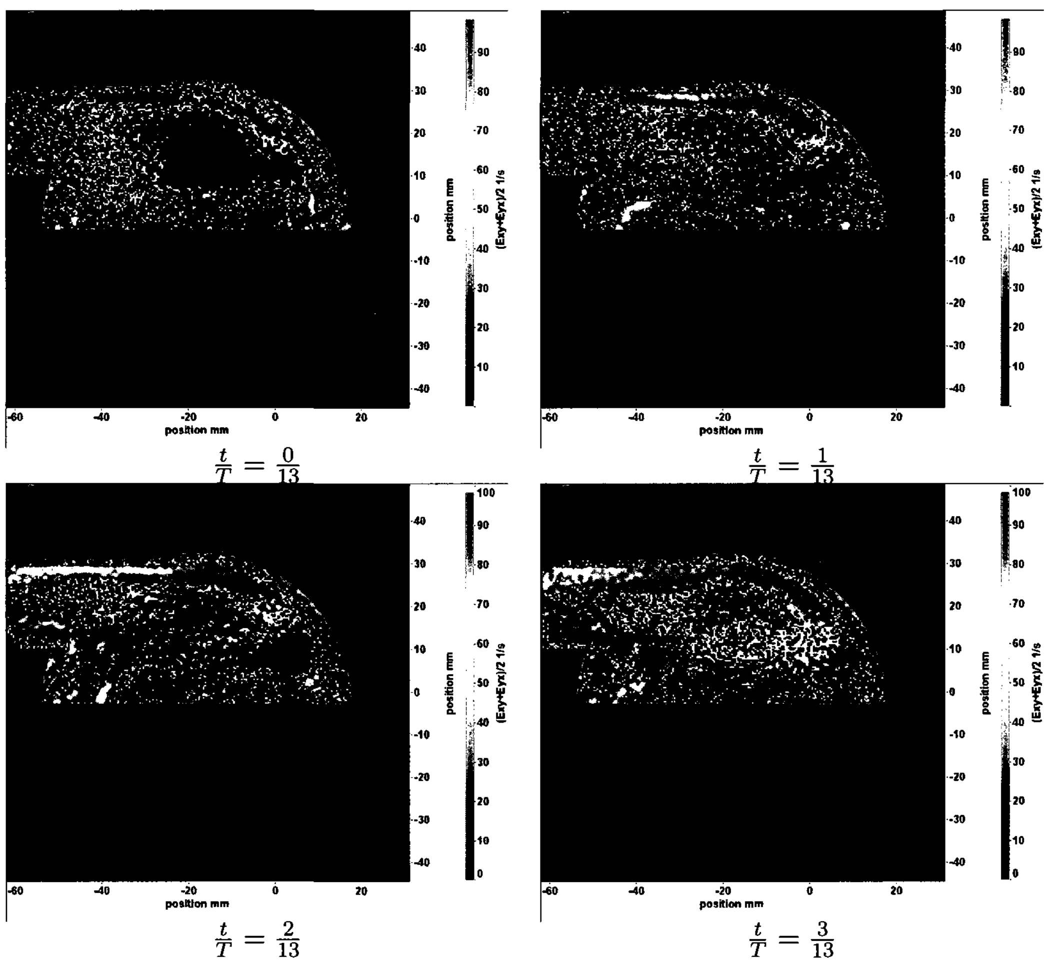

Figure 6.73: Average PIV XZ strain rate maps (y= 15 mm)

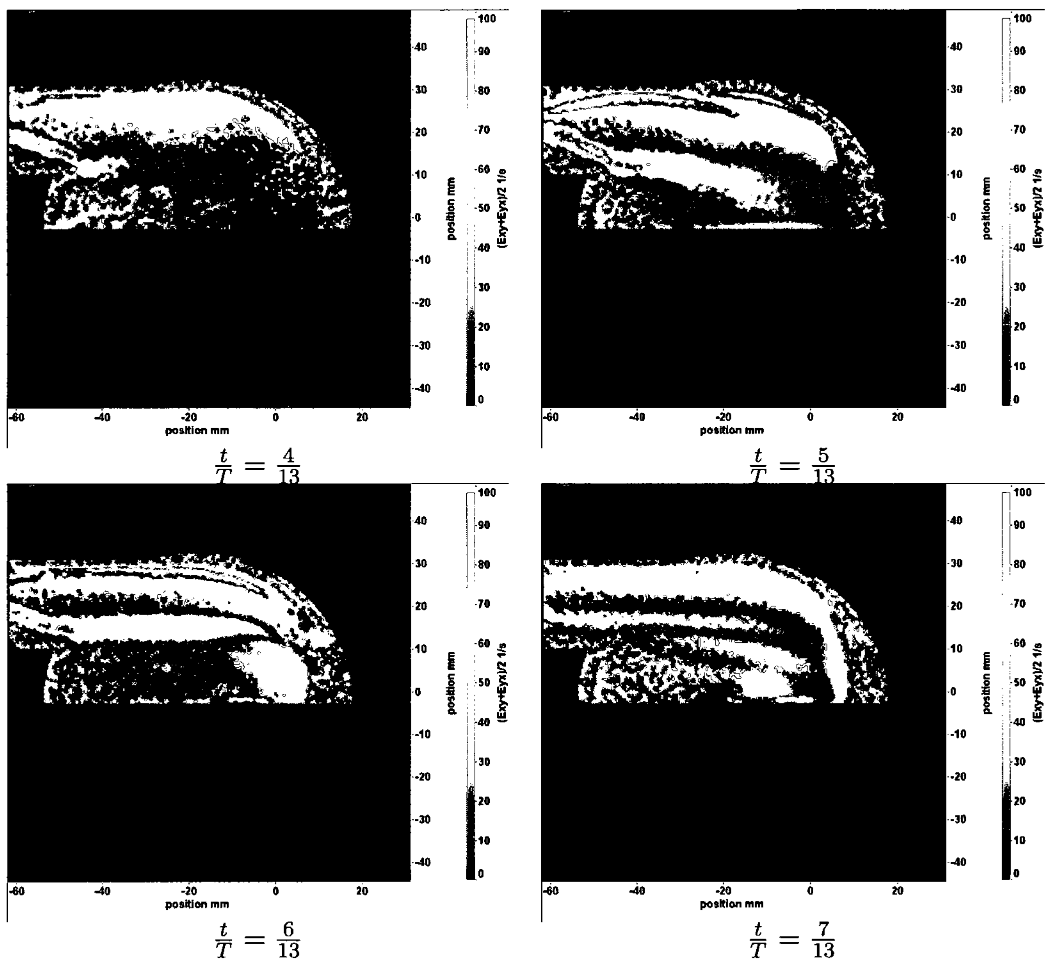

$\frac{t}{T} = \frac{4}{13}$ $\frac{t}{T} = \frac{5}{13}$

$\frac{t}{T} = \frac{6}{13}$ $\frac{t}{T} = \frac{7}{13}$

Figure 6.74: Average PIV XZ strain rate maps (y= 15 mm) (continued)

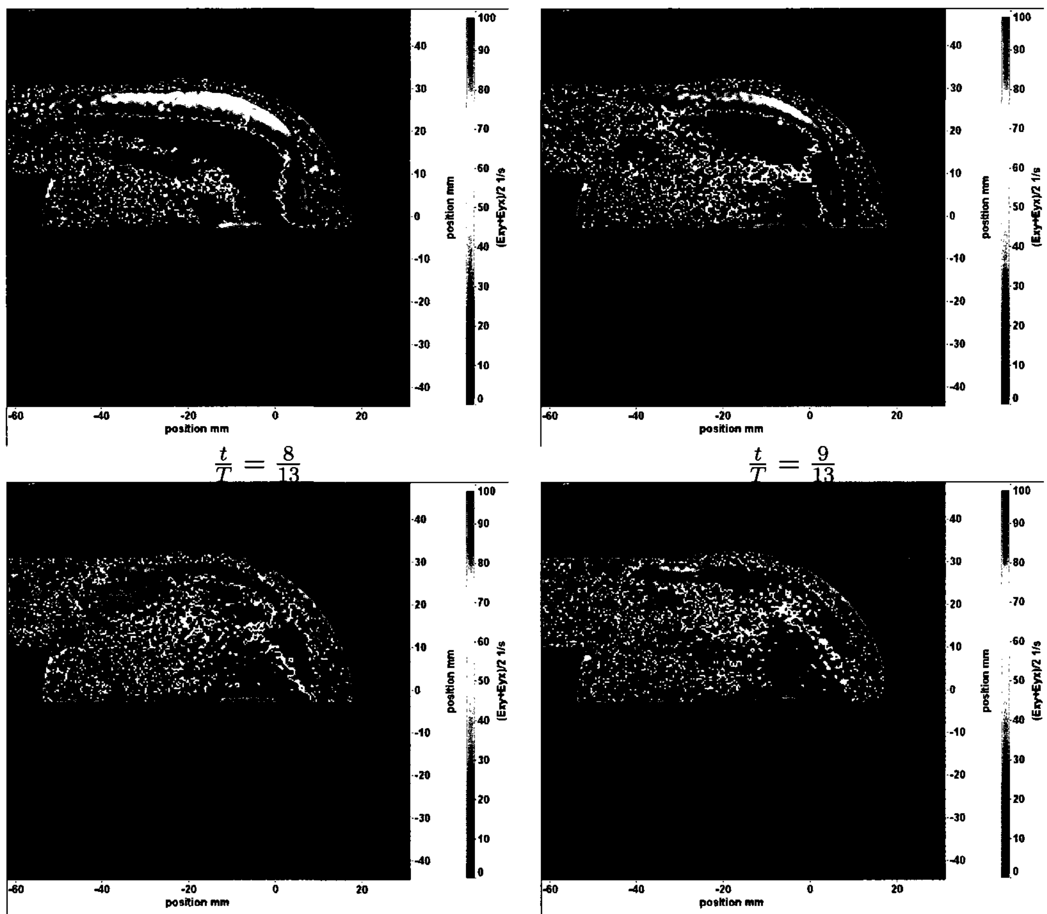

Figure 6.75: Average PIV XZ strain rate maps (y= 15 mm) (continued)

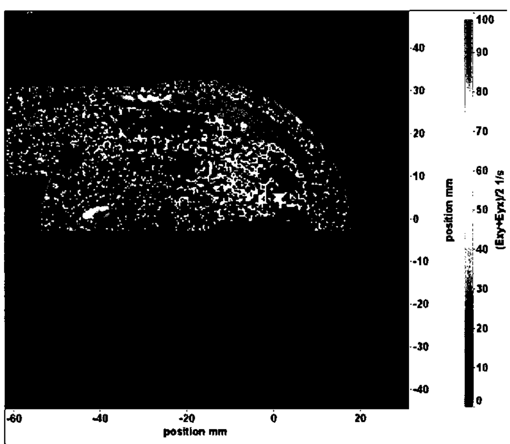

$\frac{t}{T} = \frac{12}{13}$

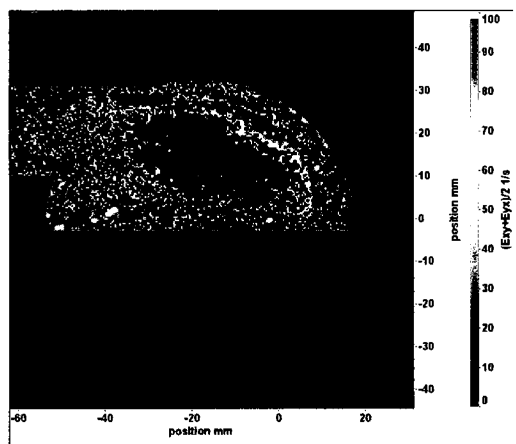

$\frac{t}{T} = \frac{13}{13}$

Figure 6.76: Average PIV XZ strain rate maps (y= 15 mm) (continued)

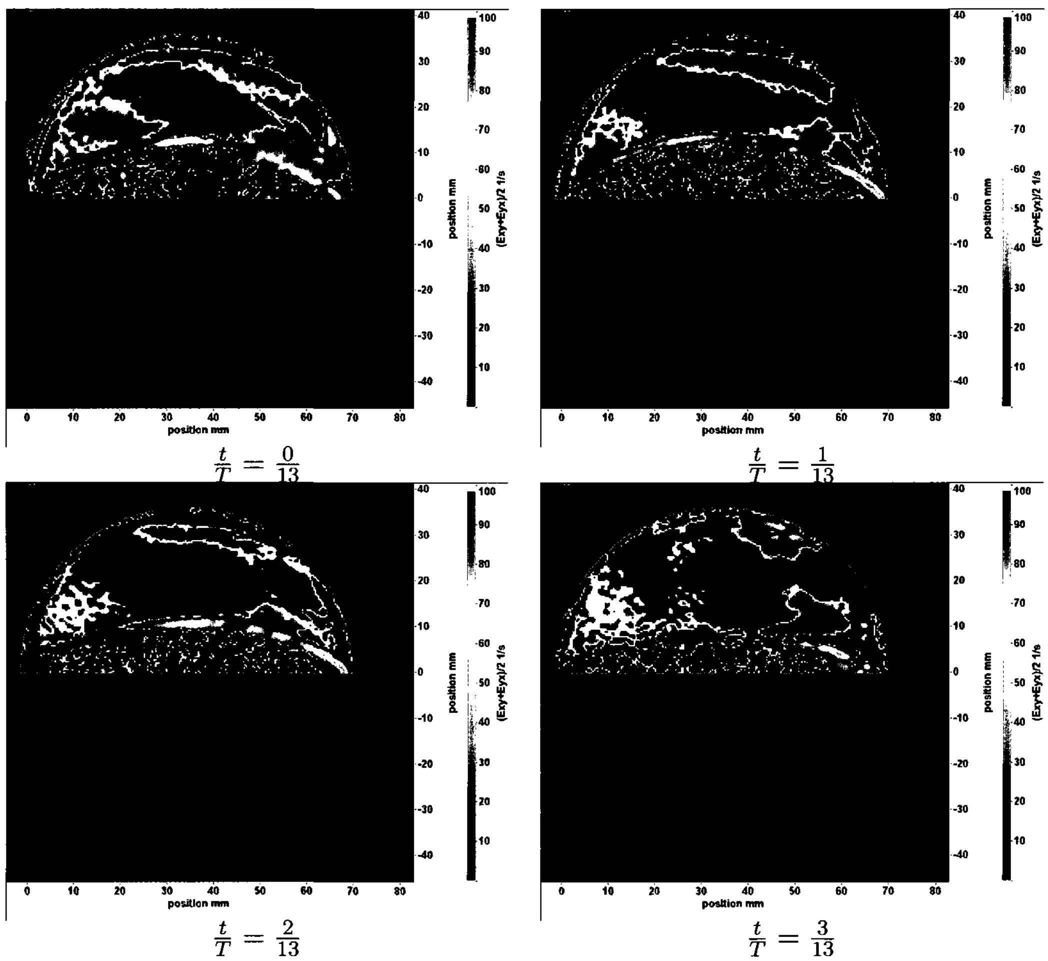

Figure 6.77: Average PIV XZ strain rate maps (y= 0 mm) (continued)

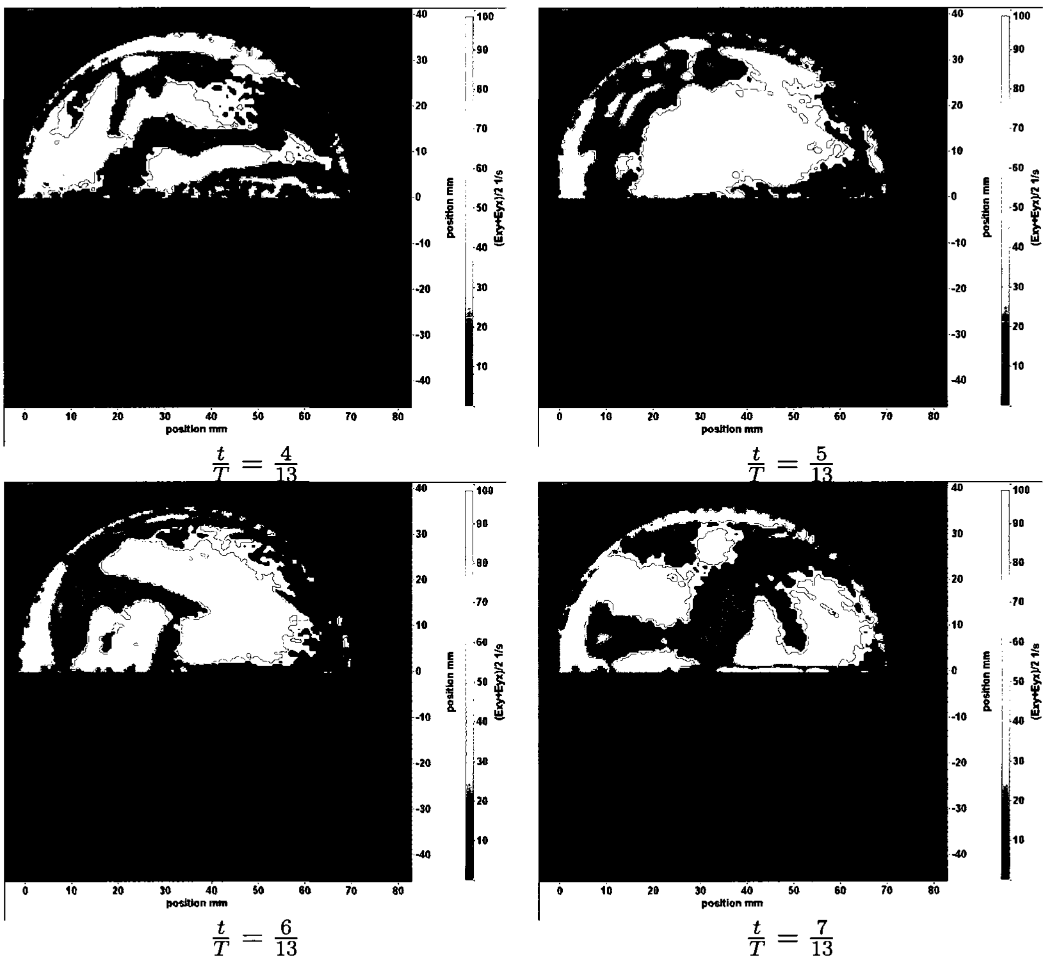

$\frac{t}{T} = \frac{4}{13}$ $\frac{t}{T} = \frac{5}{13}$

$\frac{t}{T} = \frac{6}{13}$ $\frac{t}{T} = \frac{7}{13}$

Figure 6.78: Average PIV XZ strain rate maps (y= 0 mm) (continued)

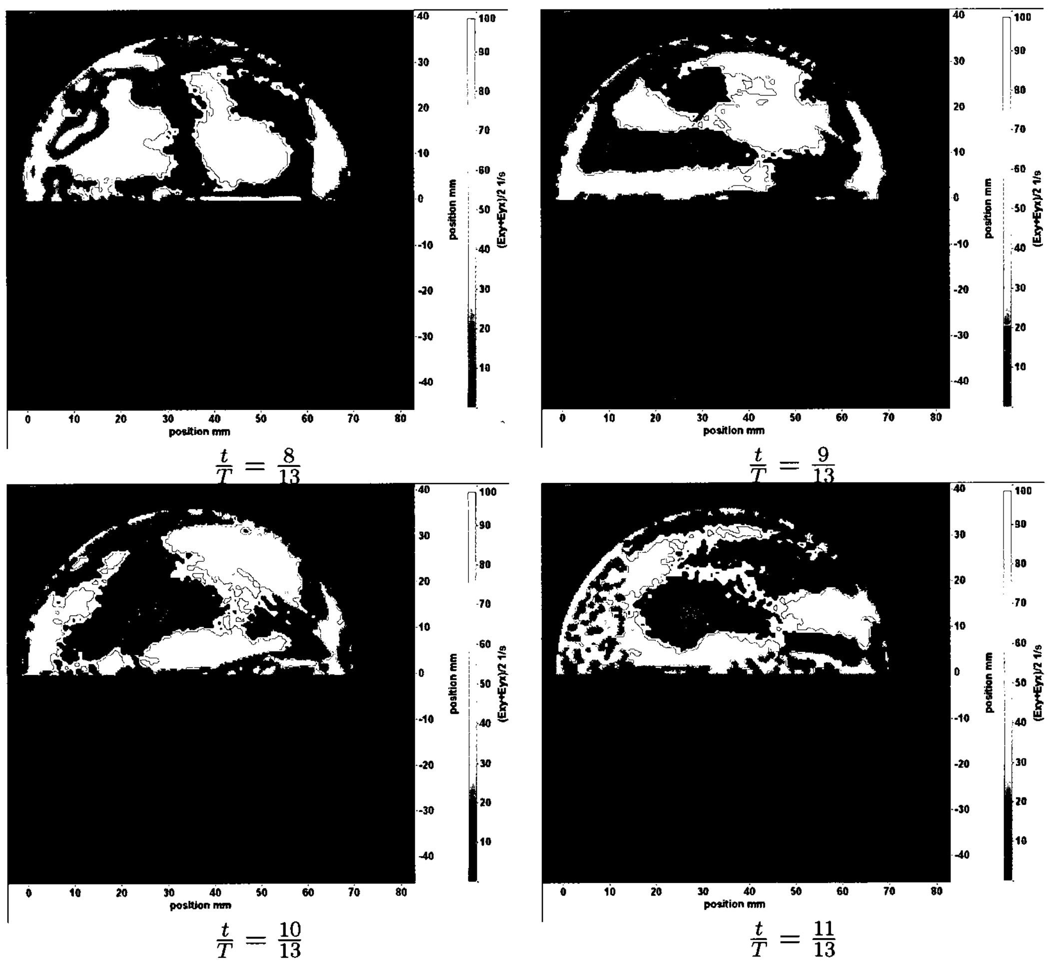

$\frac{t}{T} = \frac{8}{13}$ $\frac{t}{T} = \frac{9}{13}$

$\frac{t}{T} = \frac{10}{13}$ $\frac{t}{T} = \frac{11}{13}$

Figure 6.79: Average PIV XZ strain rate maps (y= 0 mm) (continued)

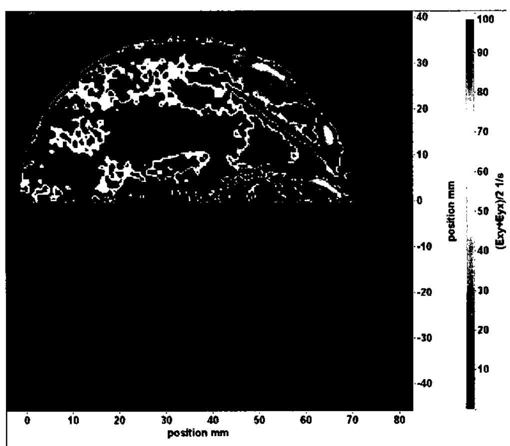

$\frac{t}{T} = \frac{12}{13}$

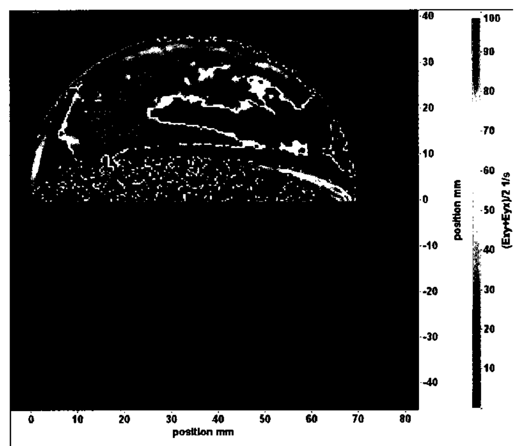

$\frac{t}{T} = \frac{13}{13}$

Figure 6.80: Average PIV XZ strain rate maps (y= 0 mm) (continued)

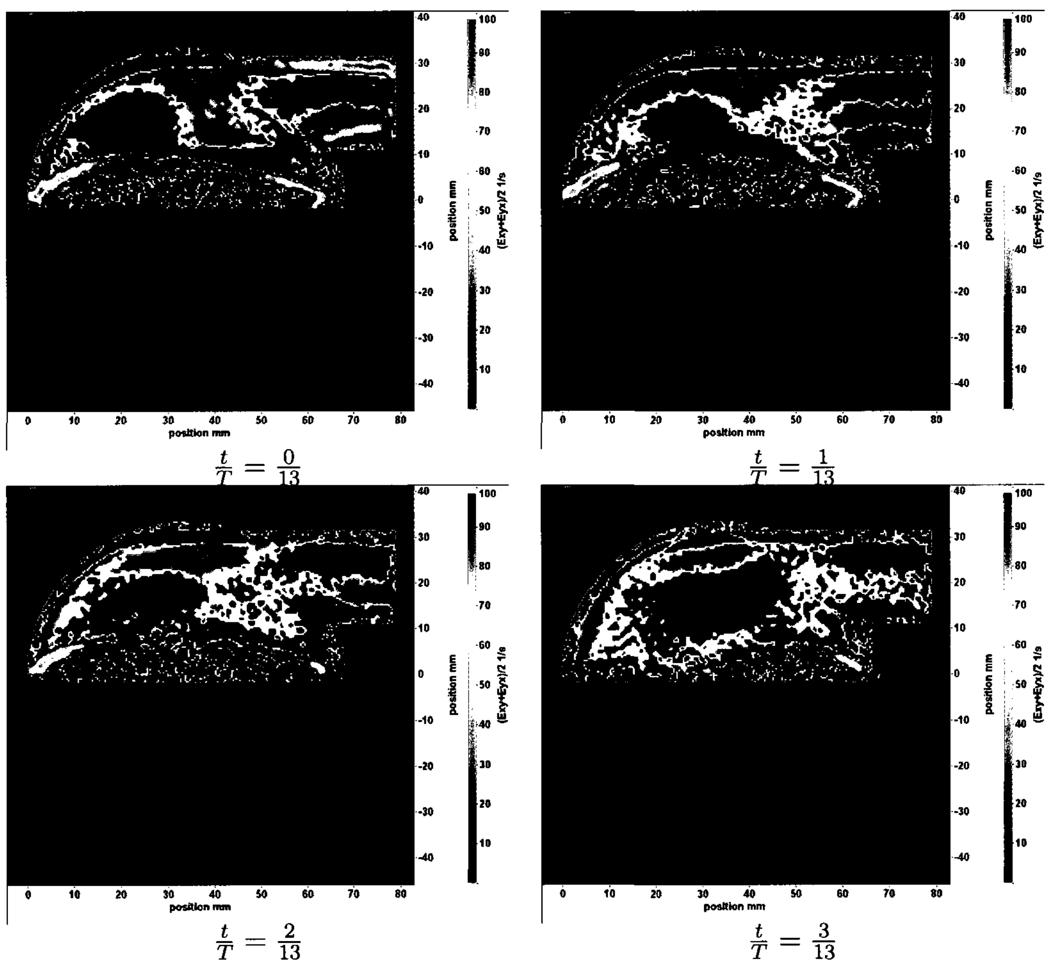

Figure 6.81: Average PIV XZ strain rate maps (y= -15 mm)

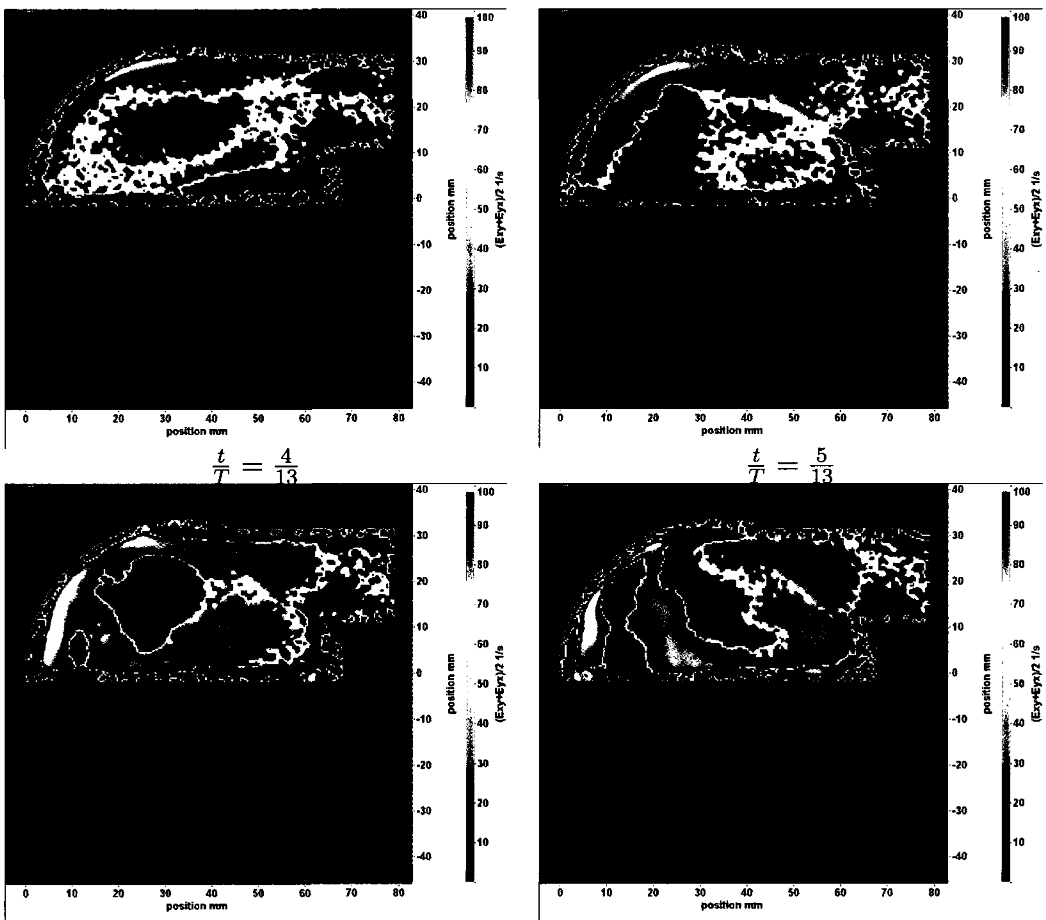

$\frac{t}{T} = \frac{4}{13}$ $\frac{t}{T} = \frac{5}{13}$

$\frac{t}{T} = \frac{6}{13}$ $\frac{t}{T} = \frac{7}{13}$

Figure 6.82: Average PIV XZ strain rate maps (y= -15 mm) (continued)

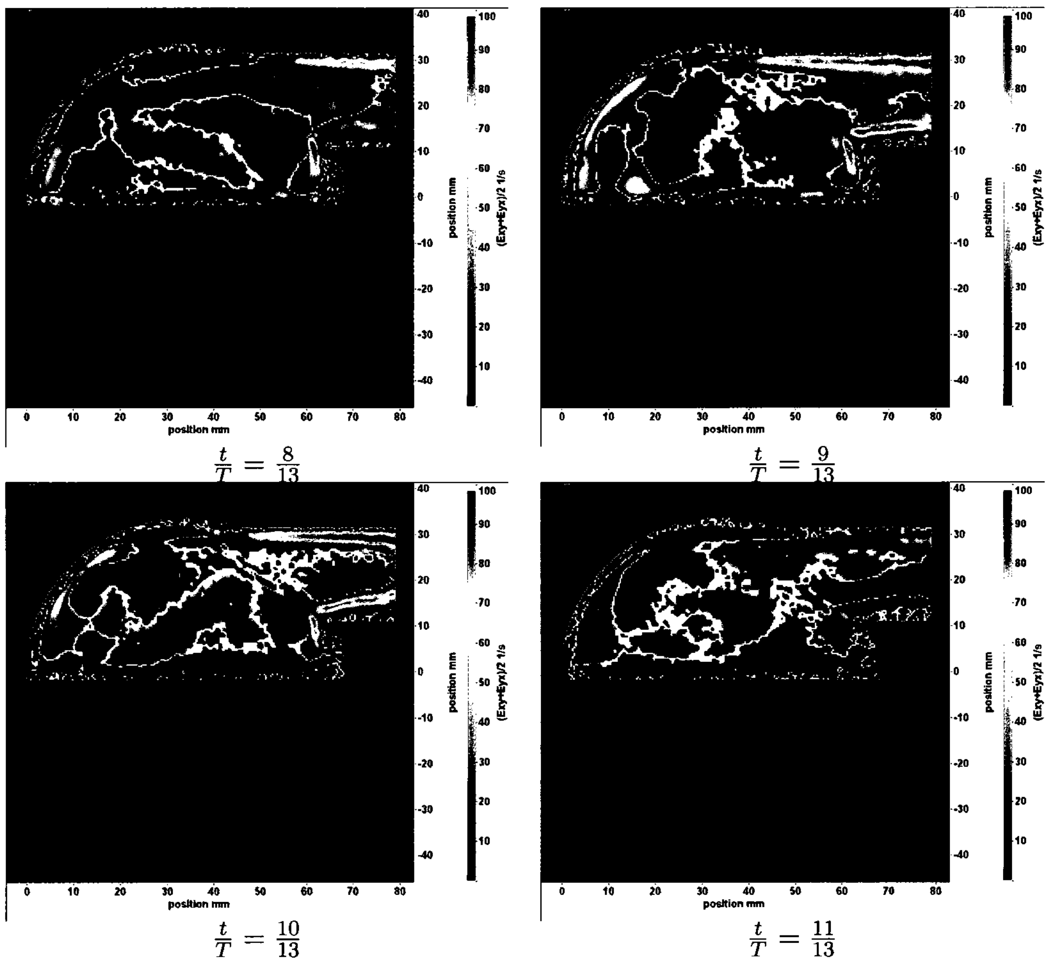

Figure 6.83: Average PIV XZ strain rate maps (y= -15 mm) (continued)

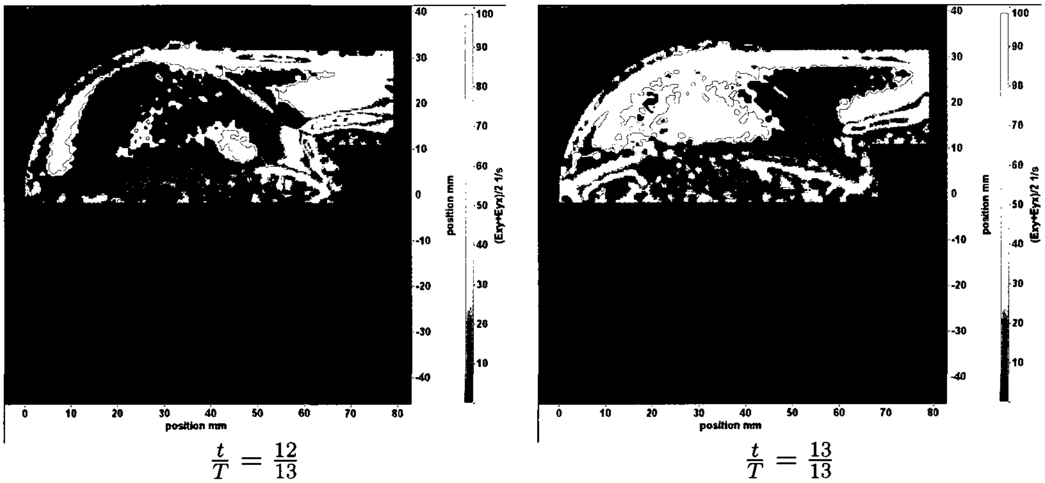

Figure 6.84: Average PIV XZ strain rate maps (y= -15 mm) (continued)

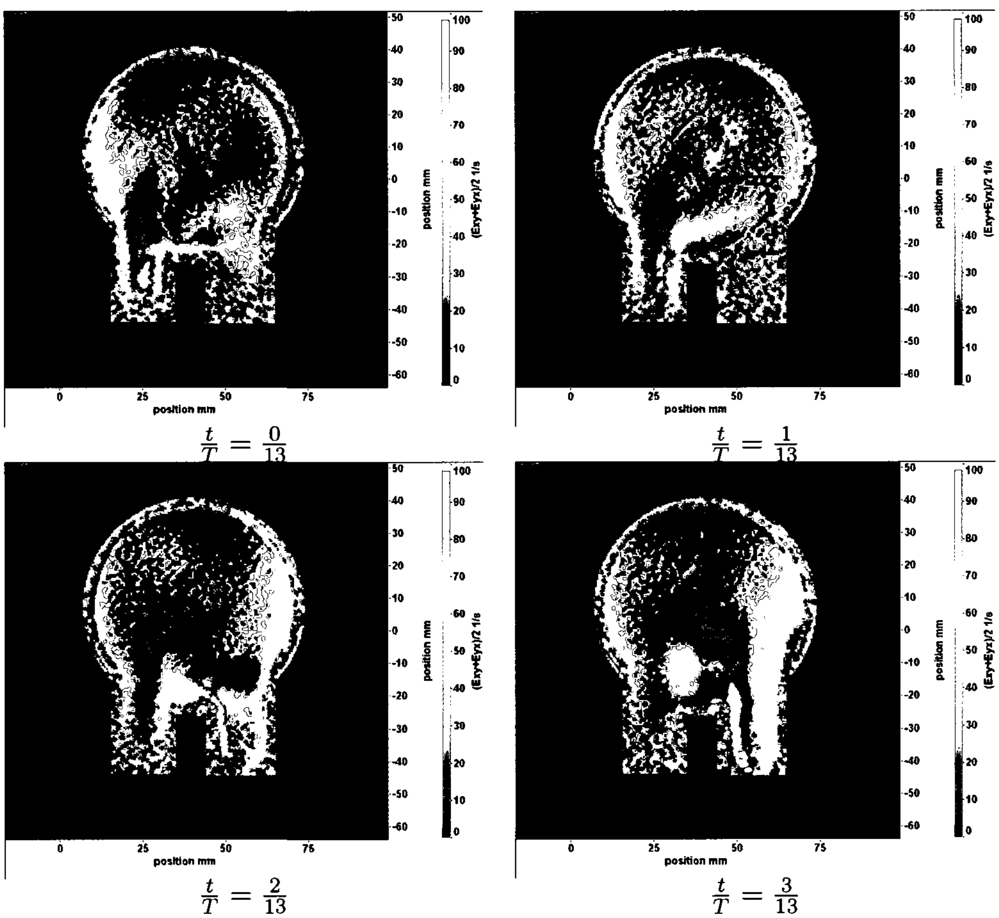

Figure 6.85: Average PIV XY strain rate maps (z= 20 mm) (continued)

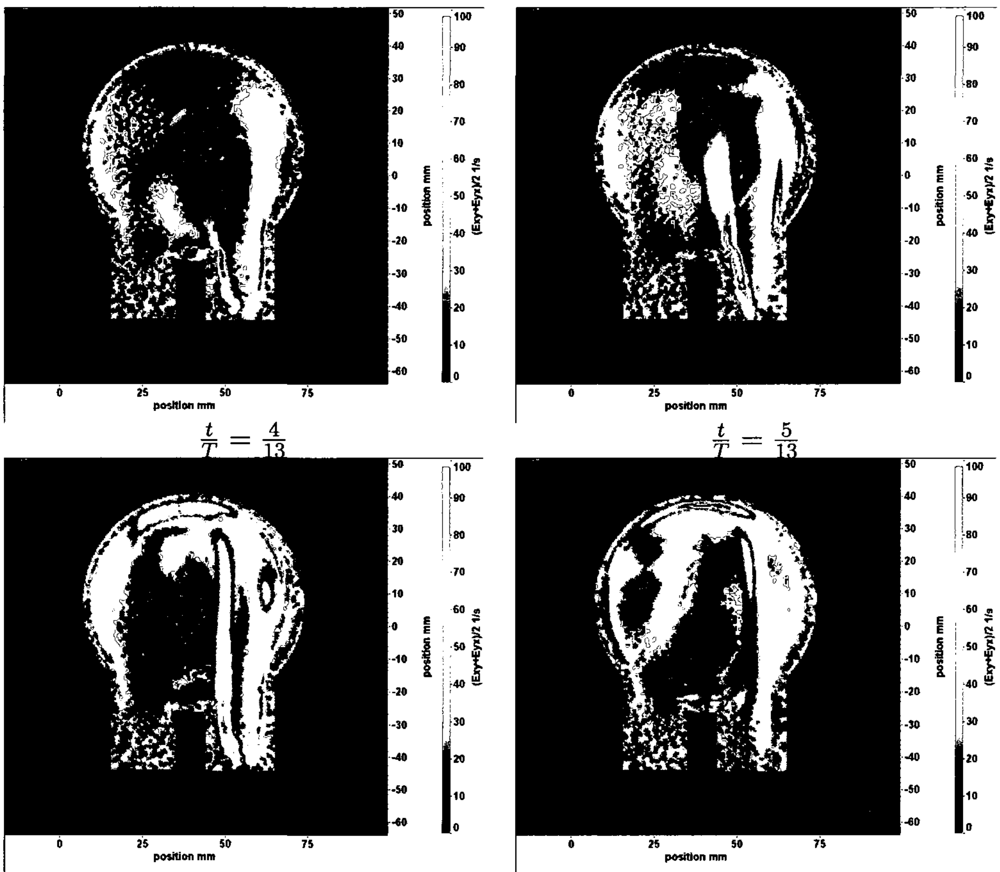

$\frac{t}{T} = \frac{4}{13}$ $\frac{t}{T} = \frac{5}{13}$

$\frac{t}{T} = \frac{6}{13}$ $\frac{t}{T} = \frac{7}{13}$

Figure 6.86: Average PIV XY strain rate maps (z= 20 mm) (continued)

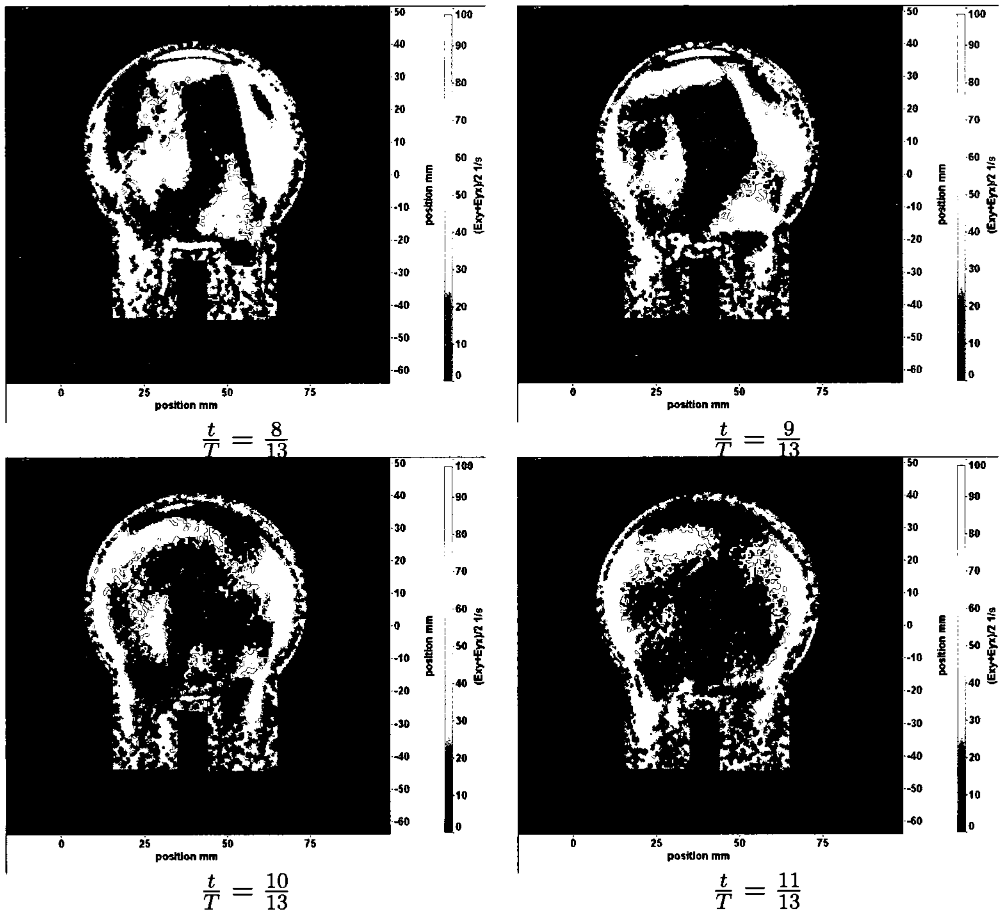

Figure 6.87: Average PIV XY strain rate maps (z= 20 mm) (continued)

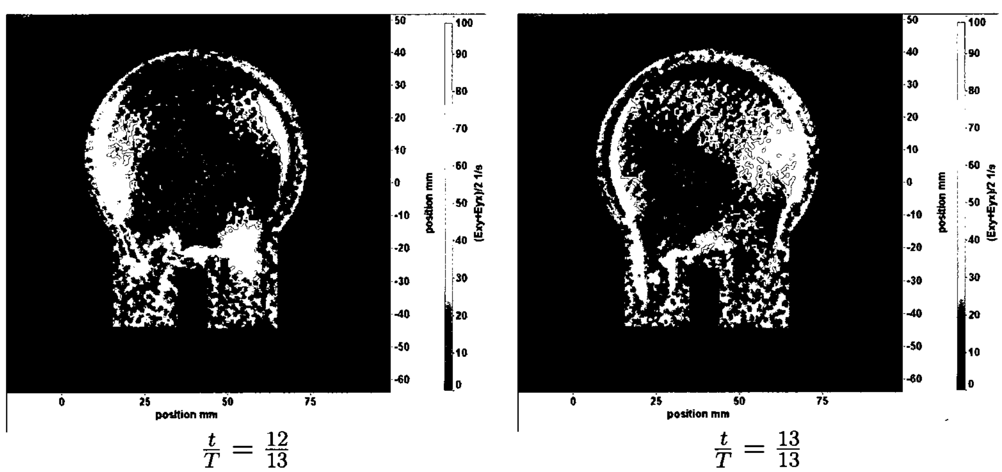

Figure 6.88: Average PIV XY strain rate maps (z= 20 mm) (continued)

Chapter 7

Analysis of the Results and Discussion

7.1 Correction of Peak Velocities Measured by LDV

Previous measurements by Vergniaud suggested that the maxium velocity that would measured by the LDV during normal VAD operation was $U = 1.2$ ms^{-1}. This value was used to set the maximum velocities for the LDV measurements (Vergniaud (2001)). However, the results for Point 1 and Point 2 from the previous chapter showed plateaus near the peaks, which do not appear to be realistic. It was assessed that the velocity magnitude at Points 1 and 2 values exceeded the set limit of the LDV system and that the measured values during the short times when plateaus were observed were lower than the actual ones, although not by large amounts. To obtain more realistic peak velocity waveforms, the signals during these short times were corrected as shown in Figure 7.1. The corrected

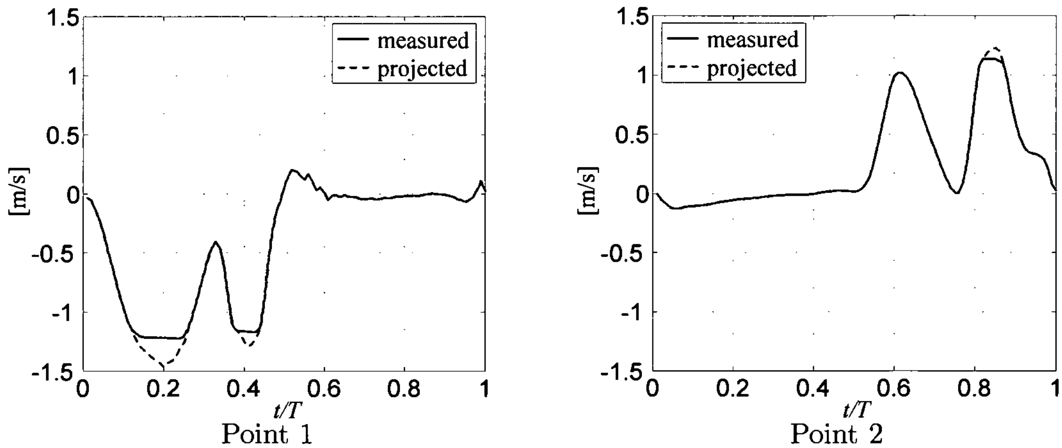

Figure 7.1: Comparison of LDV and PIV averaged velocities

peak values were $U = 1.47$ ms^{-1} at Point 1 and $U = 1.22$ ms^{-1} at Point 2. Although such correction could have been avoided if the actual velocity range were estimated more accurately before the measurements were taken, it is not of a serious concern, becasue it only affects a very small portion of the LDV data.

7.2 Estimates of Flowrate Variation

The LDV velocity measurements in the inlet and outlet tubes of the VAD model that were presented in the previous chapter indicated the presence of two strong peaks separated by a valley within which the velocity magnitude reached very low values. Such patterns are clearly undesirable and are attributed to a deviation of the driving fluid system operation from its intended design, which was meant to generate a nearly sinusoidally varying flowrate of the driving fluid into and out of the lower VAD chamber, following the shape of the ideal flow rate that was presented in Figure 4.2. Observation of the LDV signals demonstrated that the valleys in velocity occurred near the two midstrokes of the driving tank piston, on which a diaphragm was attached. Similar patterns were observed by Vergniaud (2001), who used a different diaphragm, made of relatively stiff rubber. In that case, it was noticed that the diaphragm was not kept taut at near midstroke but developed folds and as a result the fluid volume displaced by the piston during that time did not change monotonically following the ideal waveform but presented a valley. The presently used, thinner, latex diaphragm was procured to reduce or eliminate this problem, but, because it required multiple layers for sufficient strength, its stiffness increased and, like the previous one, this diaphragm could not be maintained under tension during midstroke, so the same problem as previously occurred. It was concluded that this is an inherent problem with the present design, which uses a diaphragm to seal the driving fluid tank during the piston stroke. Due to time limitations, redesign of the apparatus was not an acceptable option. In view of the fact that the main purpose of this work is to provide an experimental database for the validation of numerical simulations, the measurements were performed as planned. During analysis of the results, it was realized that some additional measurements would have been desirable, but this was no longer possible because the apparatus was dismantled. Although it is not possible to determine the exact flowrate variation, significant effort was put into estimating it from the available measurements so that some unambiguous inflow/outflow boundary conditions can be specified.

First of all, it is obvious that the best locations from which to determine the flowrate would be in the VAD inlet tube during diastole and the VAD outlet tube during systole. At first glance, it may appear that PIV measurements would be more suitable than

LDV measurements for calculating flow rates, because they provide velocity maps. However, such measurements were not spaced closely enough in time to provide a realistic waveform of the flowrate variation. Moreover, because the flow is highly unsteady and three-dimensional, rather than axisymmetric, it is not apparent that velocity maps on cross-sections of the tubes would be sufficient to estimate accurately the flowrate. Following consideration of different options, it was decided to adopt the following approximate procedure. There is no reason to believe that the time-averaged flow rate $\overline{Q}$ that was calculated from the idealized analysis of the diaphragm motion (Appendix C) is inaccurate, because, irrespectively of the diaphragm behaviour at midstroke, the maximum and minimum displaced volumes of the driving fluid should be the same as those considered in the idealized analysis. If the velocity were uniform across the inlet tube at all times, then it would be possible to calculate the time-averaged flowrate by integrating the corrected LDV-measured axial velocity U_1 at Point 1 from the previous section, during diastole as

$$\overline{Q}_1 = \frac{\pi d^2}{4} \frac{2}{T} \int_0^{T/2} |U_1(t)|\, dt \tag{7.1}$$

where d is the tube diameter. If the velocity profile were parabolic at all times, as it would have been if the flow were steady, laminar and fully developed, then the actual flowrate would have been half this value. As a rough estimate of the effect of the velocity profile, we computed the correction factor

$$\alpha_1 = \frac{\overline{Q}_1}{\overline{Q}} = 0.77 \tag{7.2}$$

Although it is understood that the velocity measured at Point 1 cannot be related to the instantaneous flowrate Q in a simple manner, a rather crude but not entirely unrealistic estimate of Q during diastole, based on the corrected LDV measurements, will be given as

$$Q_1 = \alpha_1 \frac{\pi d^2}{4} U_1 (t) \tag{7.3}$$

In a similar fashion, a coefficient $\alpha_2 = 1.24$ was determined from corrected LDV measurements of the velocity U_2 at Point 2 and the instantaneous flowrate during systole was estimated as

$$Q_2 = \alpha_2 \frac{\pi d^2}{4} U_2 (t) \tag{7.4}$$

The value of $\alpha_2 > 1$ for the inlet tube suggests that there may be much larger differences in the velocity distributions during the cycle across this tube than across the outlet tube. In any case, all these results seem to contain large uncertainties, which cannot be accounted for by conventional methods. Different estimates of the displacement volume and the flow rate variations during the cycle are presented in Figures 7.2 and 7.3, respectively.

7.3 Comparison of PIV and LDV results

Before attempting to compare measured velocities and estimated flowrates obtained using the LDV method with those using the PIV method, it seems necessary to explain an important difference between these methods. Both methods provide discrete measurements of the velocity, however, LDV has a typical sampling rate which is much higher than that for PIV, which is restricted by the repetition rate of the lasers and camera used. Therefore, LDV follows fairly well the temporal variation of the local flow velocity, but PIV does not. In fact, each PIV measurement was obtained during a different cycle from any other, conditioned to be acquired following a specified time delay after the trigger

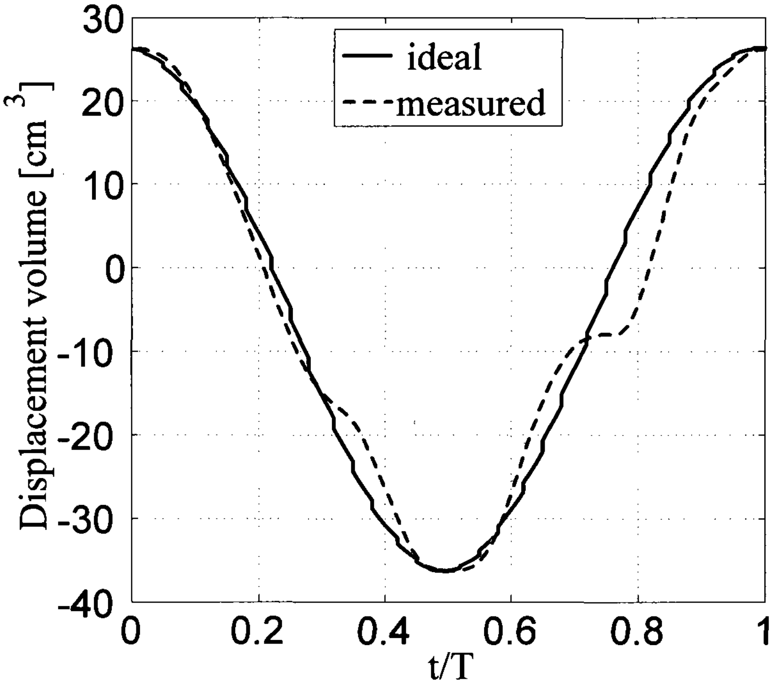

Figure 7.2: Comparison of idealized displacement volume with estimates based on corrected LDV measurements

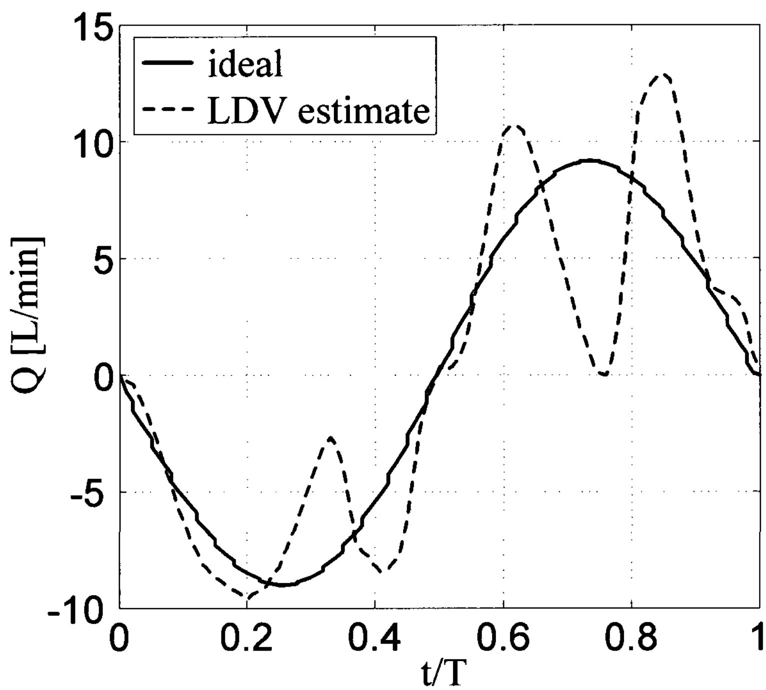

Figure 7.3: Comparison of idealized flowrate with estimates based on corrected LDV measurements

marked the beginning of the cycle. Because PIV profiles were acquired only at 14 times during the cycle, and considering that the flowrate through the VAD was a very complicated function of time, flowrate estimates based on PIV results would have a large uncertainty and will not be presented here.

Figure 7.4 compares the XY PIV velocity profiles of representative PIV cycles taken with different interframe time values Δt at the systolic peak $\left(\frac{t}{T} \simeq \frac{4}{9}\right)$ with the phase-averaged LDV velocity measurement. Immediately apparent is that the $\Delta t = 2$ ms case severely underestimates the velocity profile, whereas the $\Delta t = 1$ ms, $\Delta t = 0.5$ ms and $\Delta t = 0.25$ ms cases show a fair agreement with the phase-averaged LDV velocity measurement, even though the peak velocities are still significantly lower than that of the LDV phase average, and that this in turn would be slightly lower than the corrected LDV value. Although it would seem that the $\Delta t = 0.5$ ms produces a lower velocity than the $\Delta t = 0.25$ ms or $\Delta t = 1$ ms cases, this is likely within the PIV uncertainty and especially reflecting cycle-to-cycle variations. This comparison suggests that lower Δt values are more likely to produce a PIV velocity map that more closely agrees with the LDV phase average results in regions of high acceleration and high velocity, but that this is offset as the lower Δt values produce extraneous high-velocity vectors in low-velocity regions due to a high uncertainty. This would suggest that future PIV measurements in an unsteady flow environment such as a pulsatile VAD should use multiple Δt values for different points in the operational cycle, with smaller Δt values being used at times of high flow such as peak diastole and systole, and moderate Δt values to capture the general features of the flowfield.

Local velocity values measured by the two methods can only be compared at the

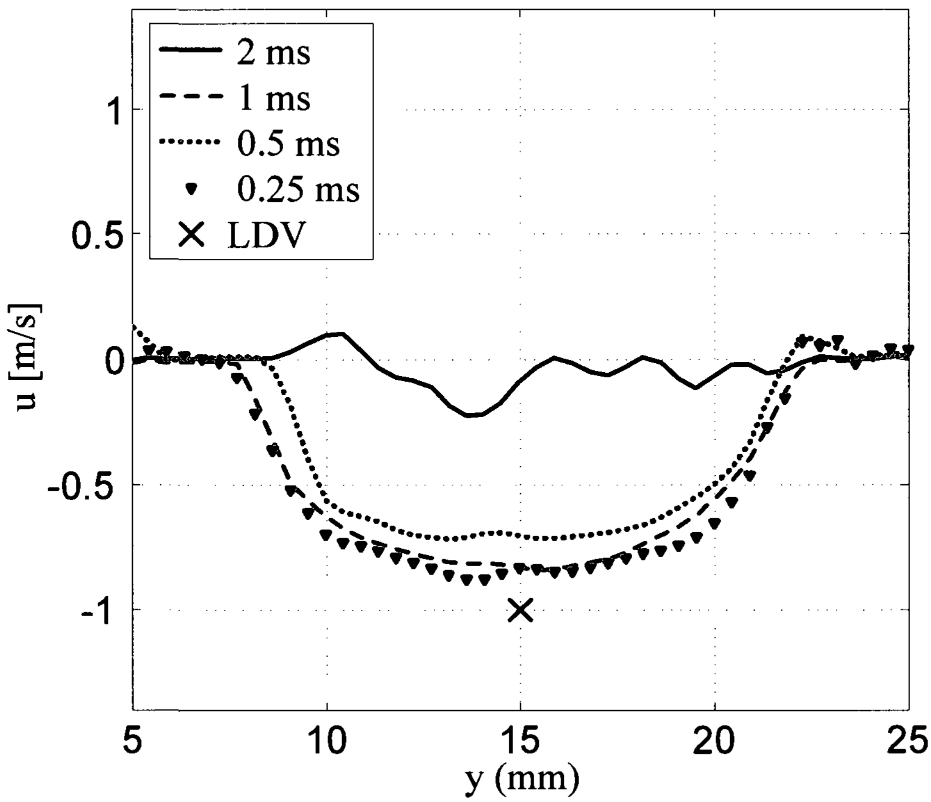

Figure 7.4: Comparison of XY PIV profiles with varying Δt values at systolic peak at Point 1

locations at which LDV measurements were taken. Figure 7.5 shows a comparison of the phase averaged LDV x-component velocity $< U >$ with the corresponding phase-averaged PIV results for Point 1, which lies at the axis of the inlet tube, Point 2, which similarly lies at the axes of the outlet tube, and Point 12 which is located along the axis of symmetry of the VAD and near the VAD wall opposite both the inlet and outlet tubes. Although the velocity values obtained by the two systems are in comparable ranges and on some instances the values match fairly well, it is clear that PIV results have significantly lower temporal resolution than LDV results. More specifically, PIV did not adequately capture the double-peak velocity pattern present in the LDV measurements, and on several instances read velocities with magnitudes much lower than the LDV values. The correction of the LDV signals at peak values would increase the difference between LDV and PIV results for Point 1 at $t/T = 5/13$, and $t/T = 6/13$, and for Point 2 at $t/T = 11/13$.

Some of these discrepancies may be due to the fact that the number of samples used for phase averaging of the PIV results was much lower than that for the LDV results. The PIV system took a single sample at a given time after the start of a cycle and the number of PIV samples used for phase averaging was 50. The LDV system collected data for 100 cycles at a relatively high sampling rate, typically recording 520 valid measurements per cycle. When the phase average was calculated, each individual cycle was divided into 100 bins of equal durations, such that each bin contained on the average 5 samples from each cycle. Therefore, the LDV phase-averages were taken over typically 520 samples, which is an order of magnitude larger than the PIV sample population. Another relevant point is that for the LDV measurements each individual cycle was divided into the same number of bins, so that, irrespectively of the cycle period T, the realative phase t/T was the same for all cycles. In contrast, for the PIV measurements, phases were selected by setting the triggering time to a fixed value. Therefore, although the phase t was the same for all cycles, t/T could vary somewhat, because the period T varied by a small amount from one cycle to the next. Because the use of a speed control reduced variations in the motor speed to a negligible level, such differences in cycle period may likely be attributed to the electromechanical relay system used for triggering the cycles. As an example, consider a cycle whose period deviates from the average by 2 standard deviations, i.e., 0.04 seconds. During that time, at $t/T = 0.55$, at Point 2, when strong acceleration is indicated by the LDV signal, the local velocity magnitude would change by 0.44 m/s or 200%. The PIV cycle-to-cycle variations as depicted by the sample cycles in Figure 7.9 show variations of velocity of 0.3 m/s during systole, suggesting that a larger sample population of PIV maps would produce a time averaged profile more comparable to that of the LDV phase average.

Additional comparisons can be made from Figures 7.6-7.9, which display PIV velocity profiles along inlet and outlet tube diameters that pass through Point 1 and Point 2, respectively, during peak flow times as well as the corresponding LDV phase-averaged values. Both phase-averaged and a few instantaneous PIV profiles are shown in these figures. Cycle-tocycle variations in the PIV measurements are significant, but not sufficient to explain all differences between the LDV and PIV results.

The previously given explanations for the differences between the measured LDV and PIV results suggest that caution is required concerning the validity of at least some among the PIV measurements. It is important to note that the regions of greatest divergence between LDV and PIV measurements occur in the inlet and outlet tubes at high velocity, but that in regions of low velocity the PIV results can be taken as valid as evidenced by their closer agreement with corresponding LDV results. In conclusion, the PIV measurements in the main VAD and away from the inlet and outlet tubes can be taken as valid quantitatively, but in high velocity regions where the velocity is known to exceed 0.6 m/s, PIV velocity maps should only be considered for qualitative purposes. The representative cycles, particularly those for the $\Delta t = 0.25$ ms case, can be accepted as they show better agreement with the LDV phase averages.

.

.

.

.

.

7.4 Diaphragm Motion

A crude estimate of the VAD diaphragm shape during the cycle can be based on the assumption that it is an initially plane circular elastic membrane deforming axisymmetrically under uniform pressure difference across its two sides (Christensen and Feng (1986)). Then, the displacement of the diaphragm can be computed from the driving fluid volume displacement that was estimated in the previous chapter by consideration of the piston motion. Further assuming that the diaphragm material is a neo-Hookean solid and that diaphragm deformation is small by comparison to its radius R in the undeformed state,

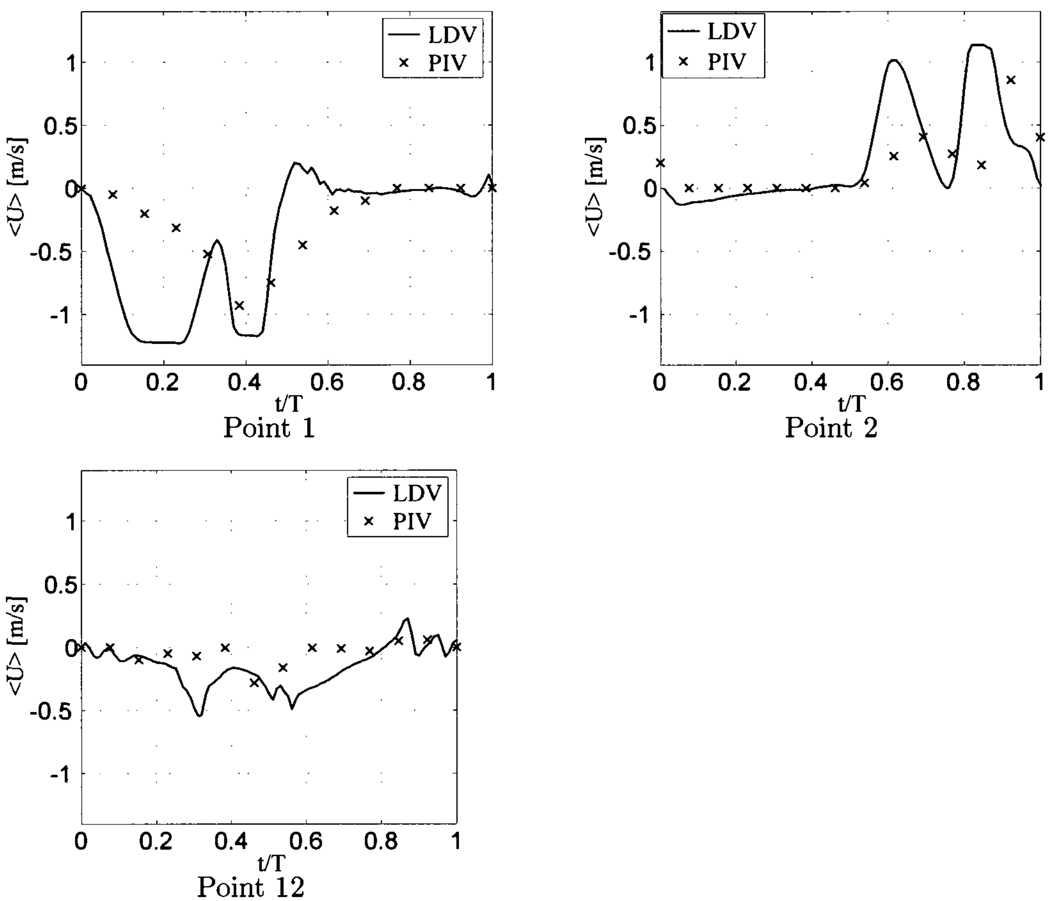

Figure 7.5: Comparison of LDV and PIV averaged velocities

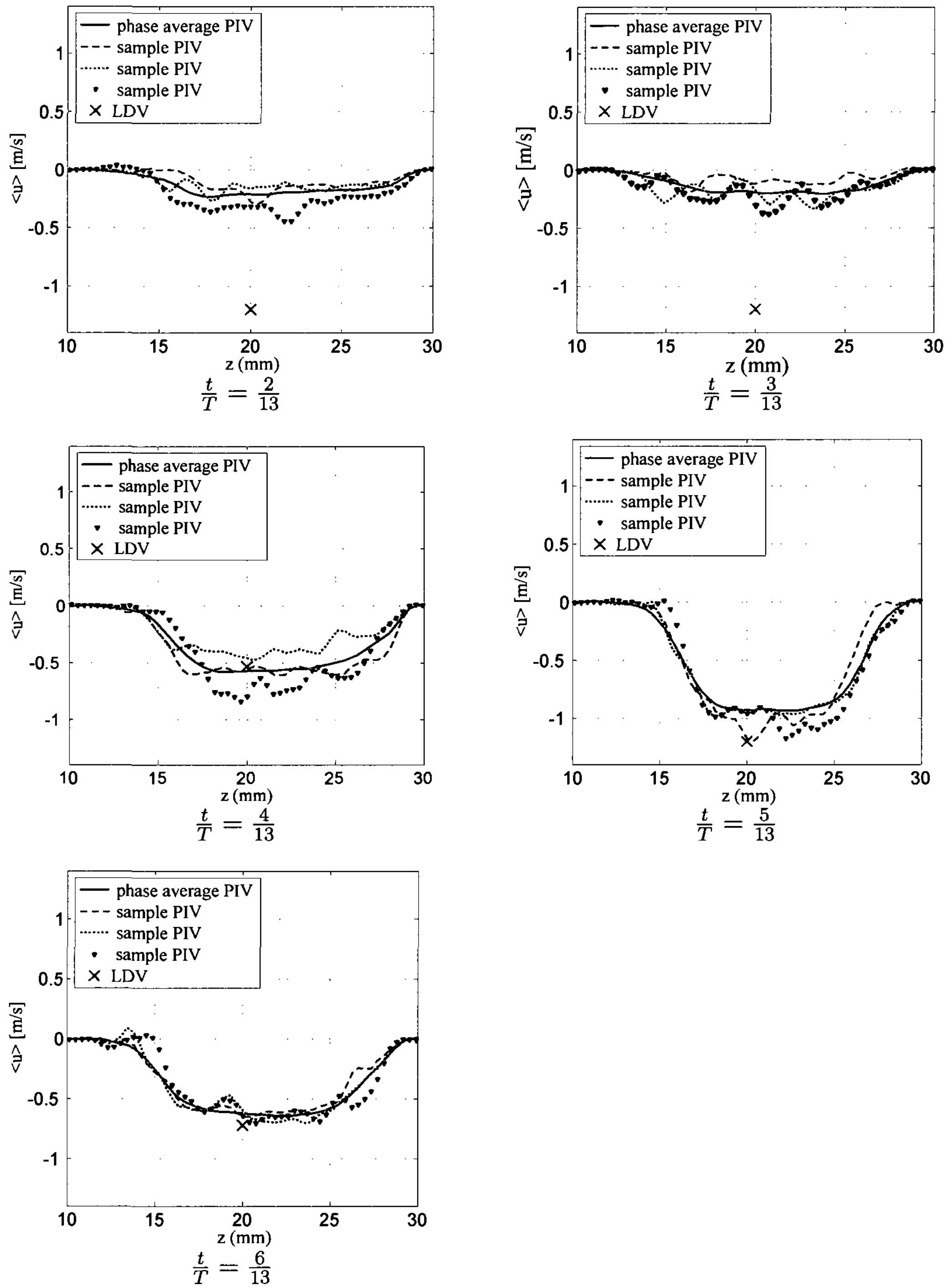

Figure 7.6: XZ PIV velocity profiles at Point 1

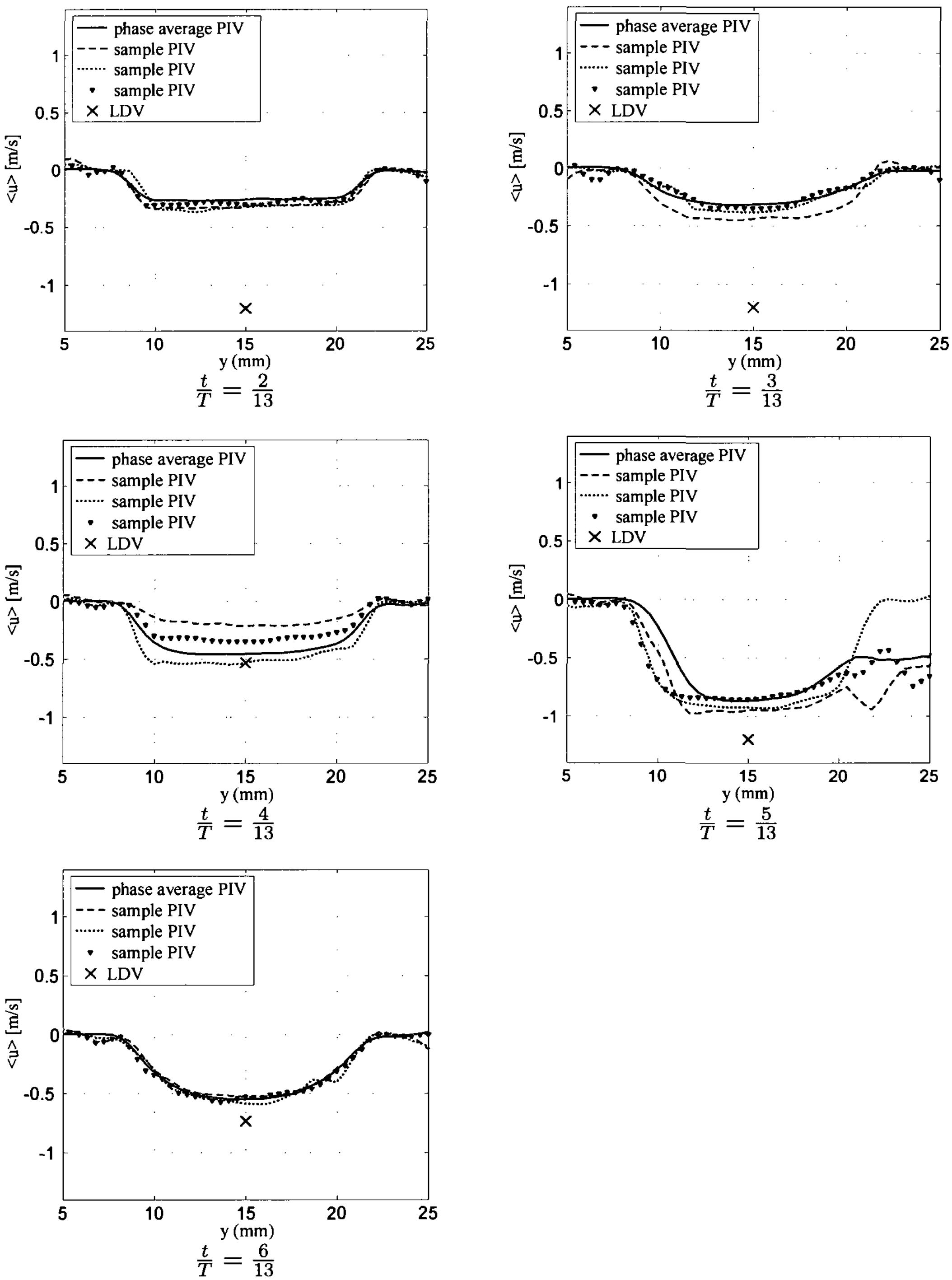

Figure 7.7: XY PIV velocity profiles at Point 1

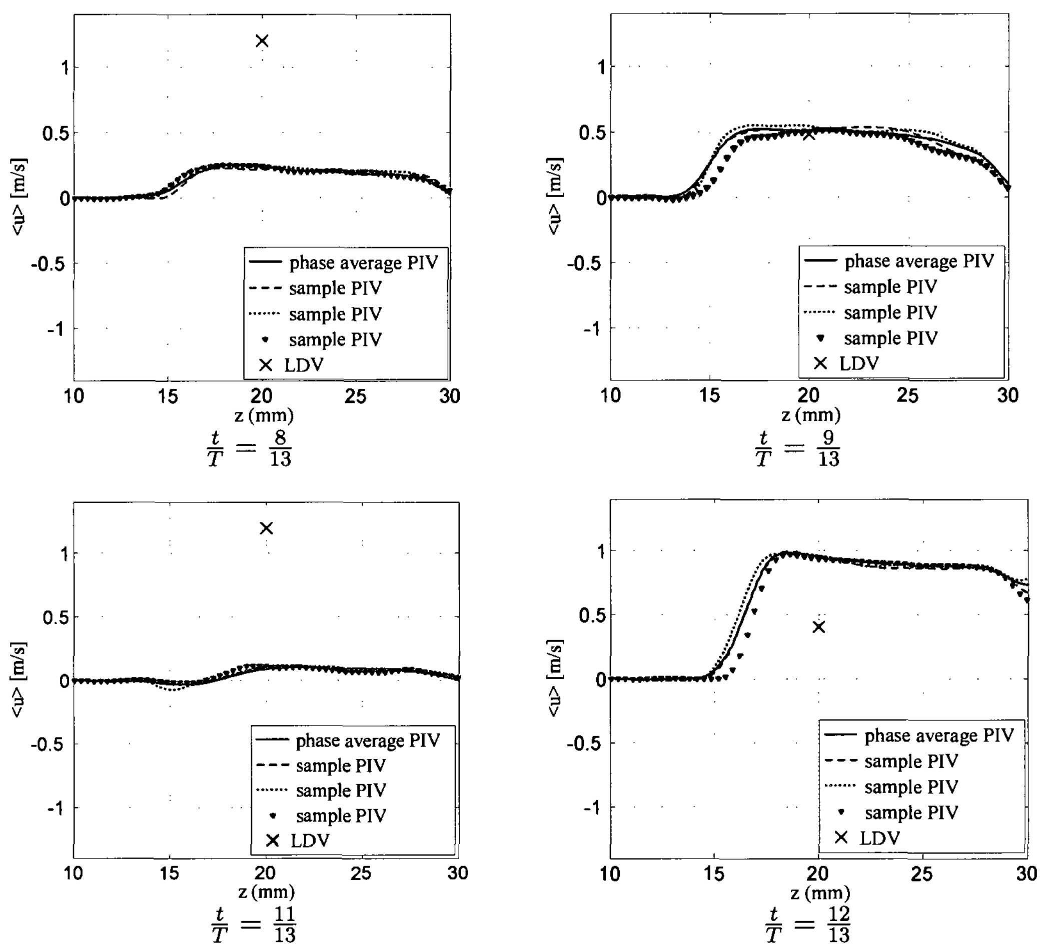

Figure 7.8: XZ PIV velocity profiles at Point 2

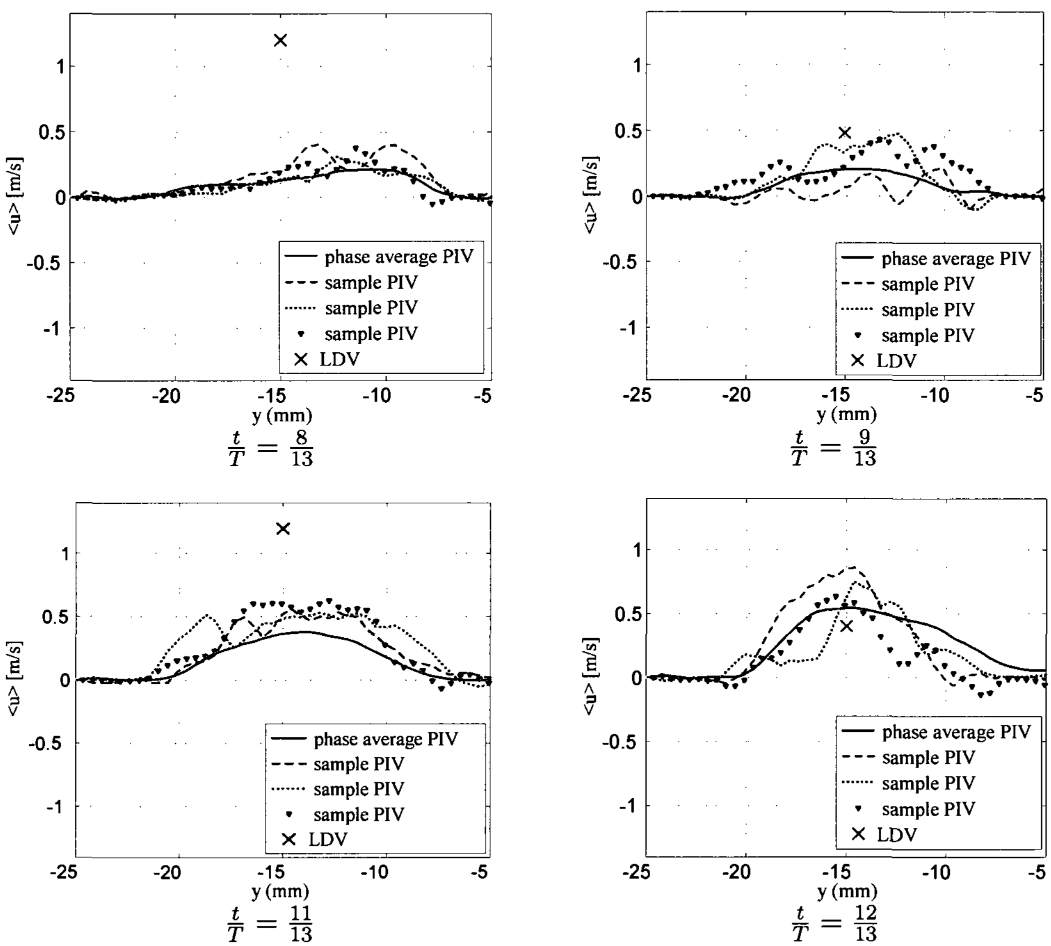

Figure 7.9: XY PIV velocity profiles at Point 2

one can relate the pressure difference ΔP across the diaphragm, its thickness H, and its maximum displacement Δ in its centre as

$$\Delta P = 32\frac{C_1 H \Delta^3}{R^4} \tag{7.5}$$

where C_1 is a material constant (Christensen and Feng (1986)). In this experimental set-up, the material was natural latex rubber with a radius of 35 mm, a thickness of 0.18 mm, maximum displacement in the range from -13mm to 14 mm, and an approximate $C_1 = 141.5$ kPa (Verron et al. (2001)), from which the pressure difference can be determined. However, the results presented in this study clearly proved that the VAD diaphragm deformation was non-axisymmetric and that its shape changed dramatically during the cycle. Although no velocity or pressure measurements were made in the driving fluid, because both the driving and the working fluids are essentially incompressible, one may estimate the flow rate variation into and out of the lower VAD chamber from the motion of the piston, with corrections applied to it based on the LDV measurements in the inlet and outlet tubes of the upper VAD chamber. This flow rate variation can then be specified as a time-dependent boundary condition at the inlet/oulet to the lower chamber for a numerical simulation of flow in the entire VAD with fluid-structure interaction that includes the VAD diaphragm deformation. Then, the skewness in the diaphragm shape can be possibly explained by the action of the high-speed jets forming during filling of the lower and upper chambers.

This three-dimensional behavior non-withstanding, the diaphragm behaviour described in the previous chapter is compatible with the findings of Hochareon *et al.* (Hochareon et al. (2003)). These authors observed that the region of the diaphragm closest to the inlet and outlet tubes experienced a more rapid inflation and slower deflation than the region opposite the tubes, and these patterns were also found in the PIV images taken in the current study. Hochareon *et al.* also noted that the diaphragm motion was insensitive to inflow conditions and showed good general agreement with the behaviour of a sac-type VAD *in vivo*. They measured the diaphragm position at only three point on the central plane, near each of the two ends and in the middle. As with the unglued diaphragm case in the study by Hochareon *et al.*, small scale motions were observed in the diaphragm that suggest the same inefficiency in the flow (Hochareon et al. (2003)), with the diaphram towards the outlet tube during systole. Hochareon *et al.* concluded that the diaphragm motion has a strong influence on the dynamics of the flowfield, particularly during diastole (Hochareon et al. (2003)). Other studies by previous authors have noted the late appearance of a vortex at the inlet during diastole, and suggest that this prevents hemolysis (Jin and Clark (1993), Oley et al. (2005)). The results from the experiments by Hochareon *et al.* suggest that the late deflation of the diaphragm in the positive x-direction may be the cause of the late vortex formation and thus, serves as a mechanism to prevent hemolysis (Hochareon et al. (2003)).

7.5 Dimensionless Groups

Several dimensionless groups have been considered for the evaluation of pulsatile flow device performance, as summarized by Deutsch (Deutsch et al. (2006)). To determine these dimensionless groups, one needs to define appropriate length, time, and velocity scales. For the present VAD experiments, a suitable time scale is obviously the cycle period T.

Among the different possible length scales, we will choose the inlet and outlet tube diameter d. Finally, the average bulk velocity U_b, defined as

$$U_b = \frac{8\overline{Q}}{\pi d^2} = \frac{8\ SV}{\pi d^2 T} \tag{7.6}$$

will be selected as the velocity scale (Bachmann et al. (2000)). For the present experiments, $U_b = 0.338\ \mathrm{ms}^{-1}$.

Then, one can define the mean Reynolds number for the pulsatile flowfield over the entire operational cycle as (Bachmann et al. (2000))

$$\mathrm{Re}_b = \frac{\rho U_b d}{\mu} \tag{7.7}$$

the Strouhal number as

$$\mathrm{St} = \frac{4}{\pi}\frac{SV}{d^3} \tag{7.8}$$

and the Womersley number as

$$\mathrm{Wm} = \frac{d}{2}\left(\frac{2\pi\rho}{\mu T}\right)^{\frac{1}{2}} \tag{7.9}$$

By comparing the previous definitions, one can find that the three dimensionless groups are not independent, but related as

$$\mathrm{Wm} = \frac{1}{2}\left(\frac{\pi\,\mathrm{Re}}{St}\right)^{\frac{1}{2}} \tag{7.10}$$

For the current VAD experiments, the values of these three groups were $\mathrm{Re}_b =$ 1950, St = 11.6 and Wm = 11.5. If, instead of the tube diameter, the VAD diaphragm diameter were used as a length scale, the corresponding values would be $\mathrm{Re}_b = 530$, St = 0.23 and Wm = 42.3, with an average bulk velocity of $U_b = 0.025\ \mathrm{ms}^{-1}$.

An additional group of interest is the maximum Reynolds value in either the inlet or outlet tubes, defined as

$$\mathrm{Re}_{\max} = \frac{\rho\,|u_{\max}|\,d}{\mu} \tag{7.11}$$

where $|u_{max}|$ is the magnitude of the maximum velocity in the x-direction (which, for the inlet and outlet tubes, can be considered to be the only velocity component at peak injection or ejection). The maximum Reynolds number in the inlet was calculated to be $\mathrm{Re}_{\max(\mathrm{inlet})} = 6400$ while at the outlet, $\mathrm{Re}_{\max(\mathrm{outlet})} = 5500$. A previous study (Konig et al. (1999)) suggested that the critical Reynolds number Re_c for transition to turbulence in a pulsatile flow was a function of the Womersley number as

$$\mathrm{Re}_c = c\mathrm{Wm} \tag{7.12}$$

where $250 < c < 1000$. For the current conditions, this gives the range $2875 < \mathrm{Re}_c < 11500$. Because in the present experiments $\mathrm{Re}_{\max}$ is within the Re_c range and Re_b is not, one cannot assess the applicability of Equation 7.12 with any confidence for the entire cycle. However, considering that the present flow had time intervals with strong deceleration, one may plausibly infer that the flow would be turbulent at least in some parts of the VAD volume and at least during some parts of the cycle. This conclusion is supported by the LDV and PIV measurements.

To allow comparison of the present VAD model performance with comparable studies in the literature, we present in Table 7.1 values of the important dimensionless groups (Bachmann et al. (2000), Deutsch et al. (2006)). This table indicates that the values of Re_b, Wm, St and Re_{cr} for the present experiments are within the corresponding ranges of previously studied devices. Overall comparison of the dimensionless parameters of the present experimental apparatus show general agreement with the Penn State devices that are most commonly used in studying pulsatile VAD flow. The relatively high value of the Womersley number suggests that the unsteady characteristics of the flow are dominant. The fact that the present Strouhal number is also relatively high indicates that strong acceleration and deceleration would be present during the cycle, which is expected to promote fluid washout from the VAD (Konstantinidis et al. (2004)). The Re_c values are useful for determining whether a flow is in transition to turbulence, which is important for accurate CFD modelling of the flow (Apel et al. (2001)). The Re_c values in Table 7.1 show that most of the devices listed have average Reynolds values well below their critical values, although transition in blood flows have been observed for Reynolds values $\mathrm{Re}_{\mathbf{max}} = 750$ in some pulsatile devices (Konig et al. (1999)) or lower in some simulations (Apel et al. (2001)). Transitional flow is known to occur in the aorta during systole due to the high velocities, but most current CFD models assume a laminar flow, which suggest that these models require the incorporation of some transition model (Conlon (2006)). The uncertainty in the Re_c values would seem to support the recommendation by Avrahami *et al* that future numerical models of pulsatile VAD should use low Reynolds number transitional turbulence models (Avrahami et al. (2006)). Further experimental and numerical simulations to more adequately define the relationship between the Womersley number and transition to turbulence in a pulsatile flow should be explored, especially the link between the Womersley number and the wall function for boundary layer modelling (Apel et al. (2001)).

Table 7.1: Comparison of Dimensionless Units

Pump model and size	Re_b	Wm	St	Re_c
Penn State 70-cc device	2482	15.3	8.3	3831 – 15300
Penn State 50-cc device	1054	13.6	4.5	3390 – 13600
Penn State 15-cc device	1567	5.2	45.3	1303 – 5200
Yonsei 34-cc device	1500	12.4	7.7	3092 – 12400
Toyobo 20-cc device	988	11.1	6.3	2774 – 11100
MEDHOS-HIA 10-cc device	655	8.3	7.4	2084 – 8300
Berlin heart 12-cc device	785	8.4	8.8	2092 – 8400
Present VAD model	1950	11.5	11.6	2875 – 11500

7.6 Comparisons with Other VAD Studies

Although the present experimental model was in no way meant to represent any actual VAD, it would be instructive to compare the general characteristics of the velocity field in this study to previous experimental results for pulsatile VAD (Avrahami et al. (2006), Avrahami et al. (2006), Doyle et al. (2008), Hochareon et al. (2003), Hochareon et al. (2004b), Hochareon et al. (2004c), Hochareon et al. (2004a), Jin and Clark (1993), Konig et al. (1999), Konig and Clark (2001), Mussivand et al. (1999), Oley et al. (2005), Yu et al. (2001)). In comparison to a recent study by Kreider *et al*, the present results showed greatest agreement with those measurements in which the bileaflet valves had an orientation of 0°, which is considered less efficient than the optimal 45° orientation (Kreider et al. (2006)). In the present study, a single jet appeared in the inlet during diastole, but in studies with bileaflet valves multiple jets were present (Avrahami et al. (2006), Kreider et al. (2006)). The inlet and outlet tubes in the present setup have no corresponding parts in implantable devices (Day and McDaniel (2005a)). In the present setup the inlet tube directs the flow during diastole in a direction parallel to the axis of symmetry but at a distance from it, which facilitates the formation of a vortex and affects the mixing process

(Avrahami et al. (2006), Avrahami et al. (2006), Hochareon et al. (2004b), Kreider et al. (2006)). Another feature in previous VAD studies by Avrahami *et al.* was the use of S-shaped tubes for the inlet and outlet, but this was considered not to have any significant effect on the flow (Avrahami et al. (2006), Avrahami et al. (2006)).

The characteristics of the flowfield during diastole were consistent with previous results, which indicated that a single jet formed and was not influenced by vortices or any other flow patterns already present within the VAD until near the end of diastole. Furthermore, the peak diastolic velocity was consistent with previous simulations and experimental results (Doyle et al. (2008), Hochareon et al. (2004b)). The flow profile during systole was consistent with the measurements obtained in a previous study; the flow was localized in the region of the outlet tube, and the peak systolic flow velocity was also similar to previous results (Hochareon et al. (2004b)). The stagnant flowfield prior to the onset of diastole in these results was a marked contrast to the results of Jin and Clark which showed that residual flow patterns from previous cycles had a significant effect on the flowfield (Jin and Clark (1993)).

This study observed a vortex core in the $x - y$ midplane that previous studies suggested to be the primary mechanism of mixing in the VAD (Avrahami et al. (2006), Avrahami et al. (2006), Doyle et al. (2008), Hochareon et al. (2003), Hochareon et al. (2004b), Hochareon et al. (2004c), Hochareon et al. (2004a), Jin and Clark (1993), Konig et al. (1999), Konig and Clark (2001), Mussivand et al. (1999), Oley et al. (2005), Yu et al. (2001)). This vortex core was consistently observed during both individual cycles of VAD operation and in the phase-averaged PIV images. The $x - y$ vortex core is produced by the inlet jet as it issues from the inlet tube and recirculates the flow in the VAD (Oley et al. (2005)). This vortex core helps explain the lower average flow velocity during systole when compared to diastole that was observed in previous studies (Konig and Clark (2001), Yu et al. (2001)), and contributes to the low-flow regions observed furthest from the inlet and outlet tubes as it is the area where the vortex is the most active during the mixing phase of late diastole and early systole (Mussivand et al. (1999)). Whereas Hochareon *et al.* observed that peak inlet flow occurred in early diastole (Hochareon et al. (2004b), Hochareon et al. (2004a)), in the present study found the inlet jet occurred in late diastole, in agreement with other studies that suggest that the vortex formation in late diastole reduces hemolysis during the operational cycle (Jin and Clark (1993), Oley et al. (2005)). The presently observed vortex core did not have a noticeable influence on the flow characteristics of the inlet jet as in the simulations by Doyle *et al.*, but the size, position, and motion of the vortex core were in very good agreement with these numerical results (Doyle et al. (2008)). The motion of the vortex core away from the centre of the $x - y$ plane towards the wall opposite the inlet and outlet tubes during diastole was not evident in previous PIV measurements (Hochareon et al. (2004b)), but this may be because results for only few time steps were shown in that study; in any case, the positions of the vortex cores at the end of systole for both experiments were approximately the same. The recirculation zone observed presently near the VAD wall opposite to the outlet tube during systole was consistent with results observed in a previous study of the 50 cc Penn State Artificial Heart (Hochareon et al. (2004a)).

Additionally, the current study shows a vortex in the $x - z$ plane during diastole directly underneath the inlet jet. This vortex was clearly shown moving along the path of the inlet jet during diastole, suggesting that it is a mechanism for mixing injected fluid with the existing volume. This vortex was also observed extending along the y-axis while maintaining a position near the wall of the VAD furthest from the openings for the inlet and outlet tubes. This vortex was a consistent phenomenon in the flow, and when combined with the core vortex in the $x - y$ plane, provides a three-dimensional mechanism for mixing and washout throughout the VAD. The vortex at injection is similar to a vortex observed by Konig *et al.* that was believed to be induced by flow separation of the inlet jet over the solid hemispherical piston used as an idealization of a moving diaphragm (Konig et al. (1999)). As the experiment in this study used a free flexible diaphragm instead of a solid hemispherical piston, it is likely that the vortex observed in these measurements is the result of flow separation of the inlet jet over the moving diaphragm during diastole. This would also explain why the vortex dissipates shortly after the onset of systole. A smaller vortex located near the VAD wall opposite to the outlet tube during systole indicates a region of recirculation, which may be correlated with the thrombus formation noted in a previous study in the same region *in vivo* (Hochareon et al. (2004a)). Such comparisons should be made with strong reservations because of the differences in geometry and operating conditions.

The present vorticity measurements are in general agreement with the results of Hochareon *et al*, if one takes into account differences in the geometry of the experimental apparatus (Hochareon et al. (2004b)). The ranges of vorticity values are comparable in both studies. Hochareon *et al.* used the vorticity maps to identify boundary layers along the walls of the VAD (Hochareon et al. (2004b)); they found high values of vorticity along the wall of the inlet tube during diastole,which followed the path of the inlet jet as it issued into the VAD and grew smaller during early systole. This is also in agreement with the observation of Avrahami *et al.* that vortices are generated during systole by the rolling up of the shear layers of the inlet jet (Avrahami et al. (2006)). Matched pairs of high vorticity magnitude regions were observed in both the $x - y$ and $x - z$ planes, confirming that the vortex structures in pulsatile VAD flow are fully three-dimensional (Verdonck (2002)).

Hochareon *et al* estimated that shear stresses were generally in the range $1.8 - 53$ dynes/cm^2, with much higher ranges measured near the valves (Hochareon et al. (2004c)). The shear stress range for the current measurements, estimated from strain rate measurements, was $0.76 - 7.6$ dynes/cm^2. The lower values of measured shear stress are due to the PIV measurement errors, which prevented us from accurately measuring high values of velocity in some parts of the flow. In addition to this bias, the lower values may also be attributed to the lower frequency of pulsation in the present experiments. Avrahami *et al* observed similar patterns in their simulation of a pulsatile VAD operation, with two layers of high shear stress entering the VAD during diastole and two layers in the outlet tube during systole. The same general regions of low shear stress were also observed along the present VAD wall adjacent to both inlet and outlet tubes, as well as the VAD wall directly opposite to the inlet and outlet tube openings (Avrahami et al. (2006)). Hochareon *et al* also observed that, in addition to high shear rates and exposure times, which could result in hemolysis, a change of sign occurred in the wall shear at the inlet during peak injection into the VAD, which is evidence of local flow separation (Hochareon et al. (2004b)). Despite the differences in geometry, the shear stress patterns observed in this study are in good general agreement with the previous work by Hochareon *et al* (Hochareon et al. (2004b)). High shear values were observed during diastole in the inlet region, particularly along the VAD wall directly adjacent to the inlet opening, although a region of rapidly changing shear was also present in these regions, suggesting a possible separation of the flow. Regions of low shear appeared starting at late diastole on the VAD wall adjacent to both the inlet and outlet openings, as well as the VAD wall directly opposite to the inlet and outlet openings. Low shear stress has in the past been correlated with thrombosis. A final note is that exposure times to high and low stresses in the present VAD were in the range from 300 to 500 ms, which is deemed to be sufficiently long for the blood to be affected.

Chapter 8

Conclusions and Recommendations for Future Work

8.1 Conclusions

The objective of this study was to document the velocity field variation of a highly idealized diaphragm-type, pulsatile-flow VAD throughout its operational cycle. The measurements obtained from PIV and LDV measurement systems showed good general agreement with previous studies, and identified several characteristic features of the flow. Representative and phase-averaged PIV images showed the inlet jet creating the core vortex in the x-y plane that is the primary means of mixing the injected fluid with the existing volume, as confirmed by vorticity maps. The development and motion of this vortex over the VAD operational cycle were documented for use in future numerical simulations. A previously unobserved vortex was also documented. This vortex appeared in the x-z plane, beneath the inlet jet at peak injection, and moved along the path of the jet during the injection phase of operation. It is believed that this vortex is created by the interaction of the inlet jet and the diaphragm in motion during injection and represents a region of recirculation in the flow, as well as possible flow separation. Other regions of recirculation were identified in the area directly adjacent to the outlet jet during ejection of the flow, and along the inner wall of the VAD directly opposite of the outlet tube just prior to the beginning of the ejection cycle. Areas of stagnant flow were observed, particularly in the inlet and outlet tubes in periods of inactivity. The flow during ejection was localized in the region of the VAD directly adjacent to the outlet tube. Ejection has a longer period and lower peak velocity than the injection, allowing for conservation of mass for the overall operational cycle. Interference from the core vortex may also contribute to the lower outlet velocity.

The motion of the VAD diaphragm was also studied and it was found that the diaphragm deformation was influenced by the inlet jet. The diaphragm shape was nearly axisymmetric during some parts of the cycle, but highly skewed during other parts. Small-scale motions were also present in the diaphragm, and fluctuated from one cycle to another, adding to irregularities in the flow. Dimensional analysis of the flow strongly suggested that the unsteady nature of the flow was the dominant feature of the flowfield.

8.2 Recommendations for Future Work

The objective of this study was to document the fluid flow in a highly-idealized pulsatile VAD, so that its results can be used for the validation of numerical simulations of

VAD with fluid-structure interactions. Several improvements and extensions are possible to these experiments. The addition of mechanical heart valves and a mock circulatory loop will add realism to the set-up. The mechanical heart valves selected should accurately model the performance of similar valves used in clinical VAD models. A mock circulatory loop should be designed to model the compliance and resistance of the human circulatory system, and should be easily adjustable to model both healthy and damaged circulatory systems. The ability to adjust the pumping rate of the apparatus, with settings that would approximate both design and off-design conditions, would also be highly desirable.

In retrospect, some of the settings used for the LDV and PIV measurements turned out to be incorrect and resulted in errors that could have been prevented, at least in part, by more careful planning. Because there are large spatial and temporal variations of velocity within the VAD, a single set of settings may be inappropriate for the entire study. A more successful approach would be to have a number of alternative settings (such as the LDV velocity range and the interframe time rate for PIV) and select the optimal one for LDV and PIV measurements in different parts of the VAD and during different parts of the cycle. Then, all these results should be synthesized to give a reliable sets of measurements for the entire process.

References

Apel, J., F. Neudel, and H. Reul (2001). Computational fluid dynamics and experimental validation of a microaxial blood pump. *ASAIO Journal 47*, 552–558.

Apel, J., R. Paul, S. Klaus, T. Siess, and H. Reul (2001). Assessment of hemolysis related quantities in a microaxial blood pump by computational fluid dynamics. *Artificial Organs 25*, 341–347.

Avrahami, I., M. Rosenfeld, and S. Einav (2006). The hemodynamics of the berlin pulsatile vad and the role of its mhv configuration. *Annals of Biomedical Engineering 24*, 1373–1388.

Avrahami, I., M. Rosenfeld, S. Raz, and S. Einav (2006). Numerical model of flow in a sac-type ventricular assist device. *Artificial Organs 30*, 529–538.

Bachmann, C., G. Hugo, G. Rosenberg, S. Deutsch, A. Fontaine, and J. M. Tarbell (2000). Fluid dynamics of a pediatric ventricular assist device. *Artificial Organs 24*, 362–372.

Baldwin, J., J. Tarbell, S. Deutsch, D. Geselowitz, and G. Rosenberg (1988). Hot-film wall shear probe measurements inside a ventricular assist device. *Transactions of the*

ASME 110, 326–333.

Burgreen, G. W., J. F. Antaki, Z. J. Wu, and A. J. Holmes (2001). Computational fluid dynamics as a development tool for rotary blood pumps. *Artificial Organs 25*, 336–340.

Christensen, R. and W. Feng (1986). Nonlinear analysis of the inflation of an initially flat, circular, elastic disk. *Journal of Rheology 30*, 157–165.

Conlon, M. (2006). *Potential Nonlinear Behaviour with VAD Use in Humans*. Ph. D. thesis, Carleton University.

Day, S. W. and J. C. McDaniel (2005a). Piv measurements of flow in a centrifugal blood pump: Steady flow. *Journal of Biomechanical Engineering 127*, 244–253.

Day, S. W. and J. C. McDaniel (2005b). Piv measurements of flow in a centrifugal blood pump: Time-varying flow. *Journal of Biomechanical Engineering 127*, 254–263.

Day, S. W., J. C. McDaniel, H. G. Wood, P. E. Allaire, X. Song, P. P. Lemire, and S. D. Miles (2002). A prototype heartquest ventricular assist device for particle image velocimetry measurements. *Artificial Organs 26*, 1002–1005.

Deutsch, S., J. M. Tarbell, K. B. Manning, G. Rosenberg, and A. A. Fontaine (2006). Experimental fluid mechanics of pulsatile artificial blood pumps. *Annual Review of Fluid Mechanics 38*, 65–86.

Doyle, M., J. Vergniaud, S. Tavoularis, and Y. Bourgault (2008). Numerical simulations of blood flow in artificial and natural hearts with fluidŰstructure interaction. *Artificial Organs 32*, 870–879.

Doyle, M. G. (2004). Simulation of blood flow in a ventricular assist device with fluid-structure interaction effects. Master's thesis, University of Ottawa.

Dynamics, D. (2008). *BSA Flow Software v4.10 Installation and User's Guide.*

GmbH, L. (2007). *Product Manual for Flowmaster Getting Started.*

Gray, N. and C. Selzman (2006). Current status of the total artificial heart. *American Heart Journal 152*, 4–10.

Haddad, M., P. Hendry, R. Masters, T. Mesana, H. Haddad, R. Davies, T. Mussivand, C. Struthers, and W. Keon (2004). Ventricular assist devices as a bridge to cardiac transplantation: The ottawa experience. *Artificial Organs 28*, 136–141.

Hochareon, P., K. B. Manning, A. A. Fontaine, S. Deutsch, and J. M. Tarbell (2003). Diaphragm motion affects flow patterns in an artificial heart. *Artificial Organs 27*, 1102–1109.

Hochareon, P., K. B. Manning, A. A. Fontaine, J. M. Tarbell, and S. Deutsch (2004a). Correlation of in vivo clot deposition with the flow characteristics in the 50 cc penn state artificial heart: A preliminary study. *ASAIO Journal 50*, 537–542.

Hochareon, P., K. B. Manning, A. A. Fontaine, J. M. Tarbell, and S. Deutsch (2004b). Fluid dynamic analysis of the 50 cc penn state artificial heart under physiological operating conditions using particle image velocimetry. *Journal of Biomechanical Engineering 126*, 585–593.

Hochareon, P., K. B. Manning, A. A. Fontaine, J. M. Tarbell, and S. Deutsch (2004c). Wall shear-rate estimation within the 50cc penn state artificial heart using particle image velocimetry. *Journal of Biomechanical Engineering 126*, 430–437.

Jin, W. and C. Clark (1993). Experimental investigation of unsteady flow behaviour within a sac-type ventricular assist device (vad). *Journal of Biomechanics 26*, 697–707.

Kim, S., K. Chandran, and C. Chen (1992). Numerical simulation of steady flow in a two-dimensional heart model. *Journal of Biomechanical Engineering Journal of Biomechanical Engineering 114*, 492–503.

Kleinstreuer, C. (2006). *Biofluid Dynamics: Principles and Selected Applications*, Chapter 1, pp. 1–160. CRC Press.

Konig, C. S. and C. Clark (2001). Flow mixing and fluid residence times in a model of a ventricular assist device. *Medical Engineering & Physics 23*, 99–110.

Konig, C. S., C. Clark, and M. R. Mokhtarzadeh-Dehghan (1999). Investigation of unsteady flow in a model of a ventricular assist device by numerical modelling and comparison with experiment. *Medical Engineering & Physics 21*, 53–64.

Konstantinidis, E., S. Balabani, and M. Yianneskis (2004). Phase-average mean flow and turbulence structure in a staggered cylinder array subjected to pulsating cross-flow. *Journal of Fluids Engineering 126*, 323–336.

Kreider, J. W., K. B. Manning, L. A. Oley, A. A. Fontaine, and S. Deutsch (2006). The 50cc penn state left ventricular assist device: A parametric study of valve orientation flow dynamics. *ASAIO Journal 52*, 123–131.

Mann, K., S. Deutsch, J. Tarbell, D. Geselowitz, G. Rosenberg, and W. S. Pierce (1987).

An experimental study of newtonian and non-newtonian flow dynamics in a ventricular assist device. *Journal of Biomechanical Engineering 109*, 139–147.

Medvitz, R., J. Kreider, K. Manning, A. Fontaine, S. Deutsch, and E. Paterson (2007). Development and validation of a computational fluid dynamics methodology for simulation of pulsatile left ventricular assist devices. *ASAIO Journal 53*, 122–131.

Moosavi, M., N. Fatouraee, and H. Katoozian (2008). Finite element analysis of blood flow characteristics in a ventricular assist device (vad). *Simulation Modelling Practice and Theory*.

Mussivand, T., K. Day, and B. Naber (1999). Fluid dynamic optimization of a ventricular assist device using particle image velocimetry. *ASAIO Journal 45*, 25–31.

Mussivand, T., R. Navarro, J. Chen, J. Braun, H. Harasaki, R. Kiraly, C. Batur, C. McMillin, and Y. Nose (1988). Flow visualization in an artificial heart using diffuse and planar laser lighting. *ASAIO Transactions 34(3)*, 317–321.

Oley, L. A., K. B. Manning, A. A. Fontaine, and S. Deutsch (2005). Off-design considerations of the 50cc penn state ventricular assist device. *Artificial Organs 29*, 378–386.

Qian, K., Z. Feng, W. Ru, P. Zeng, and H. Yuan (2007). Piv pictures of stream field predict haemolysis index of centrifugal pump with streamlined impeller. *Journal of Medical Engineering & Technology 31*, 239–242.

Ramasamy, M. and J. Leishman (2007). Benchmarking particle image velocimetry with laser doppler velocimetry for rotor wake measurements. *AIAA Journal 45*, 2622–2633.

Tavoularis, S. (2005). *Measurements in Fluid Mechanics*, Chapter 11, pp. 249–289. Cambridge University Press, Cambridge, UK.

Vandenberghe, S., P. Segers, P. Steendijk, B. Meyns, R. Dion, J. Antaki, and P. Verdonck (2006). Modeling ventricular function during cardiac assist: Does time-varying elastance work? *ASAIO Journal 52*, 4–8.

Verdonck, P. (2002). The role of computational fluid dynamics for artificial organ design. *Artificial Organs 26*, 569–570.

Vergniaud, J. (2001). Experimental study of flow in a ventricular assist device model for cfd validation. Technical report, University of Ottawa.

Verron, E., G. Marckmann, and B. Peseux (2001). Dynamic infl ation of non-linear elastic and viscoelastic rubber-like membranes. *International Journal for Numerical Methods in Engineering 50*, 1233–1251.

Yu, Y.-C., J. R. Boston, M. A. Simaan, P. J. Miller, and J. F. Antaki (2001). Pressure-volume relationship of a pulsatile blood pump for ventricular assist device development. *ASAIO Journal 47*, 293–301.

Appendix A

MATLAB Code

A.1 LDV Phase Averaging

function[V]=phaseave(W,binnumber)

%W is input array of format [AT TT LDA1 LDA2], binnumbers is the number of bins in phase averaging

%V is array organized [t/T MeanU MeanV varianceU varianceV covarianceUV numpoints]

% the numpoints is an indicator of the number of data points that fell

% in each bin.

%Sets first AT as t=0

W(:,1)=W(:,1)-W(1,1);

totalcount=length(W(:,1)); %the total number of time points in a given datafile

cyclelength=zeros(1,101); %amount of time in each cycle

```
cyclestarttime=zeros(1,101); %start time of each cycle

cyclemeasurements=zeros(1,101); %number of measurements in each cycle

cyclestartnumber=zeros(1,101); %Number for each cyclestart

cycleendnumber=zeros(1,101) ;%number for each cycle end

%local average velocity matrices

localaverageU=zeros(101,binnumber);

localaveragev=zeros(101,binnumber);

% counter variables

bincount=zeros(101,binnumber);

%variables for finding phase average

localtotalU=zeros(101,binnumber);

localtotalV=zeros(101,binnumber);

phasetotalU=zeros(1,binnumber);

phasetotalV=zeros(1,binnumber);

phaseaverageU=zeros(1,binnumber);

phaseaverageV=zeros(1,binnumber);

phasedevU=zeros(1,binnumber);

phasedevV=zeros(1,binnumber);

cycletotal=W(totalcount,5)-1;

%variable arrays for determining RMS values

RMSU=zeros(1,binnumber);
```

```
RMSV=zeros(1,binnumber);

devcounter=zeros(1,binnumber);

%%% determines the length of each cycle and the start time of each

cyclestarttime(1)=W(1,1); %sets first value to the first time

%initialization of cycles

cyclestartnumber(1)=1;

j=1;

for i=1:totalcount

if W(i,5)>j          %if the value is higher than the current cycle number, then you calculate the cyclemeasurements, the start time, the row number for the begining and ending of the cycle

                     %%and length.

cyclelength(j) = W(i-1,1)-cyclestarttime(j);

cyclestarttime(j+1)= W(i,1);

cyclestartnumber(j+1)=i;

cycleendnumber(j)=i-1;

if cyclelength(j)>=1550        %if the cycle is too long (in case of an error with the measurement system, it will cut the cycle in half.

test=cyclestarttime(j)+0.5*cyclelength(j);

k=cyclestartnumber(j);

while W(k,1)<=test

k=k+1;
```

```
end
cyclelength(j)=W(k-1,1)-cyclestarttime(j);
cycleendnumber(j)=k-1;
j=j+1;
else
j=j+1;
end
else
cyclemeasurements(j) =cyclemeasurements(j)+1;
end
end

%this next section calculates the average cycle length
cyclesum=0;
for i=1:cycletotal
cyclesum=cyclesum+cyclelength(i);
end
cycleavg=cyclesum/cycletotal

%Calculation of the standard deviation in cycle time
cycledev=0;
for i=1:cycletotal
cycledev=cycledev+(cyclelength(i)-cycleavg)^2;
end
```

cyclestddev =sqrt(cycledev/(cycletotal-1))

%Bin assignments

for i=1:cycletotal

binlength(i)=cyclelength(i)/binnumber; %determines the length of the bin for a given cycle based on the length of that particular cycle

for j=1:binnumber

%determining the start and end time values of a given bin

binstart(j)=cyclestarttime(i)+(j-1)*binlength(i);

binend(j)=cyclestarttime(i)+j*binlength(i);

for k=cyclestartnumber(i):cycleendnumber(i)

%if the time value of a given row is within the limits of that bin, assign the bin value column (6th column) to that bin value

if W(k,1)>=binstart(j) & W(k,1)<=binend(j)

W(k,6)=j;

else

end

end

end

end

%determines the phase angle

degree=360/binnumber;

```
%Sums all the values into a bin array

for i=1:cycletotal

for j=1:binnumber

for k=cyclestartnumber(i):cycleendnumber(i)

if i==W(k,5) & j==W(k,6)

%to eliminate aberrant outlier measurements, we test the x-velocity (the highest velocity and thus the best determinant) to see if it is within an acceptable range.

%If not, the measurement is replaced by a value based on the average of the two neighbouring values

if k==1

RMSforward=sqrt((W(k,7)-W(k+1,7))^2);

RMSback=sqrt((W(k,7))^2);

else

RMSforward=sqrt((W(k,7)-W(k+1,7))^2);

RMSback=sqrt((W(k,7)-W(k-1,7))^2);

end

if RMSforward >=0.5 & RMSback>=0.5

W(k,7)=(W(k-1,7)+W(k+1,7))/2;

else

end

%summing all U and V values into an array for each cycle and bin, and keeping a count of the number of measurements in each
```

```
localtotalU(i,j)=localtotalU(i,j)+W(k,7);

localtotalV(i,j)=localtotalV(i,j)+W(k,8);

bincount(i,j)=bincount(i,j)+1;

else

end

end

end

end

%determining the average value of the bin for each cycle

for i=1:cycletotal

for j=1:binnumber

if bincount(i,j)==0 & j==1

localaverageU(i,j)=0;

localaverageV(i,j)=0;

end

if bincount(i,j)==0 & j>1

localaverageU(i,j)=localaverageU(i,j-1);

localaverageV(i,j)=localaverageV(i,j-1);

else

localaverageU(i,j)=localtotalU(i,j)/bincount(i,j);

localaverageV(i,j)=localtotalV(i,j)/bincount(i,j);

end
```

```
end
end
```

%Determining the phase average for each bin overall

```
for i=1:cycletotal
for j=1:binnumber
phasetotalU(1,j)=phasetotalU(1,j)+localaverageU(i,j);
phasetotalV(1,j)=phasetotalV(1,j)+localaverageV(i,j);
end
end
for j=1:binnumber
phaseaverageU(1,j)=phasetotalU(1,j)/cycletotal;
phaseaverageV(1,j)=phasetotalV(1,j)/cycletotal;
end
```

%Determining RMS values by summing the squares of each difference for each measurement when compared to the phase average

```
for i=1:cycletotal
for j=1:binnumber
for k=cyclestartnumber(i):cycleendnumber(i)
if W(k,6)==j
phasedevU(1,j)=phasedevU(1,j)+(W(k,7)-phaseaverageU(1,j))^2;
phasedevV(1,j)=phasedevV(1,j)+(W(k,8)-phaseaverageV(1,j))^2;
devcounter(1,j)=devcounter(1,j)+1;
```

```
else
end
end
end
end

%determining the phase average
for j=1:binnumber
if devcounter(1,j)==1 | devcounter(1,j)==0
RMSU(1,j)=0;
RMSV(1,j)=0;
else
RMSU(1,j)=sqrt(phasedevU(1,j)/(devcounter(1,j)-1));
RMSV(1,j)=sqrt(phasedevV(1,j)/(devcounter(1,j)-1));
end
end

%Generating a random number so that a sample cycle can be included in a graph
f=ceil(cycletotal*rand)
for i=cyclestartnumber(f):cycleendnumber(f)
X(i,1)=(W(i,1)-cyclestarttime(f))*360/cyclelength(f);
X(i,2)=-W(i,7);
X(i,3)=W(i,8);
end
```

```
%Generating the results matrix

for j=1:binnumber

V(j,1)=j*degree;

V(j,2)=-phaseaverageU(1,j);

V(j,3)=phaseaverageV(1,j);

V(j,4)=RMSU(1,j);

V(j,5)=RMSV(1,j);

end

%writing results to file

dlmwrite('xn20yn15z10xzpa.txt',V, '\t');

%graphing results

plot(V(:,1),V(:,2),'b-',V(:,1),V(:,4),'r.',X(:,1),X(:,2),'g-')

xlabel('\fontname{Times} \phi [{}\circ]');

ylabel('\fontname{Times} [m/s]');

legend('\fontname{Times} \it <u>','u \prime','\rm sample cycle', 2)

axis ([0,360,-1.4,1.4])

grid

figure

plot(V(:,1),V(:,3),'b-',V(:,1),V(:,5),'r.',X(:,1),X(:,3),'g-')

xlabel('\fontname{Times} \phi [{}\circ]');

ylabel('\fontname{Times} [m/s]');

legend('\fontname{Times} \it <w>','w \prime', '\rm sample cycle' ,2)
```

```
axis ([0,360,-1.2,1.4])

grid
```

A.2 Diaphragm Graphing

```
function diaphragm()

% loads a given data file

load t1200.txt

%sets the x,y,z values into separate arrays

x=t1200(:,1);

y=t1200(:,2);

z=t1200(:,3)+1.29;

%graphing

xlin = linspace(min(x),max(x),17);

ylin = linspace(min(y),max(y),31);

[X,Y,Z] = meshgrid(x,y,z);

Z = griddata(x,y,z,X,Y,'cubic');

surf(X,Y,Z)

xlabel('\fontname{Times} x (mm)');

ylabel('\fontname{Times} y (mm)');

zlabel('\fontname{Times} z (mm)');
```

A.3 Flowrate and Displacement volume calculation

```
function trueflow() %calculating flowrates and displacement volumes

%loading the idealized model of VAD performance

load VADidealflow.txt

x=VADidealflow(:,1);

V=VADidealflow(:,2)*1000;

idealvolume=V*1000;

%loading corrected LDV results

load x29y15z20xypa2.txt

load x29yn15z20xypa2.txt

x1=x29y15z20xypa2(:,1)/360;

u1=x29y15z20xypa2(:,3);

u2=x29yn15z20xypa2(:,3);

%loading PIV results

load inletflow.txt

load outletflow.txt

x3=inletflow(:,1);

AREA=0.5*pi*(0.0095)*(0.0095);

y=length(x);

idealflow(1)=0;

%calculating Displacement volume from the idealized results

idealtotalV=(max(idealvolume)-min(idealvolume))
```

```
for i=2:y
flowV(i)=100*(V(i)-V(i-1));
idealflow(i)=flowV(i);
end
%calculating flowrate from LDV data
for j=1:50
flow(j)=(u2(j))*AREA*1000;
end
for j=51:100
flow(j)=(u1(j))*AREA*1000;
end
for k=1:50
realflow(k)=flow(k+50);
realflow(k+50)=flow(k);
end
%calculating displacement volume from LDV datat
volume(1)=max(V)*1000;
for m=2:50
volume(m)=volume(m-1)+(realflow(m)*0.01306*1000);
end
totalv1=volume(1)-volume(50);
%calculating alpha 1
```

```
alpha1=idealtotalV/totalv1

for j=1:50

realflow(j)=realflow(j)*alpha1;

end

for j=2:50

volume(j)=volume(j-1)+(realflow(j)*0.01306*1000);

end

for k=51:100

volume(k)=volume(k-1)+(realflow(k)*0.01306*1000);

end

totalv2=volume(100)-min(volume);

%calculating alpha 2

alpha2=idealtotalV/totalv2

%adjusting flowrates by alpha values

for j=51:100

realflow(j)=realflow(j)*alpha2;

volume(j)=volume(j-1)+(realflow(j)*0.01306*1000);

end

for i=1:7

PIVflow(i)=alpha1*inletflow(i,3)*1000;

PIVflow(i+7)=alpha2*outletflow(i+7,3)*1000;

end
```

```
totalV=max(volume)-min(volume)

Qavg=totalV*0.765*1000*60

A(:,1)=x;

A(:,2)=idealflow*60;

A(:,3)=idealvolume;

B(:,1)=x1;

B(:,2)=realflow*60;

B(:,3)=volume;

C(:,1)=x3;

C(:,2)=PIVflow*60;

dlmwrite('idealizedVADmodel.txt',A,'\t');

dlmwrite('LDVmodel.txt',B,'\t');

dlmwrite('PIVmodel.txt',C,'\t');

plot(x,A(:,2),'k-',x1,B(:,2),'b–')

grid

xlabel('\fontname{Times} t/T');

ylabel('\fontname{Times} Q [L/min]');

legend('\fontname{Times} ideal','\fontname{Times} LDV estimate',2);

figure

plot(x,idealvolume,'k-',x1,volume,'b–')

grid

xlabel('\fontname{Times} t/T');
```

```
ylabel('\fontname{Times} Displacement volume [cm^3]');

legend('\fontname{Times} ideal','\fontname{Times }measured',2);
```

Appendix B

Uncertainty Analysis

B.1 LDV Uncertainty Analysis

The reduction of measurement uncertainty was a major consideration in the design and operation of the experimental apparatus, with all equipment and the traversing system securely anchored to a common frame of reference. The main source of measurement uncertainty is deemed to be the velocity bias, that is the bias of measured velocity towards higher values, due to the higher representation of faster particles crossing the measurement volume. An estimate of this uncertainty can be made from the expression (Tavoularis (2005))

$$\frac{\overline{U}_m}{\overline{U}} \approx 1 + \frac{\overline{u^2}}{\overline{U}^2} \tag{B.1}$$

where $\overline{U}_m$ is the mean measured velocity, $\overline{U}$ is the actual mean velocity, and $\overline{u^2} = u'^2$ is the velocity variance (u' is the RMS value or standard deviation). At peak velocity at Point 1, $\overline{U}_m = 1.22$ ms^{-1} and $u' = 0.11$ ms^{-1} or $u'/\overline{U}_m \approx 9\%$. However, at a point of low velocity, such as Point 8 at $t/T = 0.75$, $\overline{U}_m \approx u' \approx 0.2$ ms^{-1}, which means the velocity bias is comparable to the measurement itself.

B.2 PIV Measurement Uncertainty Analysis

PIV analysis uses the formula

$$U = \frac{\Delta X}{M \Delta t} \tag{B.2}$$

where U represents the velocity, M represents the magnification factor, Δt is the time between successive frames, and ΔX is the displacement in the image plane. The uncertainty of the velocity can be computed as

$$\delta U = \sqrt{\left(\frac{\partial U}{\partial M}\right)^2 (\delta M)^2 + \left(\frac{\partial U}{\partial(\Delta X)}\right)^2 (\delta(\Delta X))^2 + \left(\frac{\partial U}{\partial(\Delta t)}\right)^2 (\delta(\Delta t))^2} \tag{B.3}$$

where

$$\frac{\partial U}{\partial M} = -\frac{\Delta X}{M^2 \Delta t} \tag{B.4}$$

$$\frac{\partial U}{\partial(\Delta X)} = \frac{1}{M \Delta t} \tag{B.5}$$

$$\frac{\partial U}{\partial(\Delta t)} = -\frac{\Delta X}{M (\Delta t)^2} \tag{B.6}$$

Next is to define the uncertainty in magnification, displacement, and time between frames. Magnification uncertainty occurs when distortions are introduced due to misalignment of the laser plane with respect to the camera in calibration, which is expressed in the general form as

$$\delta M = \sqrt{\left(\frac{\partial M}{\partial \alpha}\right)^2 (\delta \alpha)^2 + \left(\frac{\partial M}{\partial \beta}\right)^2 (\delta \beta)^2 + \left(\frac{\partial M}{\partial z}\right)^2 (\delta z)^2} \tag{B.7}$$

where α is a rotation about the $x-$axis, β is a rotation about the $y-$axis, and z represents a translation in the $z-$axis (Ramasamy and Leishman (2007)). The errors that result from the rotations can be defined as

$$x_e = \frac{x}{\cos(\alpha)} \tag{B.8}$$

$$y_e = \frac{y}{\cos(\beta)} \tag{B.9}$$

and in the image plane

$$X_e = \frac{X}{\cos(\alpha)} \tag{B.10}$$

$$Y_e = \frac{Y}{\cos(\beta)} \tag{B.11}$$

Using the identity

$$M = \frac{X}{x} = \frac{Y}{y} \tag{B.12}$$

and taking the respective derivatives we get

$$\frac{\partial M}{\partial \alpha} = \frac{-X\sin(\alpha)}{x\cos^2(\alpha)} = -M\sec(\alpha)\tan(\alpha) \tag{B.13}$$

$$\frac{\partial M}{\partial \beta} = \frac{-Y\sin(\beta)}{y\cos^2(\beta)} = -M\sec(\beta)\tan(\beta) \tag{B.14}$$

For the translation in the $z-$axis, the magnification can be defined as the ratio of the distances of the image and real object planes from the lens using the equation

$$M = \frac{d_i}{d_{ro}} = \frac{d_i}{z - d_i} \tag{B.15}$$

where d_i is the distance from the image plane to the focal point of the camera (also known as the camera's focal distance), and d_{ro} is the distance from the focal point to the real object plane (Ramasamy and Leishman (2007)). Taking the derivative with respect to z gives

$$\frac{\partial M}{\partial z} = \frac{2d_i}{z - d_i} \tag{B.16}$$

Substituting these expressions into Eq. B.7, and because the angles and angular changes can only be approximated, the nominal case assumes $\partial\alpha = \partial\beta = 1$ radian and $\alpha = \beta = 1$ degree, and a recorded value for $M = 0.414$. This produces a value $\delta M \approx 0.011$.

For calculating $\delta(\Delta X)$, three factors need to be considered: the error in calibration algorithm, the error due to displacement of the particle during the laser pulse (which is a non-zero timelength), and the error due to optical distortions of the size and shape of the particles in the flow. The error in the software can be calculated as

$$e_s = \frac{2t_{95}s_X}{\sqrt{N}} \tag{B.17}$$

where s_X is the standard deviation recorded by the calibration software (in pixels), N is the number of points, and t_{95} is a student t-factor of 95% certainty given N-1 degrees of freedom. Using $N = 20$, and $s_X = 0.96$ pixels, one gets $e_s = 5.71$ μm.The error due to displacement of the particle during the laser pulse is determined by the length of the laser pulse, which is usually no longer than 5 ns. Considering that the highest speed recorded in the flow did not exceed 1.5 m/s, one gets a maximum displacement of 7.5 nm, which, when doubled to account for errors at both the beginning and end of the pulse, results in an $e_l = 0.015$ μm. The error caused by distortions in the size and imaging of the particles, e_p is given in the general form

$$e_p = cd_\tau \tag{B.18}$$

where $c = 0.07$ is a constant and d_τ is the particle image diameter (Ramasamy and Leishman (2007)). This diameter is in turn a function of the true diameter of the particle d_p, the magnification, and the diffraction-limited minimum image diameter, d_{diff}, as

$$d_\tau = \sqrt{(Md_p)^2 + d_{diff}^2} \tag{B.19}$$

The diffraction-limited diameter d_{diff} is a function of the light as it is reflected off the particle and can be calculated as

$$d_{diff} = 2.44f(M+1)\lambda \tag{B.20}$$

where f is the focal number of the lens (in the present experiments $f = 2.8$) and $\lambda = 532$ nm is the wavelength of the laser light. For d_p, a value of 5 pixels was chosen as it was found to be representative of most particles in the flow. This results in a value of $e_p = 2.92$ μm. The timing uncertainty $\delta(\Delta t)$ is given by the laser temporal resolution of the PIV system, which for the PTU 9 time card is specified at 10 ns. Thus B.3 can be rewritten as

$$\partial U = \sqrt{\left(-\frac{\Delta X}{M^2 \Delta t}\right)^2 (\partial M)^2 + \left(\frac{1}{M\Delta t}\right)^2 (e_s^2 + +e_l^2 + e_p^2) + \left(-\frac{\Delta X}{M(\Delta t)^2}\right)^2 (\partial(\Delta t))^2} \tag{B.21}$$

All the previous values are substituted to give the following expression for uncertainty as a function of velocity

$$\partial U = \sqrt{0.00395U^2 + 0.00044} \tag{B.22}$$

The following table provides values of the predicted uncertainty for different measured velocities.

U (m/s)	δU (m/s)	$\delta U/U$
0.05	0.021	0.422
0.10	0.022	0.218
0.20	0.024	0.122
0.30	0.028	0.094
0.40	0.033	0.082
0.50	0.038	0.075
0.60	0.043	0.072
0.70	0.049	0.070
0.80	0.054	0.068
0.90	0.060	0.067
1.00	0.066	0.066
1.10	0.072	0.066
1.20	0.078	0.065
1.30	0.084	0.065
1.40	0.090	0.065

B.3 PIV Processing Uncertainty

In addition to the uncertainty estimated in the previous section, additional errors would be created if Δt and the interrogation window size are chosen in an improper manner. If the window size is too small for a given Δt value, particles with high velocity will completely leave the area enclosed by the window by the time of the second laser pulse, and, therefore, the velocity measurement would be biased towards the lower velocities. A rough estimate for the maximum velocity U_{max} that the PIV system will record is

$$U_{\max} = \frac{\Delta D}{\Delta t} \tag{B.23}$$

where ΔD is the length considered by the interrogation window. It is important to note that while this will provide a useful guideline, the actual maximum velocity PIV measurement will capture is highly dependent on your choice of interrogation method and processing.

Appendix C

Miscellaneous Data

This Appendix refers to an attached DVD, which contains

- the mathematical model of VAD performance as a Microsoft Excel Spreadsheet
- the PIV velocity contour maps for the $z = 11$ mm and $z = 29$ mm planes
- Raw numerical data files for the LDV and PIV for MATLAB
- Copies of all phase-locked PIV velocity contour maps
- A short manual on operation of the VAD experimental apparatus